FINAL REPORT

APPLIED THERMIONIC RESEARCH

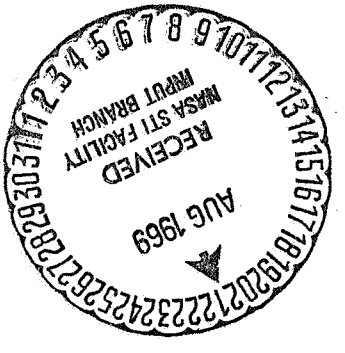

THERMO ELECTRON

CORPORATION

Thermo Electron Corporation, 85 First Avenue, Waltham, Massachusetts 02154

Report No. TE 4092/3-108-69

FINAL REPORT

APPLIED THERMIONIC RESEARCH

This work was performed for the Jet Propulsion Laboratory, California Institute of Technology, sponsored by the National Aeronautics and Space Administration under Contract NAS7-100.

Contract 952184

1 December 1967 - 1 December 1968

E. P. Gyftopoulos, G. N. Hatsopoulos
D. Lieb, F. Rufeh
M. Shaw and L. van Someren

Prepared for

Jet Propulsion Laboratory
Pasadena, California

Acknowledgments

This program was directed by Mr. O. S. Merrill of the Jet Propulsion Laboratory, California Institute of Technology.

The authors would also like to acknowledge the assistance of A. W. Donaker in the taking and reduction of data and F. J. Campagna, E. Ameen, and C. Yassamedis in the construction of the converters.

TABLE OF CONTENTS

Chapter		Page
	Acknowledgments	ii
I	Introduction and Summary	I-1
II	Electronegative Additives M. SHAW	II-1
	A. Introduction	II-1
	B. Apparatus	II-1
	1. Mass Spectrometer and Vacuum Apparatus	II-2
	2. Knudsen Cell and Cesium Oxide Capsules	II-3
	3. Electronics	II-4
	C. Electrical Characteristics	II-4
	1. Calibration with Cesium	II-4
	2. Stability of Mass Spectrometer Multiplier	II-6
	3. Noise Level	II-6
	D. Cesium Oxide Experimentation	II-7
	1. First Capsule	II-9
	2. Second Capsule	II-12
III	Quantum-Thermodynamic Meaning of Electronegativity and Work Function E. GYFTOPOULOS and G. HATSOPOULOS	III-1
	A. Electronegativity	III-1
	1. Introduction	III-1
	2. Statistics of Grand Canonical Ensembles	III-3
	3. Electrochemical Potential of Atoms and Atomic Ions	III-5
	4. Electronegativity of Atoms and Atomic Ions	III-10
	5. Orbital Electronegativity	III-12

Chapter		Page
	B. Work Function	III-15
	1. Introduction	III-15
	2. Localized Spin-Orbitals for Crystal Lattices	III-16
	3. Electronegativity and Chemical Potential	III-22
	4. Work Function and Electronegativity	III-25
	References for Chapter III	III-27
IV	Parametric Data F. RUFEH, D. LIEB, and L. VAN SOMEREN	IV-1
	A. Emission Characteristics of a Duplex Vapor-Deposited Tungsten Emitter	IV-1
	1. Introduction	IV-1
	2. Emitter Preparation	IV-1
	3. Work Function Measurements	IV-2
	4. Cesium Families	IV-3
	5. Spacing Families	IV-5
	6. Summary of the Data	IV-6
	B. Emission Characteristics of a Single Crystal Tungsten Emitter	IV-59
	1. Emitter Preparation	IV-59
	2. Work Function Measurements	IV-59
	3. Performance Data	IV-60
	C. Vacuum Work Function Measurement Apparatus	IV-85
	1. Ground and Annealed Tungsten Vapor-Deposited from the Fluoride	IV-87
	2. Abraded and Annealed Single Crystal Tungsten	IV-88

Chapter		Page
	D. Analysis and Correlations of Experimental Data	IV-95
	1. Voltage Loss Correlation	IV-95
	2. Work Function Correlation	IV-96
	References for Chapter IV	IV-111
V	Studies on Vapor-Deposited Tungsten Emitter Materials L. VAN SOMEREN	V-1
	A. Fluoride Material	V-2
	1. As Received	V-2
	2. Heat Treatment	V-5
	B. Chloride Material	V-16
	1. As Received	V-16
	2. Heat Treatment	V-18
	C. Morphology of Deposits	V-33
	1. Results	V-39
	2. As Received Material	V-40
	D. Discussion and Conclusions	V-50
VI	Plasma Analysis D. LIEB	VI-1
	A. Introduction	VI-1
	B. Discussion	VI-1
	1. Equations and Assumptions	VI-1
	2. Computer Technique	VI-5
	3. Directed Current Boundaries	VI-6
	4. Influence of Pressure and Spacing on Plasma Characteristics	VI-8
	5. Ion Mobility	VI-12
	6. Conclusions	VI-13
	References for Chapter VI	VI-15

CHAPTER I

INTRODUCTION AND SUMMARY

This report presents the work performed under Contract NAS7-100 for NASA/JPL during the one-year period ending December 1, 1968. This work is a continuation of an applied research program which has been in progress for several years. The primary objective of the program is the improvement of converter performance by a continuous interplay between theoretical analyses and experimental results.

During the past year, a modulated quadrapole mass spectrometer system was constructed in order to study the thermochemical properties of cesium-oxygen system (Chapter II). A cesium-oxygen sample was formed within a tungsten capsule, which could be fractioned within the Knudsen cell. The molecular beam issuing from the cell aperture was chopped mechanically and ionized by electron bombardment. The ionic species were then mass-analyzed by the quadropole unit, and the selected ion signal was amplified by a phase-sensitive amplifier synchronized with the beam chopper.

The mass-spectrometer system was calibrated with pure cesium in the Knudsen cell. The cell was then charged with a capsule in which cesium oxide had been formed according to the stoichiometry of CsO (equal molar quantities). Experiments with this and with a subsequent CsO capsule indicated that the effective cesium pressure from the CsO samples was considerably lower than for pure cesium at the same Knudsen-cell temperature. No mass peak attributable to oxygen or to cesium-oxygen compounds was observed; this may be due to interaction

between the CsO sample and tungsten (or other materials) within the Knudsen cell.

Rigorous definitions are given of electronegativity of atoms, neutral or ionized, and of atomic orbitals (Chapter III). The definitions are consistent with the rules of the statistics of ensembles and the quantum-mechanical picture of atomic species, and the relation between surface orbital electronegativity and work function, from the standpoints of both thermodynamics and quantum mechanics, is analyzed. It is shown, first, that the electronic structure of crystals can be described by means of spin-orbitals which are localized around individual lattice sites; second, that electronegativity is related to the chemical potential of an electron in a spin-orbital; and, third, that the work function of a uniform surface equals the neutral orbital electronegativity of a spin-orbital localized around a surface atom.

The emission characteristics of a vapor-deposited tungsten emitter with a molybdenum collector were investigated in a variable-spacing converter (Chapter IV). The set of data obtained is particularly useful for comparison with the results of theoretical analysis and for studies of interrelationships between the various converter parameters, since it includes work function measurements and variable spacing data as well as cesium pressure families. The data were used to investigate the dependence of the voltage drop on the product of cesium pressure and interelectrode spacing Pd, cesium pressure P and ion richness β. At constant values of Pd and β, a dependence on cesium pressure was observed.

Data were also obtained from a variable-spacing, guard-ring converter with a single crystal tungsten emitter and a molybdenum collector. Performance data and work function data were obtained in the emitter temperature range of 1700 to 1900°K and an inter-electrode spacing range of 0.5 to 40 mils. In the emitter temperature range investigated, the performance of this converter was higher than that of a converter with an etched rhenium emitter and a molybdenum collector by 60 to 120 millivolts.

A vacuum work function measurement apparatus was constructed and several emitter surfaces were examined. A tungsten emitter vapor-deposited from the fluoride, then ground and annealed, gave a value of 4.53 ± .02 eV, and an abraded and annealed single-crystal tungsten emitter gave a value of 5.15 ± .01 eV. The apparatus enabled the reproducible, rapid measurements of unmounted emitter disks.

Because of the increasing importance of the various techniques of the deposition of tungsten from the vapor, a study of the physical characteristics of the fluoride and chloride materials was made using photomicrographic and x-ray techniques (Chapter V). The results of examination of both the as-received material and the material after various heat treatments are described. It was concluded that material deposited from the fluoride shows excellent grain stability, superior to wrought powder metallurgy or A. V. C.* material. Material deposited from the chloride has very poor grain stability. In each case, the preferred orientation prevailing in the as-received material is reasonably stable during heat treatments which alter the microstructure. However, grinding produces a randomly-oriented surface layer, and annealing this causes only slow and partial reversion to the underlying orientation.

*A. V. C. - Arc Vacuum Cast

The computer program for plasma analysis developed previously was improved by using a different integration technique (Chapter VI). A factor of two to three improvement in running time was obtained. Directed-current boundary conditions were substituted for the random-current boundary conditions originally chosen. This substitution resulted in second-order changes in the spatial distribution of the plasma parameters. The sensitivity of the solutions of the plasma equations to inter-electrode spacing and to cesium pressure was examined. The theoretical results were in reasonable agreement with experimental data except in the location of the ignition point. The sensitivity of the solutions to ion mobility was also examined, and it was found that the spatial distribution of the plasma parameters is a strong function of ion mobility. The actual current and voltage of the converter, however, did not show a strong dependence on ion mobility.

CHAPTER II

ELECTRONEGATIVE ADDITIVES

M. Shaw

A. INTRODUCTION

A mass spectrometer has been built to study the species which volatilize from heated samples of thermionic converter additives. Experiments in the cesium-oxygen system have been carried out using this system.

B. APPARATUS

The system is comprised of three parts (see Figures II-1 and II-2):

(a) the mass spectrometer and vacuum apparatus,
(b) the Knudsen cell and associated apparatus, and
(c) the electronics for signal amplification.

The Knudsen cell contains the species to be volatilized and is situated in a separately-pumped chamber. The mass spectrometer is housed in a second separately-pumped chamber connected to the first through a small aperture. Most of the substance volatilizing from the Knudsen cell is removed by the first pump, except for those molecules contained in a small solid angle about the forward direction which comprise the molecular beam and others which have interacted with the walls of the system. The diameters of the apertures in the partition between the two chambers and in the shield around the ionizing section of the mass spectrometer are such that

molecules proceeding directly from the Knudsen cell can be distinguished (as discussed below) from those which have arrived by an indirect course; this is accomplished by modulating the direct beam and using a shutter. This is one of the principal reasons for employing the molecular beam method -- it is important to know that molecules which may have interacted with the walls of the system do not mask to the desired signal. As is typical for molecular beam systems, the number of molecules in the direct beam is small compared to the total number of molecules effusing from the Knudsen cell. Since the pumping capacity of the system is usually rather limited, it is necessary to employ some electronic means of improving the signal-to-noise ratio. We have chosen to modulate the direct beam and amplify the current from the electron multiplier of the mass spectrometer with a phase-sensitive detection system.

1. Mass Spectrometer and Vacuum Apparatus

A schematic diagram of the system is shown in Figure II-1 and a photograph in Figure II-2. The mass spectrometer is an electric quadrupole model (250) manufactured by E.A.I. The main pumps are 50 liter/sec ion pumps. Roughing is accomplished with sorption pumps. Construction of the main vacuum system has involved (1) modifying the "cross" by an apertured partition to separate the high vacuum chamber housing the mass spectrometer from the intermediate vacuum chamber housing the Knudsen cell; (2) welding in the pumping lines and leak checking; (3) mounting a shutter, chopper, and window on one of the ports (the rotary feed-throughs which drive the chopper and shutter are magnetically-coupled, bakable devices); and (4) machining of an apertured shield to surround the ionizer and

alignment both of the shield on the mass spectrometer and of the mass spectrometer with respect to the molecular beam direction. Alignment was somewhat difficult due to the unavailability of scale drawings of the mass spectrometer and the desirability of keeping it under vacuum as much as possible. The shield is coupled to a transfer tube passing through the wall of the vacuum chamber for "cryopumping" condensible vapors.

Shielding the mass spectrometer from molecules not in the direct beam is necessary to eliminate "ghost" signals when the lock-in amplifier is in operation. The modulated beam can be blocked from the ionizer with the shutter to establish the signal zero.

2. Knudsen Cell and Cesium Oxide Capsules

Photographs of the Knudsen cell assembly are shown in Figures II-3 and II-4. The purpose of the Knudsen cell is to provide an isothermal container for the volatilizing species (cesium oxide, e.g.,) under study. The desired temperature is maintained with two heaters. In addition, the apparatus is designed to keep the oxide free from contamination during pump-out and baking of the system. This is accomplished by breaking a capsule containing the oxide in the Knudsen cell in the evacuated system after bakeout. A mechanical bellows-coupled lever action is provided for this purpose.

Cesium and its oxides are highly susceptible to contamination; hence, a special apparatus was constructed for reacting desired quantities of cesium and oxygen together under vacuum. The apparatus, shown in Figure II-5, is constructed of copper tubing with a

molybdenum section and a tungsten section. The tungsten section, the capsule in which the oxide is formed, is connected to the rest of the system through a copper tube which is pinched off to seal the capsule.

The molybdenum section is a plug in the oxygen feed line which is used to isolate the oxygen line from the rest of the system during outgassing and cesiating of the capsule. When oxygen is desired, this plug is cracked open by pinching the copper tube. A measured quantity of oxygen is then allowed to react with the cesium. During the oxidation of cesium, a temperature gradient is maintained such that the tungsten section containing the cesium is kept at about 100°C (to increase the rate of oxidation), and the immediate surroundings are kept at higher temperatures to prevent condensation of cesium. After final evacuation of the system, the capsule is pinched off and is ready for use in the Knudsen cell.

3. Electronics

The particle detector of the mass spectrometer is an electron multiplier. The current output of this multiplier at a given setting of the mass spectrometer consists of the sum of the modulated beam, a dc background from molecules effusing from the Knudsen cell outside of the direct beam and reaching the ionizer after bounding off the walls of the system, and noise. This signal is fed into a phase-sensitive detection system (PAR Model 120 Lock-In Amplifier and Pre-Amplifier Model 112) to improve the ratio of signal to noise.

C. ELECTRICAL CHARACTERISTICS

1. Calibration with Cesium

The system was calibrated for cesium by loading the Knudsen cell with a capsule containing pure cesium and observing the output

of the multiplier as a function of the temperature of the Knudsen cell. The results are shown in Figure II-7. Also plotted in this figure is the cesium vapor pressure as a function of temperature. The multiplier output as observed on the scope has the slope which would be expected from the vapor pressure data. The maximum temperature at which the Knudsen cell could be operated with pure cesium was 138°C, due to the limit in the capacity of the ion pump on the Knudsen cell chamber. The calibration showed that a modulated signal of peak-to-peak amplitude 21 ± 2 mV could be observed on the scope for a Knudsen cell pressure of one micron of pure cesium.

Two additional ways of observing the multiplier output besides direct observation with the scope were employed: (1) lock-in amplifier (PAR Model 120) with an input resistor of $10^6\ \Omega$, and (2) lock-in amplifier preceded by a preamplifier (PAR Model 112). The input resistor used with the preamplifier was $10^8\ \Omega$. In mode (1),

$$\frac{\text{peak-peak scope signal (mV)}}{\text{lock-in amplifier meter (mV)}}$$

is approximately 4, but this has been observed to vary by as much as a factor of 2 depending on the harmonic content of the signal, including noise.

In mode (2):

$$\frac{\text{lock-in amplifier meter } (10^6\ \Omega \text{ resistor input})}{\text{lock-in amplifier meter (with pre-amp)}} = 10^3$$

In addition, the observations on cesium oxide were taken with an increased gain (over the cesium calibration) of approximately 5, which was obtained by decreasing the resolution of the mass spectrometer. This effect can be seen in Figure II-8, which is a graph

of the setting of the instruments resolution control vs intensity of the N_2 peak.

2. Stability of Mass Spectrometer Multiplier

A nitrogen beam produced by the gas manifold shown in Figure II-6 has been used periodically over the lifetime of the system to check the response of the multiplier. This response has been shown to be stable in spite of unavoidable instances of exposure to air. The practice of bringing the system up to atmospheric pressure with dry nitrogen has probably been helpful in this respect. Also, it is speculated that cesium may be beneficial to the multiplier and act as a countereffect to the exposure to air.

3. Noise Level

The noise placing a lower limit on the signal which can be observed has been observed to be of two types:

(a) Noise arising from the voltage supplies controlling the temperature of the Knudsen cell. The temperature, which is a strong function of heater current, varies slightly as the controllers cycle on and off, and at the lowest signal levels a corresponding variation in signal can be observed. This source could be reduced by using a different method (dc perhaps) of supplying heater power.

(b) Noise which is a function of background pressure. Noise is worse (by a factor of about 10) in the low mass range of the mass spectrometer (1 - 50) where there are many background peaks. When the background pressure was reduced by a more extensive bakeout at higher temperatures,

this noise was also significantly reduced. The noise is independent of the position of the shutter. Optimizing the resolution tends to limit this noise; however, if the resolution is too sharp, the time constant of the lock-in amplifier tends to obscure weaker signals and the intensity of the signal itself is reduced. From our experience, we believe that the most effective way to reduce this source of noise is to increase intensive bakeout of the Knudsen cell before breaking open the capsule.

Using the conversion factors given in Section B-1 of this chapter, we calculated the Knudsen cell partial pressures corresponding to the various observed noise levels, as shown in Table II-1. These values were exceeded when the temperature of the Knudsen cell was raised above the bakeout temperature, especially for the first capsule. Some gettering action was observed in the case of the second capsule, and we could gradually work beyond the bakeout temperature.

D. CESIUM OXIDE EXPERIMENTATION

Data have been obtained from two capsules of cesium oxide. Both capsules contained the stoichiometric amounts of cesium and oxygen to form "CsO". The initial amount of cesium was 1/2 gram. The apparatus and procedure for forming capsules of cesium oxide are described in Section B-2. The material of the capsule was tungsten (with a copper "pinch-off" end), chosen because tungsten is brittle enough even at 50 - 60°C to be crushed by the mechanical action of the Knudsen cell assembly and was predicted to be relatively inert with respect to cesium and its oxides (at moderate temperatures).

TABLE II-1

NOISE LEVEL

Experiment	Bakeout Temperature of Knudsen Cell	Mass/Charge Range	Partial Pressure in Knudsen Cell Corresponding to Noise Level
First Capsule	250°C	1 - 50	1×10^{-6} torr
		5 - 500	1×10^{-5} torr
Second Capsule	475°C	1 - 50	2×10^{-7} torr
		5 - 500	2×10^{-6} torr

The fuse braze between tungsten and copper was performed in vacuum. Brazing in a hydrogen atmosphere seemed to produce a porous structure in the braze.

The difference between the two capsules of cesium oxide reported here has been in the heat treatment given the pinched-off capsule following cesium oxidation. The first capsule was heated to 250°C for approximately 24 hours (before it was cracked) during system bakeout. Because analysis with the mass spectrometer indicated that the contents of the capsule may not have been in thermodynamic equilibrium, and since it is often observed that cesium oxidation is kinetically limited, the second capsule was heat treated at 475°C.

1. First Capsule

With the apparatus described in Section B-2, a capsule containing equal stoichiometric amounts of cesium and oxygen (to form "CsO") was built. The initial amount of cesium was 1/2 gm. This capsule was placed in the Knudsen cell, and the system with the Knudsen cell was baked out up to a Knudsen cell temperature of 250°C. With the entire system at room temperature the background pressures were:

$p_1 = 2 \times 10^{-8}$ torr (chamber containing Knudsen cell)

$p_2 = 1 \times 10^{-7}$ torr (chamber containing mass spectrometer)

The capsule was cracked and mass scans were taken as a function of the temperature of the Knudsen cell. Mass scans showed that the only modulated signal present (i.e., from the chopped molecular beam) was due to cesium.

Using the pre-amp, the minimum signal level limited by noise which could be observed for this capsule (see Table II-1) corresponded to about

$2 - 5 \times 10^{-6}$ torr - in mass/charge range up to 50
$2 - 5 \times 10^{-5}$ torr - in mass/charge range from 50 to 500

The noise was a function of mass setting because the background was much worse at the lower mass numbers.

Both lock-in amplifier and scope were observed to track together where the signal was large enough to be seen on the scope. Two runs (described in detail below) from room temperature up to 230°C were taken. Above 230°C the outgassing level was too high for the ion pump. At the end of the second run the ion pump surrounding the Knudsen cell showed evidence of contamination, and no further data were taken on this capsule.

a. First Run

The results are shown by curve A of Figure II-9. The shape of the curve is qualitatively the same as was found in the second run. The difference in amplitude of a factor of about two between the two runs can be explained at least in part by the fact that better resolution (resulting in lowered intensity) was used in the first run. The signal was qualitatively reproducible in the sense that the curves in Runs I and II had the same shape and the same magnitude within a factor of 2.

b. Second Run

The results are shown by curve B of Figure II-9. It would have been interesting to have followed the cooling curve all the way back

to room temperature. At this point, however, the ion pump started drawing too much current. There appears to be a small peak at 200°; however, the system was less stable due to outgassing at higher temperatures, and this peak may be an artifact.

c. Conclusions

Although only cesium was observed, the temperature dependence of the signal was very different from that to be expected from a pure cesium reservoir:

(1) the temperature dependence was not exponential;

(2) the magnitude at higher temperatures was much smaller than would be expected for pure cesium. For example, the signal from pure cesium was observed to be 48 mV at 130°C and 84 mV at 140° (see Section B-1). In this experiment with cesium oxide, the maximum cesium signal was 20 mV (145°C), and at 200°C it was less than 5 mV. The signal predicted from our data for pure cesium at 200°C would be over 600 mV. According to our calibration, a partial pressure of 1 μ of cesium in the Knudsen cell corresponds to a 21 mV signal on the scope.

No other mass peaks at the modulation frequency were observed over the mass/charge range of 1 - 500.

Questions arising from these data include:

(1) Why were no oxides or oxygen observed?

(2) Can the noise level of the system be reduced so that higher gain can be used in a search for oxides and oxygen?

(3) Were the contents of the capsule at equilibrium?

In the hope of answering these questions a second capsule was prepared.

2. Second Capsule

A second capsule was formed containing the same quantities of cesium and oxygen ("CsO") which were brought together under the same conditions as in the first capsule. The purpose of this capsule was to aid in answering the questions posed above.

The system was baked out until the background pressures were:

$p_1 = 1 \times 10^{-8}$ torr — with the Knudsen cell maintained at 475°C (24 hours at this temperature)

$p_2 = 1 \times 10^{-7}$ torr

According to the mass spectrometer analysis of the background, these gases were primarily composed of mass peaks of 1 - 44 mass/charge units.

After the capsule was cracked, it was possible to go to increasingly higher temperatures with each succeeding experimental run. Apparently the cesium and cesium oxides were "gettering." It was found that increased bakeout did improve the ratio of signal to noise.

It was thought that annealing the capsule before cracking it would bring the cesium oxide into an equilibrium state if the oxidation were kinetically limited.

A total of eight experimental runs were taken with this capsule. The gettering action has permitted each succeeding run to be taken at a temperature slightly higher than that of the preceding run.

a. Run I (See Figure II-10)

Peaks were observed at Mass No. 133 and Mass No. 66. Although it may have been present at lower temperatures, No. 66 was first observed at 210°C. No. 66 had the same temperature dependence as No. 133 (Cs^+) and is probably Cs^{++}. Since there was a relatively large amount present, we hypothesize that it was not formed directly by electron bombardment, but may be the result of fragmentation of an oxide. This mass peak was not observed in subsequent runs until Run V. Qualitatively the curve for No. 133 had the same shape as that observed for the first capsule, except that the peak occurred at a temperature higher by 60°C.

b. Run II (See Figure II-11)

Data were taken on both the heating and cooling curves. The only mass peak observed was for Cs^+. Its temperature dependence was completely different from that observed in Run I. An appreciable signal was not observed until 400°C, and the heating and cooling curves did not coincide. Again, no coherent signals for oxygen or the oxides were seen.

c. Run III (See Figure II-11)

Straight lines were drawn between points to illustrate the temperature sequence of taking data. Points were also numbered in order.

Run III again exhibited nonequilibrium behavior. The lowest level signals were quite noisy, as shown. Up to 600°C, only Cs^+ was observed. Background noise was getting more pronounced at 600°C.

d. Run IV (See Figures II-11 and II-12)

The heating and cooling points began to look more like equilibrium data in Run IV although this was shown to be illusory to Run V. (The pressure decrease at point #6 suggests a solid-vapor equilibrium.) The signal taken at 565°C remained constant for more than an hour. Most of these data points (as well as those in Run III) were taken with the pre-amp and $10^8\ \Omega$ input resistor.

e. Run V (See Figure II-12)

The data points for Run V as well as for Runs IV and VI are shown in Figure II-12. Again we see the usual nonequilibrium behavior. At point 4, the current showed a tendency to decrease over a 15-minute interval. At 700°C, the noise level was roughly 100 times worse than the values found for 475°C. The outer walls of the vacuum chamber opposite the Knudsen cell were becoming very hot, and the pressure in that chamber was rapidly rising, reaching 3×10^{-6} torr. Accordingly, some copper tubing was wrapped around the outer wall of the chamber for cooling water.

f. Run VI (See Figure II-12)

Cooling the wall of the chamber surrounding the Knudsen cell had the beneficial effect of allowing data to be taken beyond 750°C. At about

800°C the background pressure began to rapidly climb again. Between 700°C and 800°C the background was again high, but some signals of interest were also increasing with temperature. The Cs^+ signal was quite strong. In addition, signals at Nos. 66, 80, 133, and 160 were present at 800°C (see Table II-2).

TABLE II-2

SIGNALS APPEARING AT 800°C

Mass/Charge	Lock-In Signal (10^6 Ω input R)
133	0.35 mV (see Figure II-12)
66	0.035 (increasing to .12 mV)
80	0.1
160	0.01

g. Run VII

In order to reduce background pressure, the Knudsen cell was baked out at 750°C for 24 hours. On the basis of the previous runs, it was assumed that the vapor pressure of the species of interest was so low that only an insignificant amount would be lost, while background gases of no interest might boil off. The resulting background pressure was reduced to a level at which it was possible to operate at 850°C for about 10 minutes. The signals observed are shown in Table II-3.

TABLE II-3

SIGNALS OBSERVED AT 850°C

Mass/Charge	Lock-in Signal (10^6 Ω input R)
133	0.1 mV
66	0.13
16	0.1 ± .1
94	0.03
77	0.08
52	0.3
44	0.6
28	0.6

It can be seen that the 66 peak is larger than that for 133. However, this situation can hardly be regarded as stable, as the pressure was increasing. An indication at 16 appeared; the noise was worst between 1 and 28.

The peak at 77 is probably the same as the one reported at 80 in Run VI. The peaks appearing at 28, 44, 52, and 94 were presumably contaminants.

h. Summary

For all runs, the predominant mass peak observed for both capsules was 133, corresponding to Cs^+. The temperature dependence was nonexponential and not characteristic of an equilibrium system. The signal peak gradually moved to progressively higher temperatures. The magnitude of the signal at high temperatures was weak compared to that given by pure cesium.

The peak appearing at 66 in Runs I, VI, and VII of the second capsule had approximately the same temperature dependence as No. 133, as shown in Figure II-10, but was usually weaker in magnitude. We have tentatively identified it as Cs^{++} for these reasons. Since the probability of forming Cs^{++} directly from Cs by electron bombardment would be slight, we suspect that it may be formed by another and as yet unidentified process. An example might be a fragmentation process in which Cs^{++} and a negatively-charged particle (which would not be detected) were the products.

The peaks observed in Runs VI and VII at 28 and 44 were possibly N_2 or CO and CO_2. Other peaks at 94, 80, 77 and 52 might have been hydrocarbons. In Run VI a peak was seen at approximately 160 which, due to the reduced resolution setting, might have been CsO_2 (165). Other than this peak, no indication of cesium oxides was found. The oxides most likely to have been found would have been CsO (149), CsO_2 (165), Cs_2O(282), and Cs_2O_2(298).

It is apparent that these results are not yet indicative of the thermodynamic properties of the cesium-oxygen system. The intensity of the cesium signal is indeed considerably depressed below that which was observed when an oxygen-free cesium sample was used. For example, the data in Figure II-12 (Run III) indicate a cesium pressure of about $6 \times 10^{-}$ torr for a Knudsen cell temperature of 600° C, whereas the vapor pressure of pure cesium at this temperature is several hundred torr. However, the lack of any clearly defined signals from oxygen or cesium-oxygen compounds, and the lack of temperature reproducibility of the cesium signal, suggest that some other processes may be affecting the data. It is possible that materials contained within the Knudsen cell,

e. g. , tungsten, may have reacted with the cesium oxide, resulting in a relatively non-volatile metal oxide or mixed oxides of metal and cesium. Future experiments should be designed to eliminate this possible container-material effect.

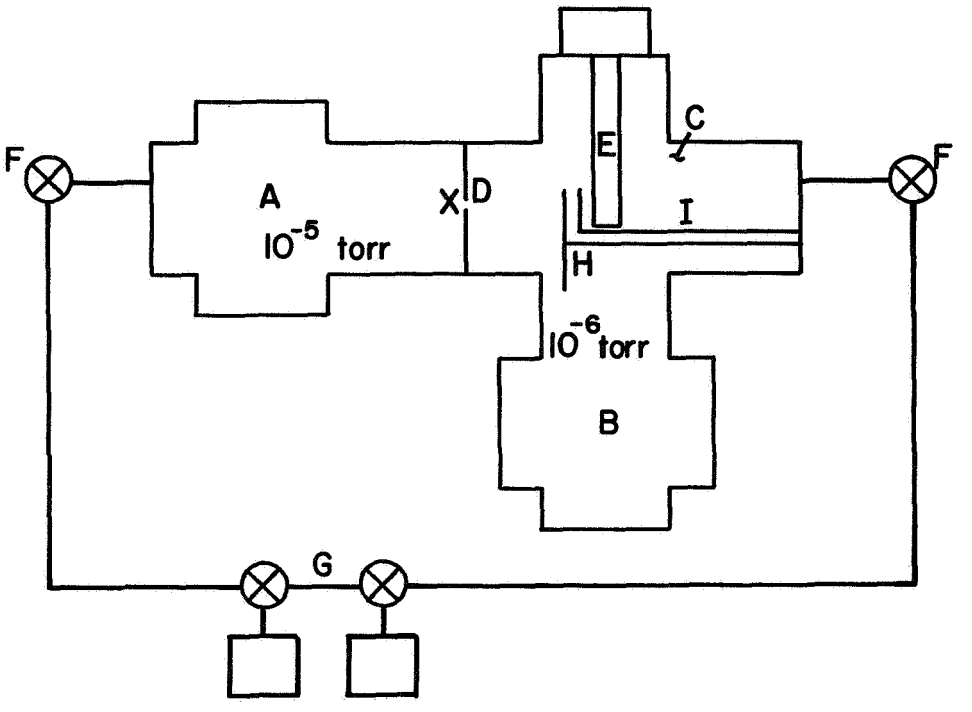

A) Double-flanged 50-liter/ sec ion pump which evacuates space where Knudsen cell resides

B) Single-flanged 50-liter/ sec ion pump which evacuates high-vacuum chamber

C) High-vacuum chamber or cross

D) Position of apertured partition between Knudsen cell chamber and high-vacuum chamber

E) Quadrupole

F) High-vacuum valves

G) Sorption pump manifold

H) Chopper

I) Shutter

X) Knudsen cell (5×10^{-3} torr)

Figure II-1 Schematic Diagram of Mass Spectrometer System.

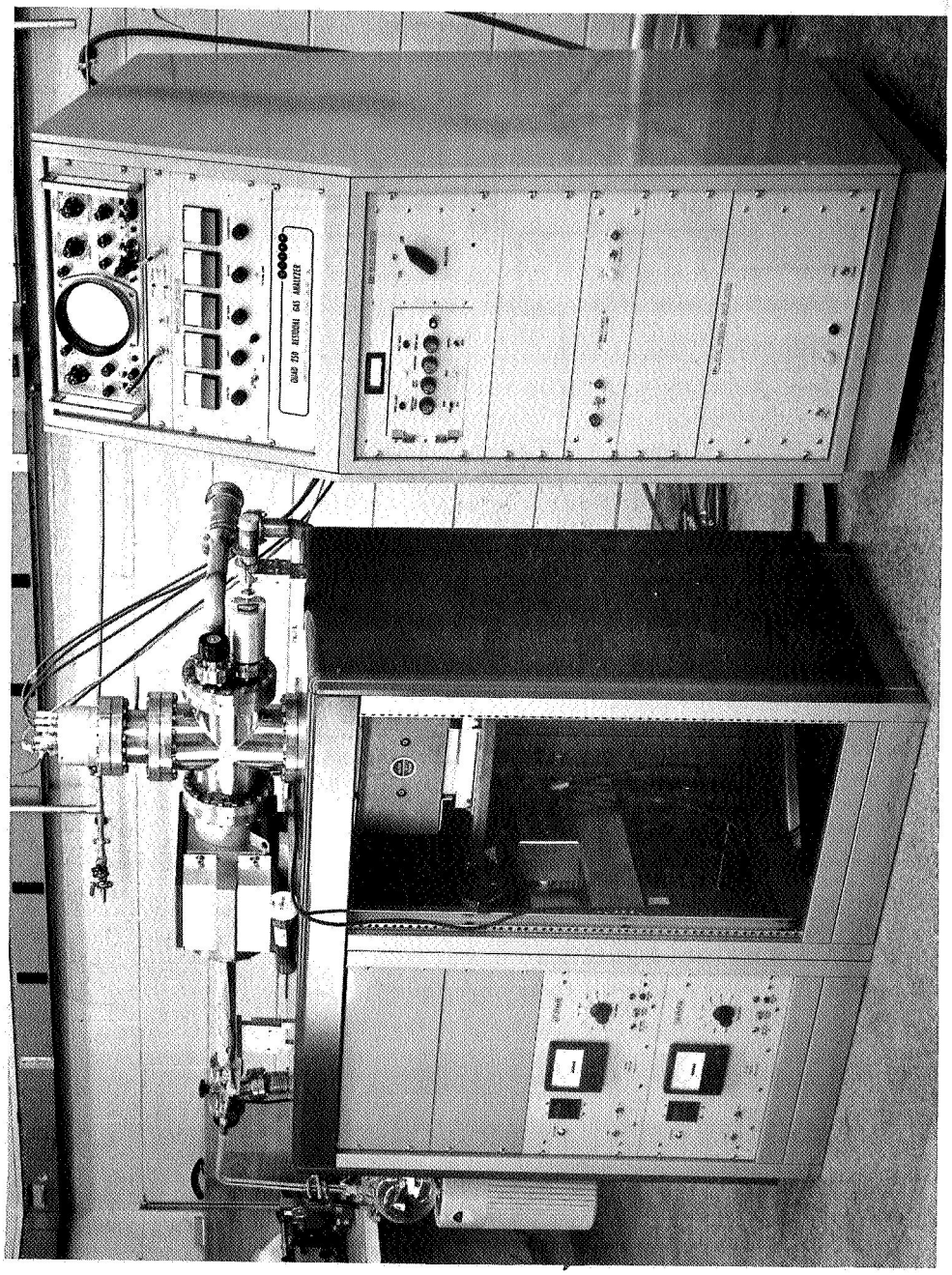

Figure II-2 Mass Spectrometer and Vacuum Apparatus.

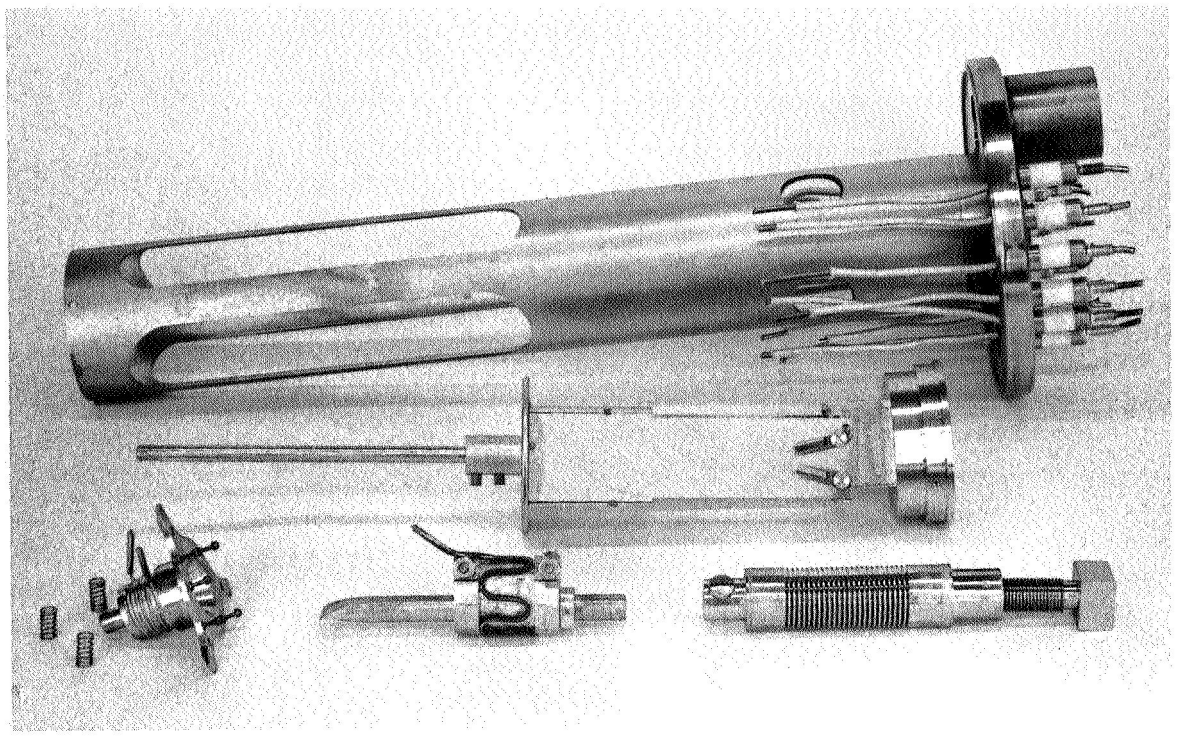

Figure II-3. Knudsen Cell Disassembled.

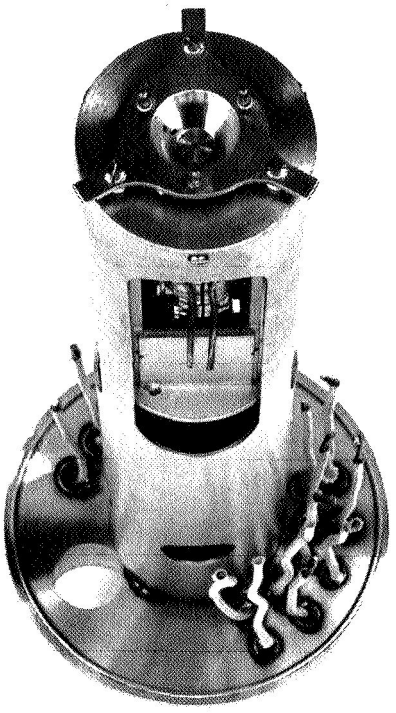

Figure II-4. Knudsen Cell Assembly.

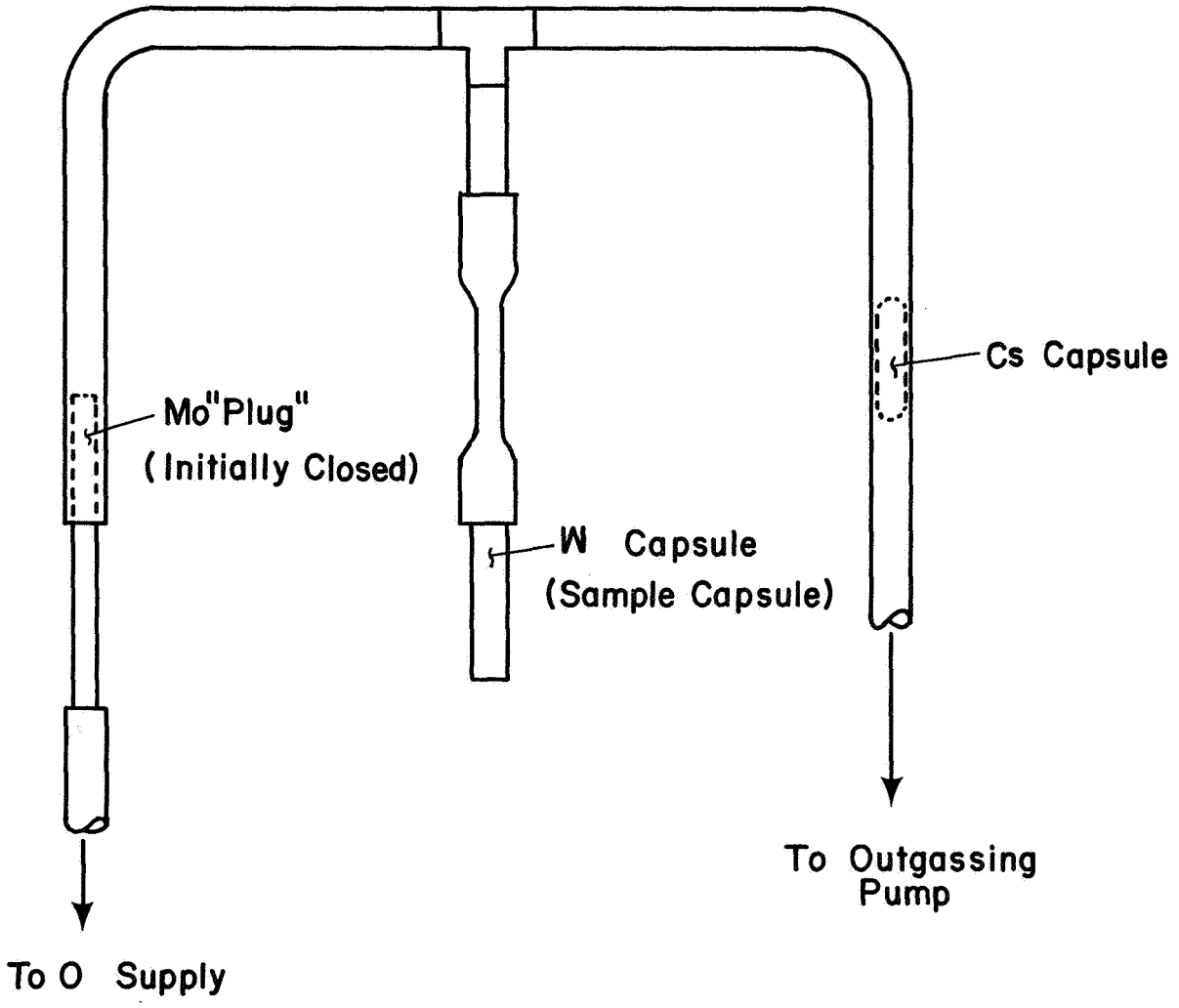

Figure II-5 Cesium Oxide Forming Apparatus.

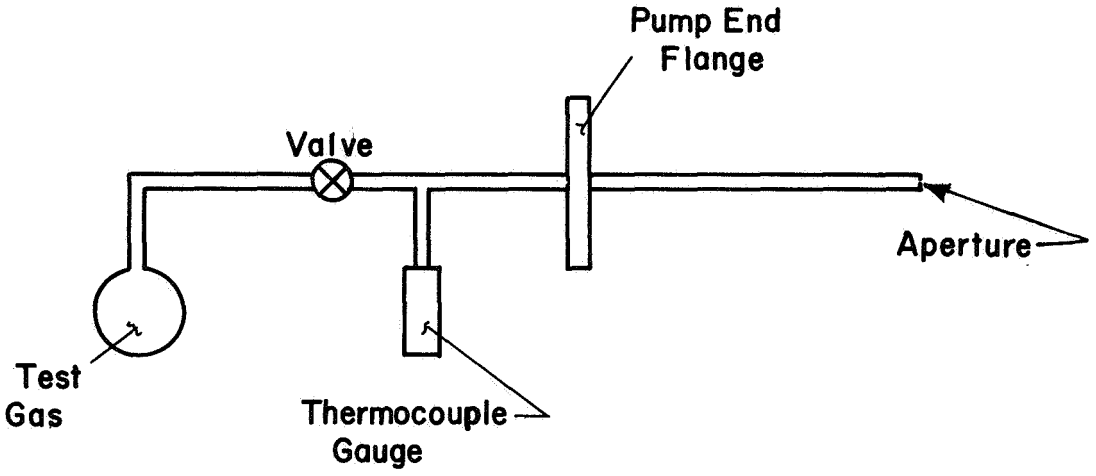

Figure II-6 Gas Manifold.

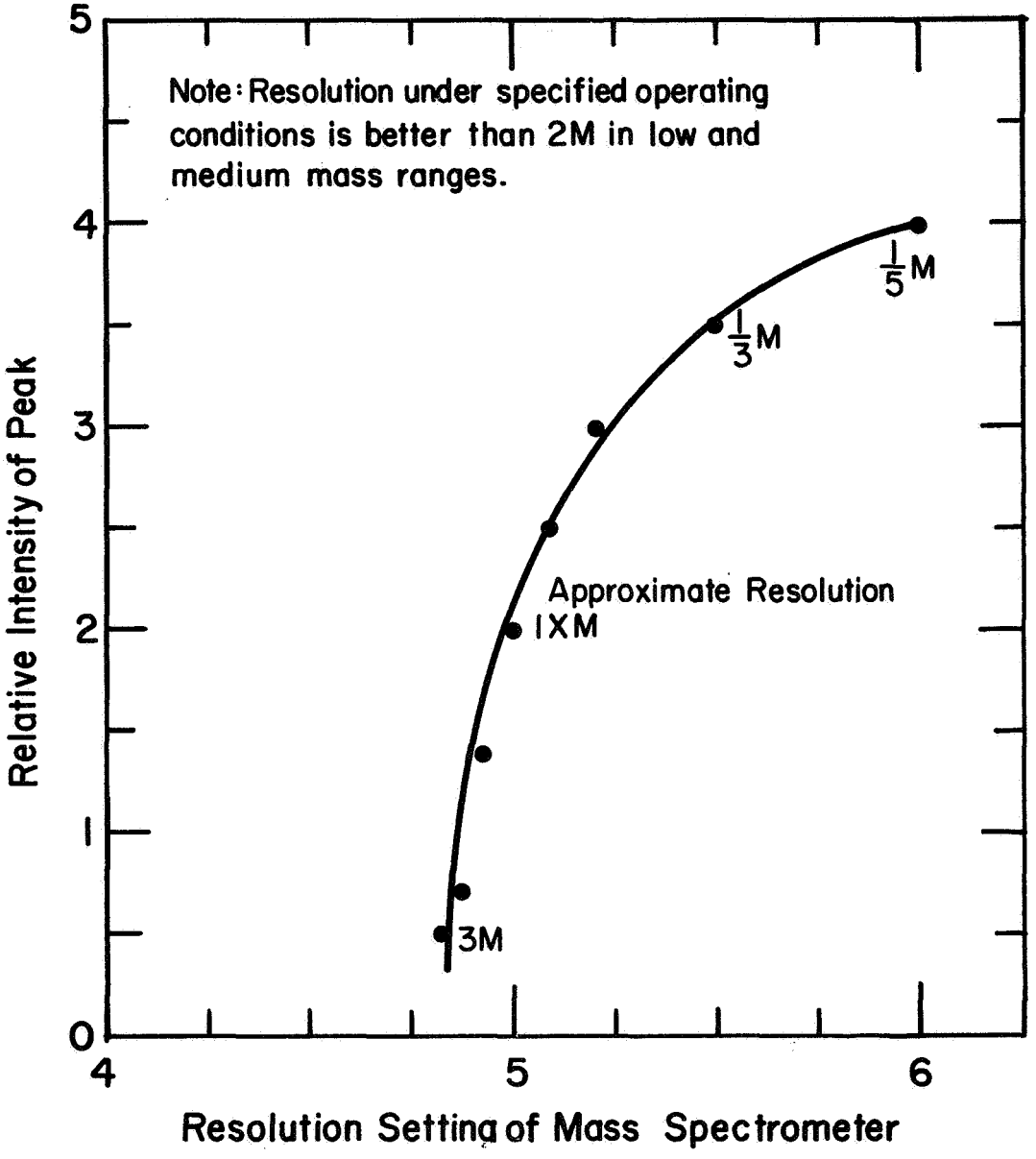

Figure II-7. Intensity as a Function of Resolution.

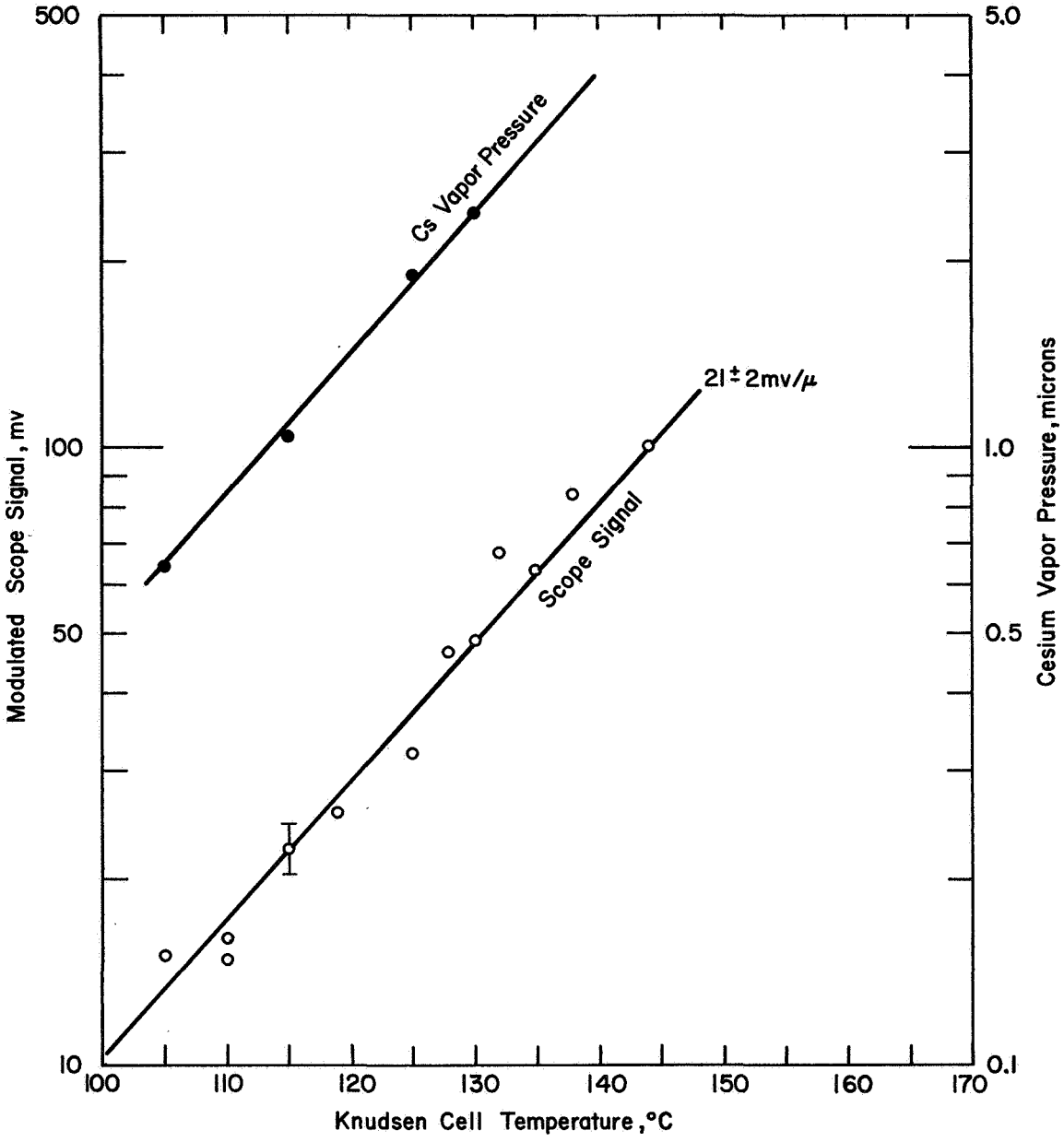

Figure II-8. Scope Signal and Cesium Vapor Pressure as Functions of Knudsen Cell Temperature.

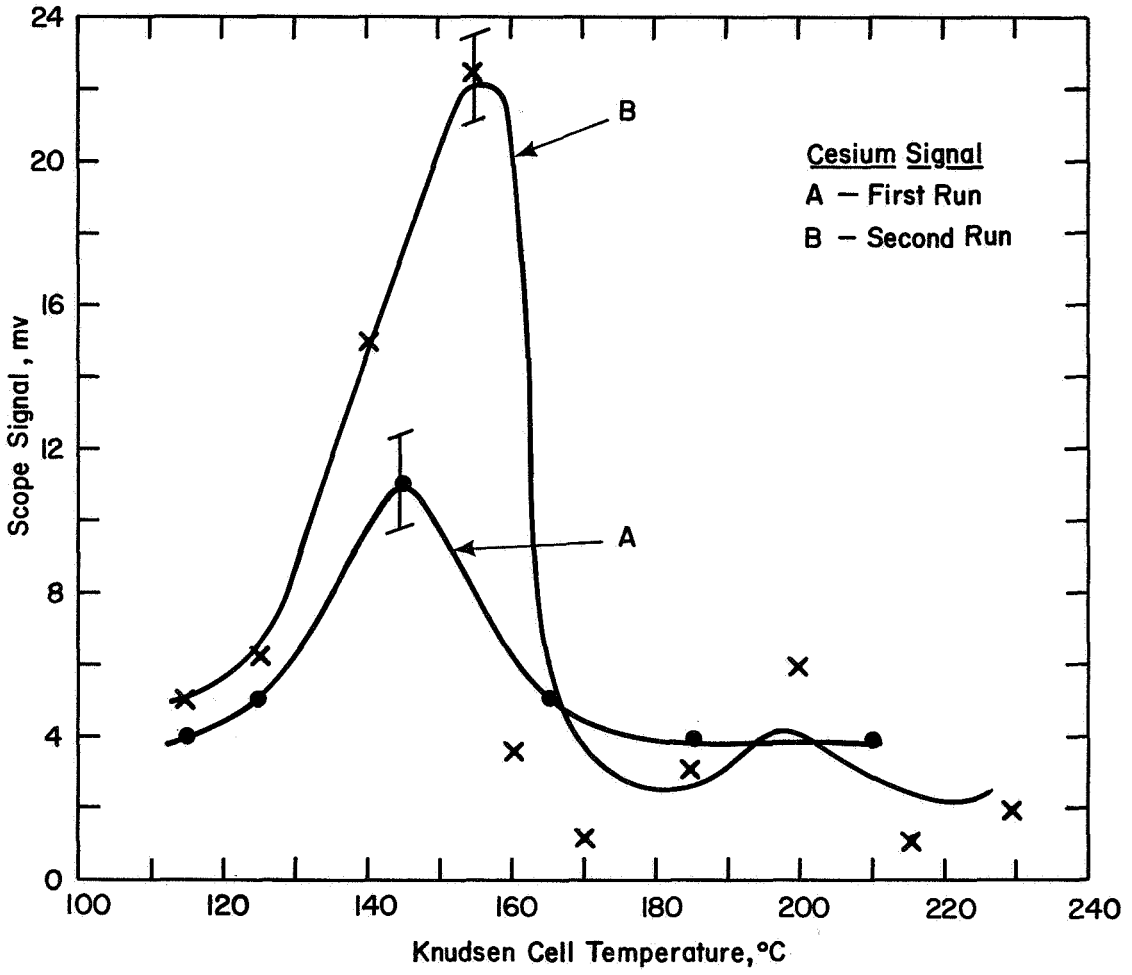

Figure II-9. Mass Spectrometric Output as a Function of Knudsen Cell Temperature, Cs^+ Peak.

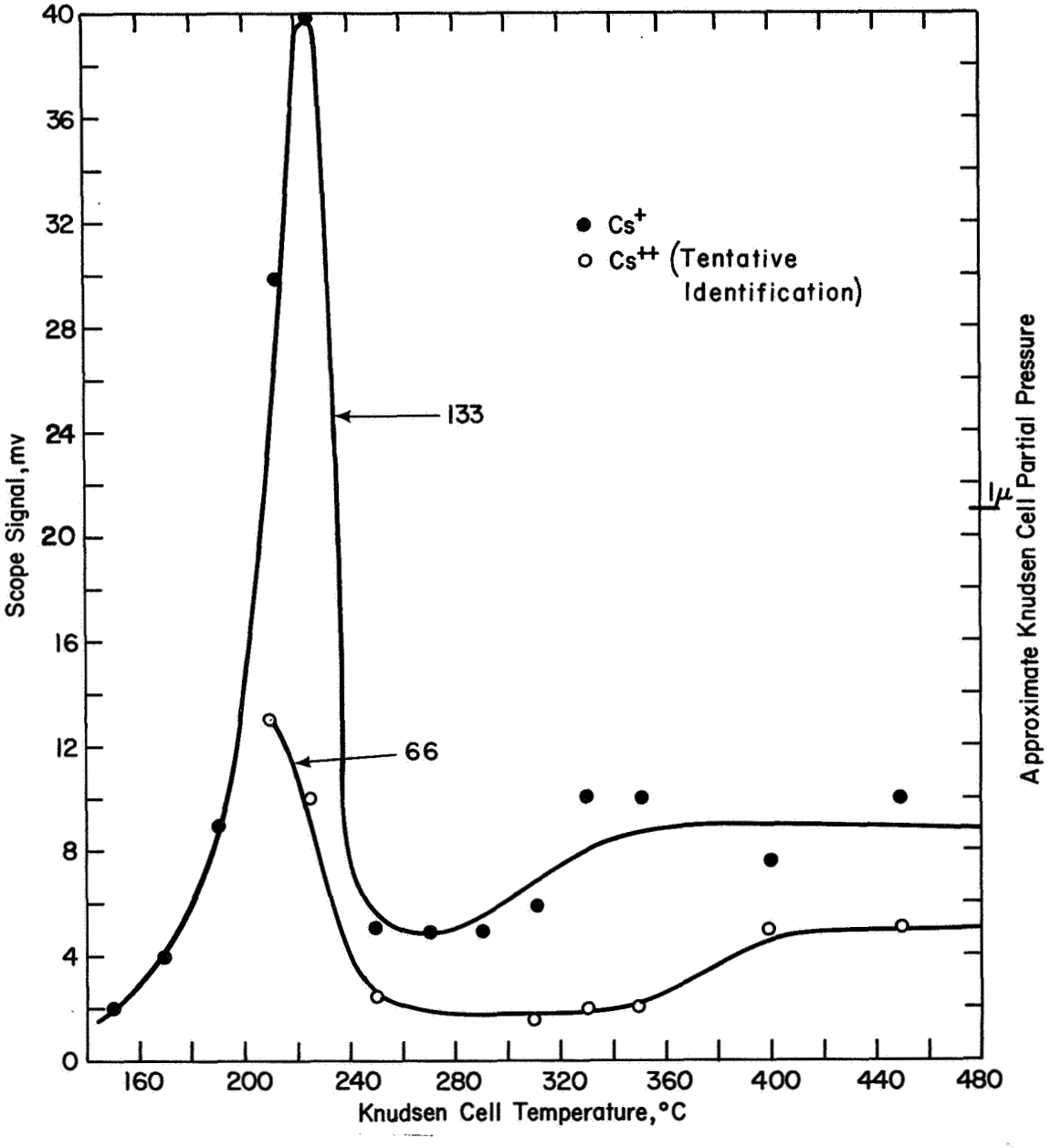

Figure II-10. Multiplier Output Versus Knudsen Cell Temperature

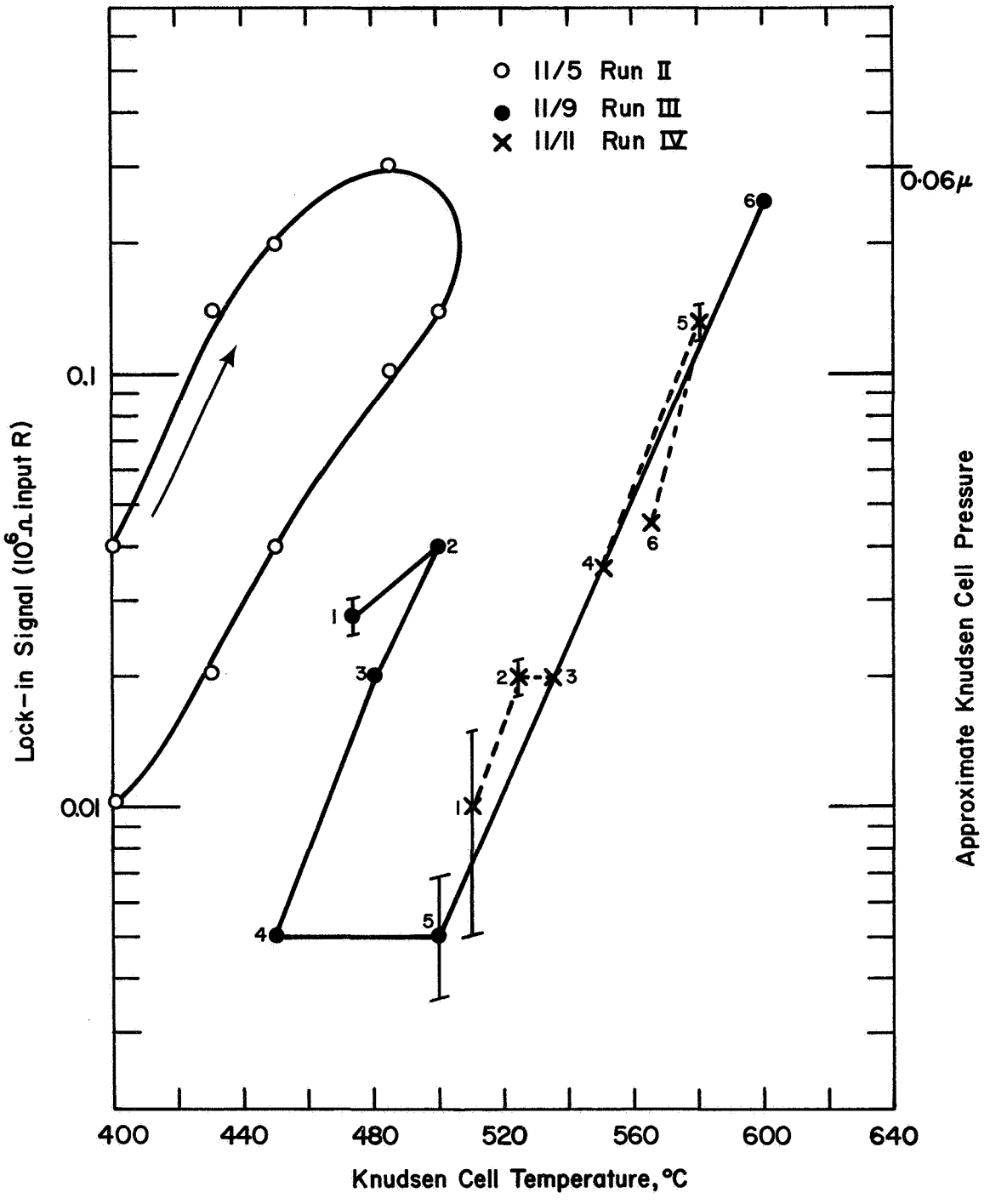

Figure II-11. Multiplier Output of "133" Peak as a Function of Knudsen Cell Temperature.

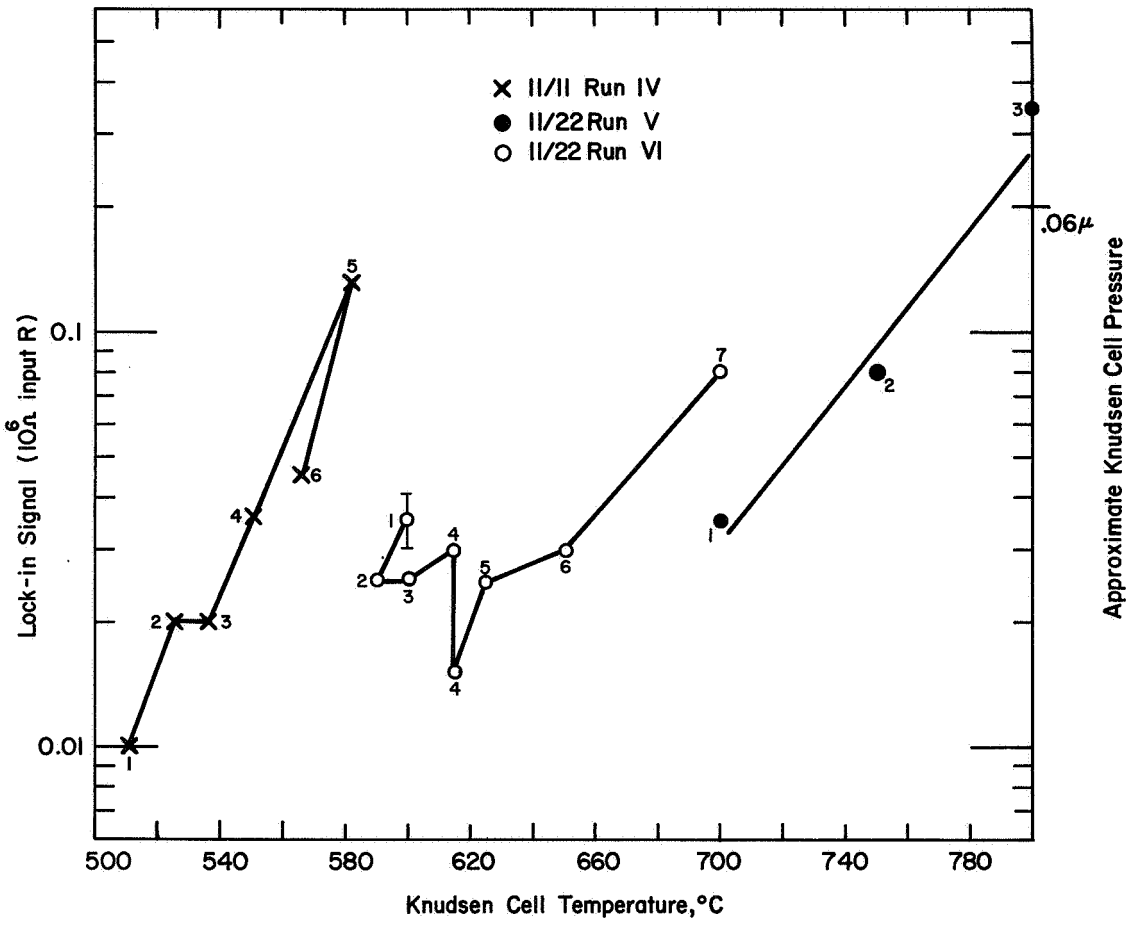

Figure II-12. Multiplier Output as a Function of Knudsen Cell Temperature.

CHAPTER III

QUANTUM-THERMODYNAMIC MEANING OF ELECTRONEGATIVITY AND WORK FUNCTION

Elias P. Gyftopoulos and George N. Hatsopoulos*

A. ELECTRONEGATIVITY

1. Introduction

Rigorous definitions are given of electronegativity of atoms, neutral or ionized, and of atomic orbitals. The definitions are consistent with the rules of the statistics of ensembles and the quantum-mechanical picture of atomic structure. The definitions have been extended to atoms in a molecule, and to atoms in a solid. The extensions, however, will be presented in future communications.

The concept of electronegativity, "the power of an atom in a molecule to attract electrons to itself,"[1] has been found to be a useful tool for the correlation of a vast field of chemical knowledge and experience.[2] But in spite of the large literature on the subject, no rigorous definition of electronegativity has been suggested. The lack of definition has resulted in some confusion with respect to both the physical concept represented by electronegativity and the units of electronegativity.[3-8]

In the present communication, a free atom or a free ion is regarded as a thermodynamic system, and the electronegativity of such a system is identified with the negative of its electrochemical potential.

The electrochemical potential of a component in a phase may be evaluated by means of the theory of statistical ensembles. This theory, whether related to classical or quantum mechanics, applies to thermodynamic systems of any size.[9] Consequently, it is possible to find ensemble

---

*One of the authors (EPG) was principally supported by the National Science Foundation, Contract GK-2581.

(thermodynamic) properties, such as the electrochemical potential, even of an atom representative of an ensemble of one-atom members. If the center of mass of each atom is fixed in space, both the one-atom members and the one-atom thermodynamic system representative of the ensemble may be regarded as open systems having one independent component, namely electrons.

Even when all the mechanical properties of an atom, such as the energy eigenvalues and the number of electrons, assume only discrete values, the thermodynamic properties of the one-atom system representative of the ensemble, such as the energy E and the number of electrons N, assume continuous values. Each of these properties may be expressed as a continuous function of two independent thermodynamic variables.

The electrochemical potential μ is defined as the partial derivative of E with respect to n at constant entropy. This derivative must be evaluated for the ensemble passing through equilibrium states because, otherwise, it is indeterminate. This fact in turn implies that in any calculation of μ, two independent thermodynamic variables, say, n and temperature T, must be considered even if the interest is in results at zero degrees Kelvin. For example, if μ is computed as the derivative mentioned above, in order to vary n at constant entropy while the ensemble passes through equilibrium states, the temperature T must be varied. Hence, both n and T must be retained in E.

In view of these remarks, the paper is organized as follows. First, a brief review of the statistics of grand canonical ensembles is given. Second, this statistic is applied to an ensemble of one-atom members. The procedure for the calculation of the electrochemical potential is thus established. Third, electronegativity is defined as the negative of the electrochemical potential. For a neutral atom at zero degrees Kelvin, this definition yields exact results which are identical to Mulliken's.[3] Finally, it is shown that when the

electronic structure of the atom is described by the Hartree-Fock approximation, that is when the electrons are treated as an ideal substance, an orbital electronegativity can be defined.

It should be noted that since the electrochemical potential is interpreted as the escaping tendency (the opposite of the power to attract) of a component from a thermodynamic system, it is reasonable to use the negative of this potential as a measure of electronegativity.

2. Statistics of Grand Canonical Ensembles

Consider an ensemble of identical members, namely members which have identical possible energy eigenstates. Suppose the ensemble is in thermodynamic equilibrium, at temperature T, and that its members can exchange energy and matter with the members of a reservoir. Such an ensemble is defined as a grand canonical ensemble.[9]

For present purposes, the members of the ensemble are specified by the following conditions: (a) each member has only one independent component; (b) the energy eigenstates of each member are $G_1, G_2, \ldots, G_j, \ldots$; and (c) each energy eigenstate $G_1, G_2, \ldots, G_j, \ldots$ is occupied by a number $n_1, n_2, \ldots n_j, \ldots$ of particles of the component, and has an energy $E_1, E_2, \ldots E_j, \ldots$, respectively. Here, separate symbols for the energy and the occupation number are used for each energy eigenstate, even though more than one of these symbols may represent the same number. For example, a g-fold degenerate state is counted as g separate states.

When the laws of thermodynamics are applied to the ensemble and the reservoir,[9] it is found that the fraction x_i of members at the

energy eigenstate G_i, the probability x_i that a member is at the state G_i, is given by the relation

$$x_i = \frac{\exp[(n_i\mu - E_i)/kT]}{\sum_i \exp[(n_i\mu - E_i)/kT]}, \tag{1}$$

where μ is the electrochemical potential of the component in the ensemble and in the reservoir, and k is Boltzmann's constant. Note that at T equals zero, x_i can be computed only as a limit.

By virtue of Eq. 1, it follows that, statistically, the average number n of particles representative of the ensemble is given by the relation

$$n = \sum_i n_i x_i$$

$$= \frac{\sum_i n_i \exp[(n_i\mu - E_i)/kT]}{\sum_i \exp[(n_i\mu - E_i)/kT]}. \tag{2}$$

Equation 2 indicates that n is a continuous function of the continuous variables μ and T. Conversely, Eq. 2 can be solved for the continuous function $\mu(n, T)$ of the continuous variables n and T. The range of n is the same as that of the discrete values n_i.

It also follows from Eq. 1 that the average energy E of the ensemble is given by the relation

$$E = \sum_i E_i x_i. \tag{3}$$

This energy can be thought of as a continuous function of any two of the continuous variables n, μ, and T, and it is related to the electrochemical

potential by the expression

$$\mu = \frac{\partial E}{\partial n} \text{ at constant entropy.} \tag{4}$$

The derivation of the last relation is given in reference 9.

3. Electrochemical Potential of Atoms and Atomic Ions

Consider the special ensemble of identical, one-atom members, of atomic number Z. Suppose each member may exchange energy and only electrons with a reservoir. In thermodynamic equilibrium, this thermodynamic system constitutes a grand canonical ensemble of one component (electrons) members.

To proceed with the statistical analysis of the system, suppose first that only the ground state of the singly charged negative ion of the atomic species exists. Thus, the possible energy eigenstates of each one-atom member of the ensemble are as follows:

a. Ground States. Figure III-1 shows schematically the possible occupation numbers n_i,

$$n_i = 0,\ 1,\ 2,\ \ldots,\ Z,\ Z+1, \tag{5}$$

and the corresponding energies E_i of the ground states of the neutral atom and all the positive and negative ions. It is seen from the figure that as the electron occupation number increases from zero, fully ionized atom, to Z + 1, singly charged negative ion, the energies of the corresponding ground states satisfy the relations

$$E_o > E_1 > \ldots > E_{z-1} > E_z > E_{z+1}\ . \tag{6}$$

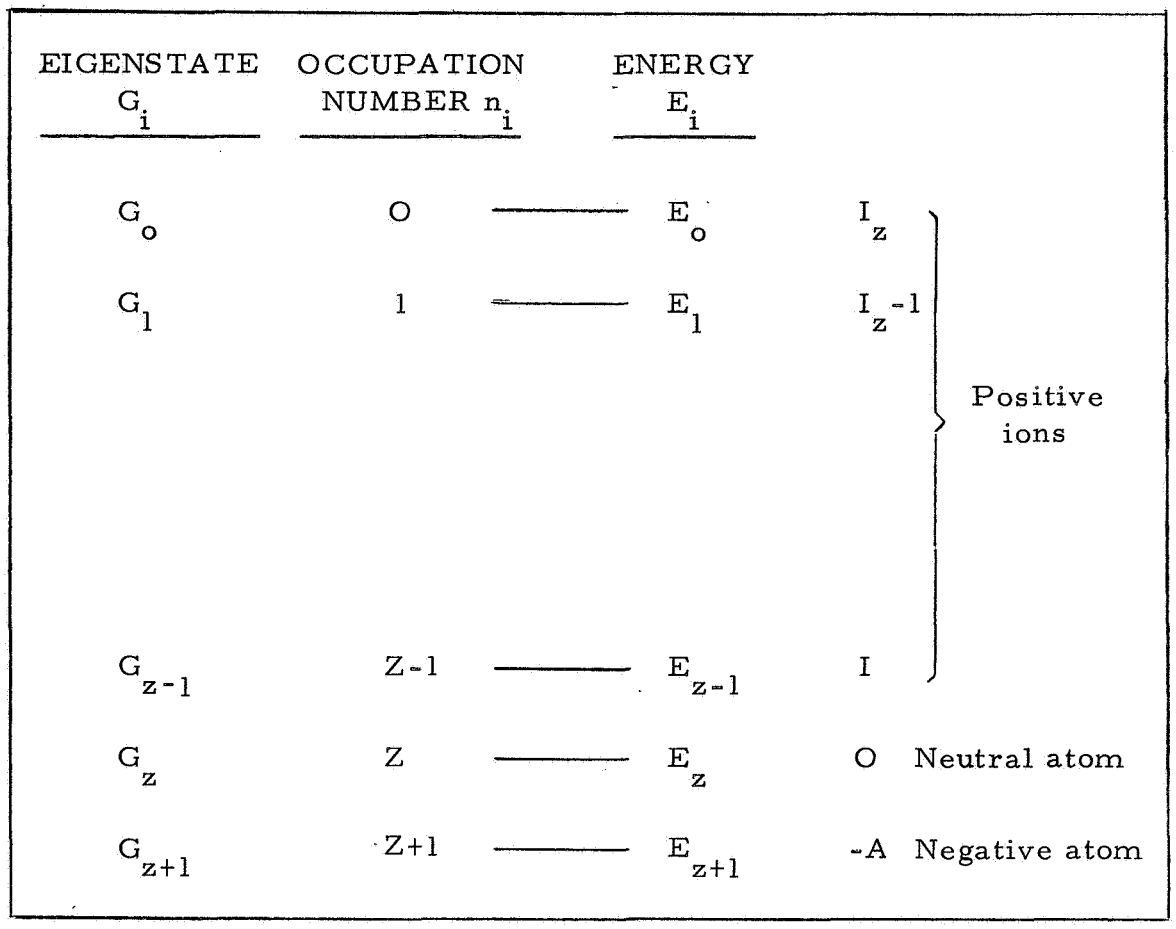

Figure III-1. Schematic of Ground States of the Neutral Atom and all the Positive and Negative Ions, of an Atom Forming only Singly Charged Negative Ions. No Degeneracies are Shown.

If the arbitrary zero energy reference level is set at the energy E_z of the neutral atom, relation 6 may be written in the form

$$I_z > I_{z-1} > \ldots > I_1 > 0 > -A_1, \tag{7}$$

where I_i and A_i are the i-th ionization energy and electron affinity of the atom, respectively.

b. Excited States. To each occupation number n_i, smaller than or equal to Z, there corresponds an infinite number of excited states. Let the energy of each such state be denoted by E_{ij}. Each energy E_{ij} is greater than the energy E_i of the corresponding ground state.

In terms of the above energy eigenstates, the average number n of electrons representative of the ensemble is given by the relation

$$n = \frac{\sum_{i=0}^{Z+1} n_i \exp\left[(n_i\mu - E_i)/kT\right] + \sum_{i=0}^{Z} \sum_j n_i \exp\left[(n_i\mu - E_{ij})/kT\right]}{\sum_{i=0}^{Z+1} \exp\left[(n_i\mu - E_i)/kT\right] + \sum_{i=0}^{Z} \sum_j \exp\left[(n_i\mu - E_{ij})/kT\right]} \tag{8}$$

It follows from Eq. 8 that the number of electrons of the atom, viewed as a thermodynamic system, may assume any value between 0 and Z + 1, even though the occupation numbers n_i assume only discrete values. Moreover, for given values n and T, Eq. 8 can be solved for μ. Although the general solution is numerically tedious, some general results can be readily established.

(i) If the ensemble is representative of either the fully ionized atom, (n equals zero) or the singly charged negative ion, (n equals Z + 1), Eq. 8 yields

$$\mu = -\infty \qquad \text{for} \qquad n = 0, \tag{9}$$

or

$$\mu = +\infty \qquad \text{for} \qquad n = Z + 1, \tag{10}$$

respectively, for all values of T. These extreme values of μ are as expected since for n equals 0 and Z + 1 the variations dn of the electron component are restricted to be only positive and negative, respectively.[10]

(ii) For values of n in the range

$$Z < n \leq Z + 1, \tag{11}$$

μ is positive. For all other values of n, the electrochemical potential is negative. These facts can be readily verified by substitution of a non-negative value of μ in Eq. 8.

(iii) If the ensemble is representative of a neutral atom, n equals Z. For this value of n and in the limit of small temperatures, T approximately equals zero degrees Kelvin, Eq. 8 yields

$$\mu = -(I_1 + A_1)/2 + kT \ln g_{Z-1} \qquad \text{for } n = Z, \text{ and } T \to 0, \tag{12}$$

where g_{Z-1} is the degeneracy of the state G_{Z-1}. Equation 12 is a special case of a more general result discussed below.

(iv) If the ensemble is representative of a positive ion with an integral number σ of electrons, n equals σ. For such a value of n, Eq. 8 may be written in the equivalent form

$$\sum_{i=0}^{\sigma-1} (\sigma - n_i) \exp\left[(n_i\mu - E_i)/kT\right] + \sum_{i=0}^{\sigma-1} \sum_{j} (\sigma - n_i) \exp\left[(n_i\mu - E_{ij})/kT\right] =$$

$$= \sum_{i=\sigma+1}^{Z+1} (n_i - \sigma) \exp\left[(n_i\mu - E_i)/kT\right] + \sum_{i=\sigma+1}^{Z} \sum_{j} (n_i - \sigma) \exp\left[(n_i\mu - E_{ij})/kT\right]. \tag{13}$$

For μ negative and in the limit of small temperatures, the first sum on either side of Eq. 13 is much greater than the second. Hence, a good approximation to Eq. 13 is given by the relation

$$\sum_{i=0}^{\sigma-1} (\sigma - n_i) \exp[(n_i\mu - E_i)/kT] = \sum_{i=\sigma+1}^{Z+1} (n_i - \sigma) \exp[(n_i\mu - E_i)/kT]$$

$$\text{for } n = \sigma \text{ and } T \to 0. \tag{14}$$

For different ranges of negative values of μ, the exponents $n_i\mu - E_i$ on either side of Eq. 14 can be ordered. Given a range of values of μ, suppose that the largest exponents are $\ell\mu - E_\ell$ and $r\mu - E_r$ on the left and right hand side, respectively, where

$$\ell \leq \sigma - 1 \qquad \text{and} \qquad r \geq \sigma + 1. \tag{15}$$

It follows that, in the limit of small temperatures, Eq. 14 can be approximated by the simple expression

$$g_\ell(\sigma - \ell) \exp[(\ell\mu - E_\ell)/kT = g_r(r - \sigma) \exp[(r\mu - E_r)/kT], \tag{16}$$

where g_ℓ and g_r are the degeneracies of the states G_ℓ and G_r, respectively. The last expression is satisfied for the value of μ given by the relation

$$\mu = -\left[(E_r - E_\ell) + kT \ln \frac{g_\ell(\sigma - \ell)}{g_r(r - \sigma)}\right]/(r - \ell) =$$

$$= -\left[(I_{z-r} - I_{z-\ell}) + kT \ln \frac{g_\ell(\sigma - \ell)}{g_r(r - \sigma)}\right]/(r - \ell) \text{ for } n = \sigma, \text{ and } T \to 0. \tag{17}$$

The value of μ is acceptable if it is within the range of values assumed for the ordering of the exponents, namely within the range which resulted

in approximate Eq. 16. Otherwise, another range of μ and different values of ℓ and r must be considered.

For n equal to or smaller than Z-1, consideration of the ionization energies of atoms as specified above results in values of μ which are much smaller than that for n equals Z. For practical purposes, it is convenient (but not necessary) to assume

$$\mu = -\infty \qquad \text{for } n \leq Z - 1 \qquad \text{and all T.} \tag{18}$$

The preceding statistical analysis can be readily applied to atoms which either can form both singly and doubly charged negative ions, or cannot form negative ions. Thus, for example, for atoms which form both singly and doubly charged negative ions, n_i ranges from 0 to Z+2, it is found that for n equals Z a possible value of μ is given by the relation

$$\mu = -(I_2 + A_2)/4 \quad \text{for } n = Z \text{ and } T = 0, \tag{19}$$

provided that

$$3I_2 < 4I_1 + A_2, \qquad \text{and} \qquad 4A_1 < 3A_2 - I_2. \tag{20}$$

4. Electronegativity of Atoms and Atomic Ions

The electronegativity of a neutral or charged atomic species is defined here as the negative of the electrochemical potential of the species viewed as a one-component member of a grand canonical ensemble. Thus, the electronegativity x(n, T) is given by the relation

$$x(n, T) = -\mu \tag{21}$$

and is a continuous function of the continuous variables n, and T.*

Qualitatively, this definition of electronegativity is consistent with heuristic descriptions given previously. The negative of μ, the negative of the escaping tendency, represents a power to attract. A power to attract is the notion associated with electronegativity. Moreover, equality of the electrochemical potentials of a component in two different phases implies that there is no flow of this component between the two phases. In direct analogy, equality of electronegativities of two atoms implies that there is no flow of electronic charge from one atom to the other.

Quantitatively, for atoms which can form singly charged negative ions, it is seen from Eqs. 12 and 21 that the exact value of the electronegativity x(Z, 0) of the neutral atom is given by the relation

$$x(Z, 0) = (I_1 + A_1)/2. \tag{22}$$

This value is identical to the approximate value recommended by Mulliken.[3] Also, the exact value of the electronegativity given by the

---

* Note that when the zero energy level is set at the level of the ground state of the neutral atom, the value of the electrochemical potential equals that of the chemical potential. For this energy reference level, the electronegativity equals the negative of the chemical potential.

Note also that x can be expressed as a continuous function of another pair of continuous thermodynamic variables, say, entropy and temperature.

negative of Eq. 10 was suggested by Mulliken[3] without reference to the restrictions represented by relations 20.

5. Orbital Electronegativity

The discussion in Section C and the definition of electronegativity in Section D are presented without any reference to the procedure employed for the determination of the possible energy eigenstates of the members of the ensemble. Consideration of the approximate methods used for the calculation of the energy eigenvalues leads to the concept of orbital electronegativity.

To see this point clearly, consider a Z-electron atom. The quantum-mechanical analysis of the electronic structure of this atom is very difficult. The difficulty is avoided if the electrons are treated as an ideal substance, that is the Z-electron Hamiltonian operator is reduced to an approximate sum of Z separable, one-electron Hamiltonian operators. The reduction can be made by means of different approximate methods. One of these is the Hartree-Fock method.

The Hartree-Fock, one-electron operator defines an energy eigenvalue problem. Each eigenfunction of this operator, one-electron orbital, can accommodate at most two electrons with opposite spins. When the orbital is occupied by an electron with a given spin, it is called a spin-orbital. The negative of each eigenvalue is interpreted as an ionization energy. This interpretation is based on the assumption that the extraction of the electron from the corresponding orbital does not perturb the eigenstates of the other electrons, and it is known as Koopmans' theorem.[11] Finally, the energy of a given state of the atom is given approximately by the sum of the energies of the occupied spin-orbitals.

This way of thinking about the atom has the following implications for an atom which forms only singly charged negative ions.

(a) The energies I_1 and A_1 of the atom may be thought of as the ionization energy and the electron affinity of a valence orbital, respectively.

(b) Variations of the charge of the atom, regarded as a thermodynamic system, in the range

$$Z - 1 \leq n \leq Z + 1 \tag{23}$$

may be thought of as occurring because of continuous variations of the charge in the valence orbital.

(c) For values of n in the range represented by relations 23, the energy E(n, T) (Eq. 3) is a function of the charge in the valence orbital only. This statement is justified by Koopmans' theorem.

(d) Suppose that the average charge in the valence orbital is represented by q, so that

$$q = +e \text{ for } n = Z - 1,\ q = 0 \text{ for } n = Z, \text{ and } q = -e \text{ for } n = Z + 1,$$

where e is the electronic charge. At zero temperature, the energy and electrochemical potential of the atom may be thought of as the energy $\epsilon_o(q)$ and the electrochemical potential $\mu_o(q)$ per unit charge of the valence orbital, respectively. From the results of Section 4, it is readily verified that for

$$\begin{array}{lll} q = e & \epsilon_o(q) \equiv I_1 & \mu_o(q) \equiv -\infty \\ q = 0 & \epsilon_o(q) \equiv 0 & \mu_o(q) \equiv -(I_1 + A_1)/2e \\ q = -e & \epsilon_o(q) \equiv -A_1 & \mu_o(q) \equiv +\infty. \end{array} \tag{24}$$

These values suggest that $\epsilon_o(q)$ and $\mu_o(q)$ may be represented by the approximate continuous functions given by the relations

$$\epsilon_o(q) = \frac{I_1 + A_1}{2e} q + \frac{I_1 - A_1}{2} \left[1 - \left(1 - \frac{q^2}{e^2}\right)^{1/2} \right], \tag{25}$$

and

$$\mu_o(q) = - \frac{d\epsilon_o(q)}{dq} =$$

$$= - \frac{I_1 + A_1}{2e} - \frac{I_1 - A_1}{2} \frac{(q/e)}{\left[1 - (q/e)^2 \right]^{1/2}} . \tag{26}$$

(e) It follows that, at zero temperature, the electronegativity of the atom may be thought of as an orbital electronegativity $x_o(q)$ given by the approximate relation

$$x_o(q) = \frac{d\epsilon_o}{dq} = \frac{I_1 + A_1}{2e} + \frac{I_1 - A_1}{2} \frac{(q/e)}{\left[1 - (q/e)^2 \right]^{1/2}} . \tag{27}$$

(f) Similar statements can be made about other types of atoms.

Expressions somewhat analogous to those represented by Eqs. 24 and 26 have been introduced heuristically by other authors.[12] These authors expressed doubts about the validity of the assumption that both $\epsilon_o(q)$ and $x_o(q)$ are continuous functions of the continuous variable q. In view of the present work, it is seen that orbital electronegativity is obtained from basic quantum-thermodynamic arguments and that, indeed, $\epsilon_o(q)$ and $x_o(q)$ are continuous functions of the continuous thermodynamic variable q.

The preceding approach to the definition of electronegativity has been extended to atoms in molecules and solids. The results will be presented in future communications.

B. WORK FUNCTION

1. Introduction

In previous publications by Steiner and Gyftopoulos[13-15], emission phenomena occurring at metallic surfaces are analyzed in terms of surface atoms and their orbital electronegativity. For example, in Reference 13, the view is advanced that electrons emitted thermionically from a pure uniform surface of a crystal originate from a "valence orbital" of an "atom on the surface." It is assumed that the shape, the ionization energy, the electron affinity, and the excitation energies of this orbital are precisely defined, although not necessarily spectroscopically observable, and that they are determined by the many-body interactions of the crystal. On the basis of this picture, it is concluded that the work function of the surface must equal the neutral orbital electronegativity of the valence orbital of the surface atom.

This way of thinking about a crystal and its surface raises two questions. The first relates to the validity of viewing the electronic structure of a crystal in terms of orbitals which are associated with individual lattice sites, such as a valence orbital of a surface atom. It is customary to think of the electrons as belonging to the crystal as a whole, and therefore it is not obvious that electrons can be assigned to, localized around, individual lattice sites.

The second is a relatively old question. It refers to the meaning of electronegativity. This quantity has been found useful in many chemical studies, and yet it has not been given a rigorous definition.

The purpose of this chapter is to discuss the preceding two questions, in the context of the one-electron approximation for the electronic structure of many-electron systems. It is shown that the picture of localized orbitals is valid, and that electronegativity equals the negative of the chemical potential of an electron in an orbital.

The chapter is organized as follows: First the procedure for the derivation of the localized orbitals is discussed. These orbitals are shown to provide a description of the electronic structure of crystals which is entirely equivalent to the well known quantum-mechanical picture of electrons in metals. Second, the work of the authors on the identification of electronegativity[16] with the chemical potential is summarized. Third, it is shown that the work function of a pure uniform surface equals the orbital electronegativity of a surface atom.

2. Localized Spin-Orbitals for Crystal Lattices

The equivalence between the descriptions of the electronic structure of crystals by means of either non-localized, band structure theory, or localized spin-orbitals is best understood through a brief review of procedures employed for the analysis of any N-electron system.

Quantum-mechanically, the analysis of the energy eigenstates of the electronic structure of N-electron systems is very difficult. To avoid the difficulty, the electrons are treated as an ideal substance. In other words, the N-electron Hamiltonian operator is reduced to a sum of N separable one-electron Hamiltonian operators. Various methods are used for the reduction. Differences between methods arise from the degree to which exchange and correlation effects are

included in the one-electron potential energy. In this regard, all methods are approximate and not all methods are equally accurate.

A given one-electron Hamiltonian operator defines an energy eigenvalue problem. The eigenfunctions and eigenvalues of this operator can be more readily found than those of the complete N-electron operator. Each eigenfunction, one-electron orbital, of a system with more than one nucleus, is delocalized throughout the system and is given the same interpretation as, say, the eigenfunctions of the hydrogen atom. For example, the orbital can accommodate at most two electrons with opposite spins. The negative of the eigenvalue equals approximately the energy required to extract an electron from the orbital, and it represents an ionization energy of the system. When the orbital is occupied by an electron with a given spin, it is called a spin-orbital. In many applications, a different orbital is used for each spin. In other words, each spin-orbital has its own spatial dependence.

By virtue of the ideal substance assumption, the eigenfunction ψ_N, for a given state of the system as a whole, should be given by the product of the occupied spin-orbitals. This, however, is not consistent with the symmetry rules of quantum mechanics.[17] For this reason ψ_N is represented by an antisymmetric, determinantal function of spin-orbitals, a Slater determinant.[18] The determinant is given by the relation

$$\psi_N = \frac{1}{(N!)^{1/2}} \begin{vmatrix} u_1(q_1) & u_2(q_1) & \cdots & u_N(q_1) \\ u_1(q_2) & u_2(q_2) & \cdots & u_N(q_2) \\ \vdots & \vdots & \cdots & \vdots \\ u_1(q_N) & u_2(q_N) & \cdots & u_N(q_N) \end{vmatrix}, \qquad (1)$$

where q_j represents the coordinates and spin of the j-th electron, u_i is the i-th orbital, and $u_i(q_j)$ is the i-th spin-orbital occupied by the j-th electron.

In general, it is found that one-electron energies E_i, eigenvalues E_i, are in good agreement with experimentally observed ionization energies of the system (atom, molecule, or crystal). However, the sum of the E_i, the eigenvalue of ψ_N with respect to the sum of the N one-electron operators, is not in good agreement with the total energy of the system, namely, the energy which would be derived from the exact ψ_N and the exact N-electron operator. Nevertheless, ψ_N in the form of Eq. 1 is often considered as an adequate approximation for the exact ψ_N.

For crystals, the one-electron results can also be described in terms of localized orbitals by means of the following procedure: Consider a crystal bounded by a uniform surface. Suppose that a relatively accurate one-electron equation has been established, say, by the method suggested by Slater.[19] The one-electron eigenvalue problem may be written in the form

$$(H_o + H_1)\, u = E\, u, \tag{2}$$

where H_o is the one-electron, spatially periodic, Hamiltonian operator that would be derived if the solid were embedded in an infinite lattice, and H_1 is the one-electron operator which accounts for the perturbation introduced by the uniform surface. The spatial part of the eigenfunctions of Eq. 2 can be expanded into a series of Wannier functions[20] $a_n(\underline{r} - \underline{R}_s)$

associated with the operator H_o.* Thus the i-th eigenfunction is given by the relation[21]

$$u_i(\underline{r}) = \sum_s \sum_n U_{in}(\underline{R}_s)\, a_n(\underline{r} - \underline{R}_s) , \qquad (3)$$

where $U_{in}(\underline{R}_s)$ is a constant, and the sums are over all lattice sites $\underline{R}_s$ and over all bands n. Mathematically, Eq. 3 is exact if an infinite number of bands is included in the expansion. As in all practical problems, however, through a judicious choice of localized, Wannier-like functions $W_n(\underline{r}, \underline{R}_s)$ (for example, a suitable linear combination of Wannier functions at the site $\underline{R}_s$, the summation over n may be reduced to a number equal to the number of valence electrons per atom, without great loss of accuracy. Thus, if different orbitals are used for different spins, a spin-orbital $u_i(q_j)$ may be adequately

---

* Recall that the Block functions $b_n(\underline{k}, \underline{r})$ of the n-th band of the infinite crystal are given by the relation[22]

$$H_o b_n(\underline{k}, \underline{r}) = E_n(\underline{k})\, b_n(\underline{k}, \underline{r}),$$

and that the Wannier functions $a_n(\underline{r} - \underline{R}_s)$ of the n-th band are determined by the expression

$$a_n(\underline{r} - \underline{R}_s) = N_L^{-1/2} \sum_k b_n(\underline{k}, \underline{r}) \exp(-i\underline{k} \cdot \underline{R}_s),$$

where $\underline{R}_s$ is the s-th site of the lattice, and N_L is the number of lattice sites. The Wannier functions form a complete, orthonormal set over all bands and over all lattice sites, namely

$$\int a_m^*(\underline{r} - \underline{R}_j)\, a_n(\underline{r} - R_i)\, d\underline{r} = \delta_{mn}\, \delta_{ij}.$$

Moreover, each Wannier function $a_n(\underline{r} - \underline{R}_s)$ is localized around, associated with, the s-th site, represented by the function

represented by the relation

$$u_i(q_j) = \sum_s \sum_n^{v} c_{in}(\underline{R}_s)\; w_n(q_j, \underline{R}_s), \tag{4}$$

where v is the number of valence electrons per atom, and $c_{in}(\underline{R}_s)$ is a constant.

Without loss of generality, suppose the crystal is that of a monovalent metal, v equals unity and the number N_L of lattice sites equals the number N of valence electrons. For this crystal, substitution of Eq. 4 into the determinantal relation, Eq. 1, for the overall eigenfunction ψ_N yields

$$\psi_N = \frac{1}{(N!)^{1/2}} \begin{vmatrix} \sum_s c_1(\underline{R}_s)\, w(q_1, \underline{R}_s) & \cdots & \sum_s c_N(\underline{R}_s)\, w(q_1, \underline{R}_s) \\ \sum_s c_1(\underline{R}_s)\, w(q_2, \underline{R}_s) & \cdots & \sum_s c_N(\underline{R}_s)\, w(q_2, \underline{R}_s) \\ \vdots & \cdots & \vdots \\ \sum_s c_1(\underline{R}_s)\, w(q_N, \underline{R}_s) & \cdots & \sum_s c_N(\underline{R}_s)\, w(q_N, \underline{R}_s) \end{vmatrix} \tag{5}$$

where the subscript n equals unity has been omitted from the w's and the c's. Note that each column of the determinant in Eq. 5 is a linear combination of the N Wannier-like functions associated with the N sites of the crystal. It follows from the rules for the product of two determinants that Eq. 5 can be written in the form

$$\psi_N = \frac{1}{(N!)^{1/2}} \begin{vmatrix} w(q_1, \underline{R}_1) & \cdots & w(q_1, \underline{R}_N) \\ w(q_2, \underline{R}_1) & \cdots & w(q_2, \underline{R}_N) \\ \vdots & \cdots & \vdots \\ w(q_N, \underline{R}_1) & \cdots & w(q_N, \underline{R}_N) \end{vmatrix} \begin{vmatrix} c_1(\underline{R}_1) & c_2(\underline{R}_2) & \cdots & c_N(\underline{R}_1) \\ c_1(\underline{R}_2) & c_2(\underline{R}_2) & \cdots & c_N(\underline{R}_2) \\ \vdots & \vdots & \cdots & \vdots \\ c_1(\underline{R}_N) & c_2(\underline{R}_N) & \cdots & c_N(\underline{R}_N) \end{vmatrix} \tag{6}$$

In the form of Eq. 6, the eigenfunction ψ_N for the whole crystal admits the localized spin-orbital interpretation which is sought. Indeed, note that each Wannier-like function $w(q, \underline{R}_s)$ is a spin-orbital associated with, localized around, lattice site $\underline{R}_s$ (the set of constants $C_i(\underline{R}_s)$, for $i = 1, 2, N$, is also associated with the same site $\underline{R}_s$). If the N electrons of the crystal are distributed among the N spin-orbitals $w(q, \underline{R}_s)$, an antisymmetric determinantal function, Eq. 6, can be formed. This function is completely equivalent to that obtained from the delocalized orbitals. In other words, the ψ_N's constructed from either the localized or the delocalized spin-orbitals are identical.

It should be noted that the localized spin-orbitals $w(q, \underline{R}_s)$ are not energy eigenfunctions of the one-electron equations. Only ψ_N, Eq. 6, is an approximate eigenfunction of the Hamiltonian operator for the whole crystal. Nevertheless, each localized spin-orbital can be assigned precise values for the ionization energy, electron affinity, and excitation energies of the electron in the spin-orbital, in a manner which is consistent with the usual definitions of these quantities. The values of the ionization energy, electron affinity, etc., of a localized spin-orbital are not equal to the corresponding values of the delocalized spin-orbitals. This point can be seen from the definition of the ionization energy given below.

Suppose that ψ_N, Eq. 6, represents the ground state of the crystal. The ionization energy of a spin-orbital localized around lattice site $\underline{R}_s$ is defined as the difference between the energy corresponding to an eigenfunction ψ_{N-1} and that of the ground state. The eigenfunction ψ_{N-1} is given by Eq. 6 except that the s-th column and the s-th row of the first and the second determinants are replaced by zeros, respectively, and

$(N!)^{1/2}$ is replaced by $[(N-1)!]^{1/2}$. The Hamiltonian operator for ψ_{N-1} is that corresponding to N lattice sites and N-1 valence electrons. This definition of the ionization energy assumes that removal of a localized spin-orbital from the system does not alter the functional dependence of the other N-1 localized spin-orbitals. Such an assumption is used in practically all approaches to the analysis of the electronic structure of solids (see, for example, Koopman's theorem for the one-electron Hartree-Fock equations[23]).

The other energies of a localized spin-orbital can be defined in a manner analogous to that used for the ionization energy.

3. Electronegativity and Chemical Potential

In this section, the work of the authors[16] on the identification of electronegativity with the negative of the chemical potential of an electron in an atom is summarized.*

In Reference 16, an ensemble of identical, one-atom systems is considered. Each atom is thought of as consisting of two components, electrons and ions. The systems are in thermodynamic equilibrium with a reservoir of electrons and ions at a small temperature T (degrees Kelvin). The components can flow back and forth between the systems and the reservoir. The energy eigenstates of the atoms are assumed to be derivable from the one-electron Hartree-Fock equations.[24] In other words, the electrons are viewed in an ideal substance.

---

* Strictly speaking, the electronegativity has been identified with the electrochemical potential. For the reference level of energy selected in this chapter, however, the values of the chemical and the electrochemical potential are identical.

According to the theory of statistics of ensembles,[9] the physical situation described above obeys the rules of grand canonical ensembles. Use of these rules yields the following important conclusions:

(1) Statistically, the energy E of a one-atom system can be expressed as a continuous function E(q) of a continuous variable q which represents a statistical measure of the charge in a valence spin-orbital. The range of the value of the charge q is from minus one electronic charge (-e)(the orbital is doubly occupied) through zero (the orbital is occupied by one electron) to plus one electron charge (+e)(the orbital is ionized).

(2) The chemical potential μ_c of a valence electron is given by the relation

$$\mu_c = (\partial E(q)/\partial q) \text{ at constant entropy.} \qquad (7)$$

In the limit of very small temperatures, this potential is found to have the following exact values:

$$\mu_c = (I + A)/2e \quad \text{for } q = 0 \text{ (neutral atom)},$$

$$\mu_c = \infty \quad \text{for } q = e \text{ (positive ion)},$$

and

$$\mu_c = -\infty \quad \text{for } q = -e \text{ (negative ion)},$$

where I and A are the first ionization energy and the electron affinity of the atom, respectively. The quantities I and A can also be referred to the valence electron spin-orbital.

(3) For fractional values q and for small T, μ_c is a function of both q and T.

(4) By virtue of (2) above, it is found that for small temperatures (in the limit of zero temperature) an excellent approximation for E(q) is given by the relation

$$E(q) = \frac{I + A}{2e} q + \frac{I - A}{2} \left[1 - \left(1 - \frac{q^2}{e^2}\right)^{1/2}\right] \qquad (8)$$

when the zero energy level is taken to be at the energy of the neutral atom (q equals zero). Note that this approximation yields exact values for E(q) and μ_c for q = -e, 0, e.

(5) The orbital electronegativity x(q) of a valence electron is defined as

$$x(q) = (\partial E(q)/\partial q) \text{ at constant entropy}$$

$$= -\mu_c$$

This is the first time that a rigorous definition of x(q) is given.

(6) The value of the neutral orbital electronegativity x(0) obtained from Eq. 8 is identical to the value of electronegativity suggested by Mulliken.[25] It should be noted, however, that Mulliken's value is considered to be approximate. Here the thermodynamic analysis yields that, in the limit of small temperatures, x(0) has the exact value given by the relation

$$x(0) \equiv \frac{I + A}{2e} \qquad (9)$$

(7) The definition of the orbital electronegativity given above can be easily extended to orbitals in systems other than atoms. Such an extension is discussed in the next section.

4. Work Function and Electronegativity

Without loss of generality, consider a crystal of a monovalent metal, bounded by a uniform surface. Suppose the analysis of the electronic structure of this metal has been carried out with respect to a zero energy level taken at the points just outside the surface. Moreover, suppose that both the delocalized and the localized spin-orbitals have been established, in accordance with the procedure discussed in Section B.

Thermodynamically, for a system of N electrons, any set of N spin-orbitals which describes the system may be thought of as representing N degrees of freedom. When these N degrees of freedom are treated statistically, the following results can be obtained:

(1) Given the N delocalized spin-orbitals, one-electron spin-orbitals, the negative of the chemical potential of the surface, with respect to the points just outside the surface, equals the work function. This is the well known thermodynamic definition of work function.[26,27]

(2) Given the N localized spin-orbitals, Wannier-like functions, suppose that all degrees of freedom are frozen except that corresponding to the spin-orbital localized around the surface site $\underline{R}_s$. Under this condition, the surface spin-orbital can be treated statistically by the same procedure as that used for atoms in Section C. In other words, this orbital may be thought of as a surface atom. Thus a chemical potential for the electron in the orbital can be defined. For example, in the limit of small temperatures, the value of the chemical potential of the localized spin-orbital equals

$$-(I_s + A_s)/2e,$$

where I_s and A_s are the ionization energy and the electron affinity of the orbital as defined in Section B. This value equals the negative of the neutral orbital electronegativity of the spin-orbital, Eq. 9.

(3) From thermodynamic equilibrium considerations, it can be shown that the chemical potential of the localized spin-orbital as defined in (2) must be equal to the chemical potential of the surface, as defined in (1).*

(4) By virtue of (1), (2), and (3), it follows that the work function equals the neutral orbital electronegativity of a spin-orbital localized around a surface atom.

In conclusion: (1) the characterization of the electronic structure of metals by localized spin-orbitals is equivalent to the ordinary picture of electrons in metals; (2) electronegativity can be given a rigorous thermodynamic definition; and (3) the neutral orbital electronegativity of a surface spin-orbital, atom, equals the work function of the surface.

*The proof of this statement is analogous to that used in the study of chemical reactions with or without a catalyst.[28]

REFERENCES FOR CHAPTER III

1. L. Pauling, The Nature of the Chemical Bond, Cornell University Press, Ithaca, New York, 3rd edition, pp. 3-27 (1960).

2. C. A. Coulson, Proc. Roy. Soc. (London), A207, 63, (1951).

3. R. S. Mulliken, J. Chem. Phys. 2, 782, (1934); 3, 573, (1935).

4. J. G. Malone, J. Chem. Phys. 1, 197, (1933).

5. W. E. Gordy, and W. J. Orville Thomas, J. Chem. Phys., 24, 439, (1956).

6. H. O. Pritchard, and H. A. Skinner, Chem. Rev. 55, 745, (1955).

7. J. Hinze, and H. H. Jaffe, J. Am. Chem. Soc. 84, 540 (1962).

8. R. Rerreiva, J. Phys. Chem. 68, 2240, (1964).

9. G. N. Hatsopoulos and J. H. Keenan, "Principles of General Thermodynamics," J. Wiley, New York, Ch. 48 (1965).

10. J. W. Gibbs, "The Scientific Papers of J. Willard Gibbs," Vol. 1, Dover Publications, New York, pp. 135-138, (1961).

11. J. C. Slater, "Theory of Molecules and Solids," Vol. 1, McGraw Hill, New York, p. 96 (1963).

12. J. Hinze, M. A. Whitehead, and H. H. Jaffe, J. Am. Chem. Soc. 85, 148, (1963).

13. Steiner, D., Gyftopoulos, E. P., "An Equation for the Prediction of Bare Work Functions," Report 27th Annual Conf. Physical Electronics, MIT, Cambridge (1967), p. 160.

14. Gyftopoulos, E. P., and Steiner, D., "Orbital Electronegativity and Physical Properties of Bimetallic Adsorption Systems," Report 27th Annual Conf. Physical Electronics, MIT, Cambridge (1967), p. 169.

15. Steiner, D. and Gyftopoulos, E. P., "Orbital Electronegativity and Physical Properties of Metal-Gas Adsorption Systems," Report Thermionic Conversion Specialist Conf., San Francisco, (1967), 145.

16. Gyftopoulos, E. P., and Hatsopoulos, G. N., "Quantum Thermodynamic Definition of Electronegativity," to be published.

17. Tolman, R. C., The Principles of Statistical Mechanics, University Press, New York (1938), pp. 312-324.

18. Slater, J. C., Quantum Theory of Molecules and Solids, Vol. 1. McGraw-Hill, New York (1963), p. 43.

19. Slater, J. C., Quantum Theory of Molecules and Solids, Vol. 3. McGraw-Hill, New York (1967), pp. 265-271.

20. Slater, J. C., Quantum Theory of Molecules and Solids, Vol. 2. McGraw-Hill, New York (1965), pp. 154-158.

21. Koster, G. F. and Slater, J. C., "Wave Functions for Impurity Levels," Phys. Rev. 95 (1954), p. 1167.

22. Reference 18, Chapter 9.

23. Ibid., p. 96.

24. Ibid., Appendix 4.

25. Mulliken, R. S., "A New Electroaffinity Scale," J. Chem. Phys. 2, (1934), p. 782.

26. Reference 29, pp. 557-558.

27. Herring, C. and Nichols, M. H., "Thermionic Emission," Rev. Modern Phys. 21 (1949), p. 190.

28. Reference 29, pp. 329-330.

CHAPTER IV

PARAMETRIC DATA

F. Rufeh, D. Lieb and L. van Someren

A. EMISSION CHARACTERISTICS OF A DUPLEX VAPOR-DEPOSITED TUNGSTEN EMITTER

1. Introduction

The emission characteristics of a vapor-deposited tungsten emitter with a molybdenum collector were investigated in a variable spacing converter. The converter is equipped with a collector guard ring which is maintained at the same temperature and potential as the collector (Figure IV-1). Flexible bellows allow the interelectrode spacing to be varied from zero to 100 mils. The set of data obtained is particularly useful for comparison with the results of theoretical analysis and for studies of the interrelationships between the various converter parameters, since it includes work function measurements and variable spacing families as well as cesium pressure families.

2. Emitter Preparation

The raw material consisted of a piece of fluoride vapor-deposited tungsten from an ingot previously used on this program (Chapter V). A slab was ground down to about 0.155 inch thick, and then a layer of tungsten about 0.02 inch thick was vapor-deposited onto it from the chloride and its surface was ground. The result was to give an emitter with the strength and grain stability of fluoride tungsten combined with the superior emission properties expected from (110) oriented chloride tungsten.

Discs 0.77 inch in diameter were cut from the raw material, and annealed for 3 hours at 2220°K in a tungsten container in a resistance furnace. This was expected to produce a grain structure which would be stable during subsequent converter operation. To ensure removal of the randomly oriented layer introduced by grinding, the emitter face of the disc was electropolished in 5% NaOH solution at 10 volts for two minutes.

An attempt was made to obtain a partial pole figure from the surface of the emitter, but the highly irregular curve which resulted was an indication that the heat treatment had produced a grain size too large to provide a good sample of grains for x-ray examination.

A cross-section of the substrate and deposit was prepared metallographically on another specimen subjected to the same treatment; the photomicrograph after polishing and etching is shown in Figure IV-2. This picture shows the chloride deposit, now recrystallized, on top of the still-columnar fluoride substrate. The circular marks are artifacts of the polishing process.

3. Work Function Measurements

The bare work function of the emitter was determined in the converter prior to the introduction of cesium. The calculated results using Richardson's equation are shown in Figure IV-3. There was no significant dependence of emitter work function on emitter temperature in the range of 1750 to 1950°K, which indicates the absence of oxygen contamination. The bare work function was found to be about 4.87 eV. After the introduction of cesium, the cesiated work function was determined under highly ion-rich conditions and at an interelectrode

spacing of 1 mil. The calculated values of work function are plotted versus the ratio of the emitter to cesium reservoir temperature in Figure IV-4.

4. Cesium Families

Families of volt-ampere characteristics were obtained by changing the cesium pressure while the other converter parameters were held constant. Figures IV-5 through IV-29 show these families in the emitter temperature range of 1600 to 1900°K and the interelectrode spacing range of 0.5 to 40 mils. The emitter temperature indicated represents the temperature at the emitting surface, and the collector temperatures were chosen to be in the vicinity of the optimum values. The output voltage is measured from voltage tap at the cold end of the emitter sleeve and requires a correction of 1.5 mV per amp/cm^2 for conversion to electrode voltage. In order to facilitate the use of these data for analysis and correlations of converter parameters, the cesium pressures (P) and the interelectrode spacings (d) in these data are chosen to provide the Pd products of ..., 5, 10, 20, 40, ... mil-torr. A table for conversion from cesium reservoir temperature to cesium pressure is shown in Table IV-1, and the envelopes of the cesium families are summarized in Figures IV-30 through IV-33. Each curve in these figures represents the optimized performance with respect to cesium pressure and collector temperature. The fully optimized performance is shown in Figure IV-34. The efficiency of this converter was calculated at a spacing of 10 mils since this spacing is of practical interest. The converter efficiency was defined as:

$$\eta \equiv \frac{P_o}{Q_T}$$

TABLE IV-1

CESIUM VAPOR PRESSURE

CESIUM TEMPERATURE		CESIUM PRESSURE
°C	°K	Torr
163	436	0.016
171	444	0.022
179	452	0.031
187	460	0.044
196	469	0.063
204	477	0.088
214	487	0.13
223	496	0.178
234	507	0.25
244	517	0.35
255	528	0.50
266	539	0.71
278	551	1.0
291	564	1.4
304	577	2.0
318	591	2.8
332	605	4.0
347	620	5.7
363	636	8.0
380	653	11.
398	671	16.
416	689	23.

where P_o is the electrode power output and Q_T is the total heat loss as given by:

$$Q_T = Q_{EC} + Q_R + Q_C$$

where Q_{EC} is electron cooling, Q_R is radiation cooling and Q_C is cesium conduction. Figure IV-35 shows the graph used for calculations with the emissivity of 0.18 and cesium conduction of 1.5 watts/cm^2, which represent the average values of these parameters for this set of data. The calculated efficiency is plotted versus emitter temperature at electrode voltages of 0.6, 0.7 and 0.8 volts in Figures IV-36, IV-37, and IV-38. The efficiency of two other converters[1] with chloride tungsten and fluoride tungsten emitters and niobium collectors is also shown in these figures. The efficiency of the duplex W-Mo converter is about the same as the chloride W-Nb converter although they do not have similar collectors. Unfortunately there has been no systematic evaluation of molybdenum versus niobium collectors and it is not possible to apply an exact correction for the difference between the two collectors. However, even if we allow 50 mV for the difference in collector work function, the duplex emitter is by far superior to the fluoride emitter.

5. Spacing Families

Variable-spacing families were obtained covering the spacing range of 0.5 to 40 mils for the cesium pressure range of 0.5 to 4 torr and the ion richness range of 0.1 to 10. Figures IV-39 through IV-41 show such families at an ion richness of 10 and cesium pressure of 0.5, 1, and 2 torr. Note that for the Pd of 0.25 mil-torr (Figure IV-39) there is a clear saturation and no ignition. At a Pd of 0.625 mil-torr ignition still does not occur, but the saturation current is slightly reduced. The

higher Pd curves show a definite ignition, and the observed currents are significantly higher than the saturation current. This is probably caused by ion current and Schottky effects, as suggested by Hansen[2,3] and Wilkins.[4] The spacing families for the ion richness conditions of 1 and 0.1 and the cesium pressure range of 0.5 to 4 torr are shown in Figures IV-42 through IV-48. In each family, the extinguished mode and the ignited mode including a large portion of the quasi-saturation region are recorded. The pre-ignition region was deleted for the sake of clarity.

6. Summary of the Data

Based on the work function measurements, an emission map of the surface was constructed, as shown in Figure IV-49. The electron and ion currents are shown by the dashed and the solid curves, and the ion richness is indicated by the solid lines. Emitter work function (the open circles) measurements were performed under highly rich conditions and cesium families (the open triangles) were obtained mostly under electron rich conditions. A total of ten spacing families (solid squares) were obtained, three at the ion richness of 10, four at the ion richness of 1, and three at the ion richness of 0.1.

The effect of β and Pd on the J-V characteristics was studied from this set of data in the manner suggested in Reference 5. The general shapes of the J-V characteristics are shown for various values of β and Pd in Figure IV-50. Near ideal characteristics are observed at high β and low Pd conditions (curve a). As the ion richness is reduced, the unignited current is also reduced and ignition occurs (curves b and c). The same behavior is obtained by increasing the Pd values (curves d and g) except that the slope of the quasi-saturation

region increases rapidly due to electron scattering. Curve e represents a typical J-V characteristic at moderate values of Pd and β. The pre-ignition region is clearly observed at low ion richness conditions and becomes stronger as Pd increases (curves c, f, i and h) for moderate values of β and Pd. The presence of the pre-ignition region depends on cesium pressure and is generally observed at cesium pressures lower than 0.5 torr (the dashed lines in curves b, d, e, and g). It is interesting to note that cesium pressure affects the volt-ampere characteristics at constant values of Pd and β. The parameters Pd and β, however, are quite useful in describing the region of operation, and, to the first approximation, they can be combined into a quantity such as Pd/β to the general characteristics of the J-V curve. For example, note the similarities in curves c, e and g.

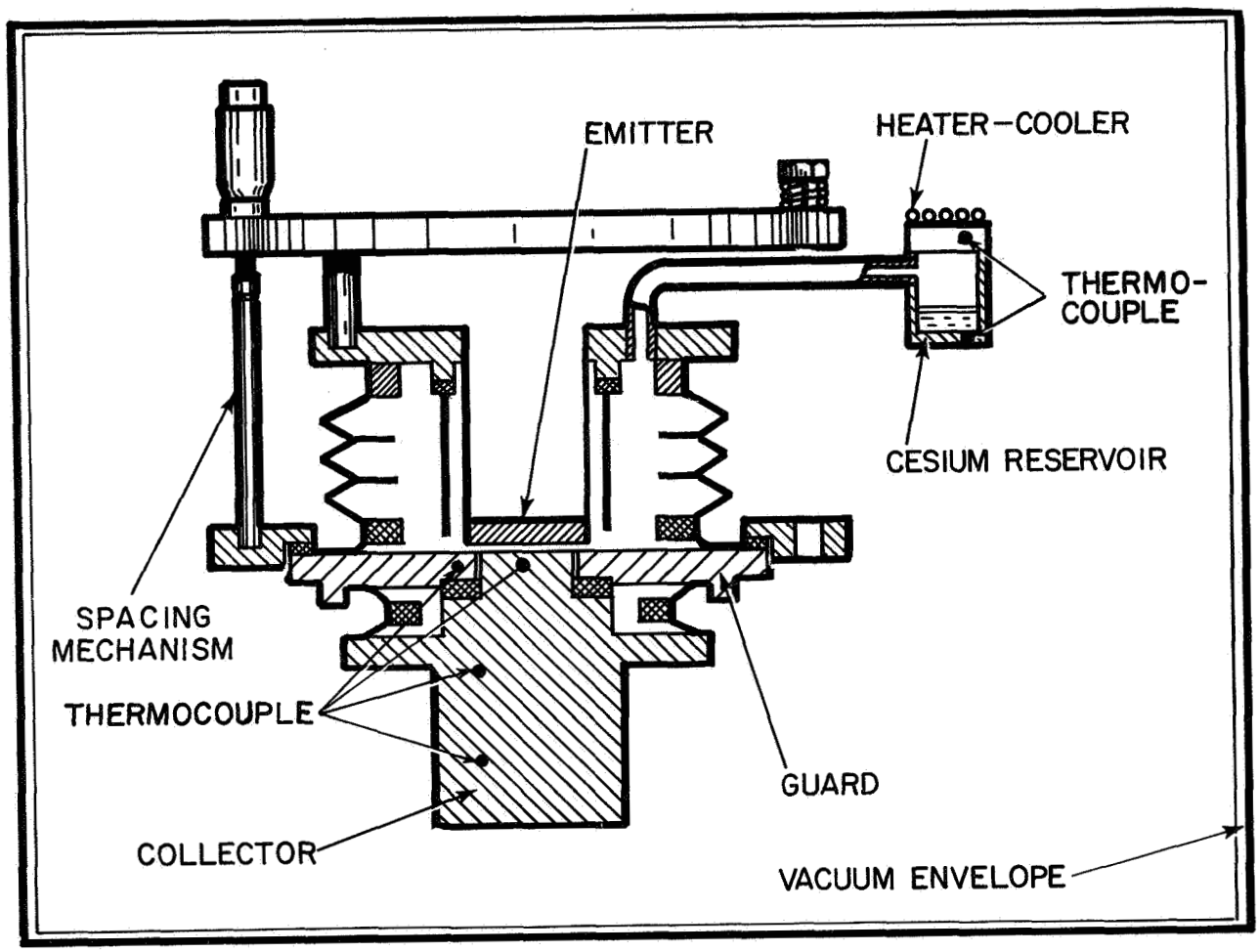

Figure IV-1. Schematic Diagram of a Research Thermionic Converter.

Figure IV-2. Cross-Section of Emitter Showing Columnar Deposit of Tungsten from the Chloride Which Provides Emitting Surface.

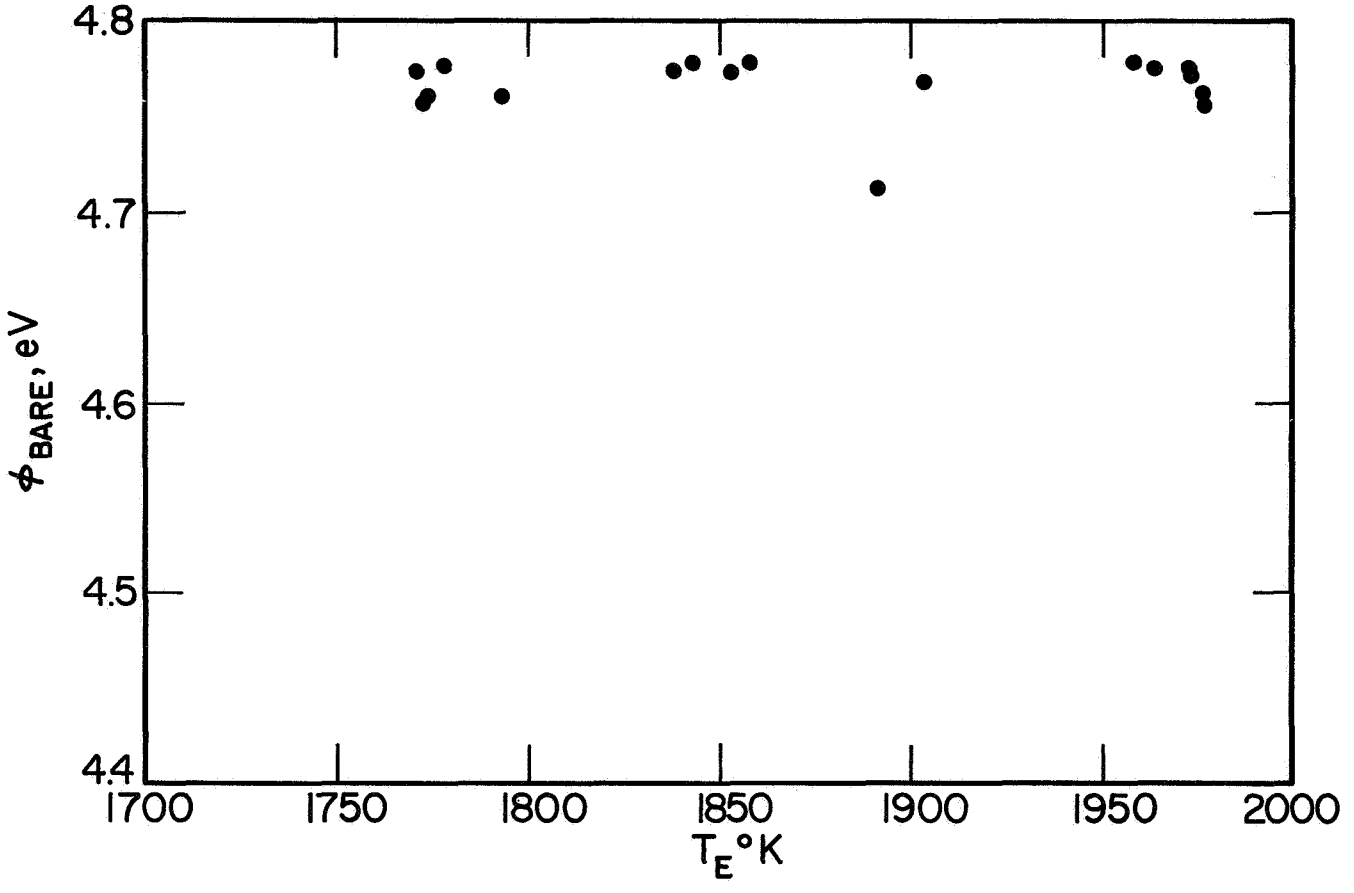

Figure IV-3. Summary of Bare Work Function Data.

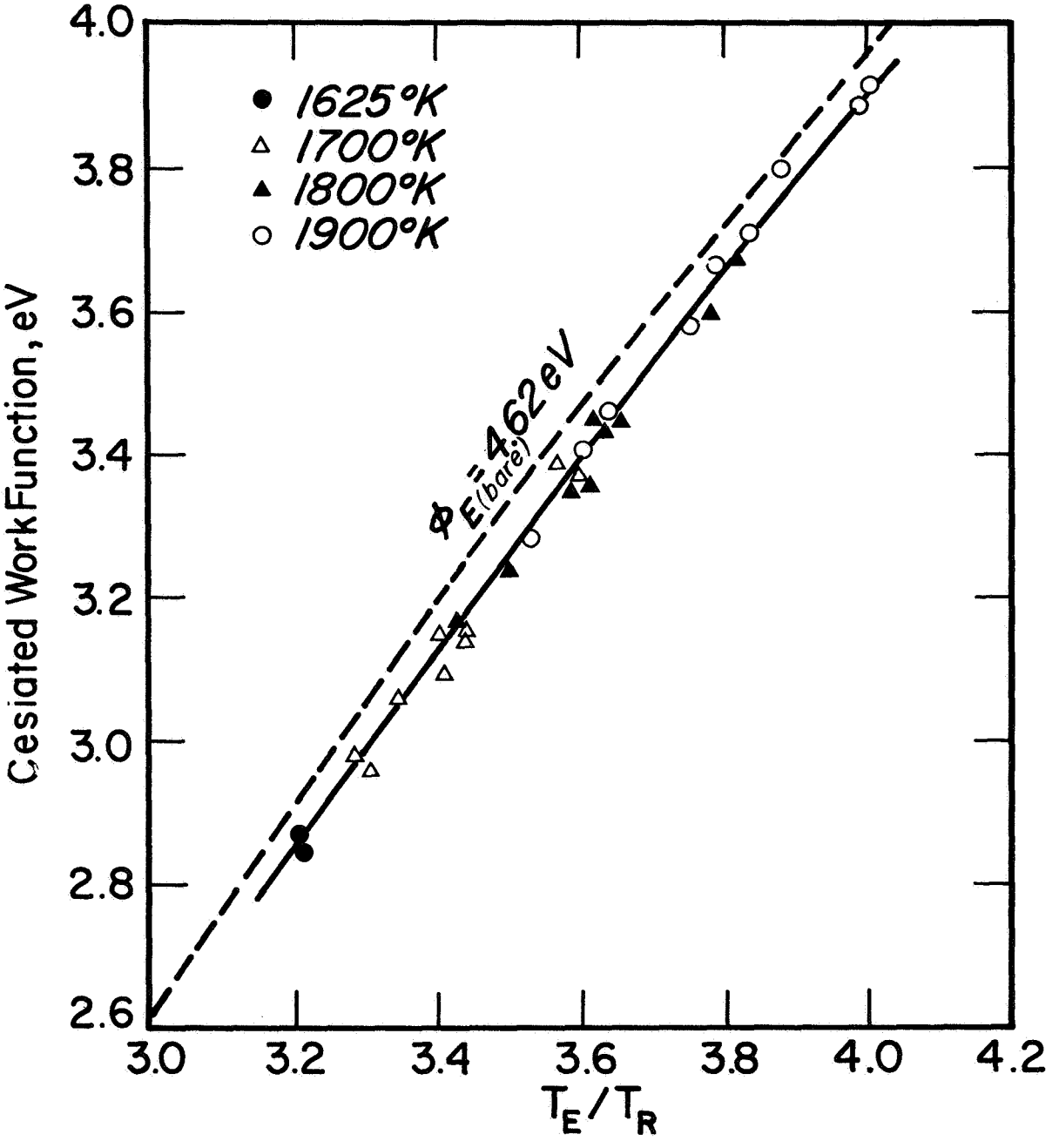

Figure IV-4. Emitter Work Function Data.

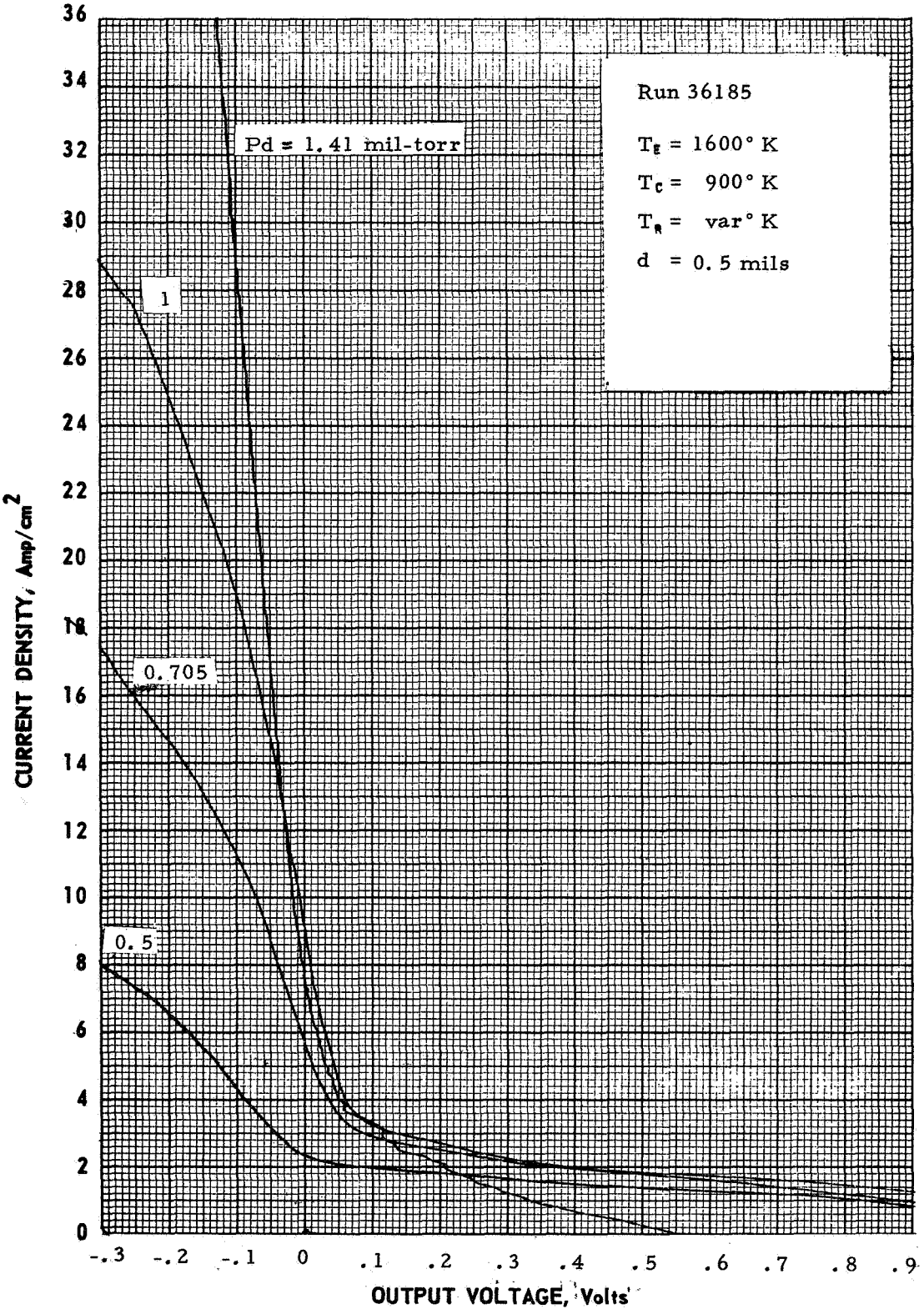

Figure IV-5. Variable Cesium Pressure Family at T_E = 1600° K and d = 0.5 mils.

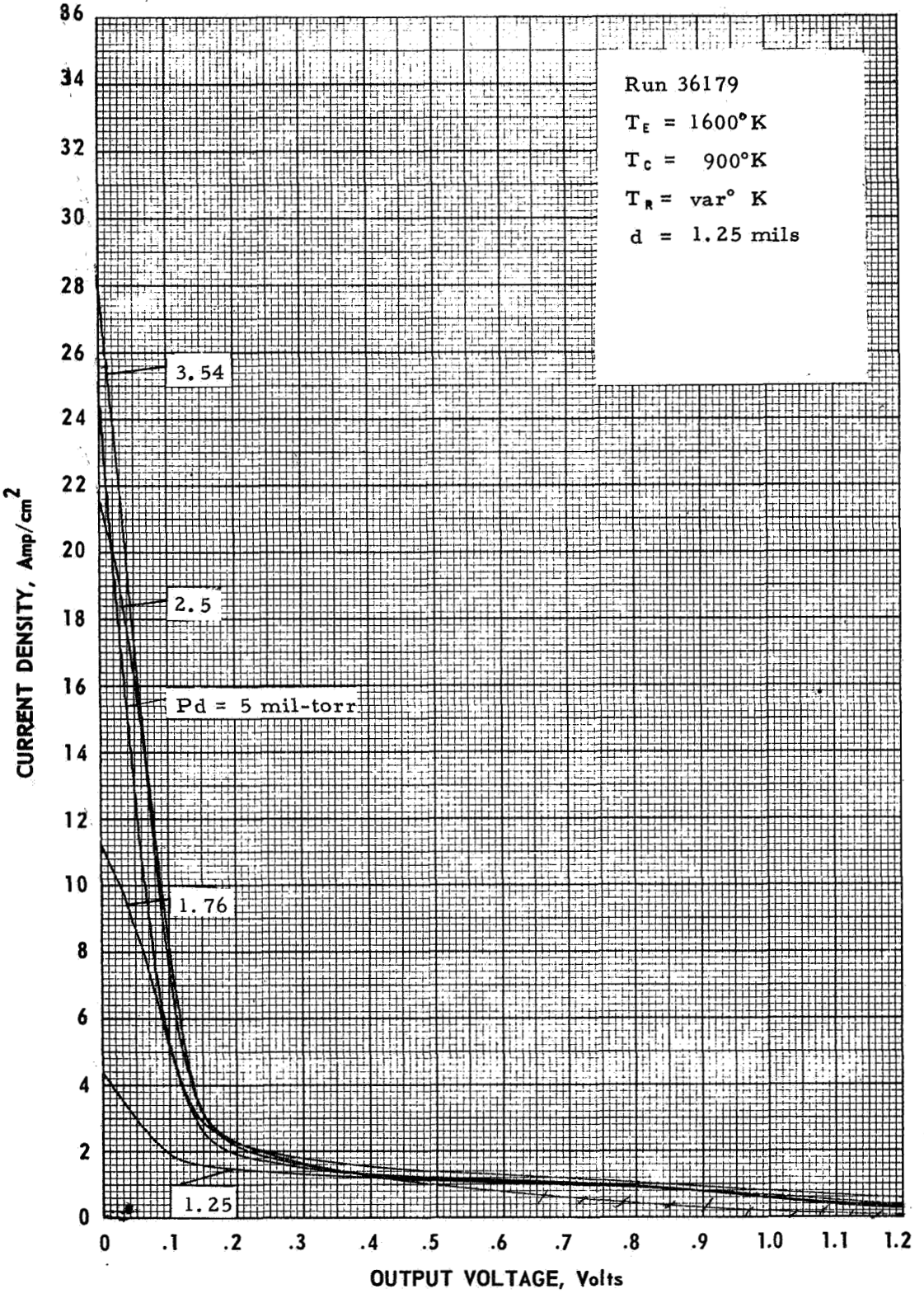

Figure IV-6. Variable Cesium Pressure Family at T_E = 1600° K and d = 1.25 mils.

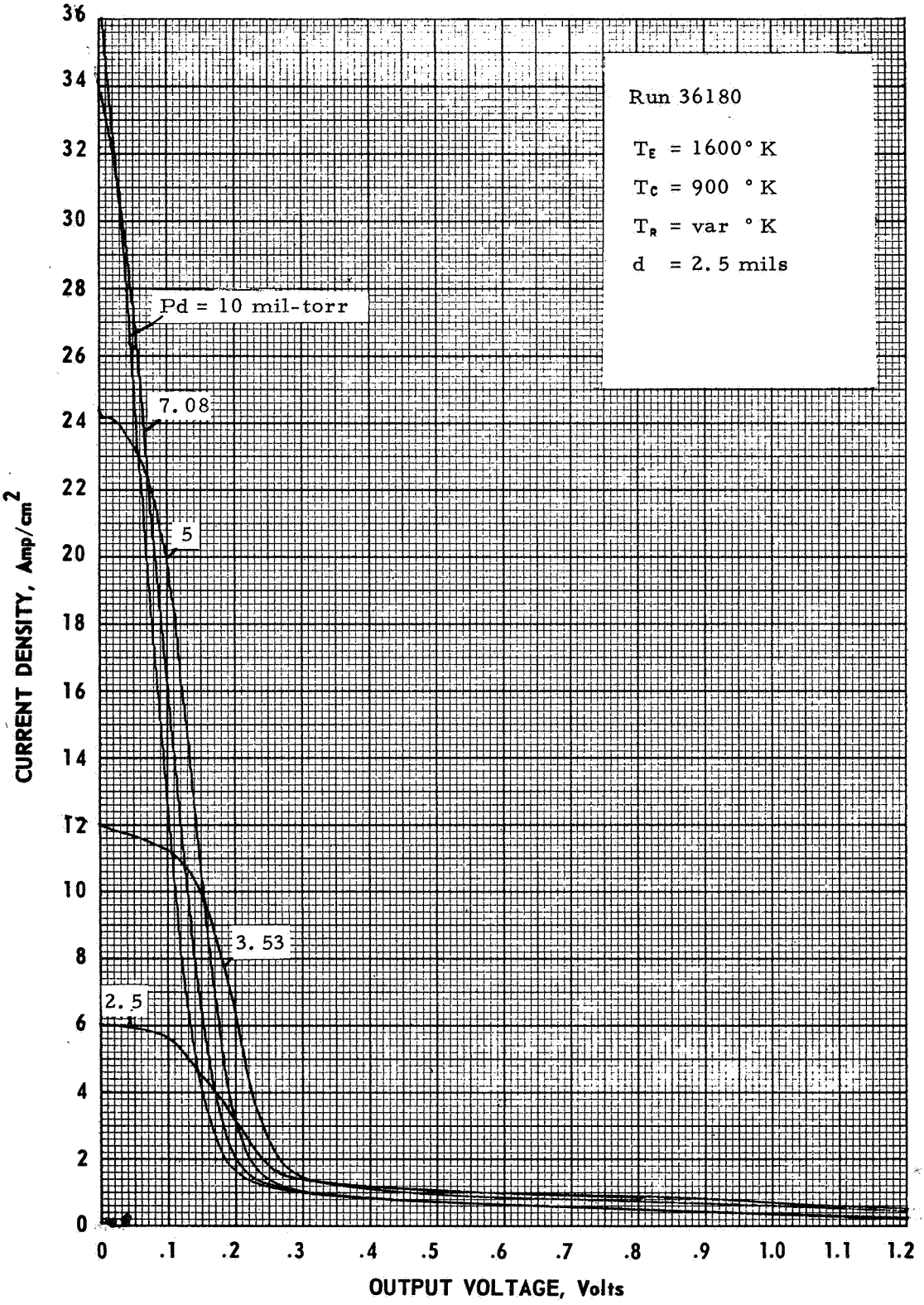

Figure IV-7. Variable Cesium Pressure Family at T_E = 1600° K and d = 2.5 mils.

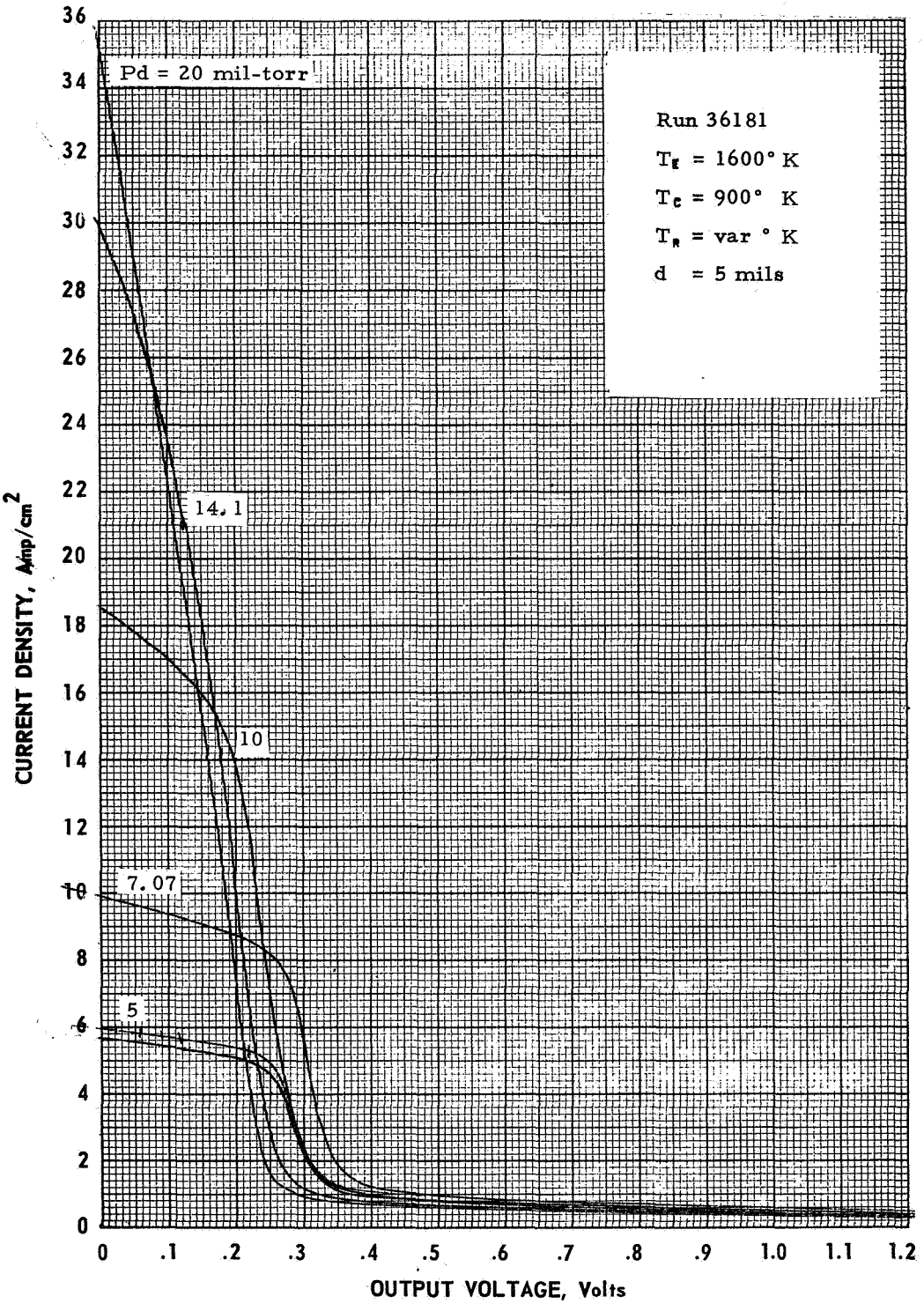

Figure IV-8. Variable Cesium Pressure Family at T_E = 1600° K and d = 5 mils.

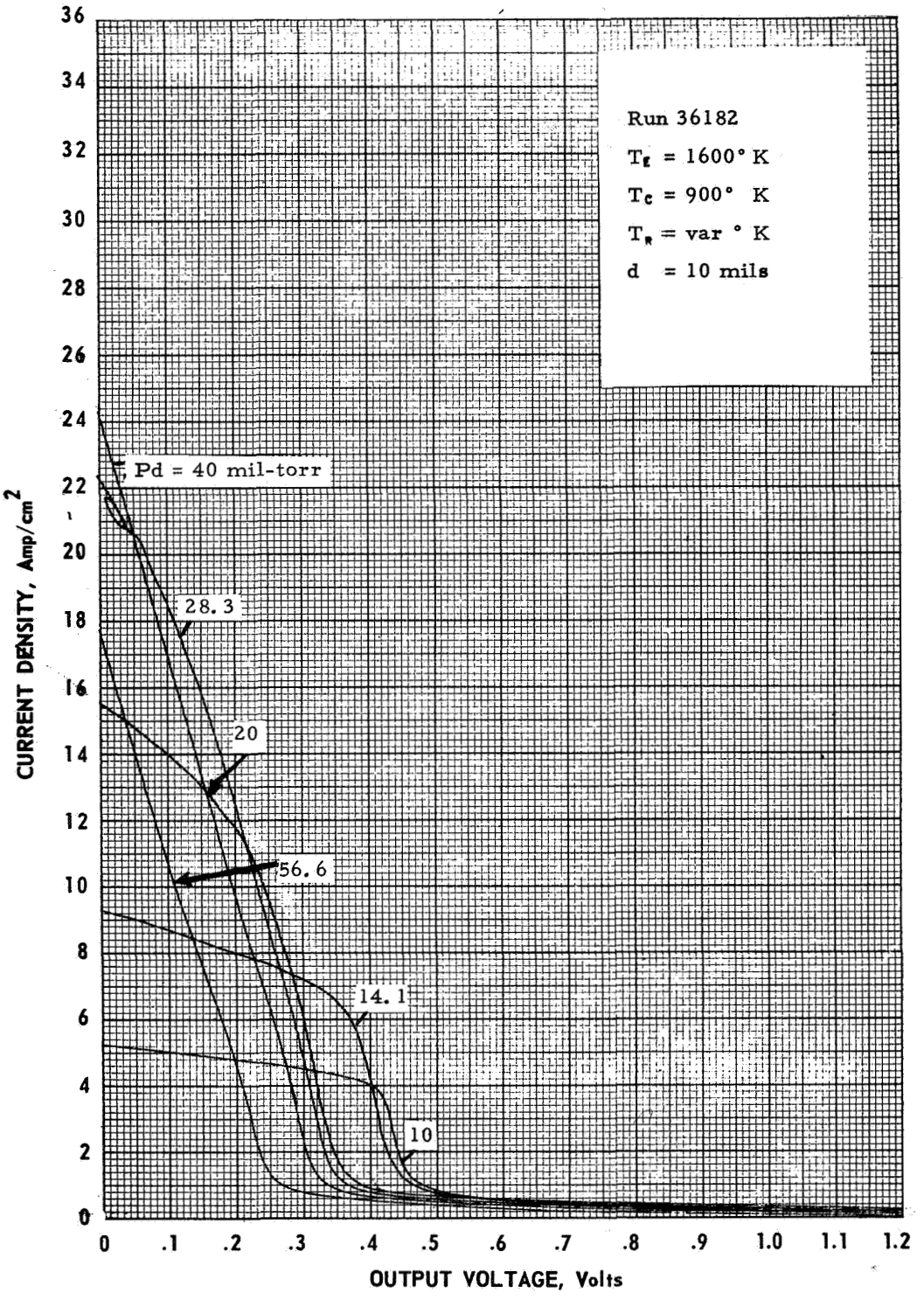

Figure IV-9. Variable Cesium Pressure Family at T_E = 1600° K and d = 10 mils.

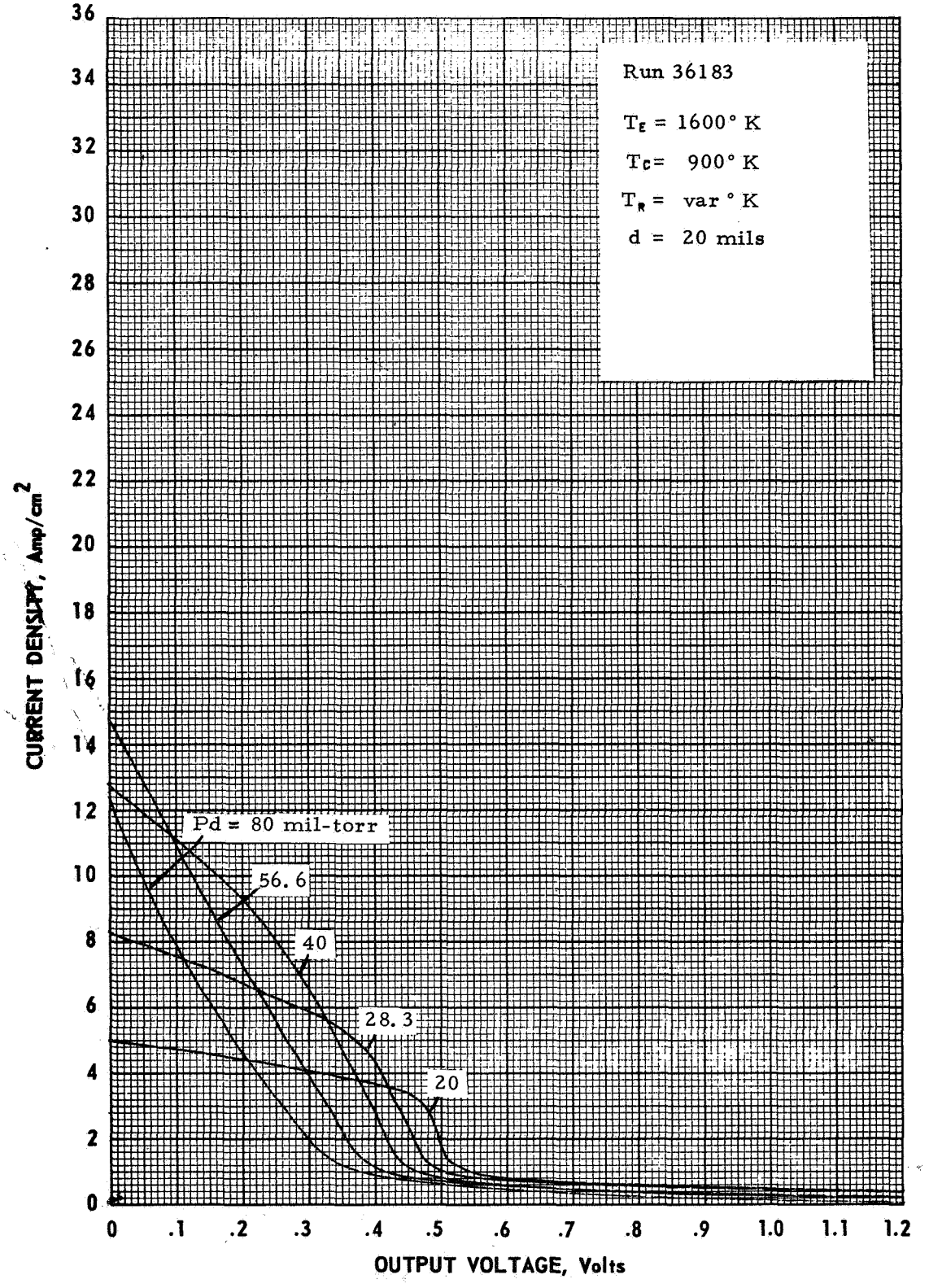

Figure IV-10. Variable Cesium Pressure Family at T_E = 1600° K and d = 20 mils.

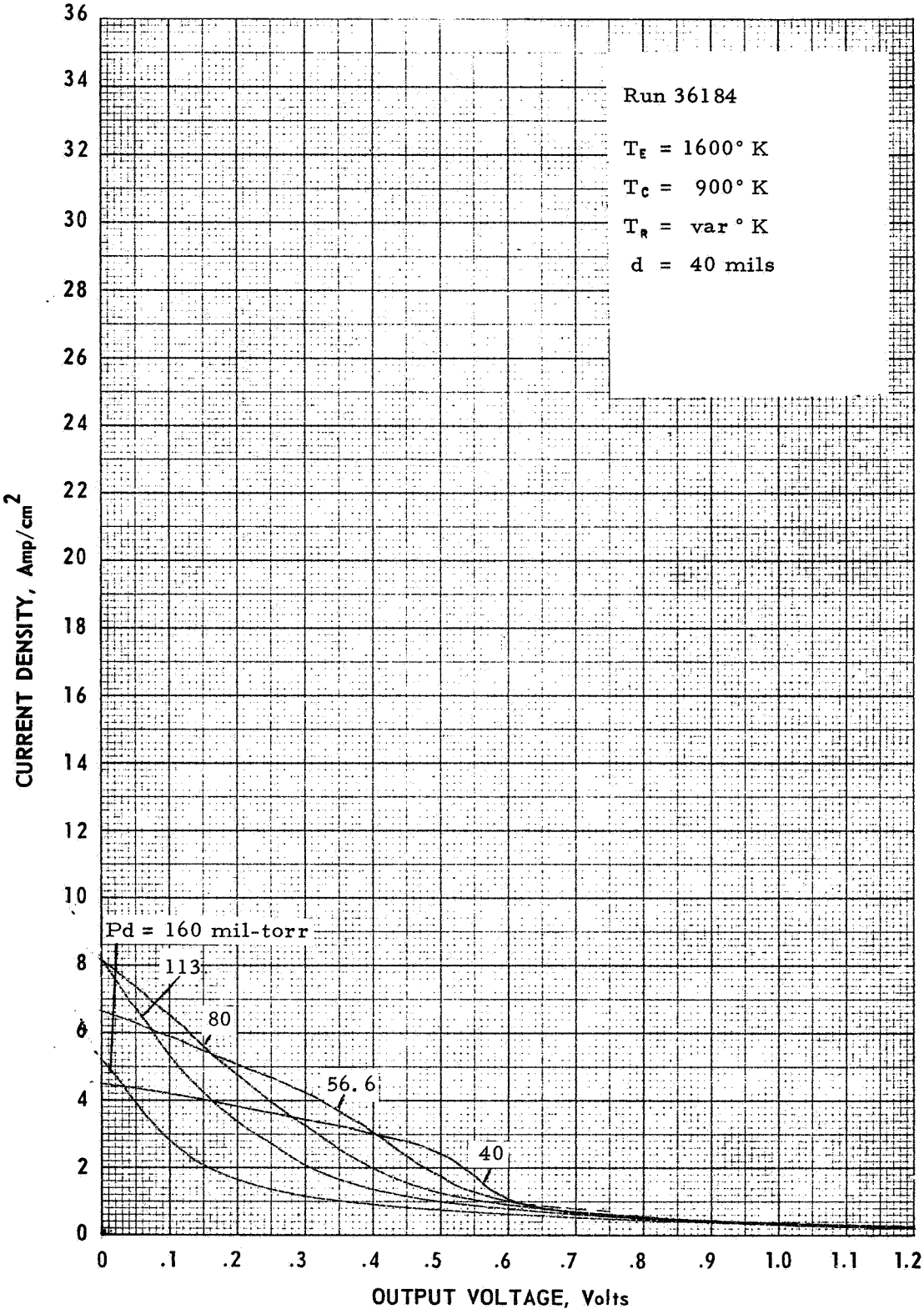

Figure IV-11. Variable Cesium Pressure Family at T_E = 1600° K and d = 40 mils.

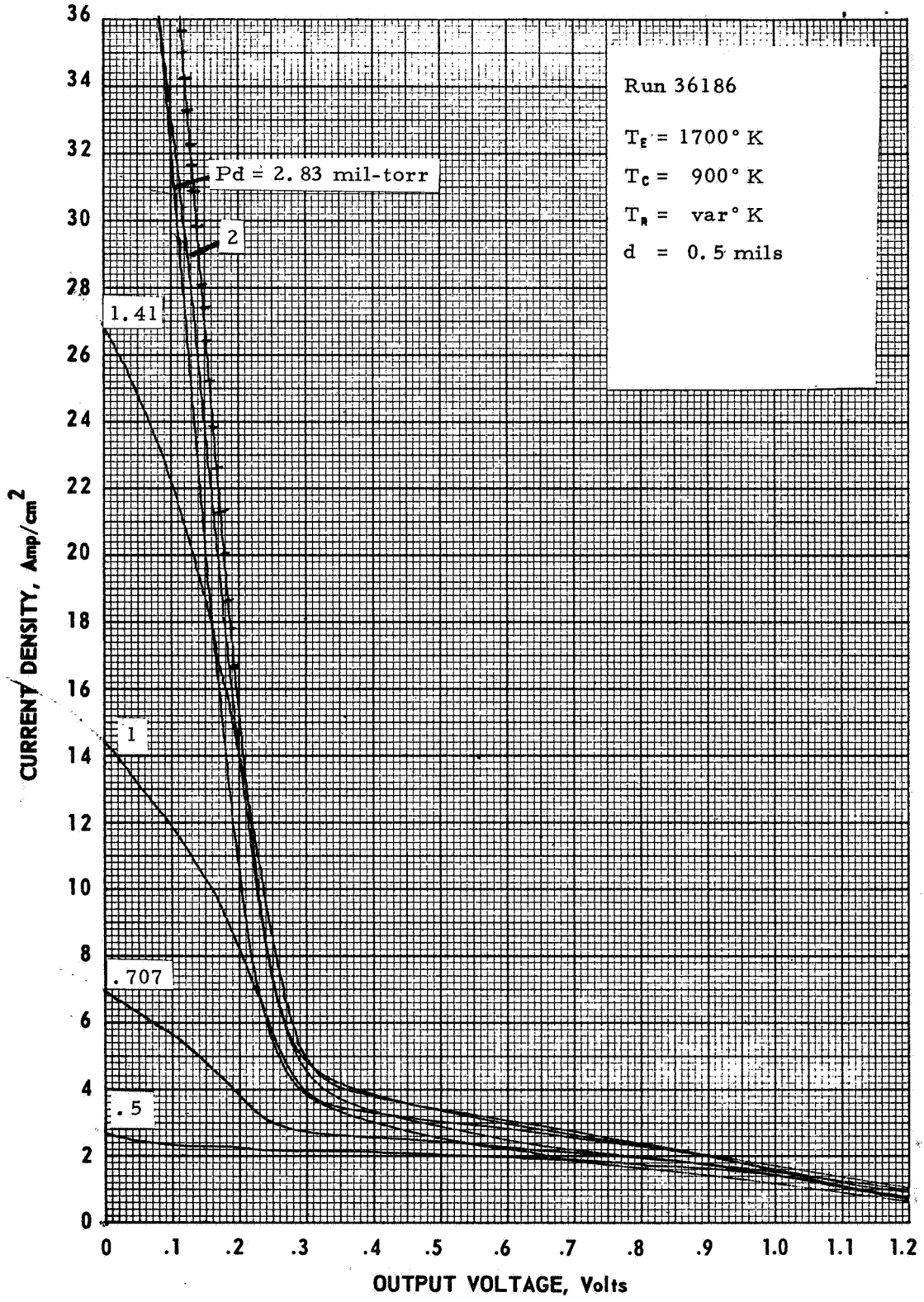

Figure IV-12. Variable Cesium Pressure Family at T_E = 1700°K and d = 0.5 mils.

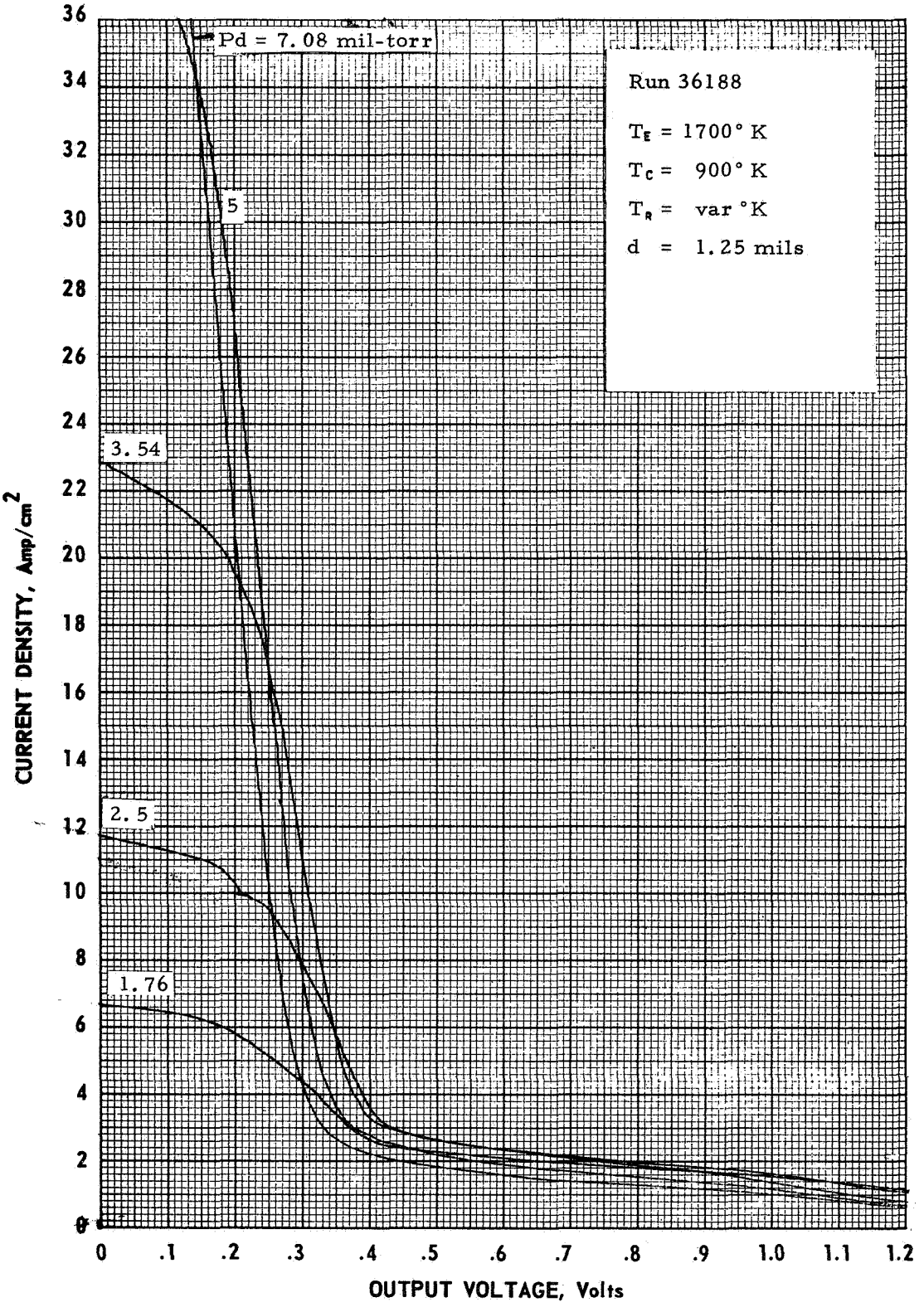

Figure IV-13. Variable Cesium Pressure Family at T_E = 1700°K and d = 1.25 mils.

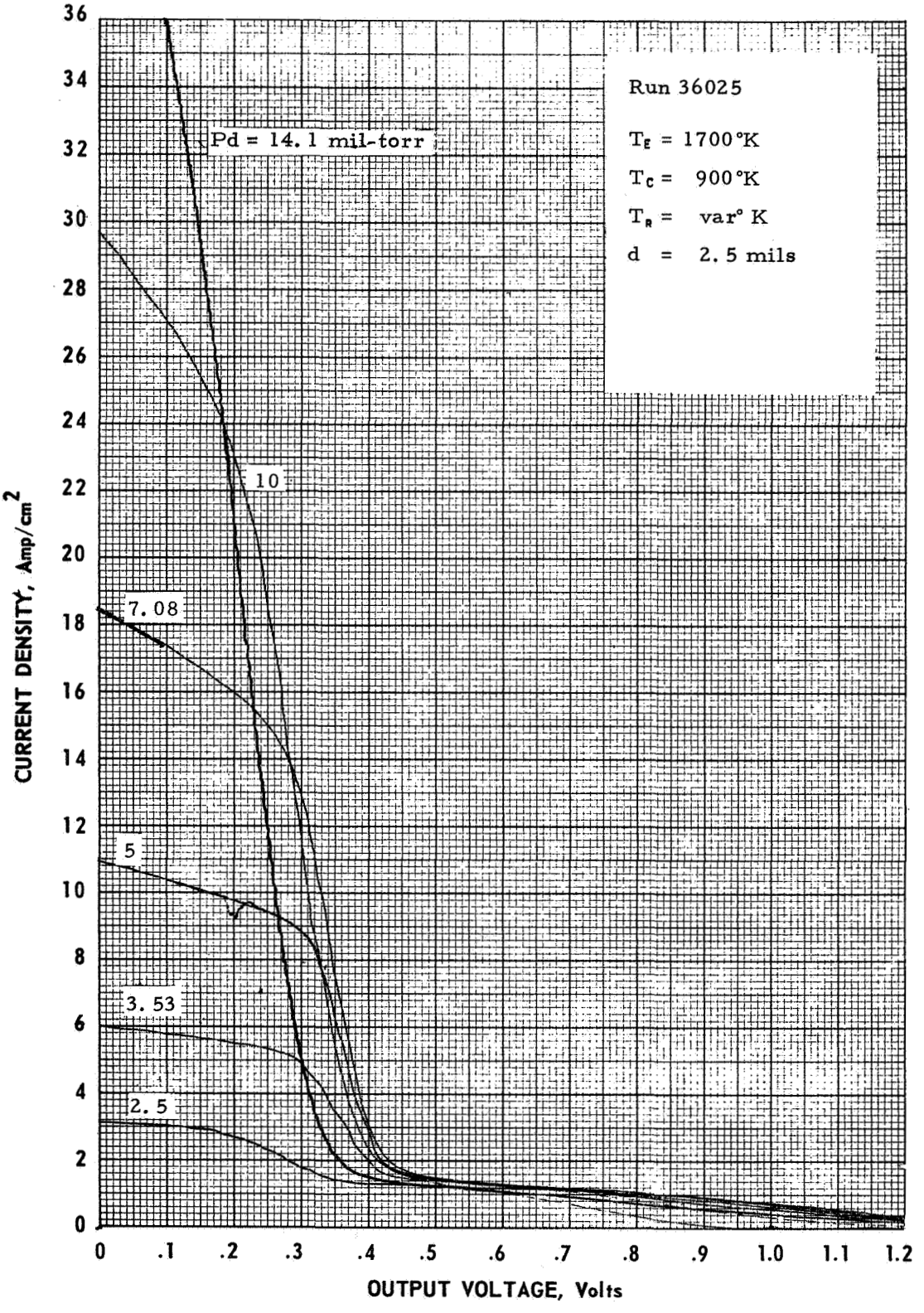

Figure IV-14. Variable Cesium Pressure Family at T_E = 1700° K and d = 2.5 mils.

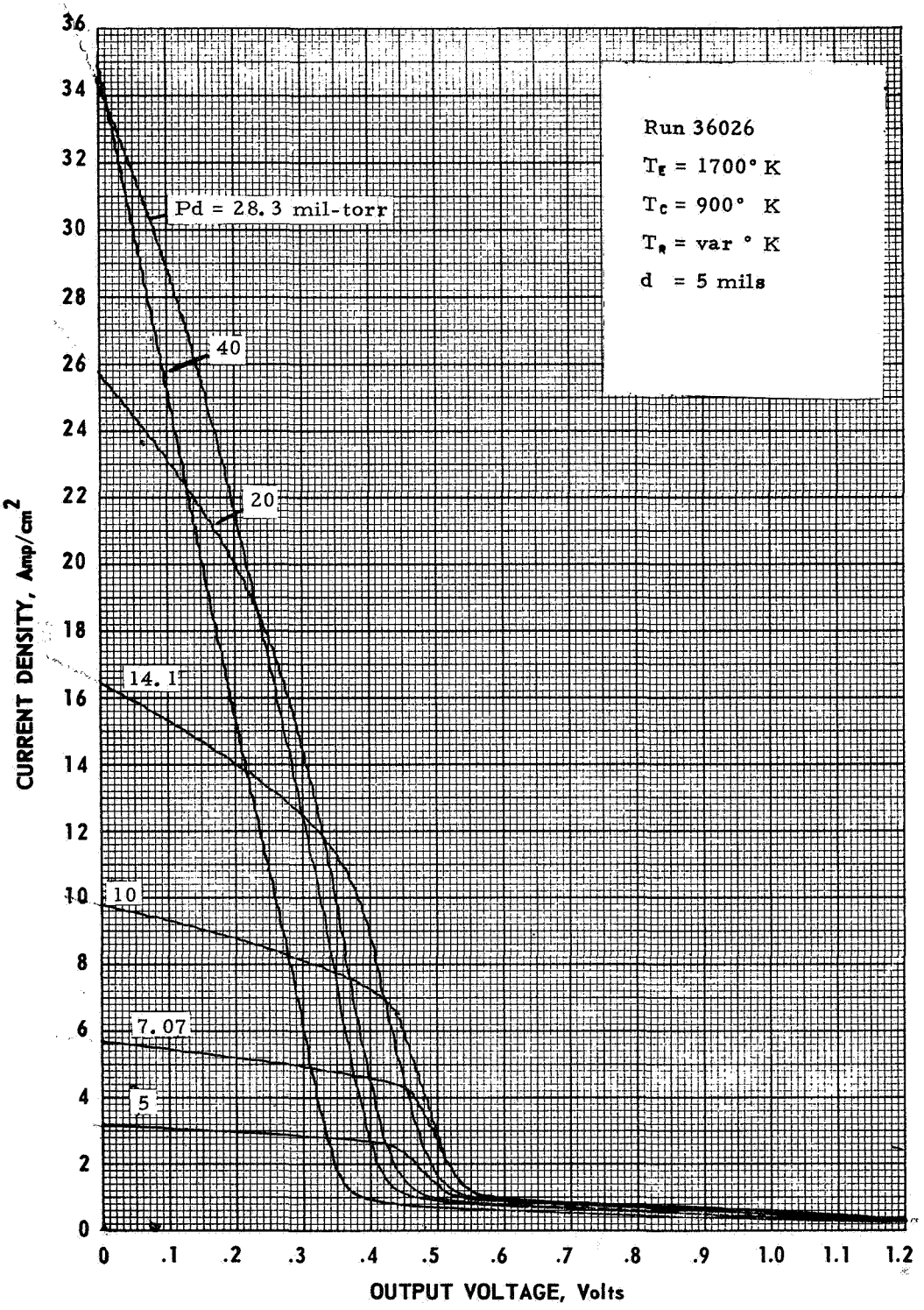

Figure IV-15 Variable Cesium Pressure Family at T_E = 1700° K and d = 5 mils.

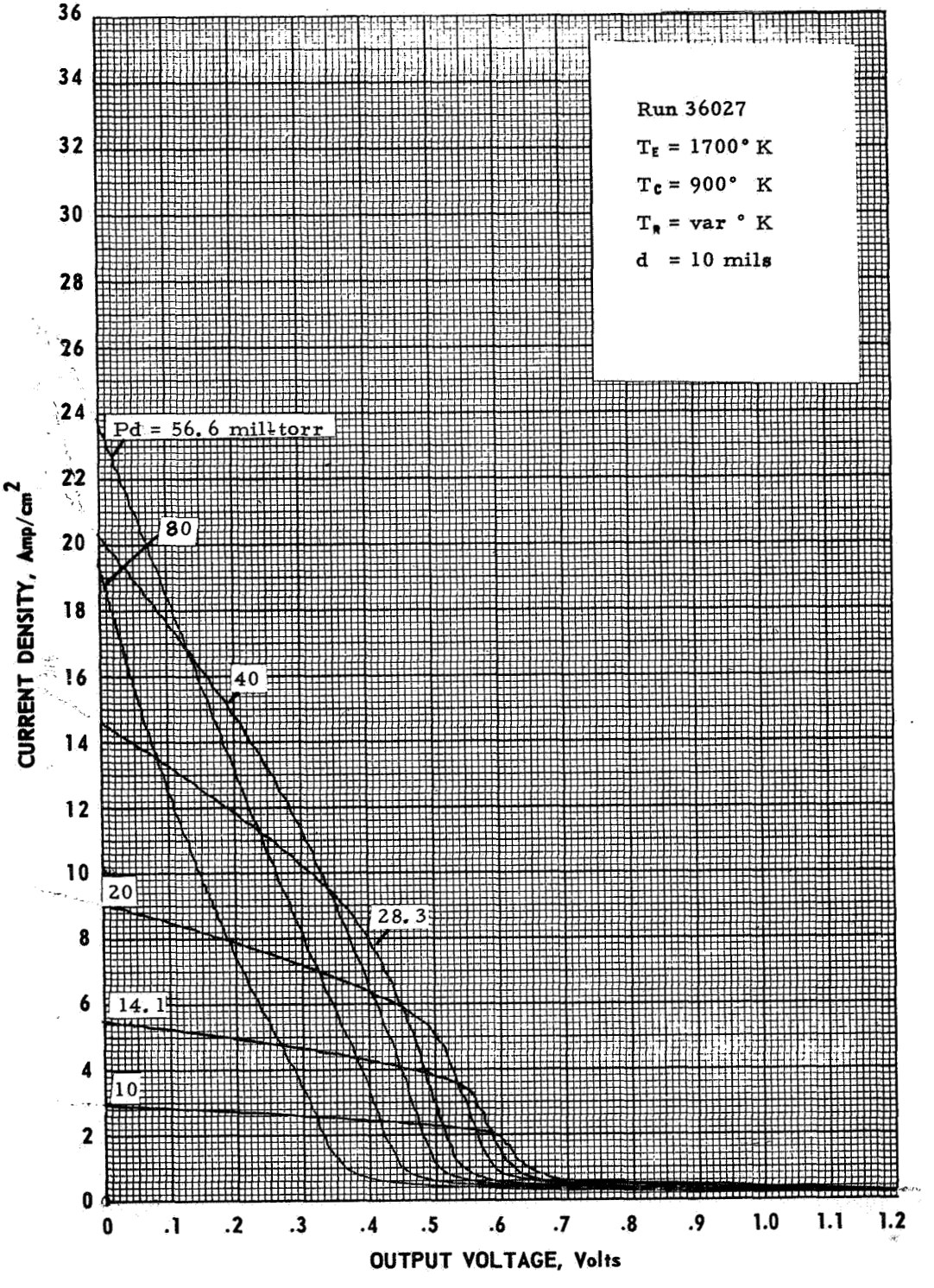

Figure IV-16. Variable Cesium Pressure Family at T_E = 1700° K and d = 10 mils.

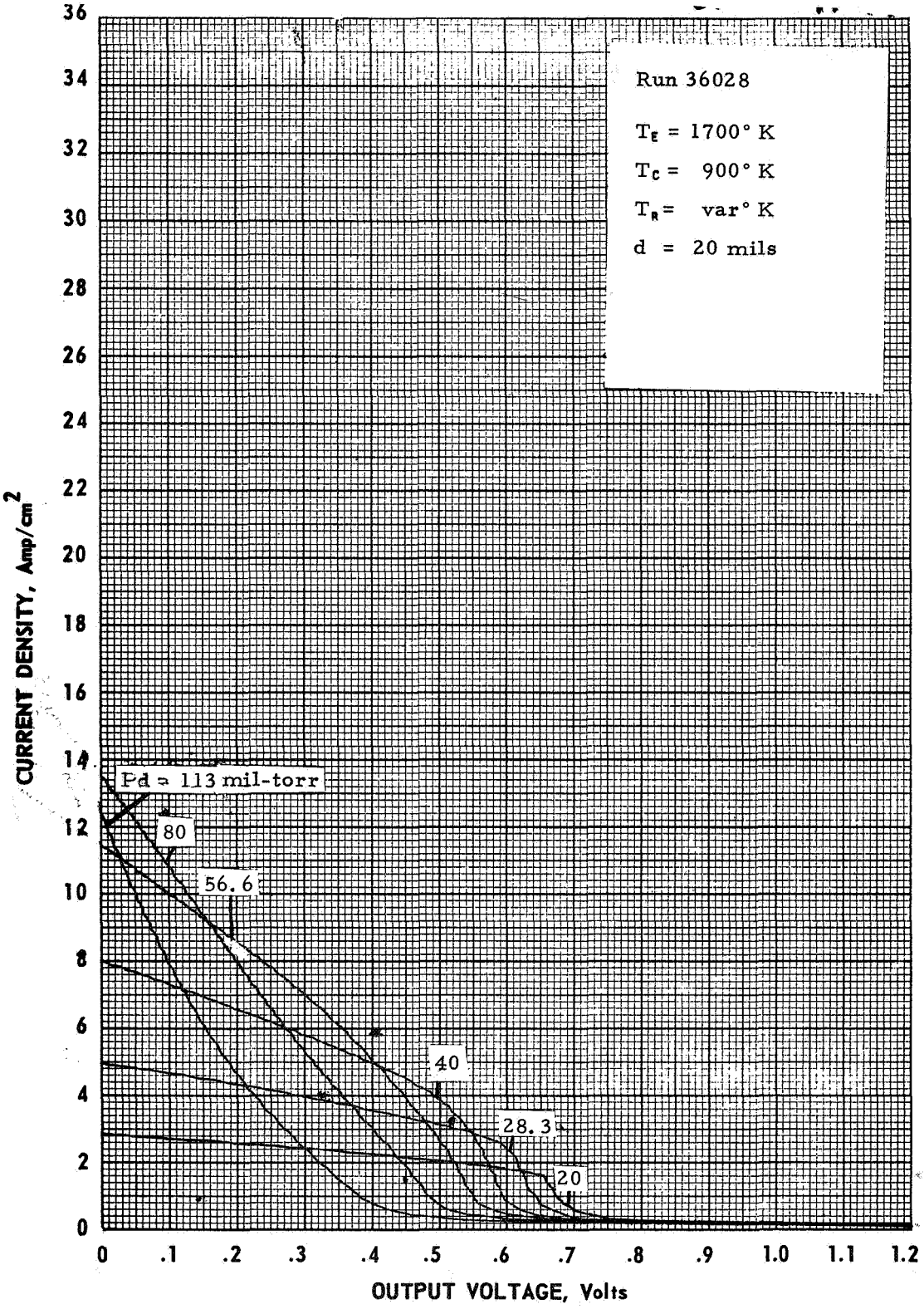

Figure IV-17. Variable Cesium Pressure Family at T_E = 1700° K and d = 20 mils.

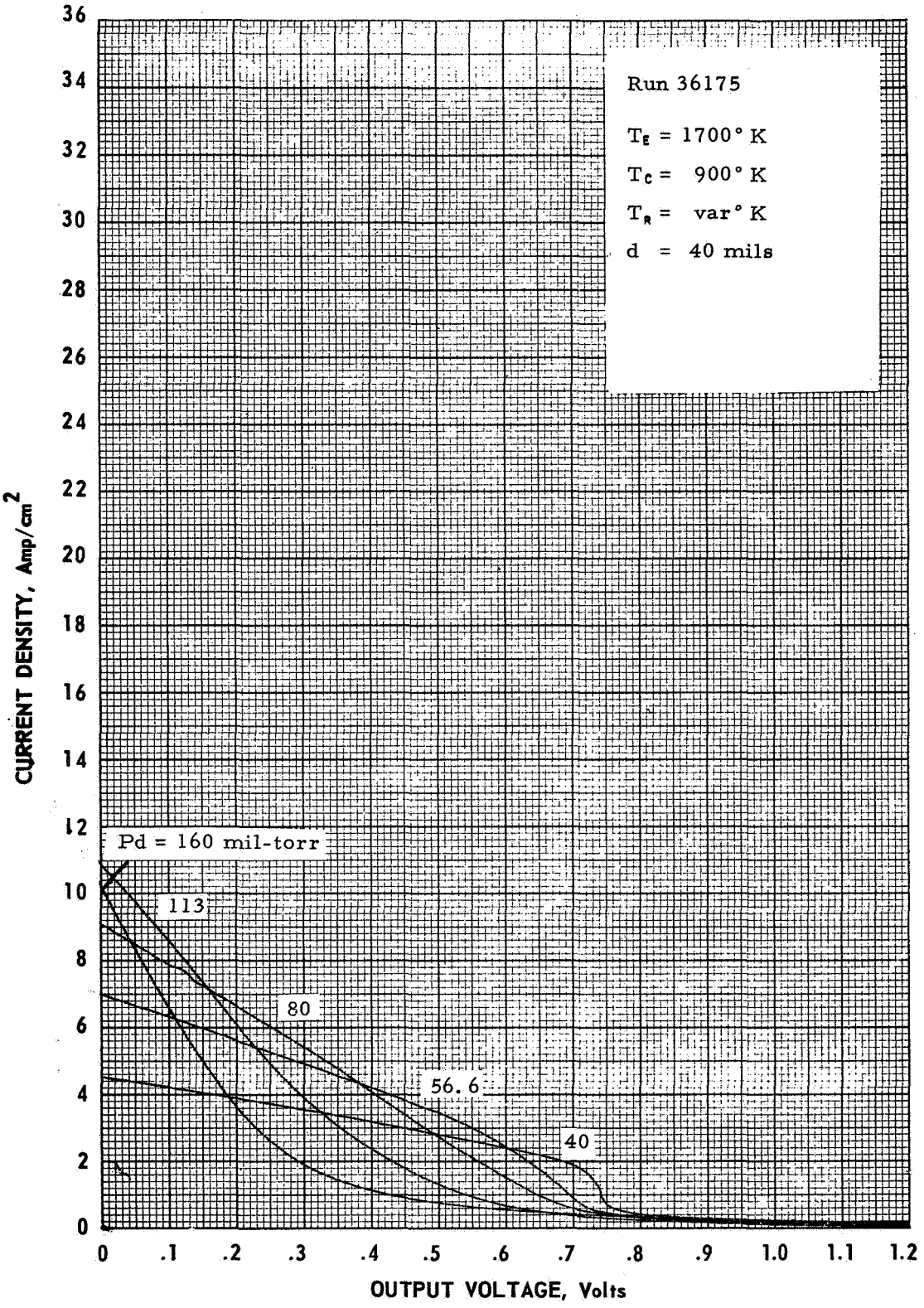

Figure IV-18. Variable Cesium Pressure Family at T_E = 1700° K and d = 40 mils.

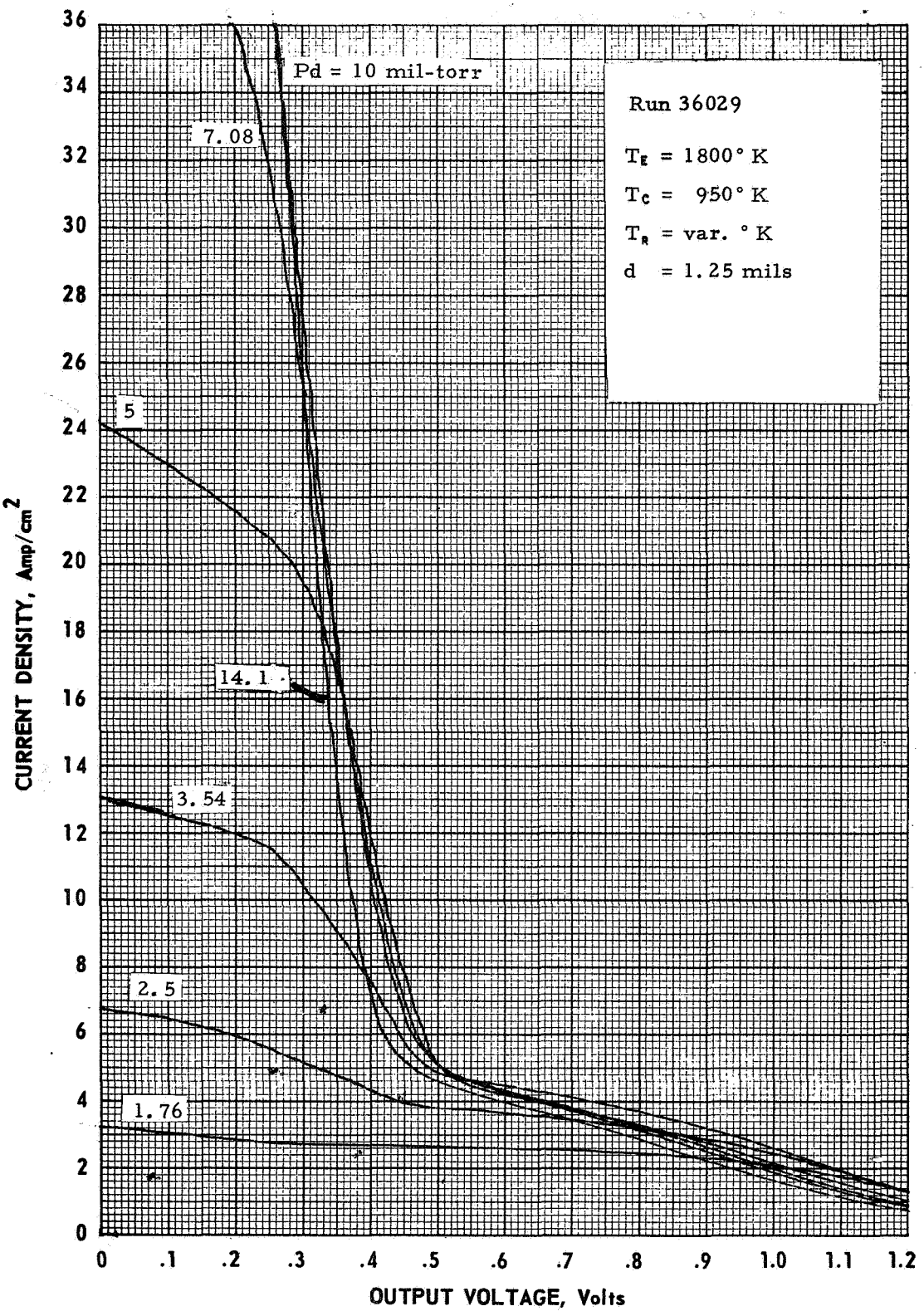

Figure IV-19. Variable Cesium Pressure Family at T_E = 1800° K and d = 1.25 mils.

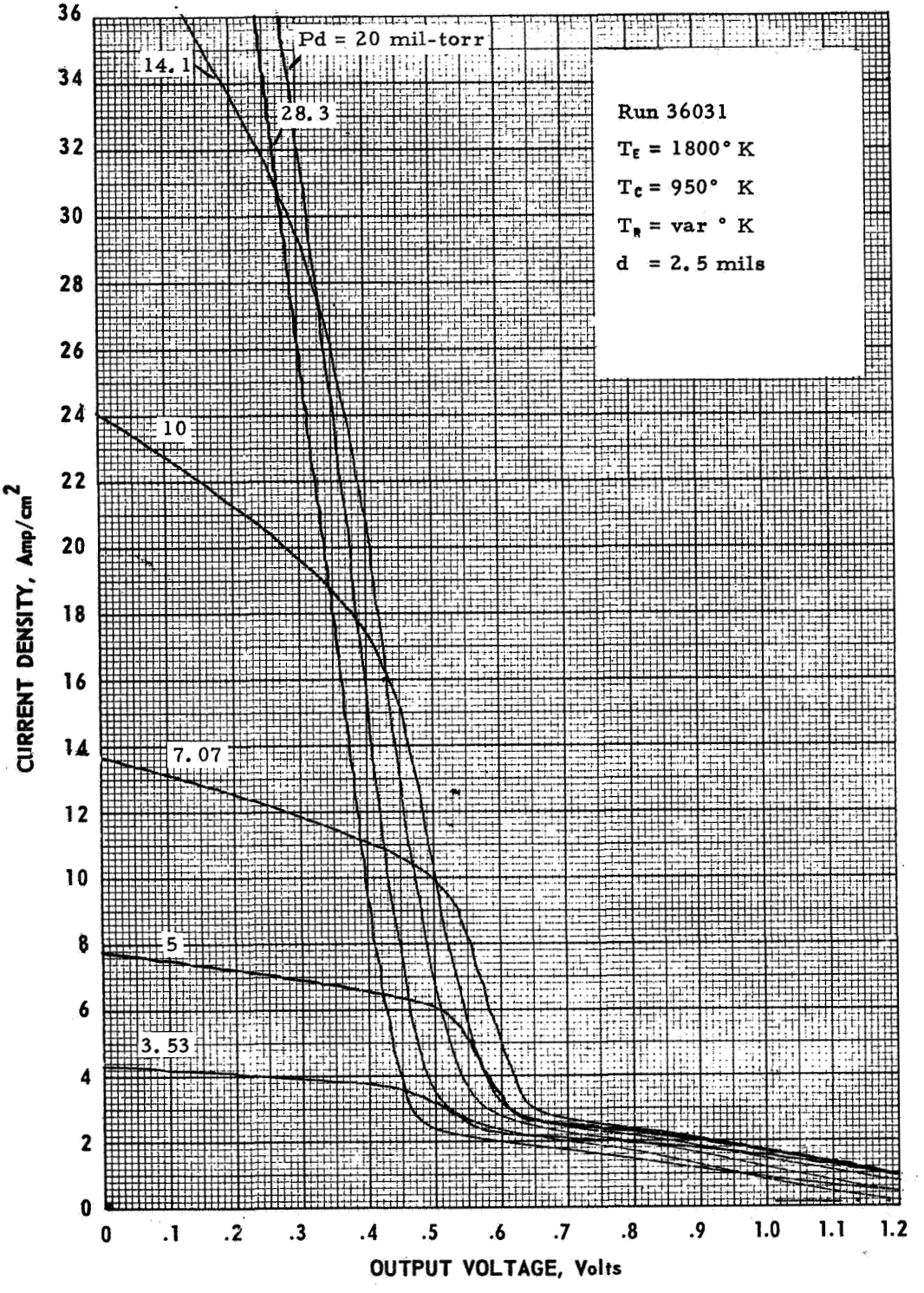

Figure IV-20. Variable Cesium Pressure Family at T_E = 1800° K and d = 2.5 mils.

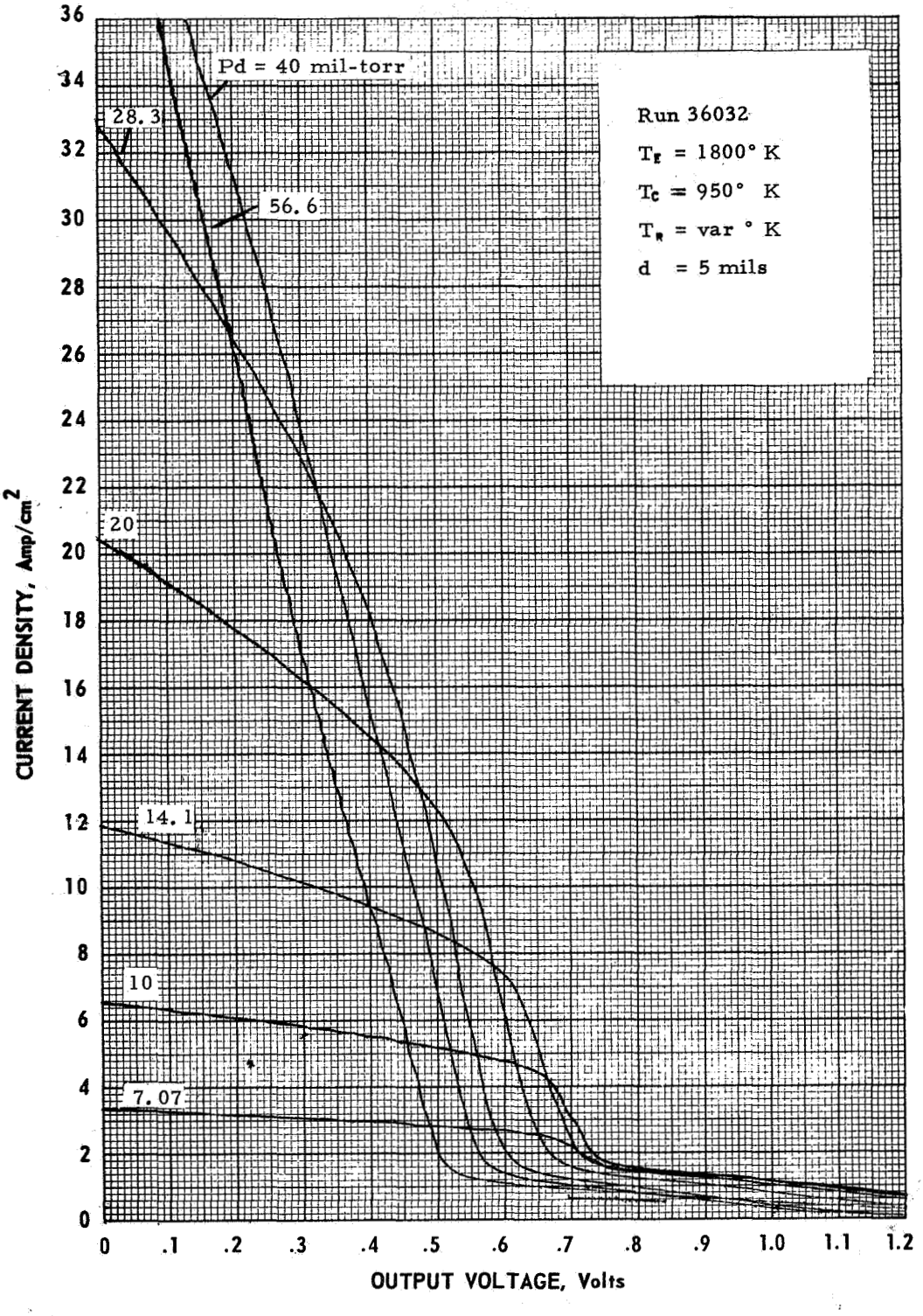

Figure IV-21. Variable Cesium Pressure Family at T_E = 1800° K and d = 5 mils.

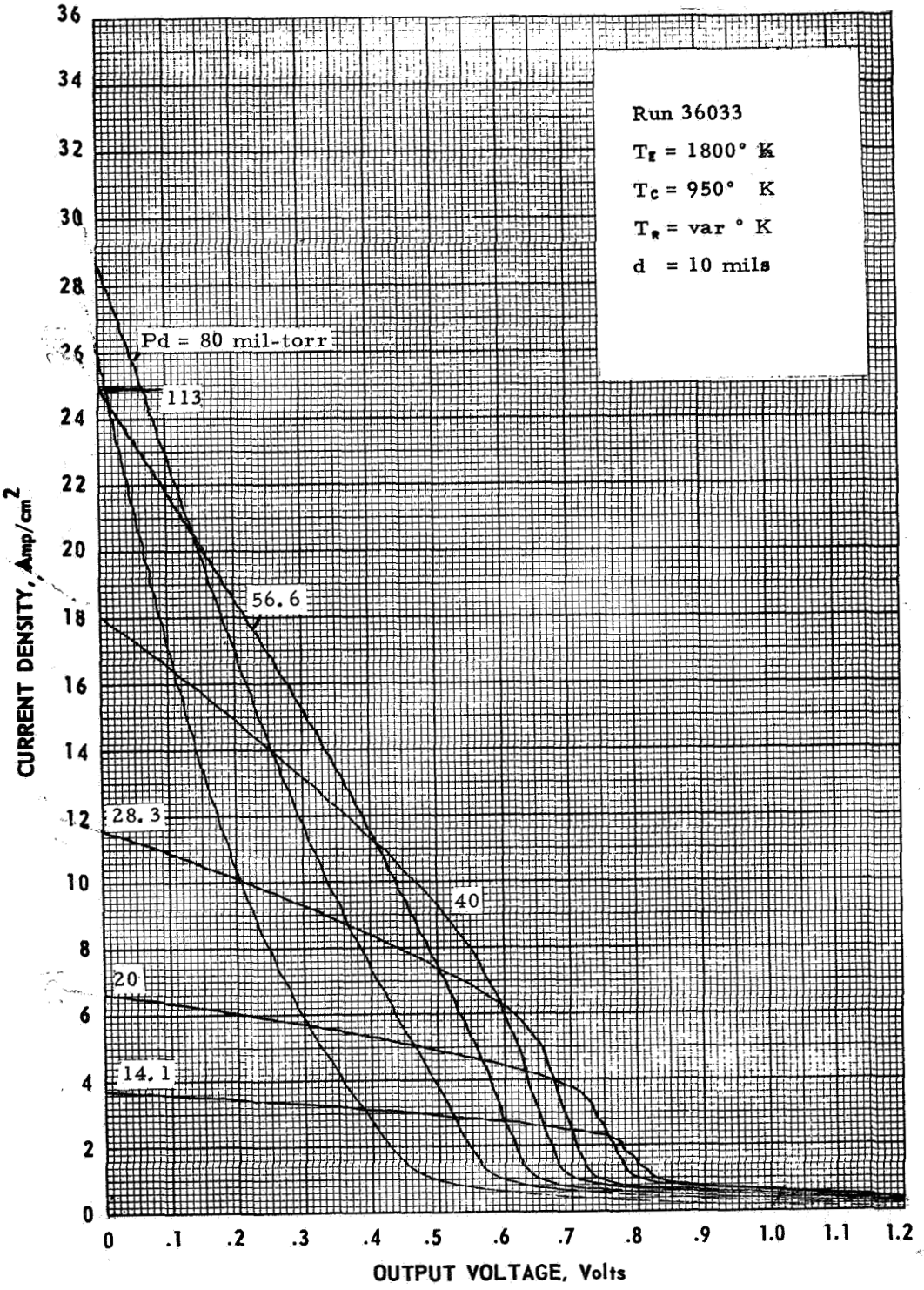

Figure IV-22. Variable Cesium Pressure Family at T_E = 1800° K and d = 10 mils.

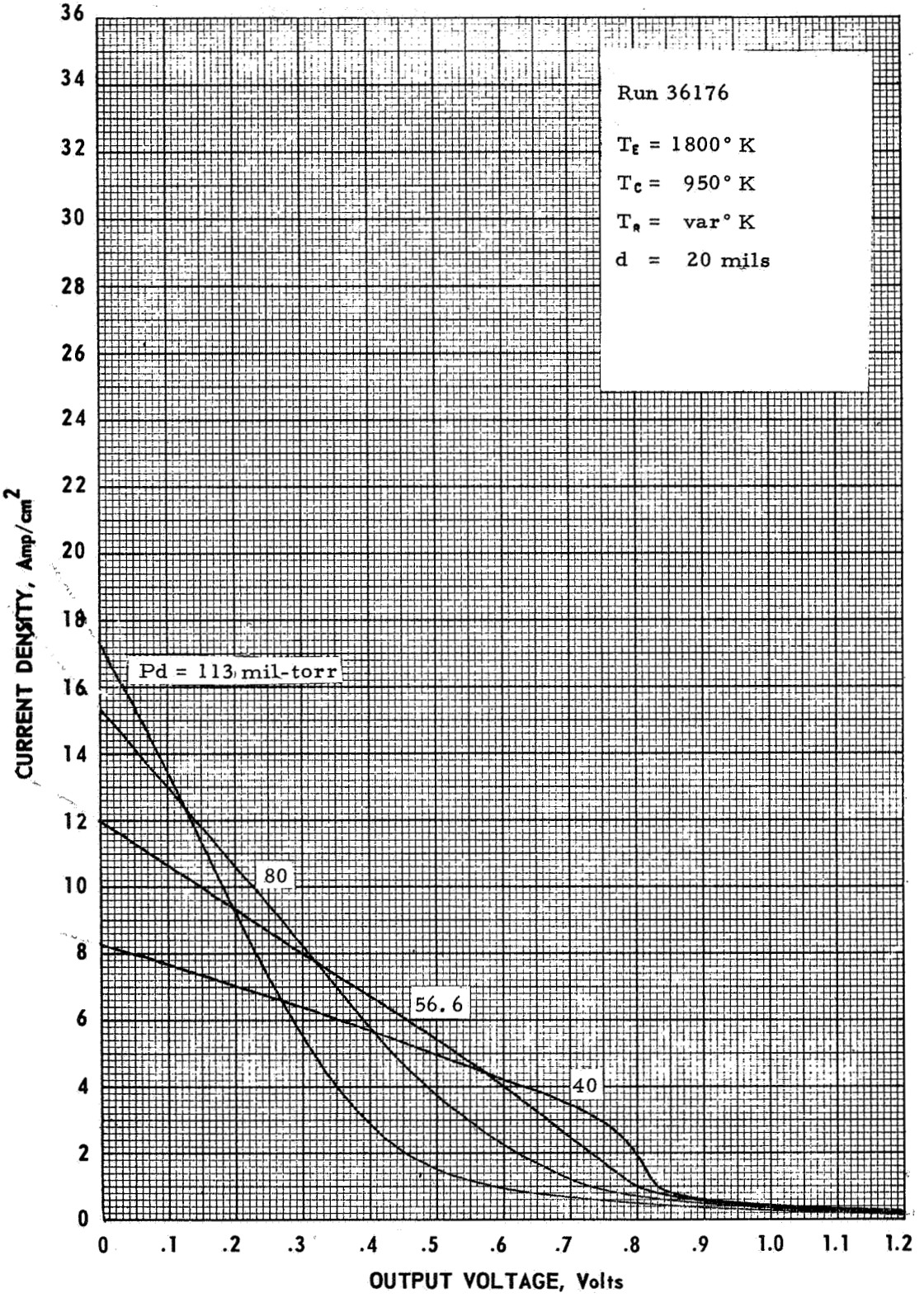

Figure IV-23. Variable Cesium Pressure Family at T_E = 1800° K and d = 20 mils.

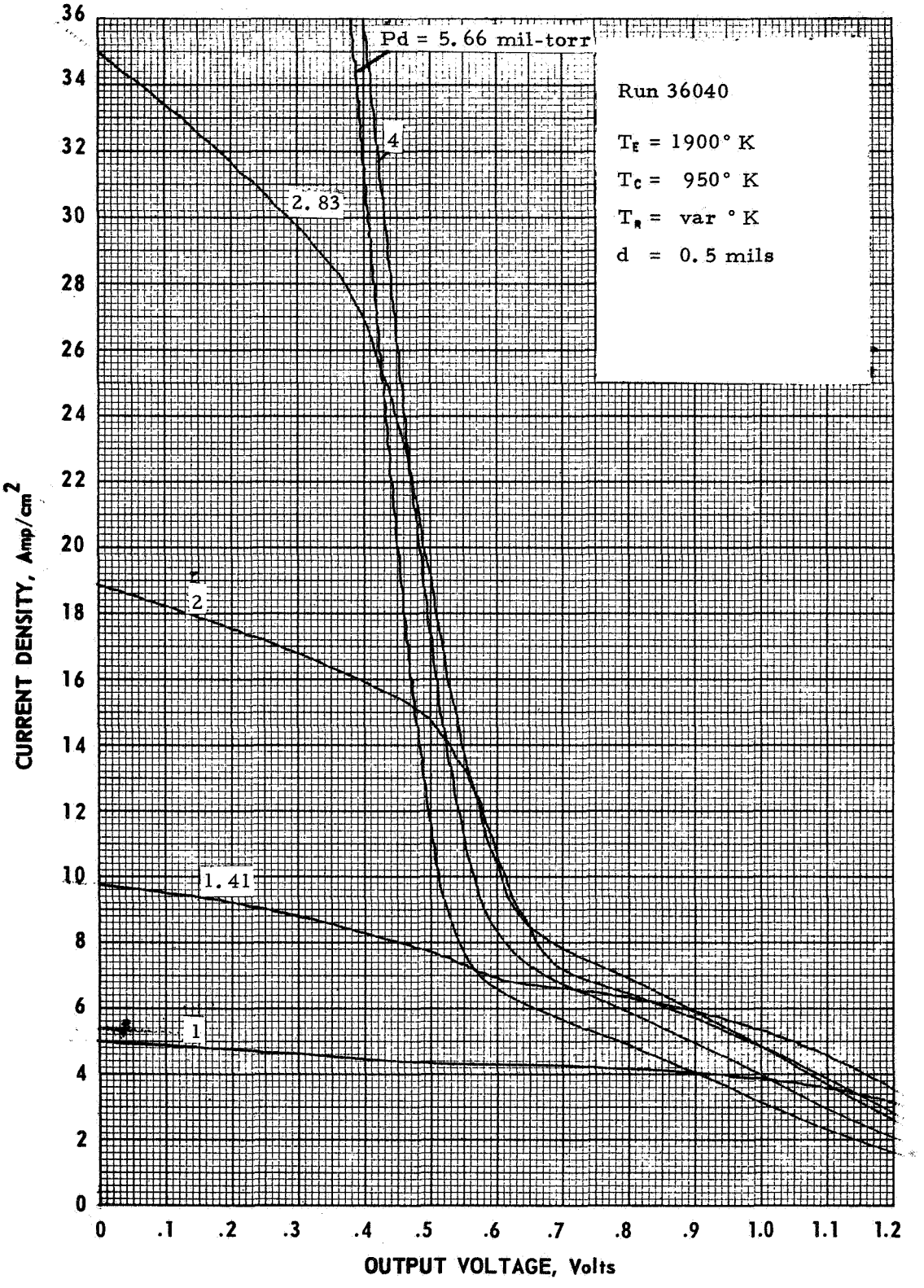

Figure IV-24. Variable Cesium Pressure Family at T_E = 1900° K and d = 0.5 mils.

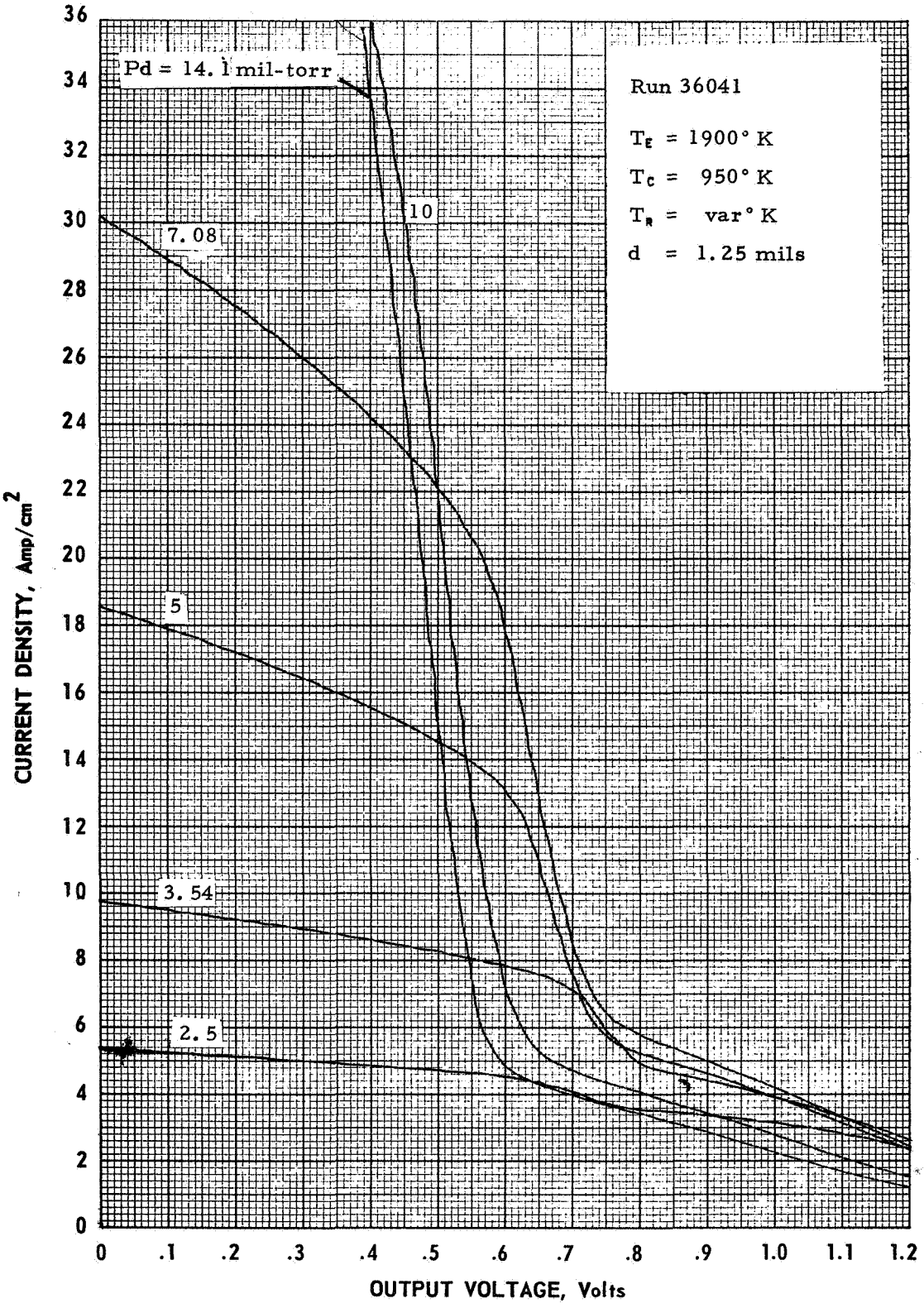

Figure IV-25. Variable Cesium Pressure Family at T_E = 1900° K and d = 1.25 mils.

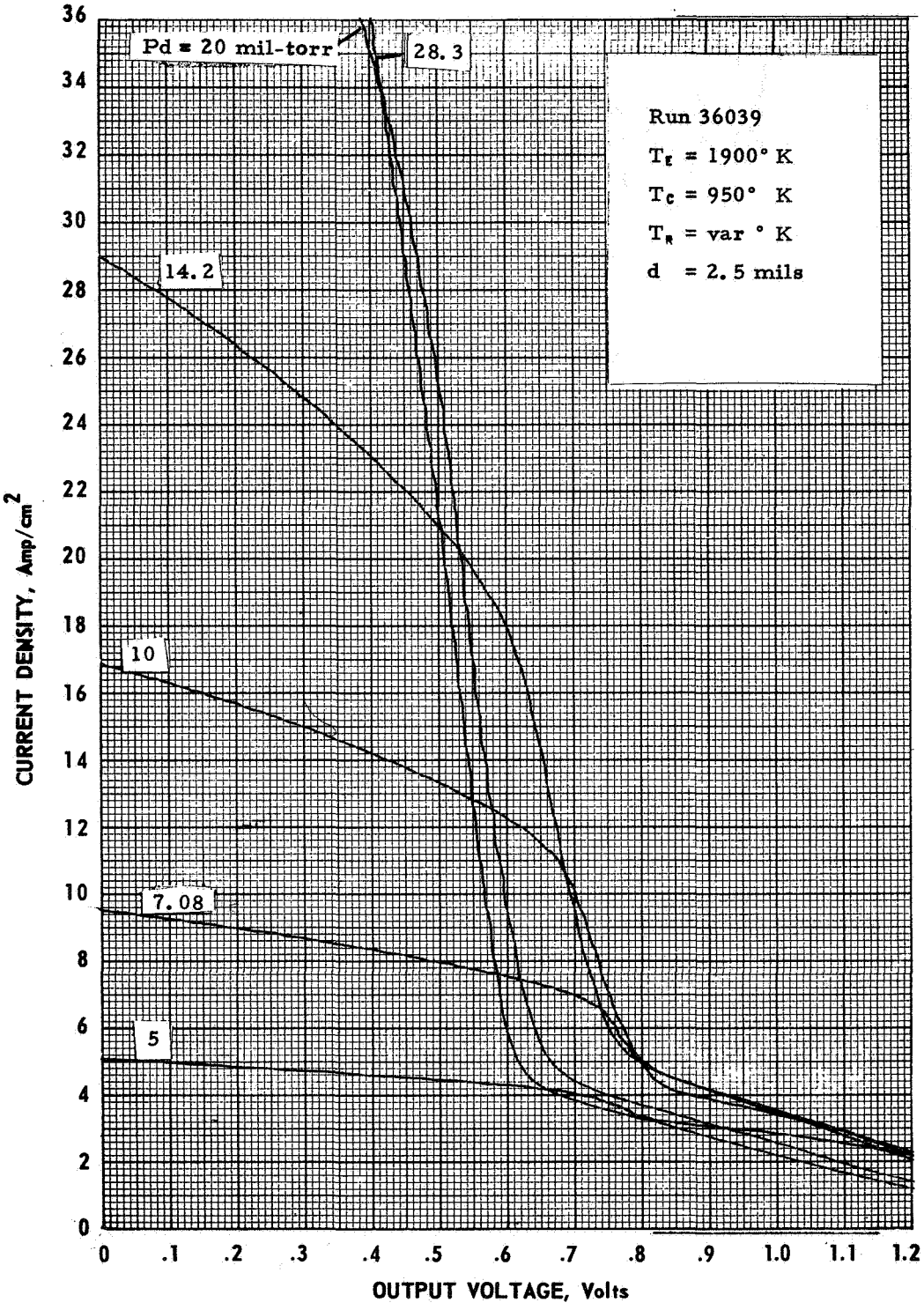

Figure IV-26. Variable Cesium Pressure **Family** at T_E = 1900° K and d = 2.5 mils.

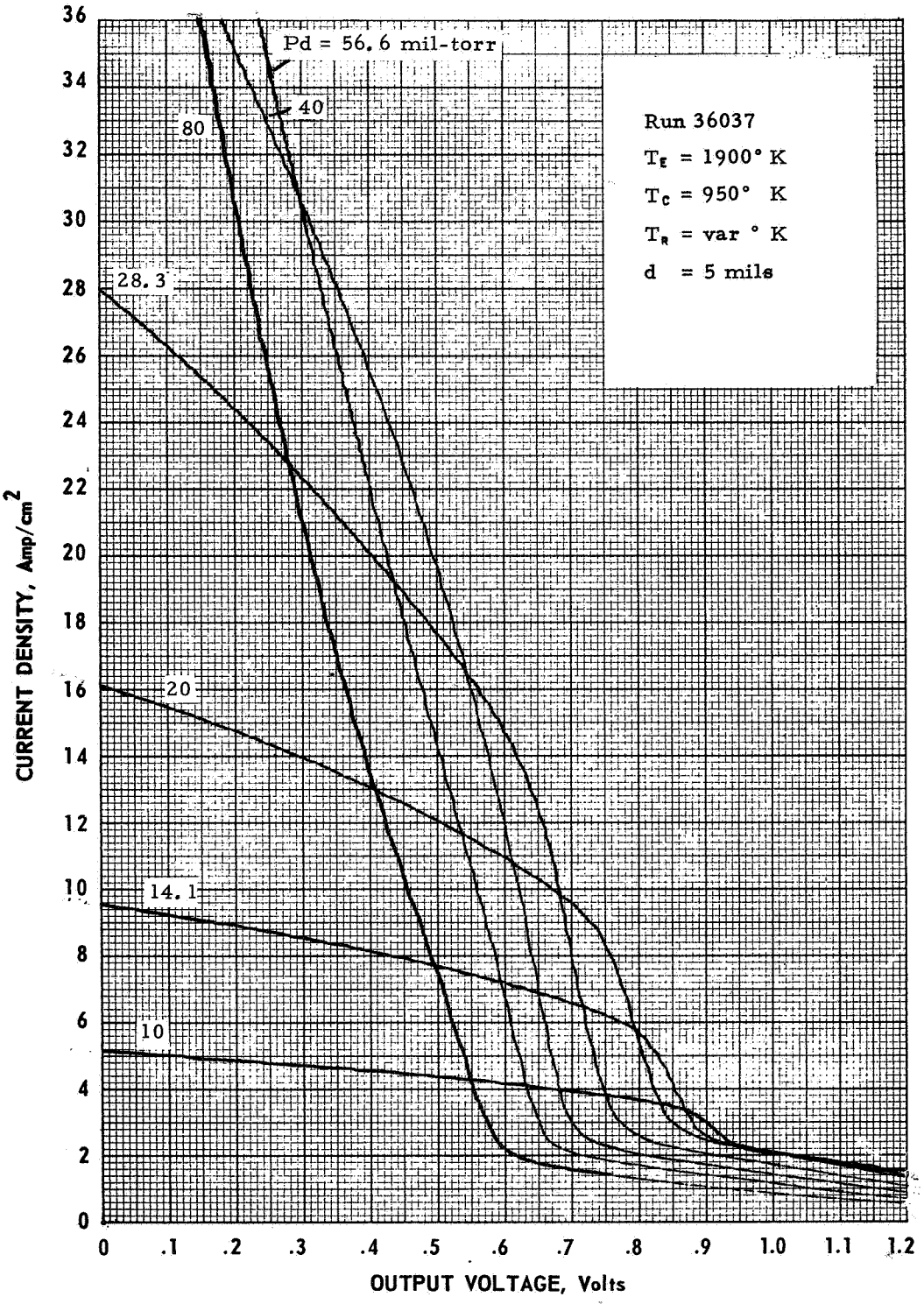

Figure IV-27 Variable Cesium Pressure Family at T_E = 1900° K and d = 5 mils.

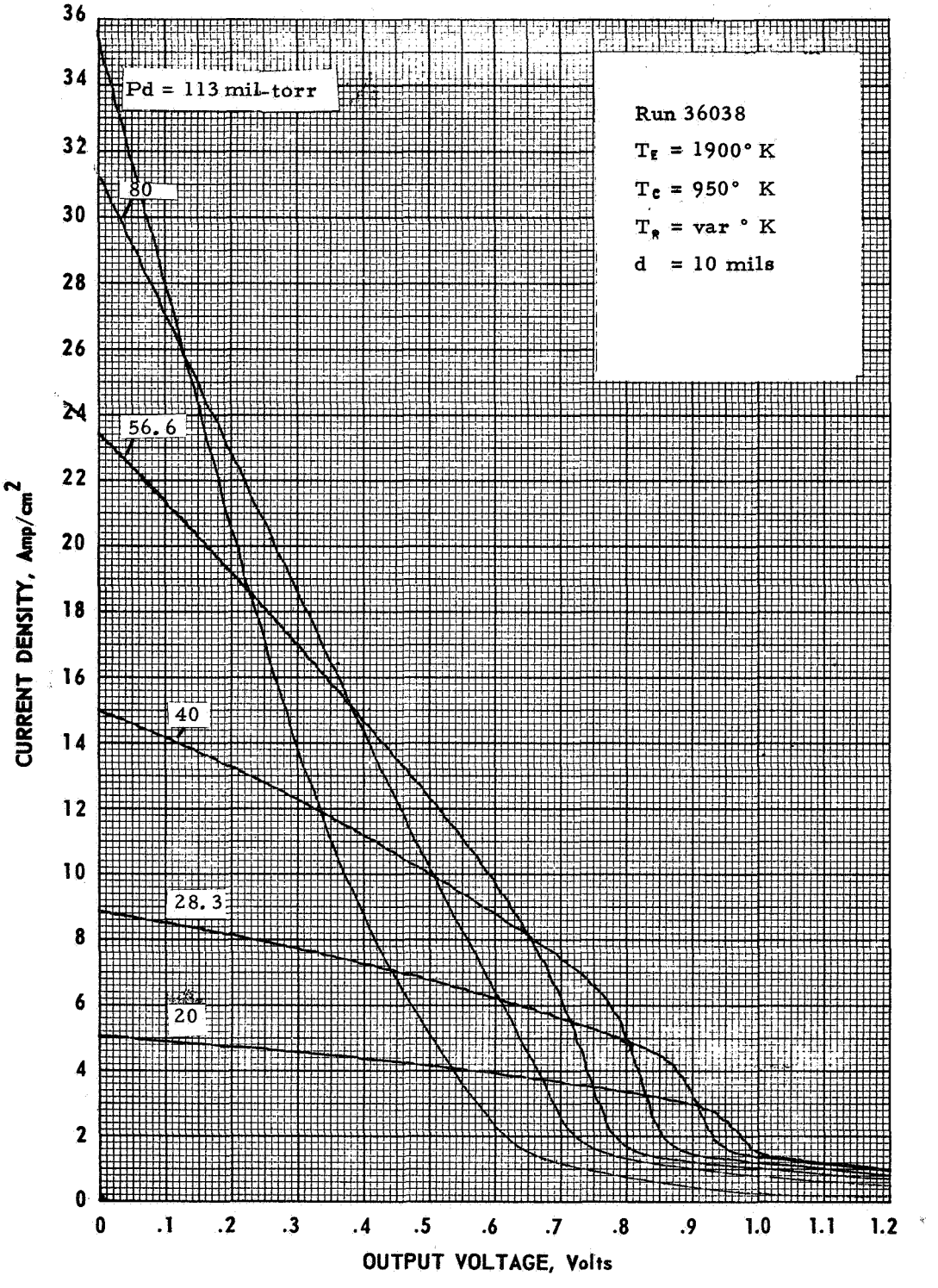

Figure IV-28. Variable Cesium Pressure Family at T_E = 1900° K and d = 10 mils.

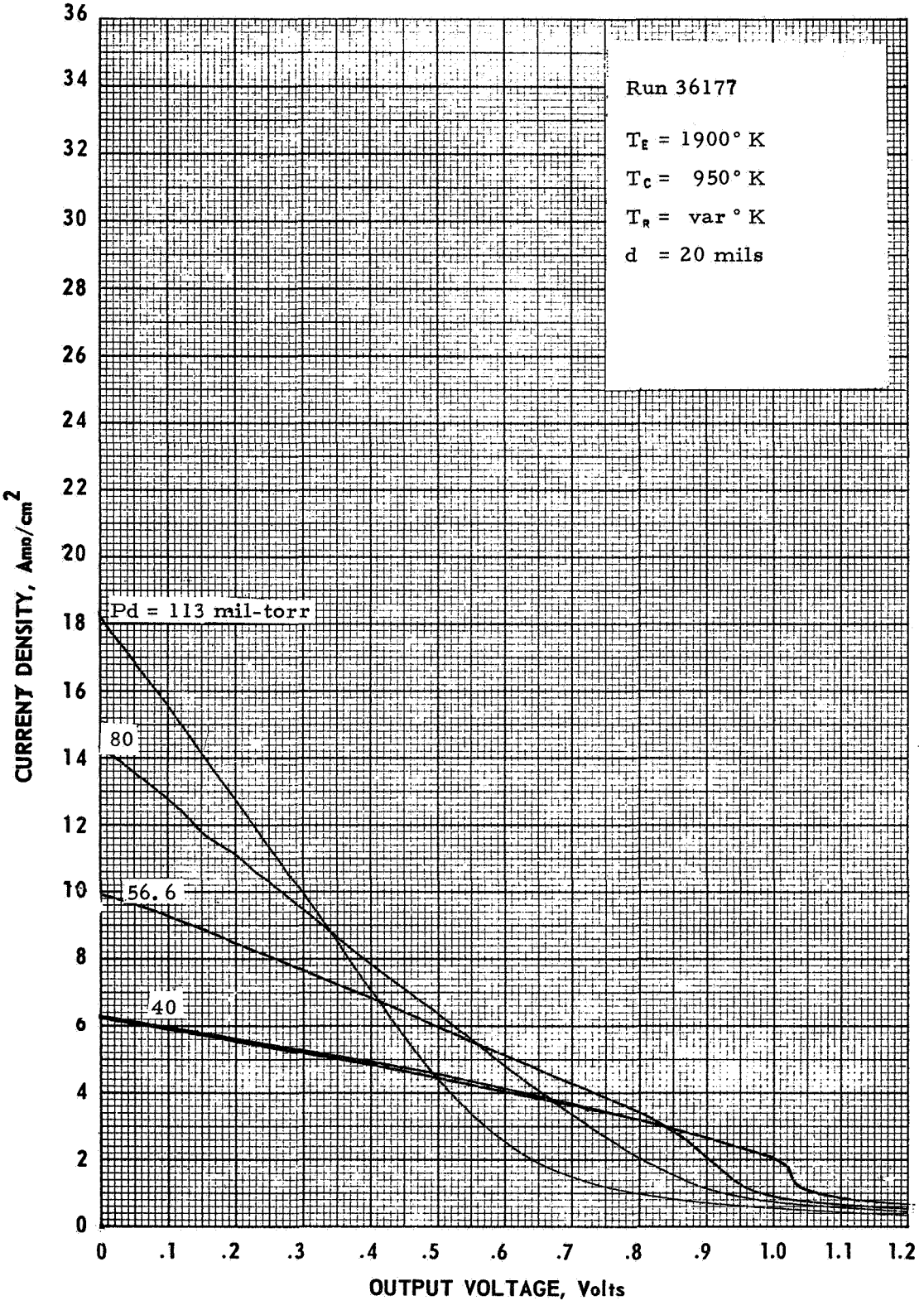

Figure IV-29. Variable Cesium Pressure Family at T_E = 1900° K and d = 20 mils.

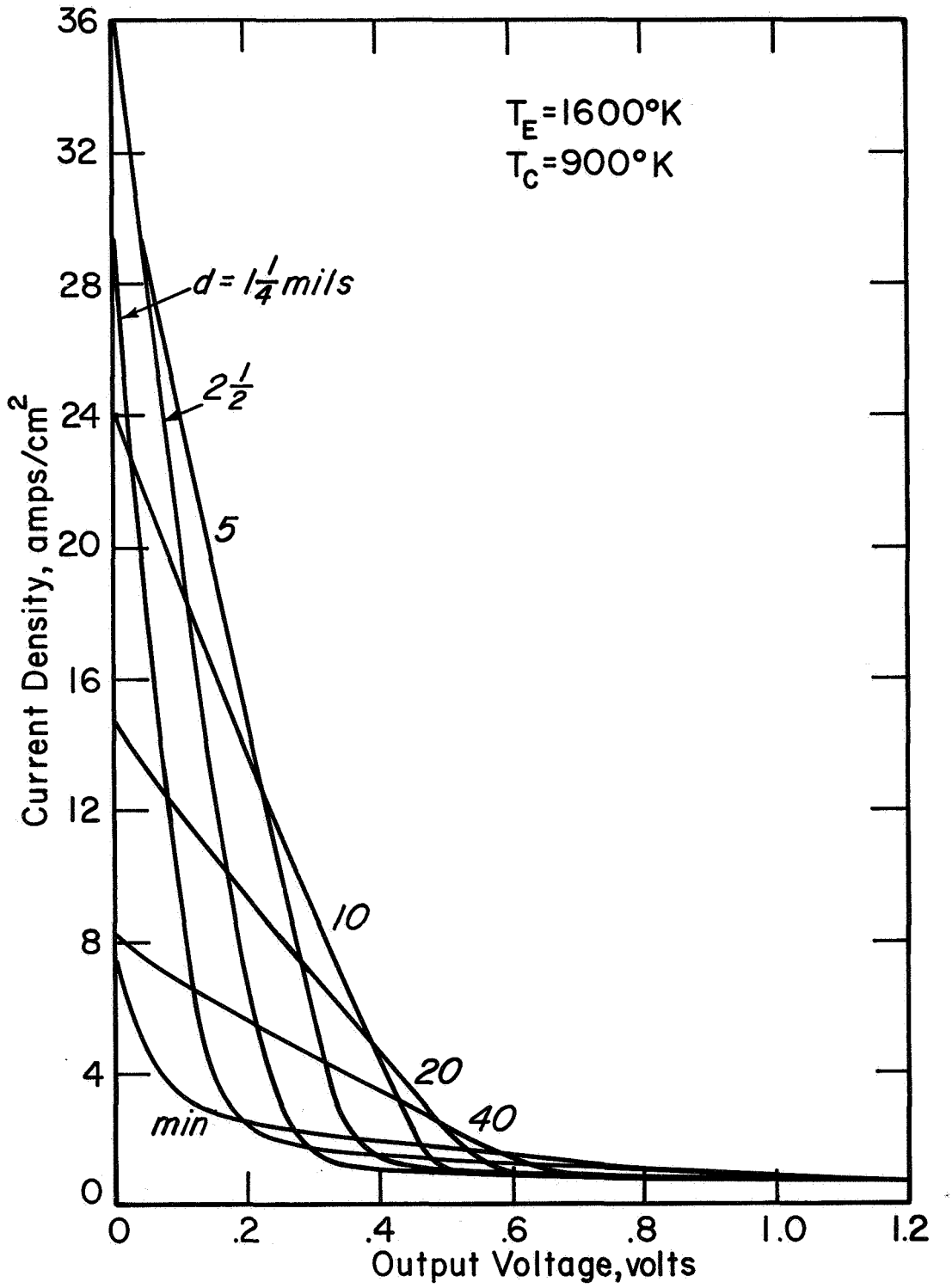

Figure IV-30. Cesium Optimized Performance for Several Interelectrode Spacings at T_E = 1600° K.

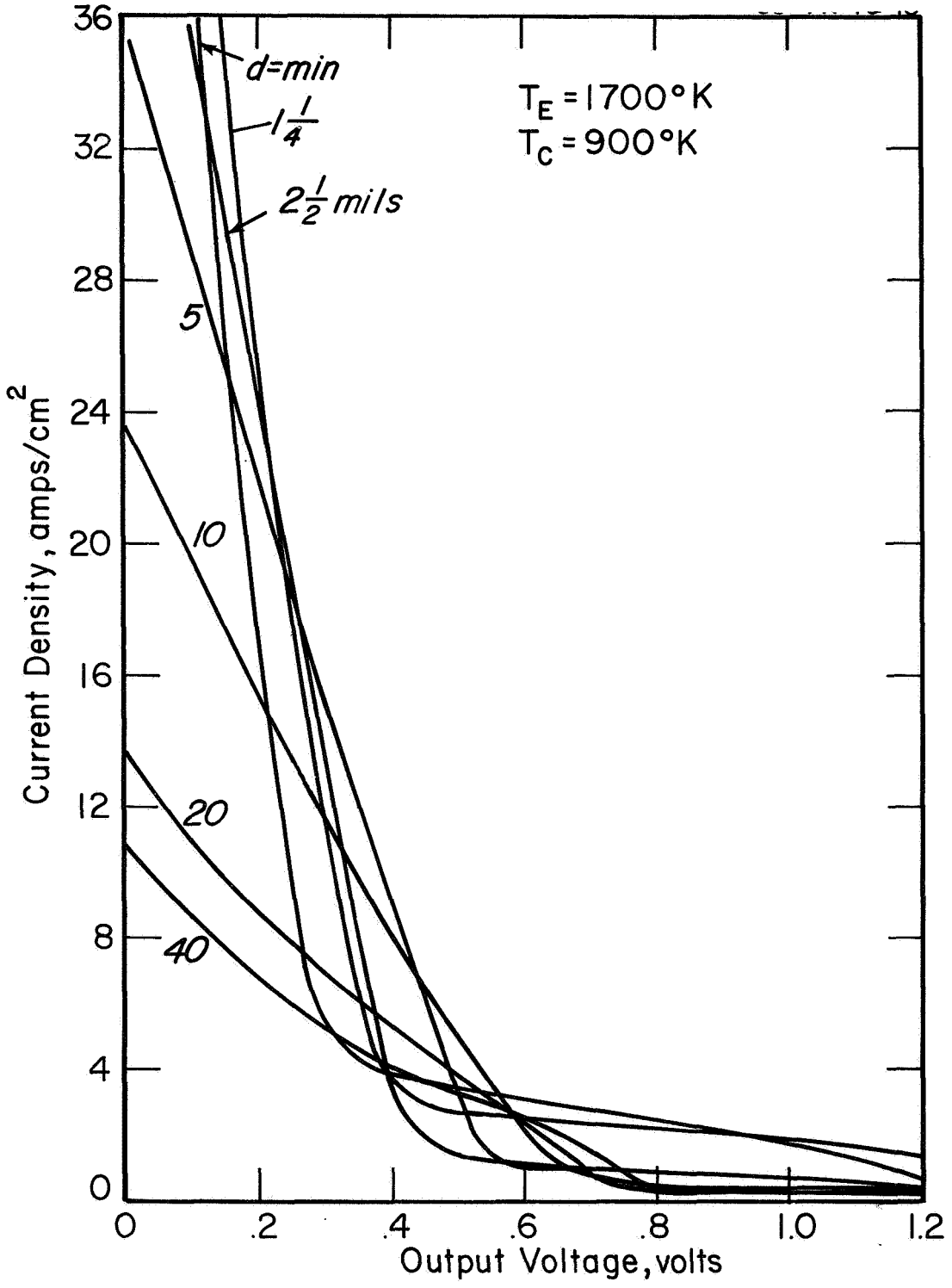

Figure IV-31. Cesium Optimized Performance for Several Interelectrode Spacings at T_E = 1700° K.

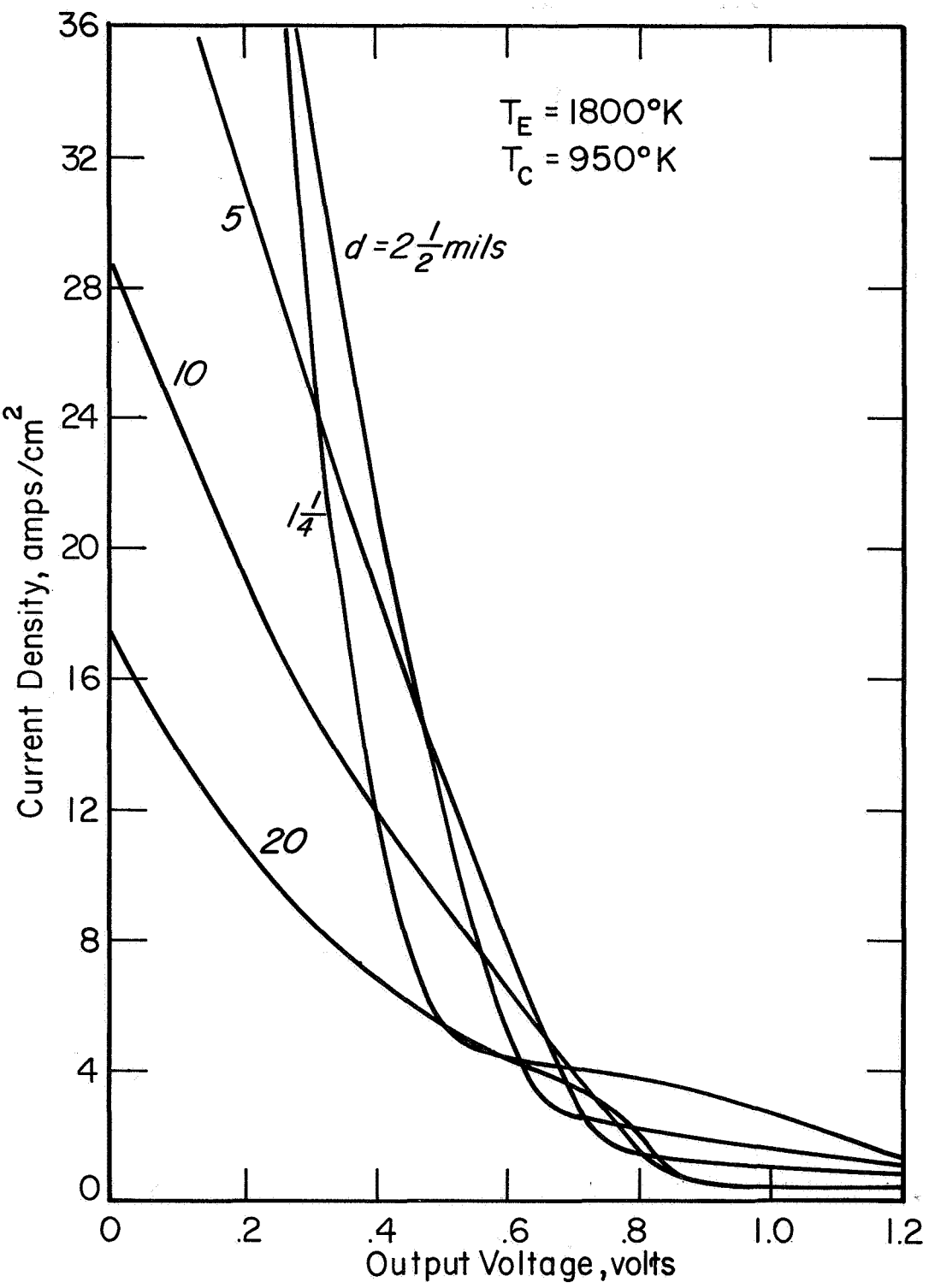

Figure IV-32. Cesium Optimized Performance for Several Interelectrode Spacings at T_E = 1800° K.

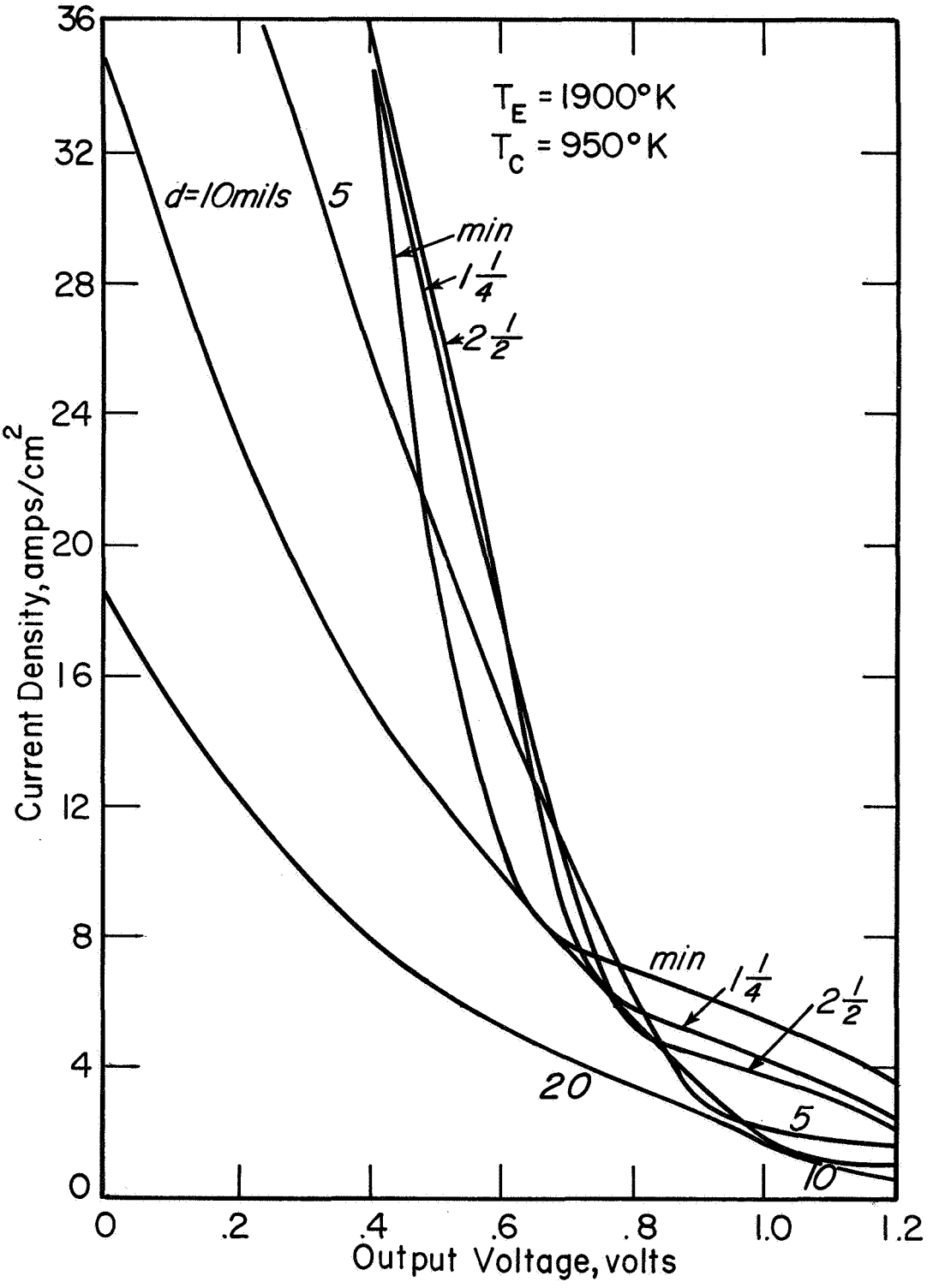

Figure IV-33. Cesium Optimized Performance for Several Interelectrode Spacings at T_E = 1900° K.

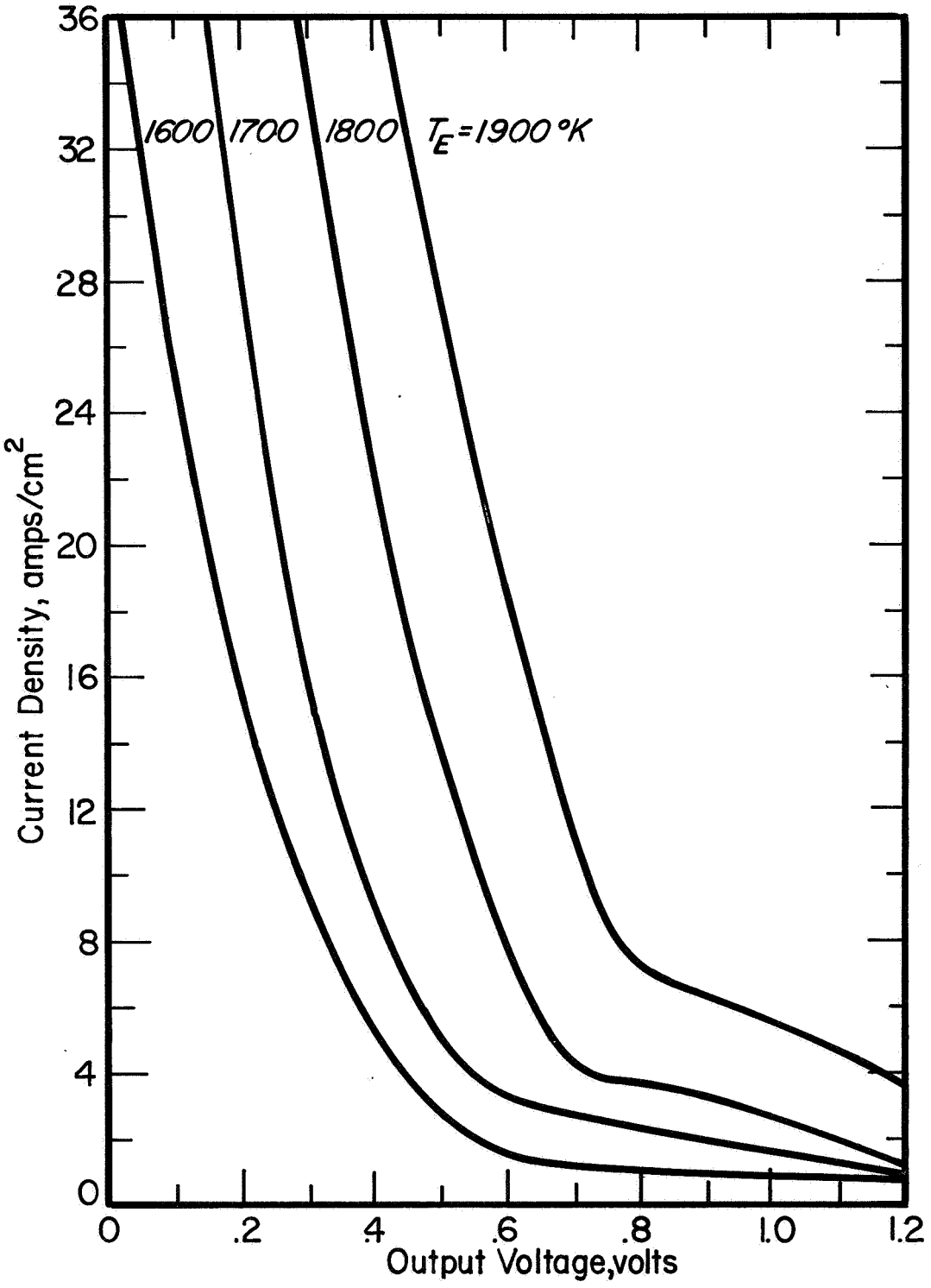

Figure IV-34. Fully Optimized Performance at Several Emitter Temperatures.

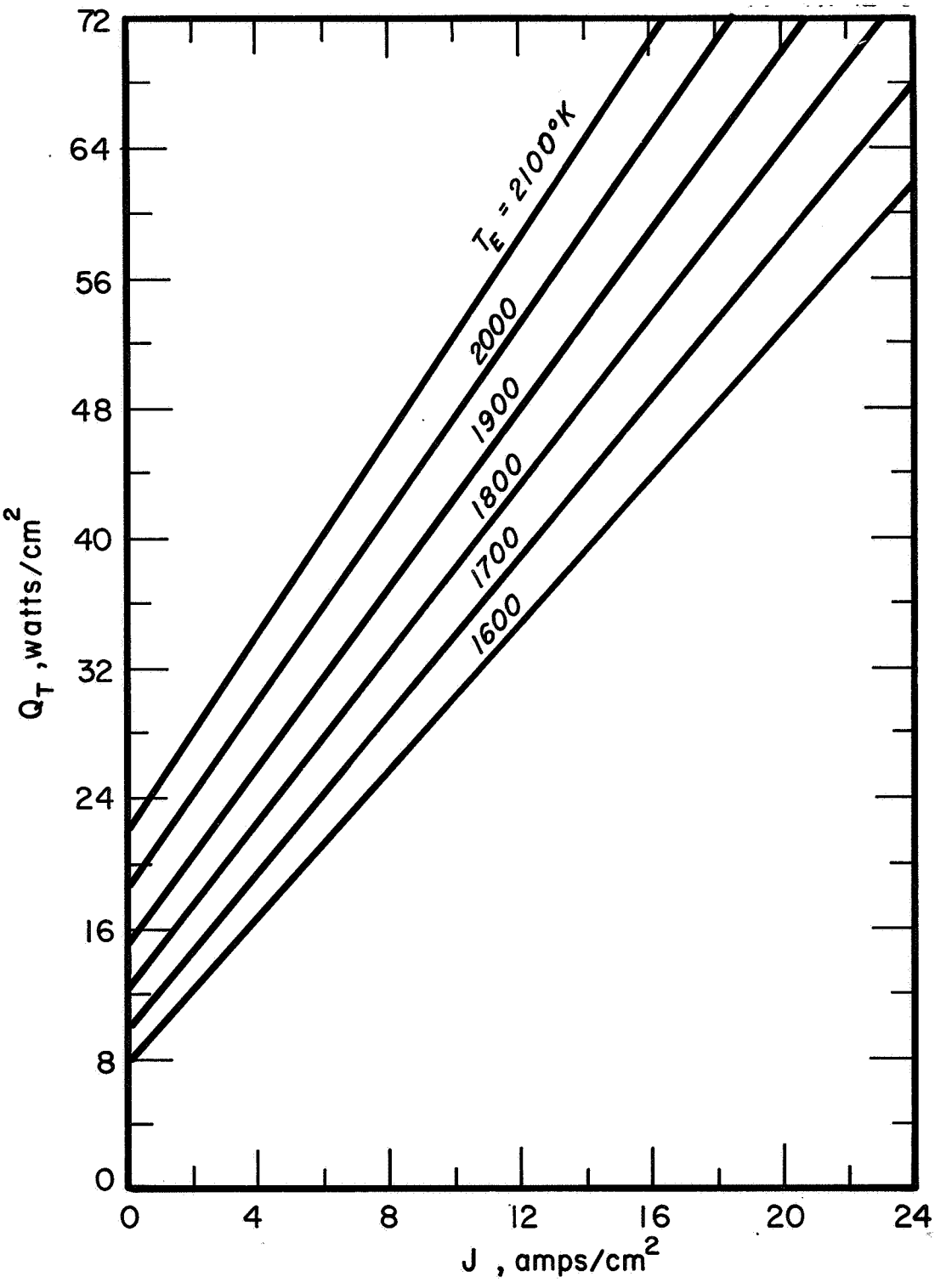

Figure IV-35. Calculated Heat Loss as a Function of Current Density at Various Emitter Temperatures with an Emissivity of 0.18 and Cesium Conduction of 1.5 watts/cm^2.

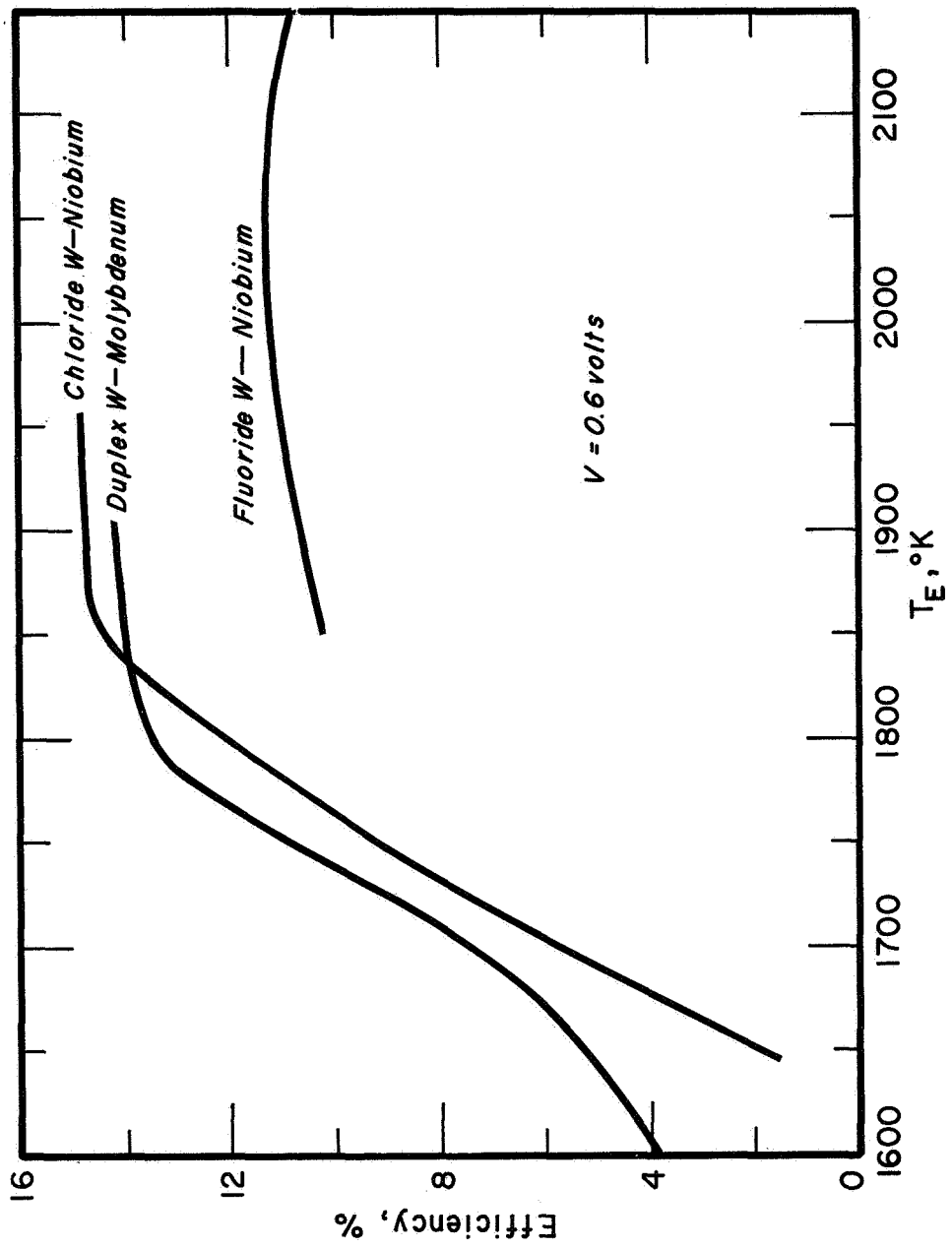

Figure IV-36. Efficiency at 0.6 Volt as a Function of Emitter Temperature for Vapor-Deposited Tungsten Emitters.

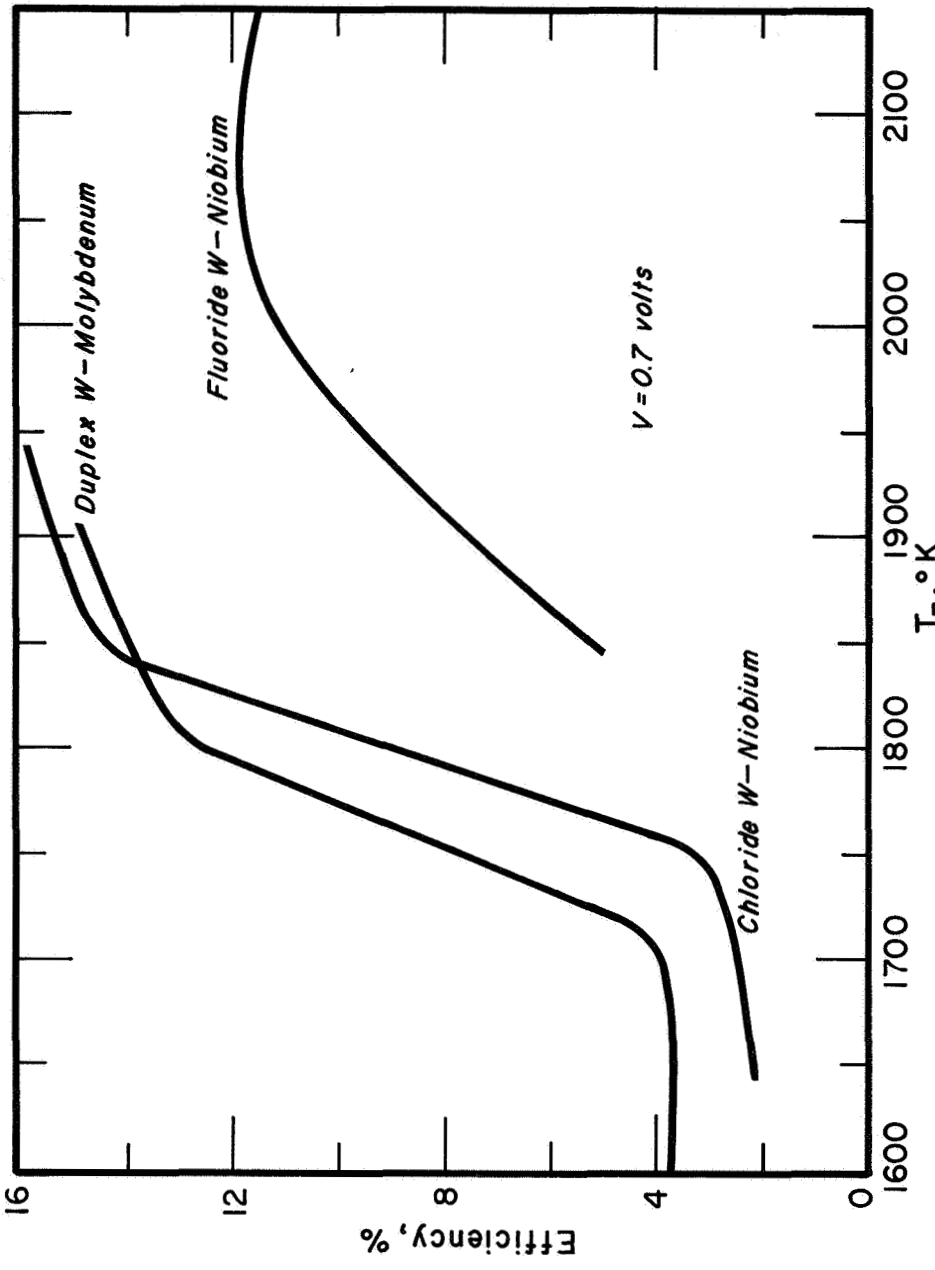

Figure IV-37. Efficiency at 0.7 Volt as a Function of Emitter Temperature for Vapor-Deposited Tungsten Emitters.

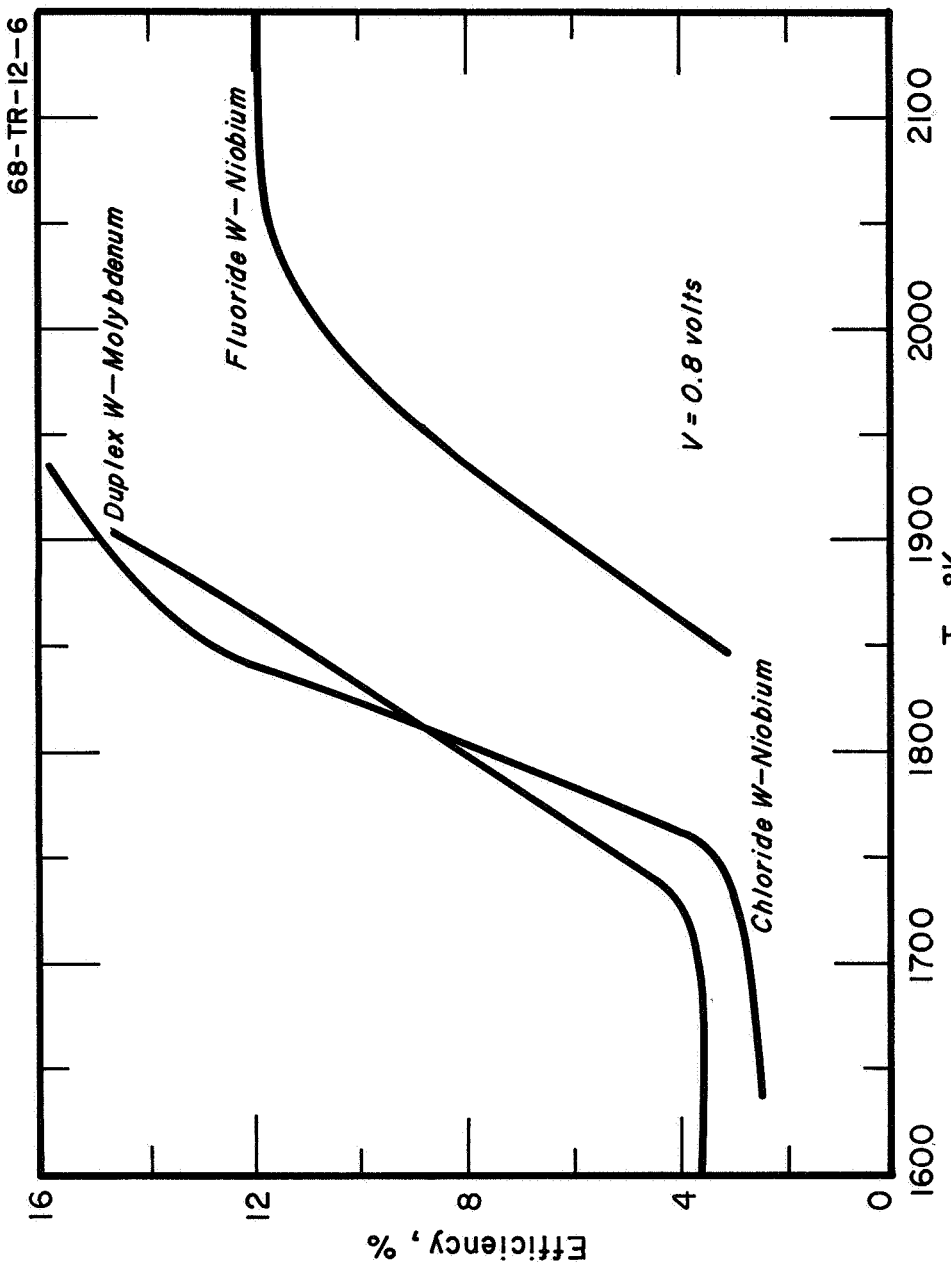

Figure IV-38. Efficiency at 0.8 Volt as a Function of Emitter Temperature for Vapor-Deposited Tungsten Emitters.

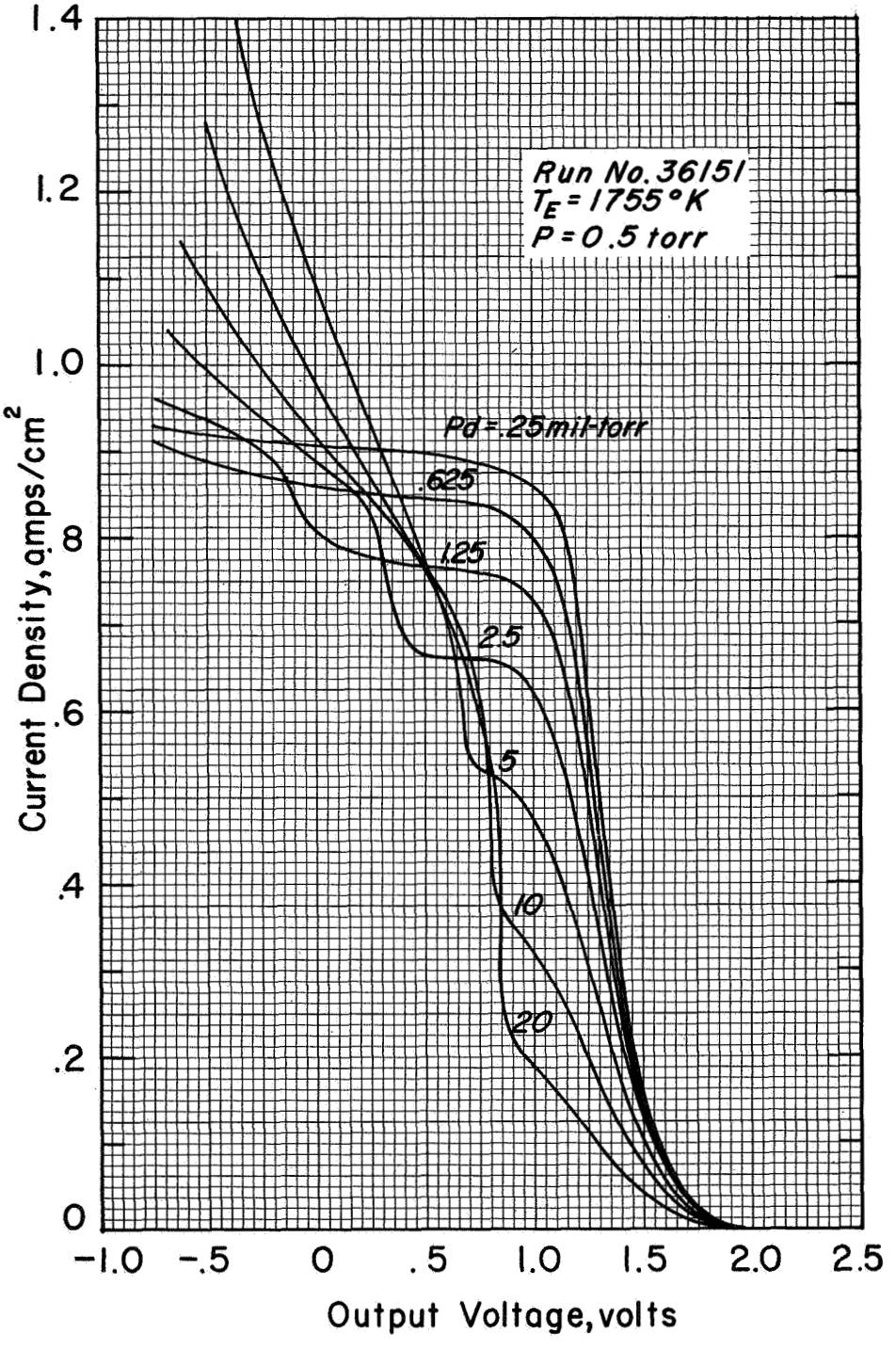

Figure IV-39. Variable Spacing Family at β = 10 and P = 0.5 torr.

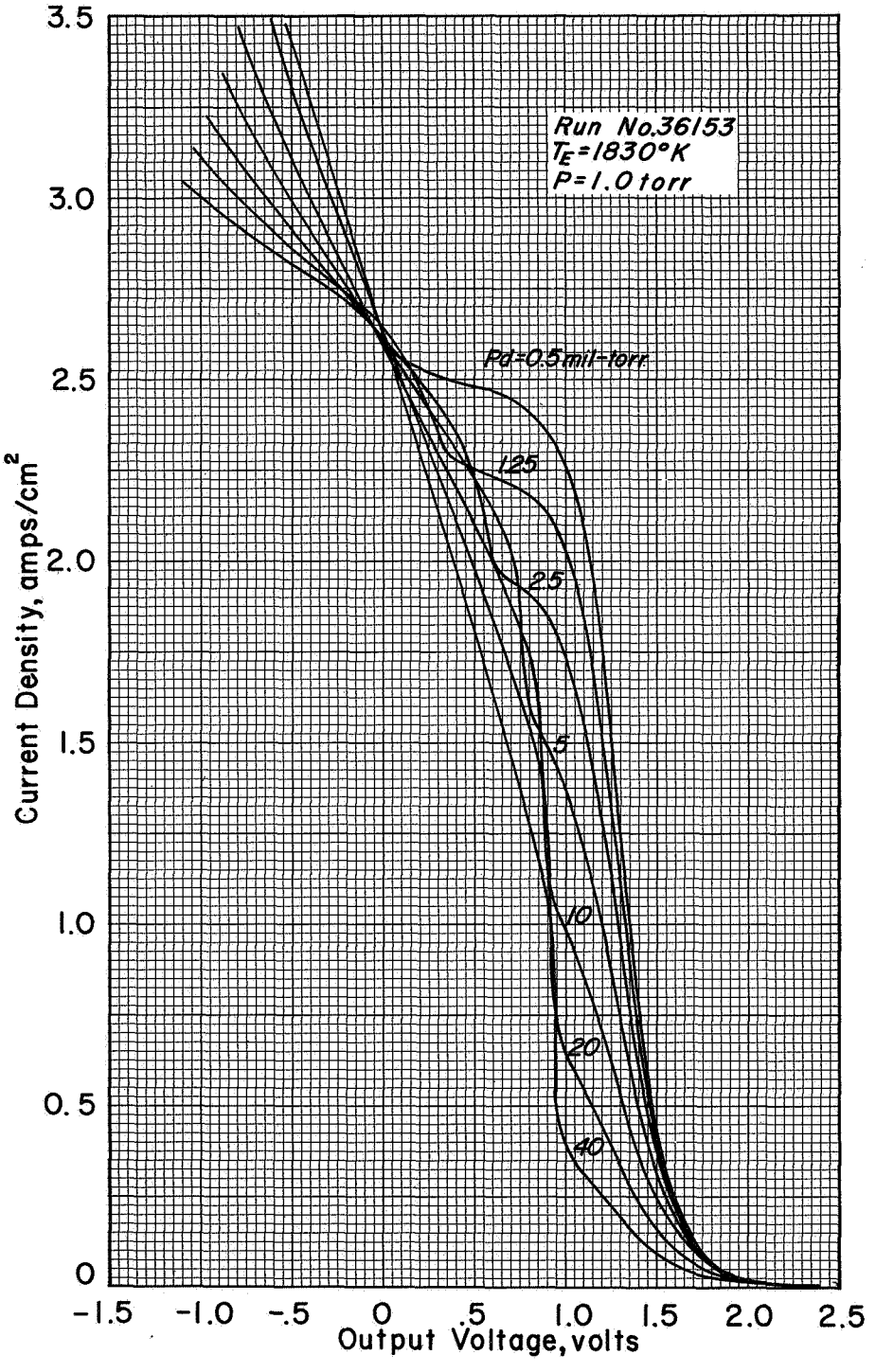

Figure IV-40. Variable Spacing Family at β = 10 and P = 1 torr.

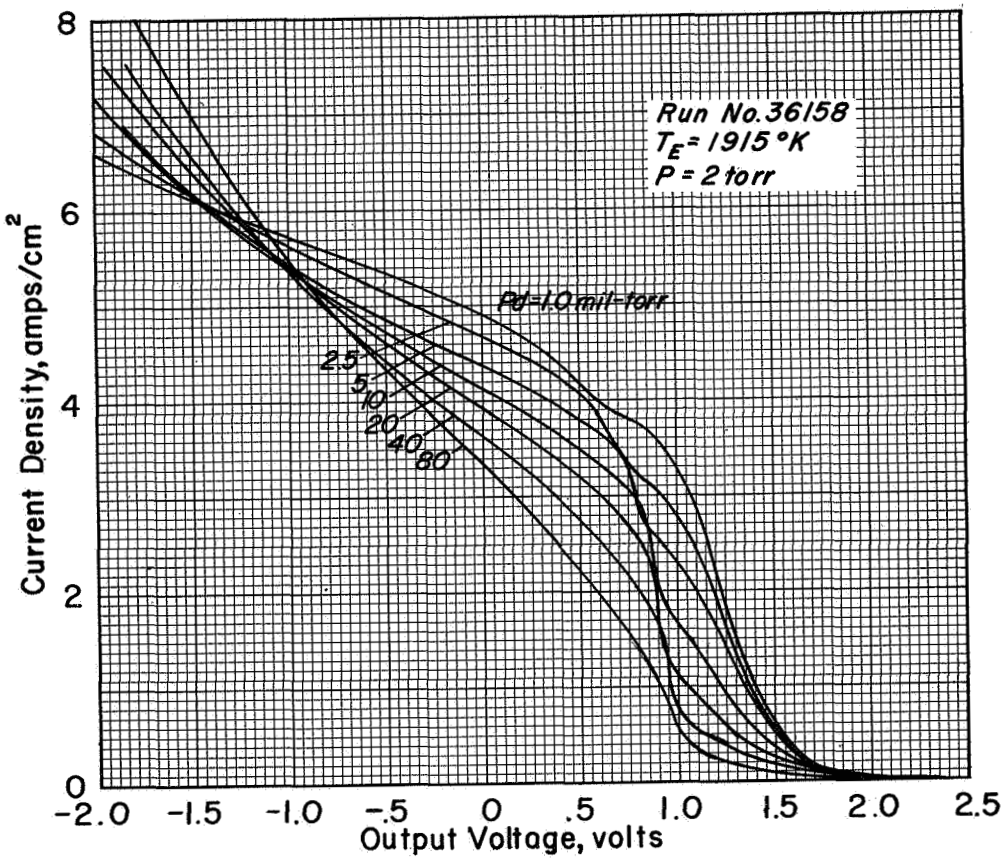

Figure IV-41. Variable Spacing Family at β = 10 and P = 2 torr.

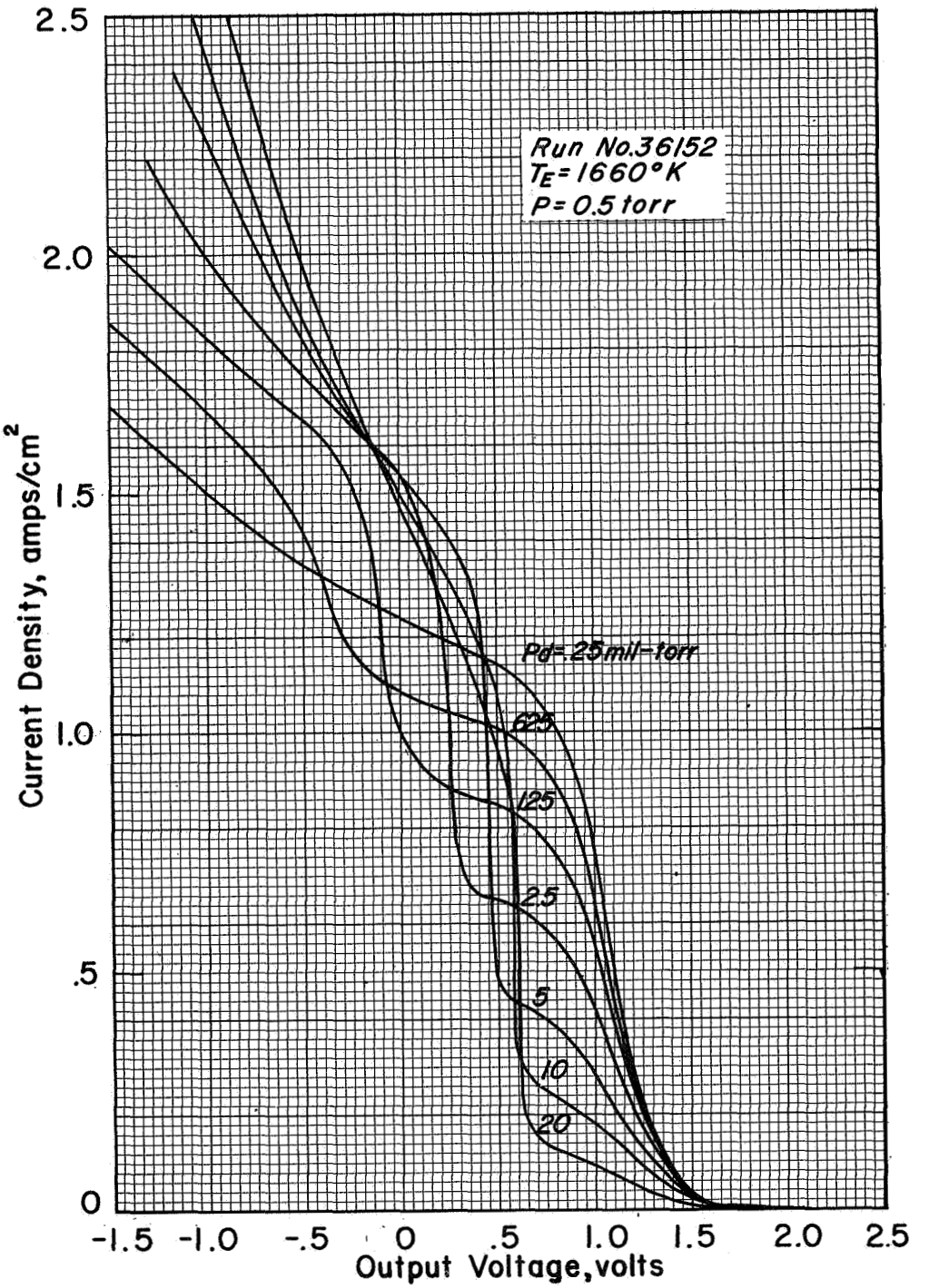

Figure IV-42. Variable Spacing Family at β = 1 and P = 0.5 torr.

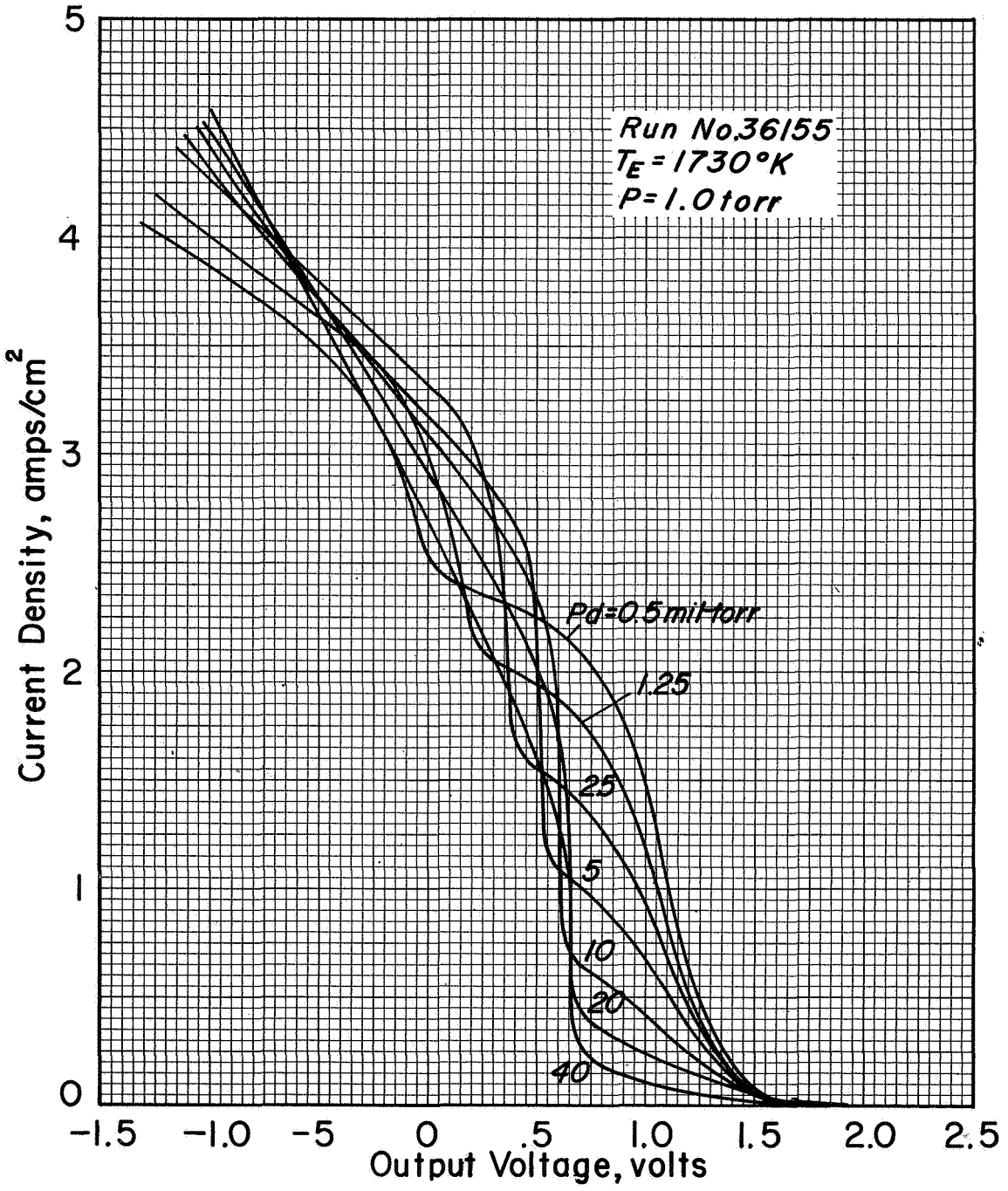

Figure IV-43, Variable Spacing Family at β = 1 and P = 1 torr.

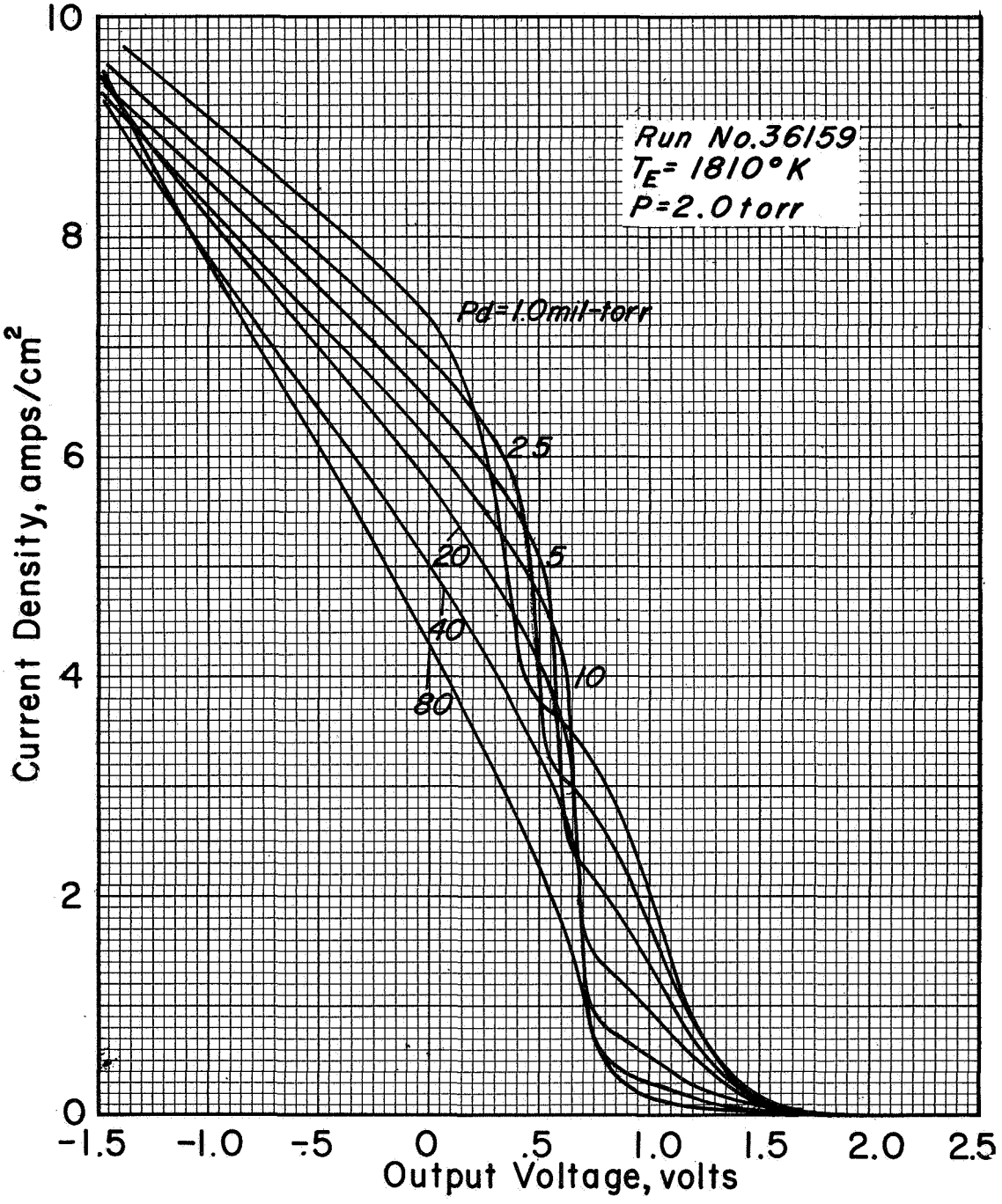

Figure IV-44. Variable Spacing Family at β = 1 and P = 2 torr.

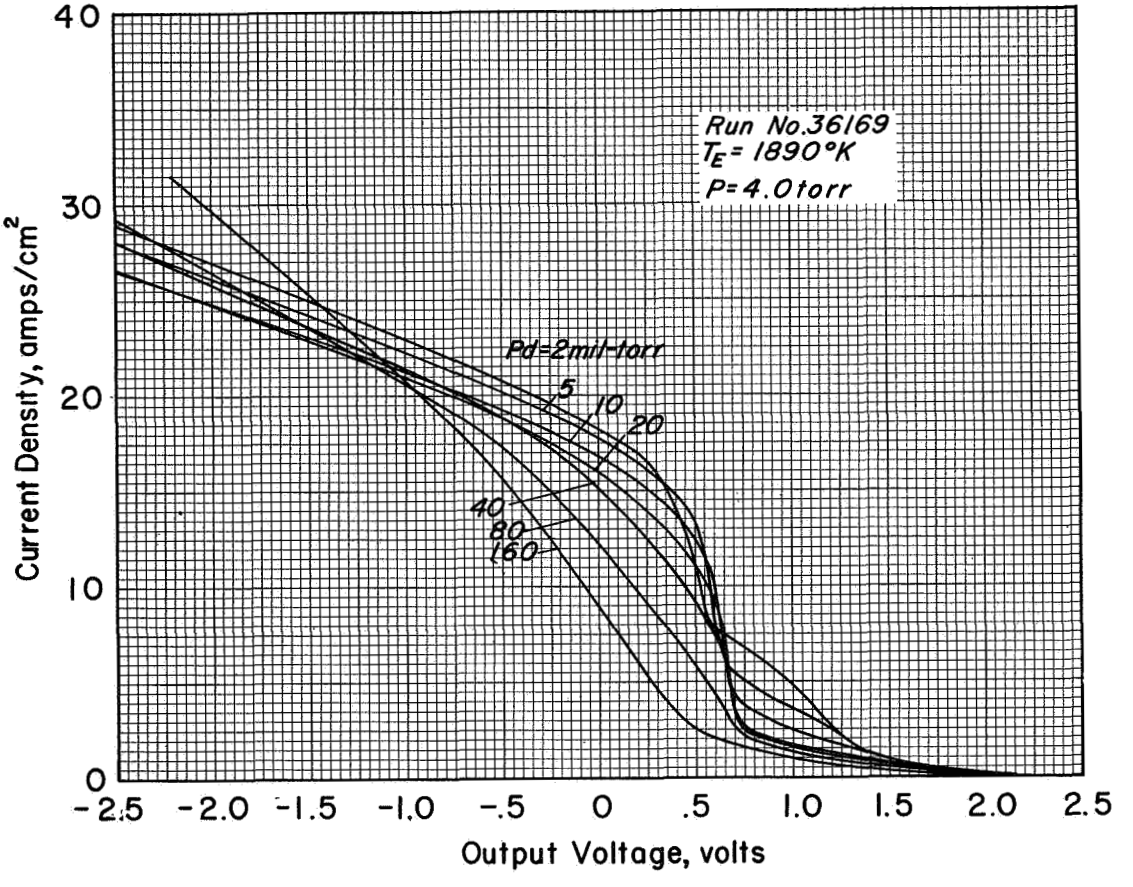

Figure IV-45. Variable Spacing Family at β = 1 and P = 4 torr.

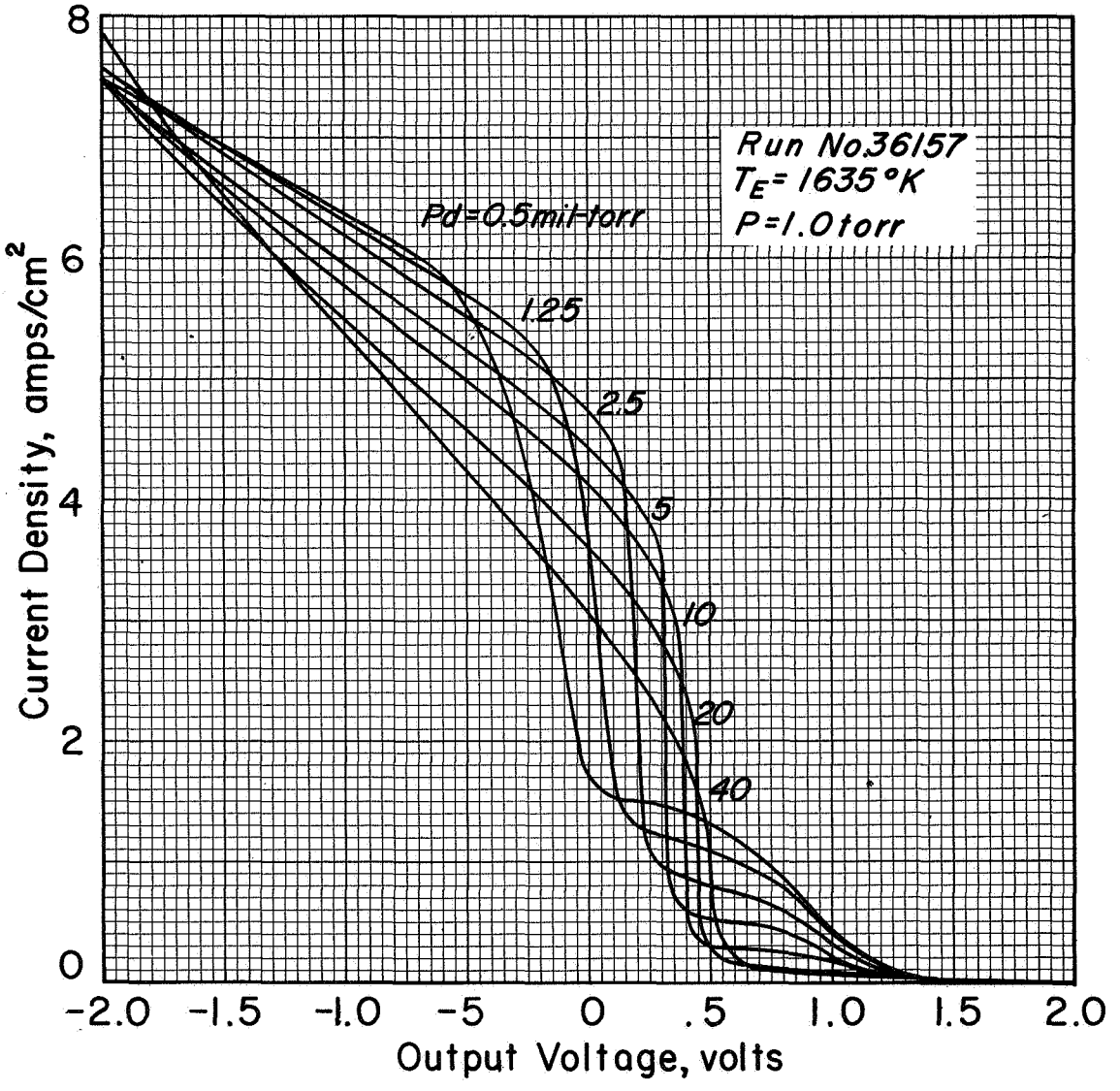

Figure IV-46. Variable Spacing Family at β = 0.1 and P = 1 torr.

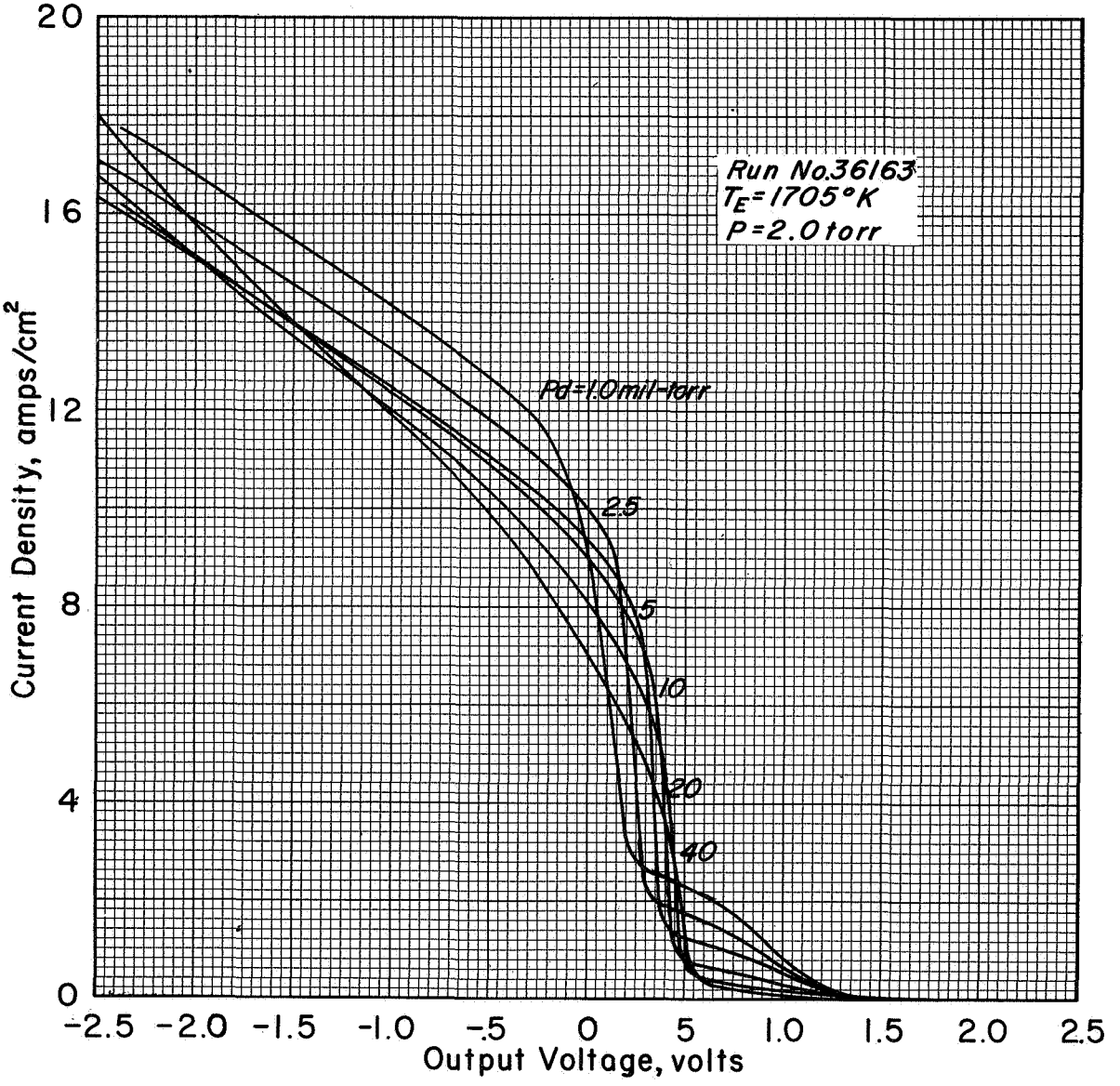

Figure IV-47. Variable Spacing Family at β = 0.1 and P = 2 torr.

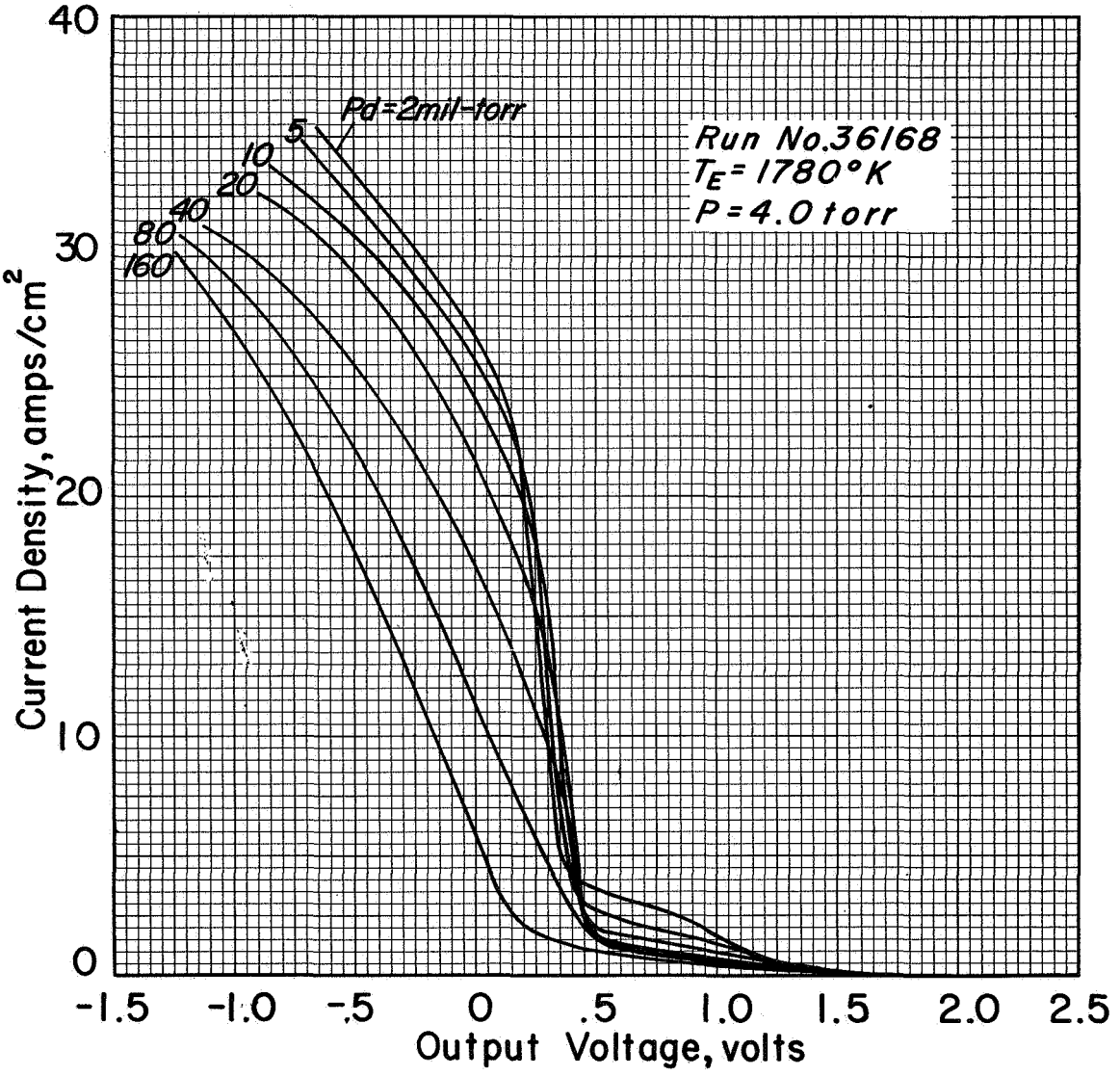

Figure IV-48. Variable Spacing Family at β = 0.1 and P = 4 torr.

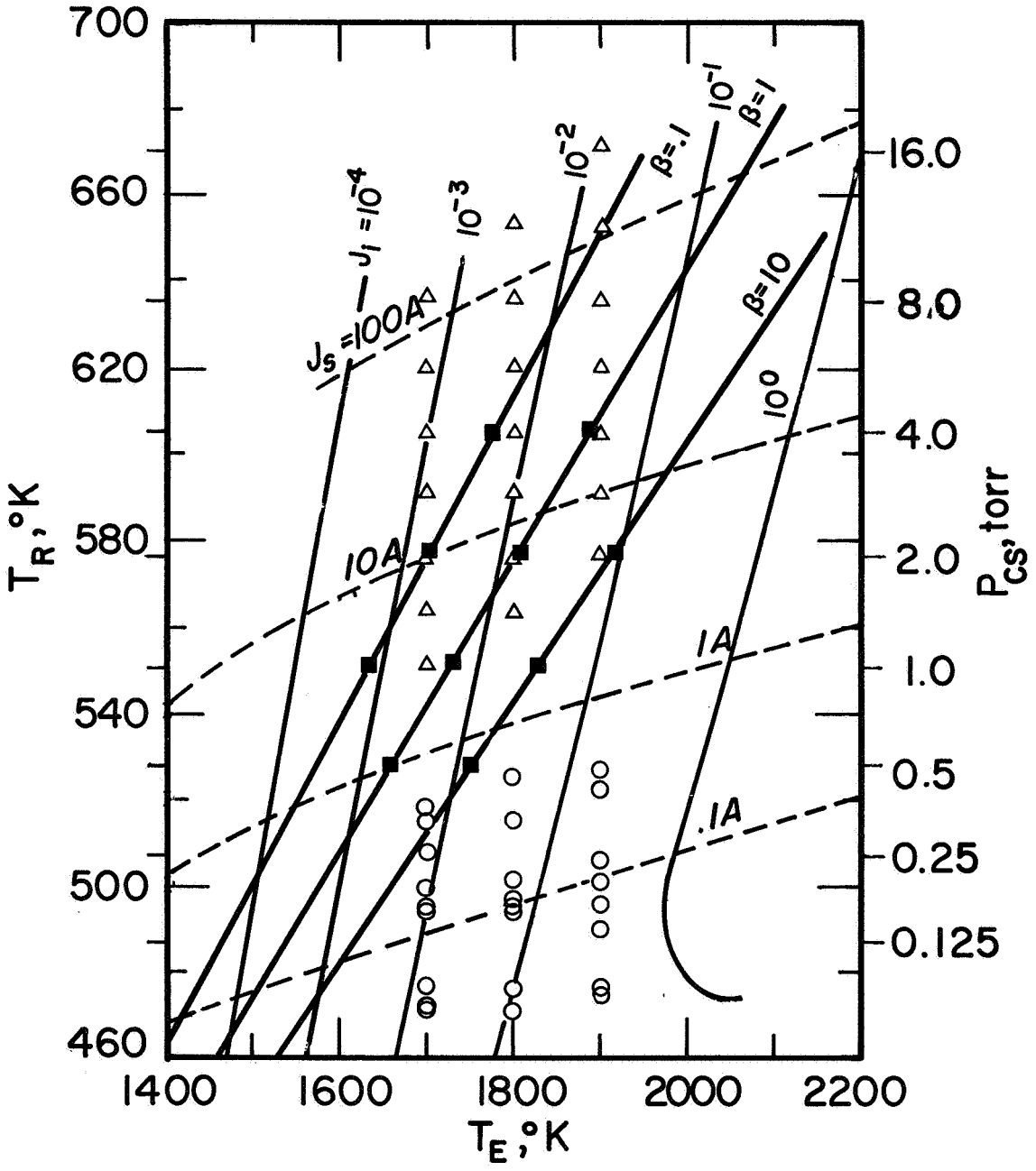

Figure IV-49. Emission Map of the Emitter Showing Location of the Data Points.

○ Work Function Data
△ Cesium Families
■ Spacing Family

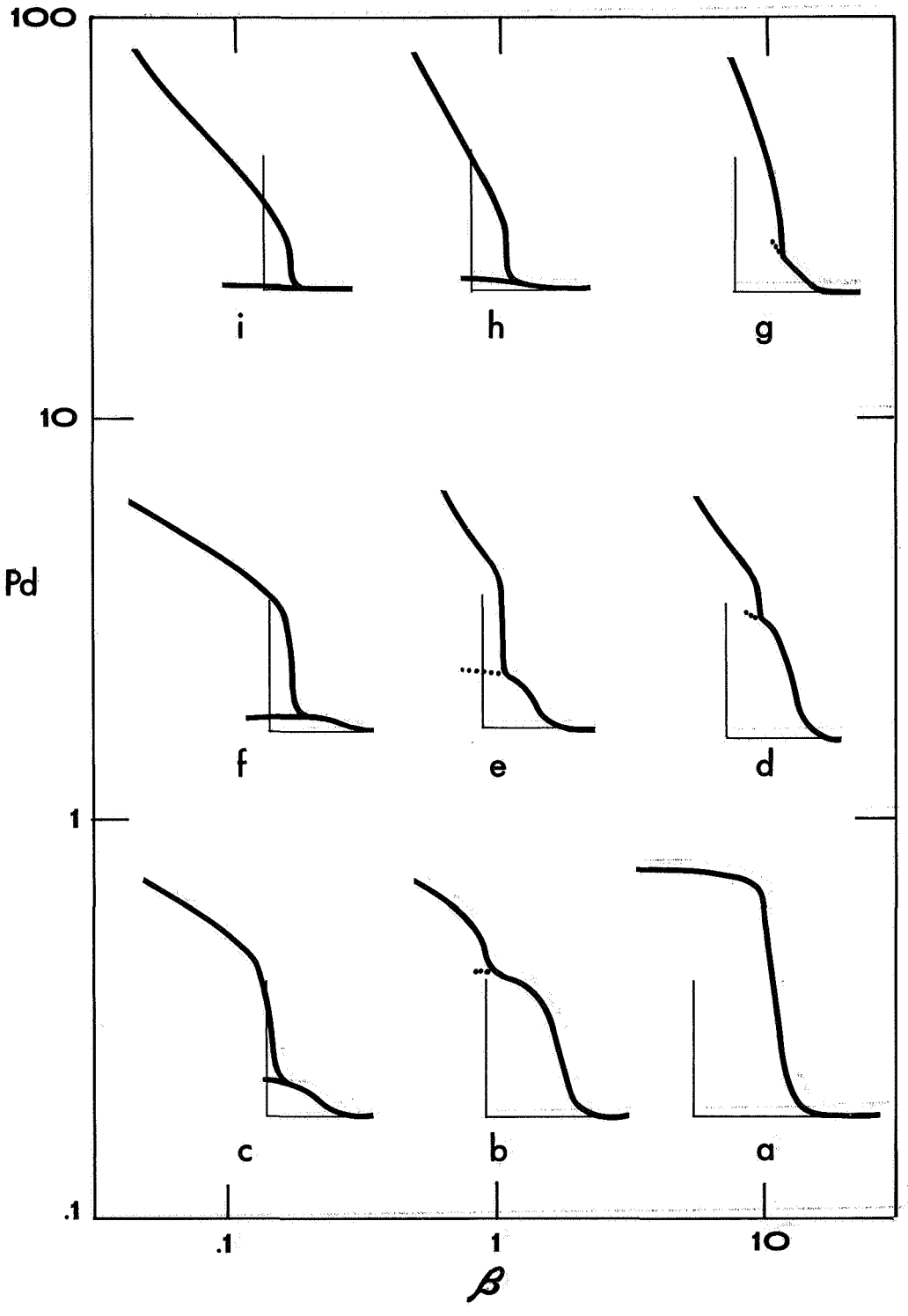

Figure IV-50. Plot Showing the General Shape of the Volt-Ampere Characteristics as a Function of Pd and β.

B. EMISSION CHARACTERISTICS OF A SINGLE CRYSTAL TUNGSTEN EMITTER

The performance of a single crystal tungsten emitter with a molybdenum collector was recorded in the variable spacing converter shown in Figure IV-1. The data cover an emitter temperature range of 1700°K to 1900°K, and an interelectrode spacing range of 0.5 mil to 40 mils.

1. Emitter Preparation

The emitter (W25) was prepared from an ingot of nominal single-crystal tungsten made by the Linde Division of Union Carbide Corporation. X-ray studies using the Laue back-reflection technique indicated that the material contained considerable substructure which was stable to annealing, but that all areas had an orientation that was grossly (110) along the ingot axis, and that exact (110) directions always lay within 4° of the ingot axis.

After polishing and heat treatment, the emitter showed several distinct grains, which glinted in slightly different directions. The microscopic examination revealed that the surface was composed of flat areas of (110) plane bounded by curves and connected by an undulating background, while occasional well-defined plateaus or mesas stood out against this background. The surface of the whole emitter (to within 0.4 inch of the edge) was qualitatively similar; a representative photomicrograph is shown in Figure IV-51.

2. Work Function Measurements

The cesiated work function of the emitter was determined from the measured values of the saturation current under ion rich conditions. The calculated values are compared with the work function of polycrystalline tungsten in Figure IV-52. For a given T_E/T_R, the cesiated

work function of single-crystalline 110 tungsten is about 0.2 volt less than that of polycrystalline tungsten.

3. Performance Data

The performance of this converter was recorded in terms of cesium temperature families for various values of emitter temperature and interelectrode spacing. To simplify cross-plotting and to increase the usefulness of the data for analysis, the cesium pressures and the interelectrode spacings were chosen to provide the Pd products of . . . , 5, 10, 20, 40, ... mil-torr.

Figures IV-53 to IV-56 show these families at the emitter temperature of 1700°K, with an interelectrode spacing range of 5 to 40 mils. The collector temperature in these runs was held constant in the vicinity of its optimum value. The emitter temperature indicated represents the temperature at the surface of the emitter; the output voltage is measured from a voltage tap at the cold end of the emitter sleeve. The correction factor for conversion to electrode voltage is approximately 1.5 mV per A/cm^2. A summary of the cesium optimized envelopes at an emitter temperature of 1700°K is shown in Figure IV-57.

Cesium-temperature families obtained at an emitter temperature of 1800°K are shown in Figures IV-58 through IV-64, and a summary of these envelopes is shown in Figure IV-65. Similar data recorded at the emitter temperature of 1900°K are shown in Figures IV-66 through IV-71. The fully optimized envelopes of this converter are compared with those of an etched Re:Mo converter[6] in Figure IV-72. The output voltage of the W(110)-Mo converter is higher than that of the etched

Re-Mo converter by about 60 to 120 millivolts. A comparison at an interelectrode spacing of 10 mils is shown in Figure IV-73. The increase in output power (by about a factor of two) is probably due to the better uniformity in the emitter surface.

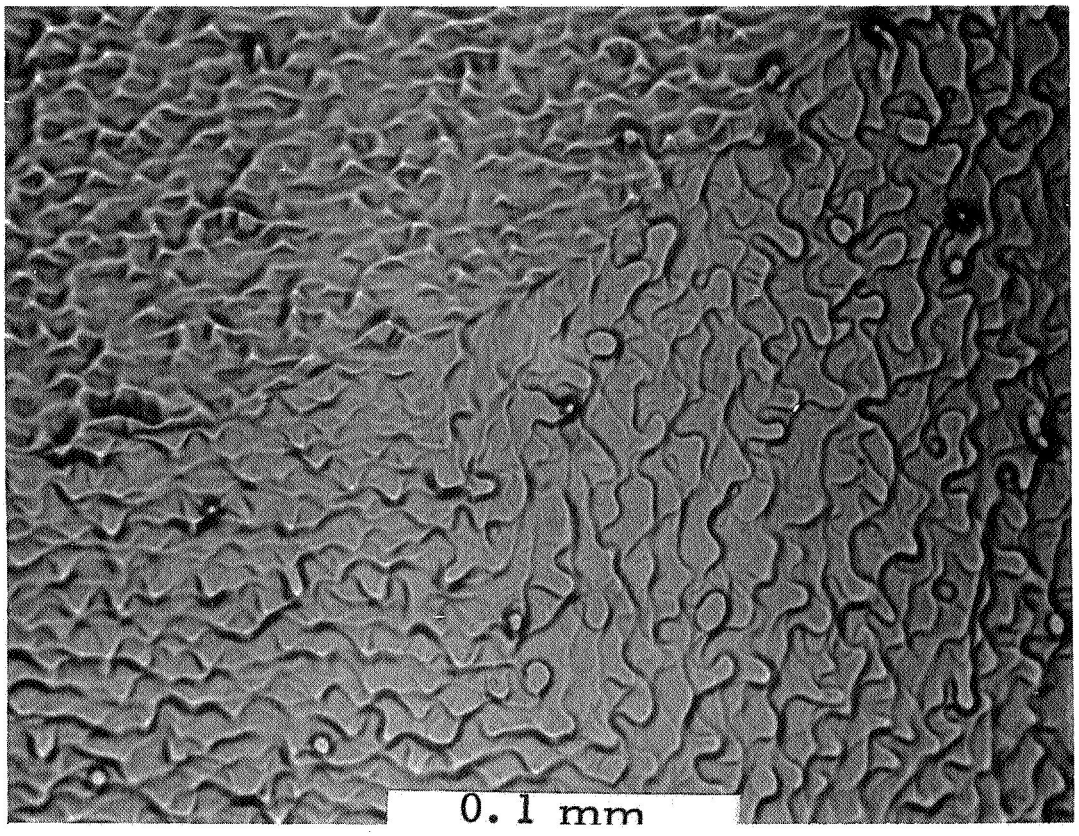

Figure IV-51. Photomicrograph of Representative Area of Emitter W25 Before Operation in Converter.

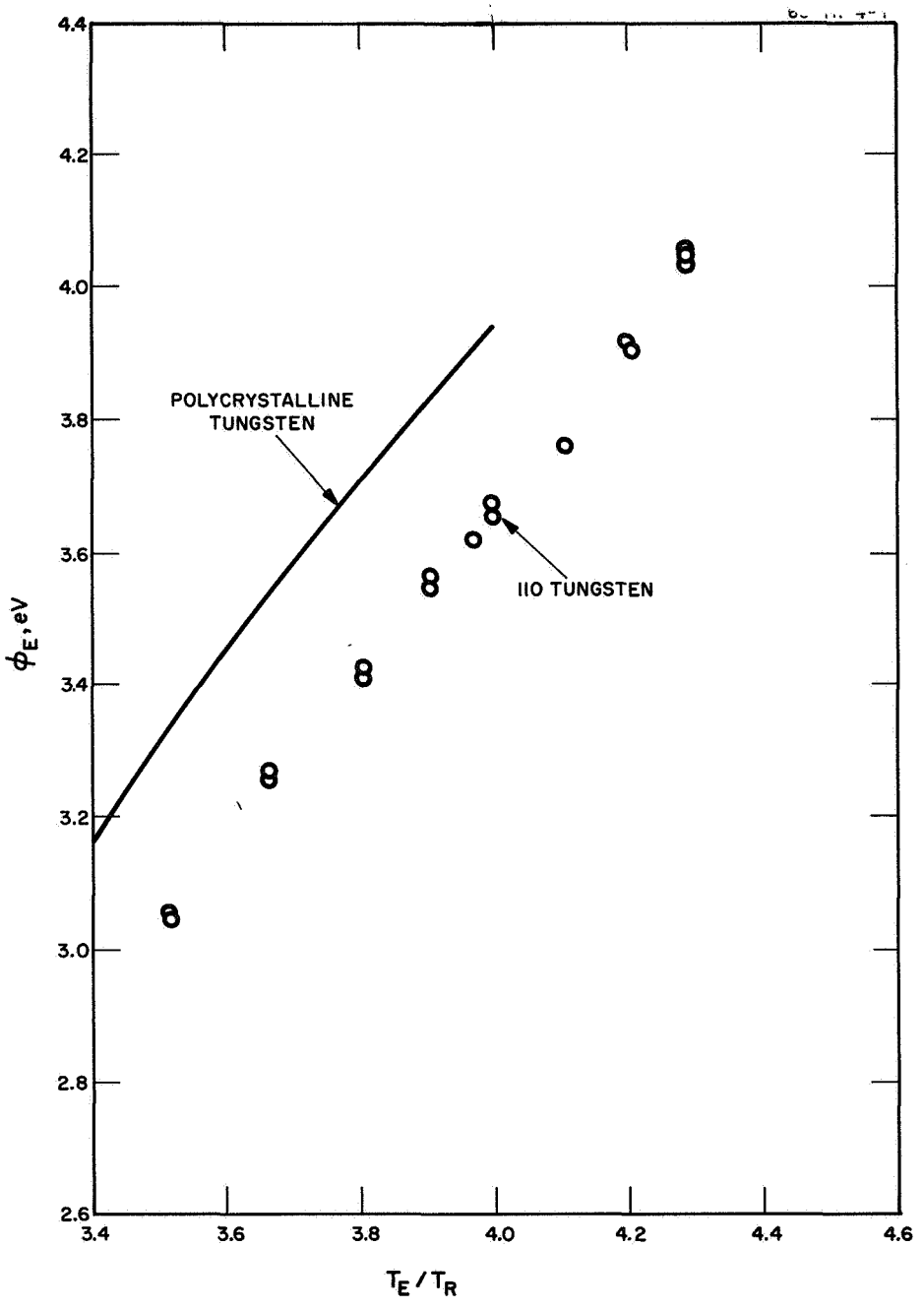

Figure IV-52. Work Function Data Obtained from Emitter W25 in Cesiated Converter.

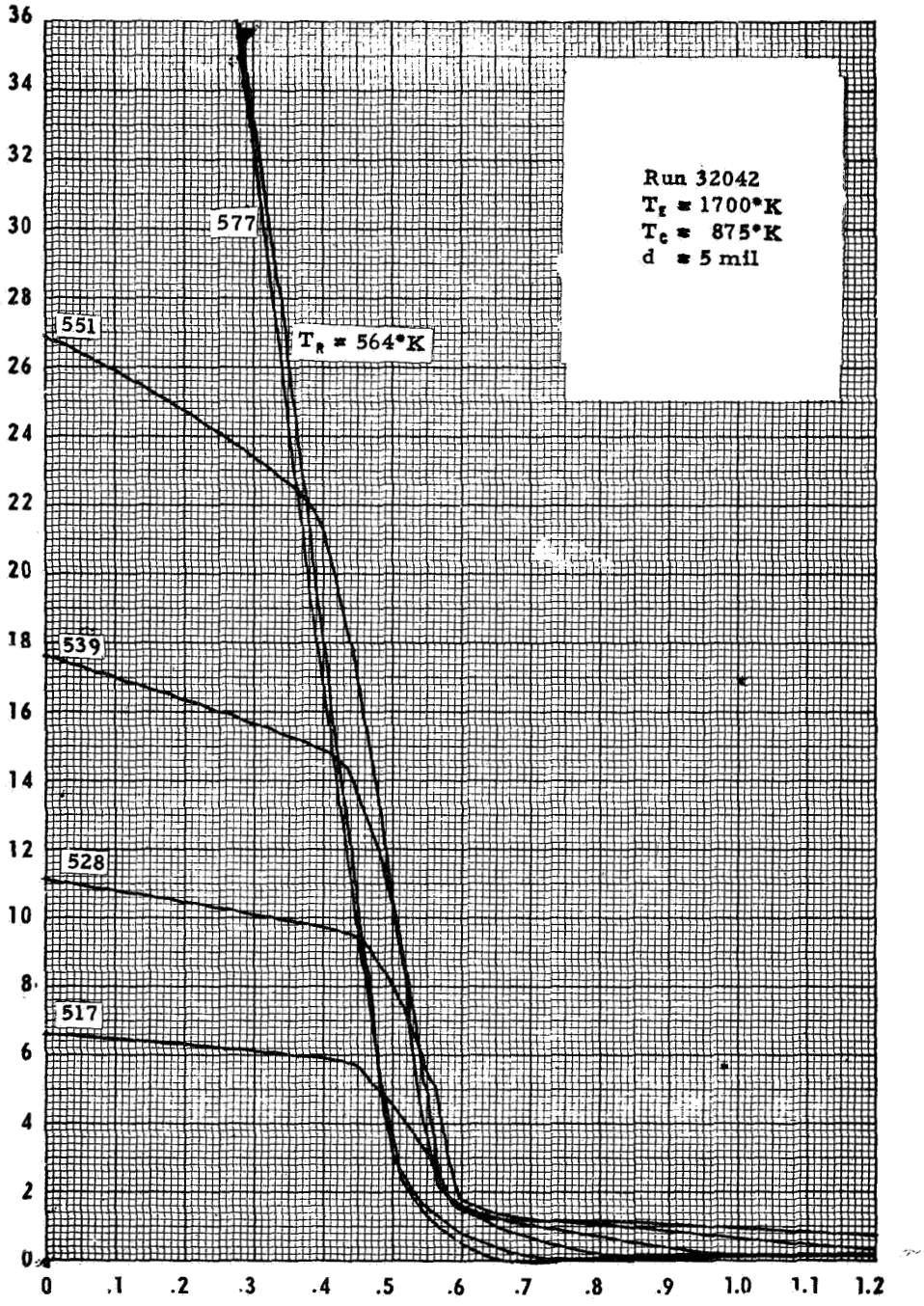

Figure IV-53. Variable Cesium Temperature Family at T_E = 1700° K and d = 5 mil.

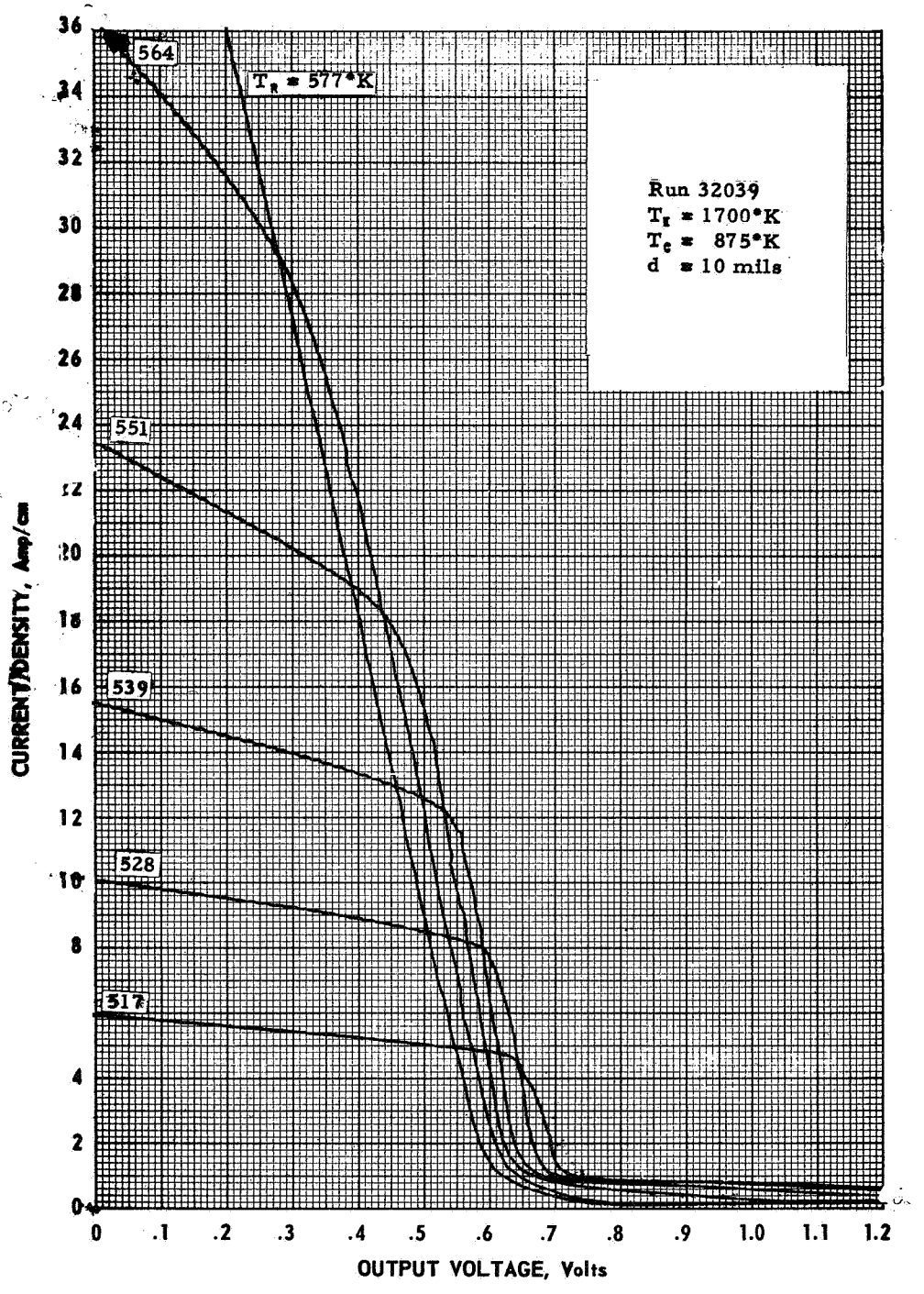

Figure IV-54. Variable Cesium Temperature Family at T_E = 1700° K and d = 10 mil.

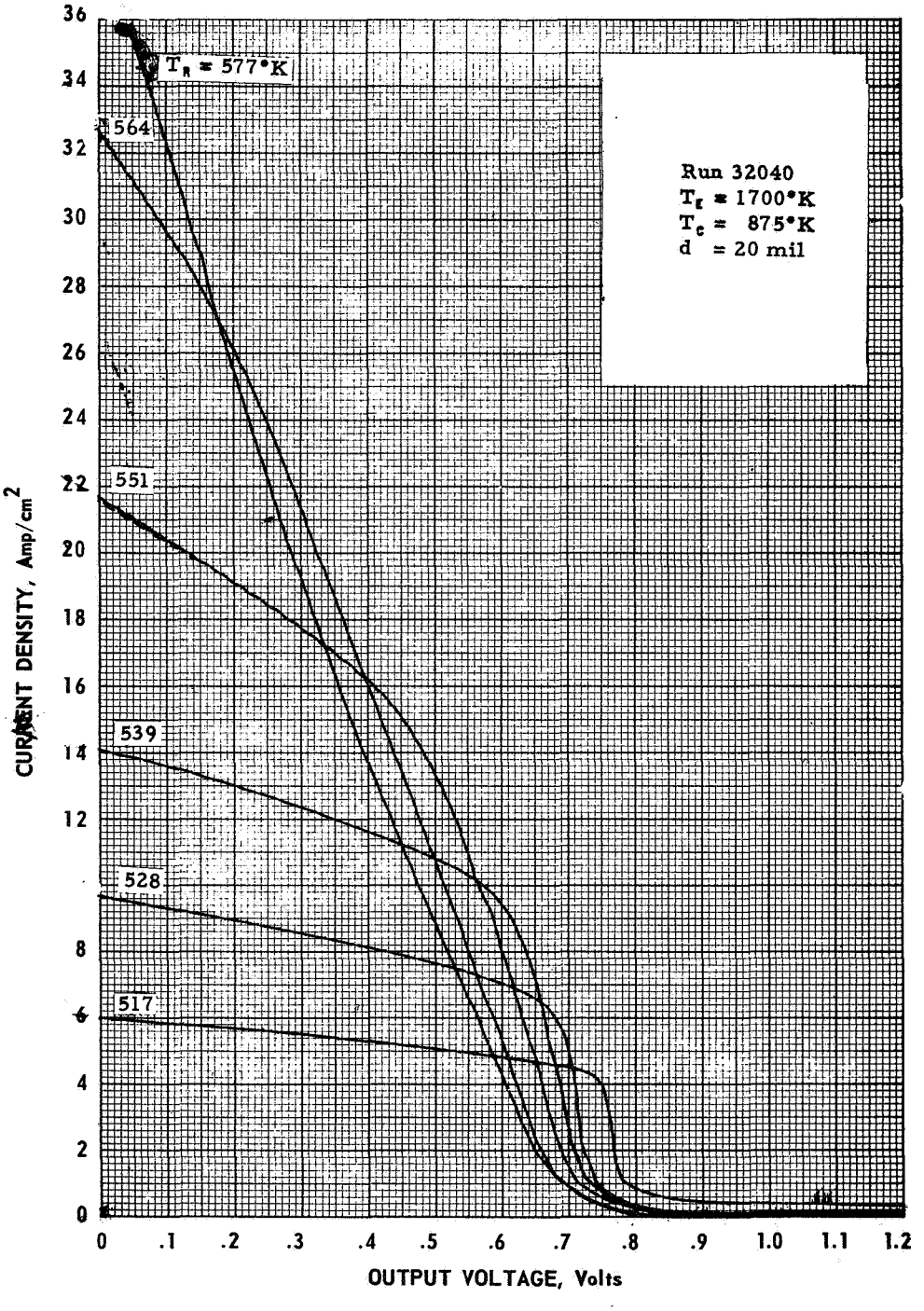

Figure IV-55. Variable Cesium Temperature Family at T_E = 1700° K and d = 20 mil.

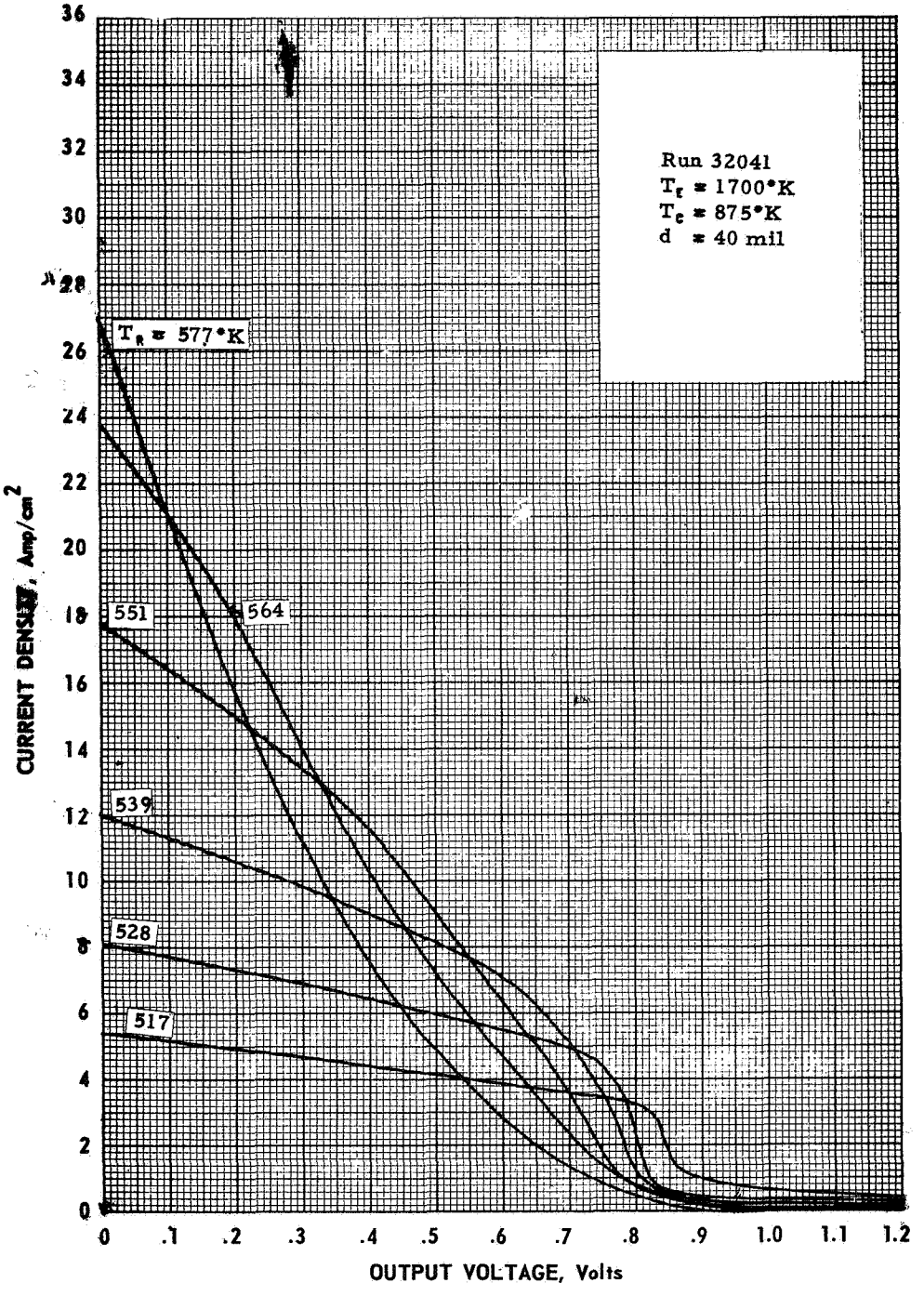

Figure IV-56. Variable Cesium Temperature Family at T_E = 1700° K and d = 40 mil.

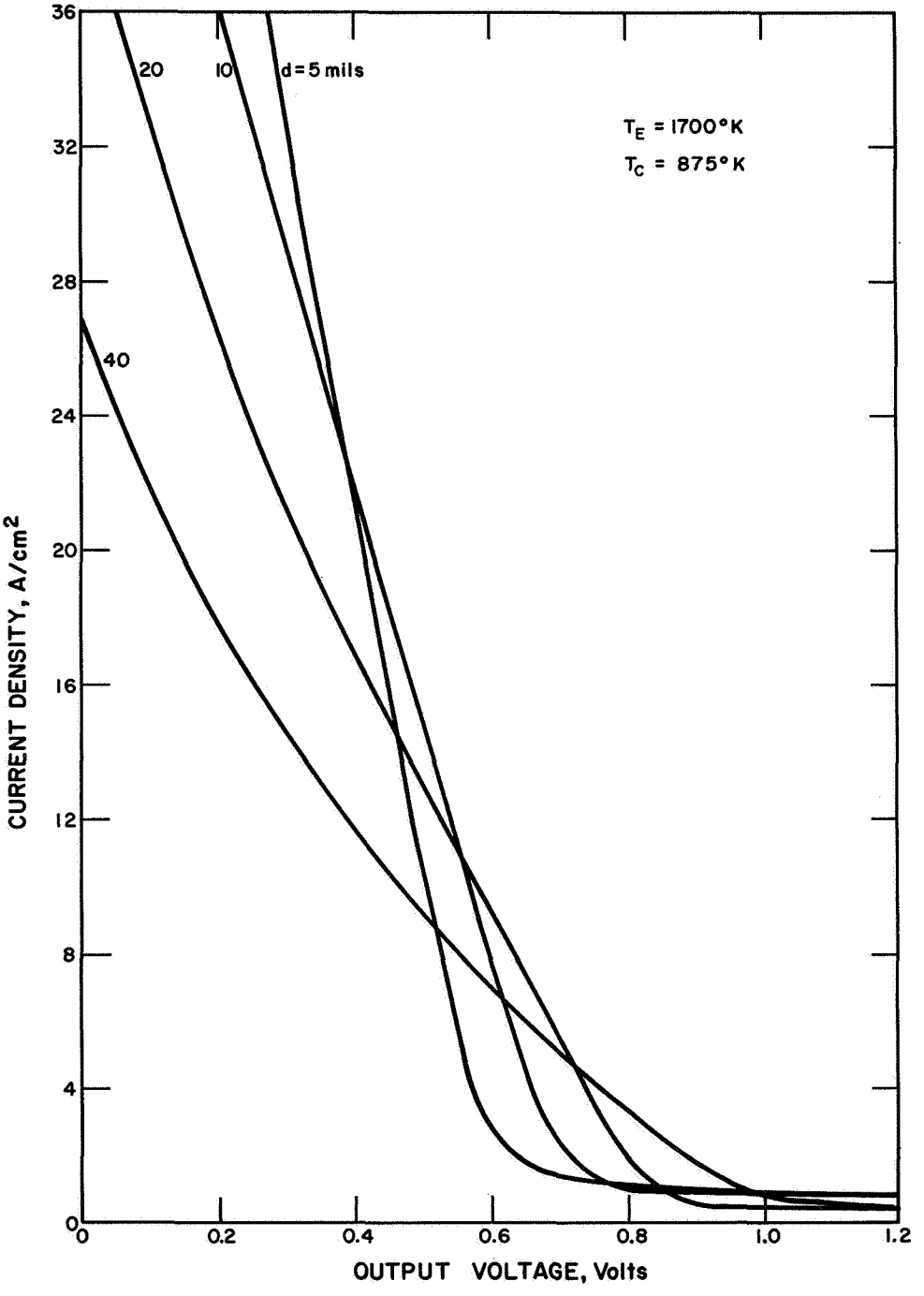

Figure IV-57. Summary of Cesium Envelopes at T_E = 1700° K.

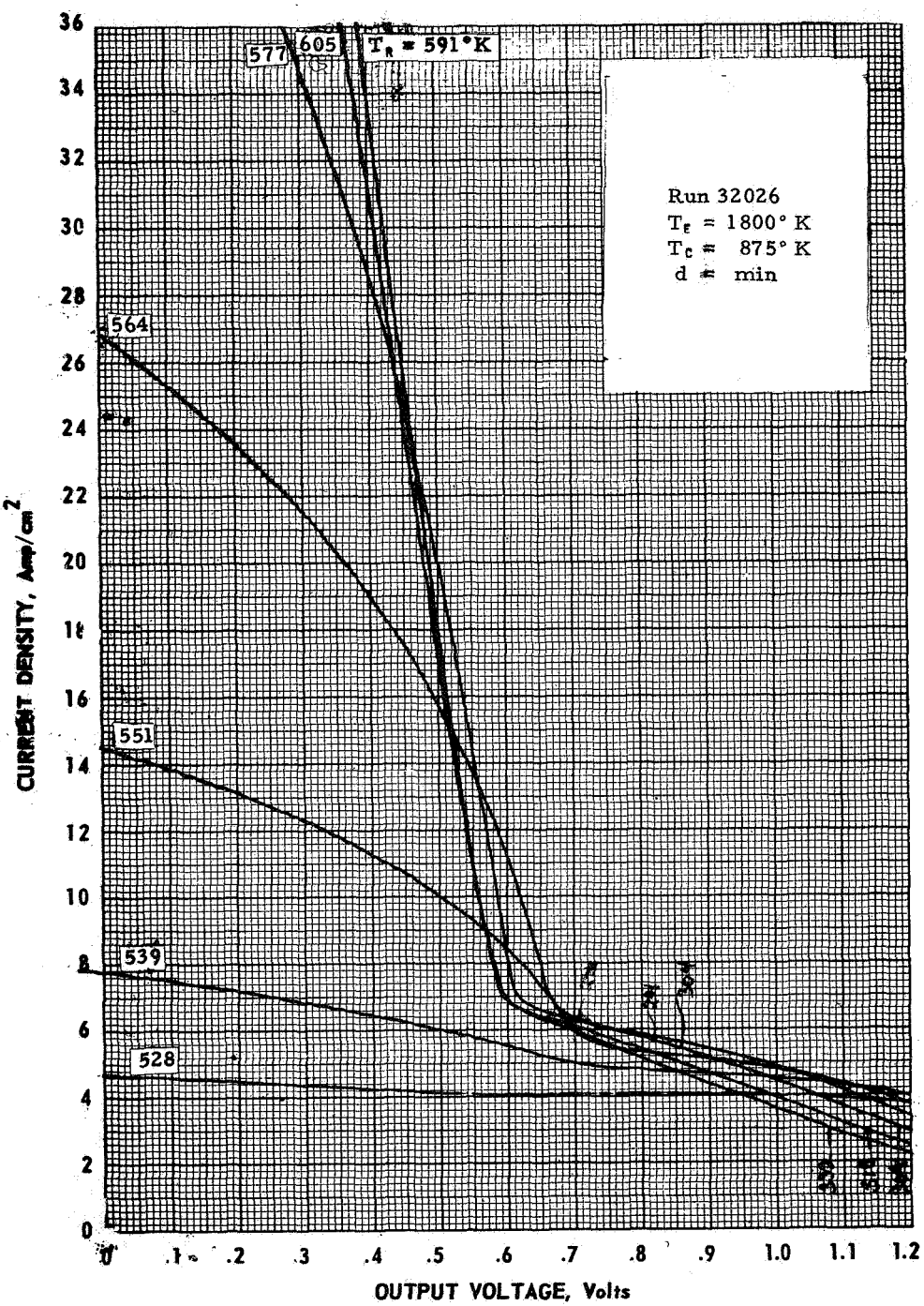

Figure IV-58. Variable Cesium Temperature Family at T_E = 1800° K and d = min.

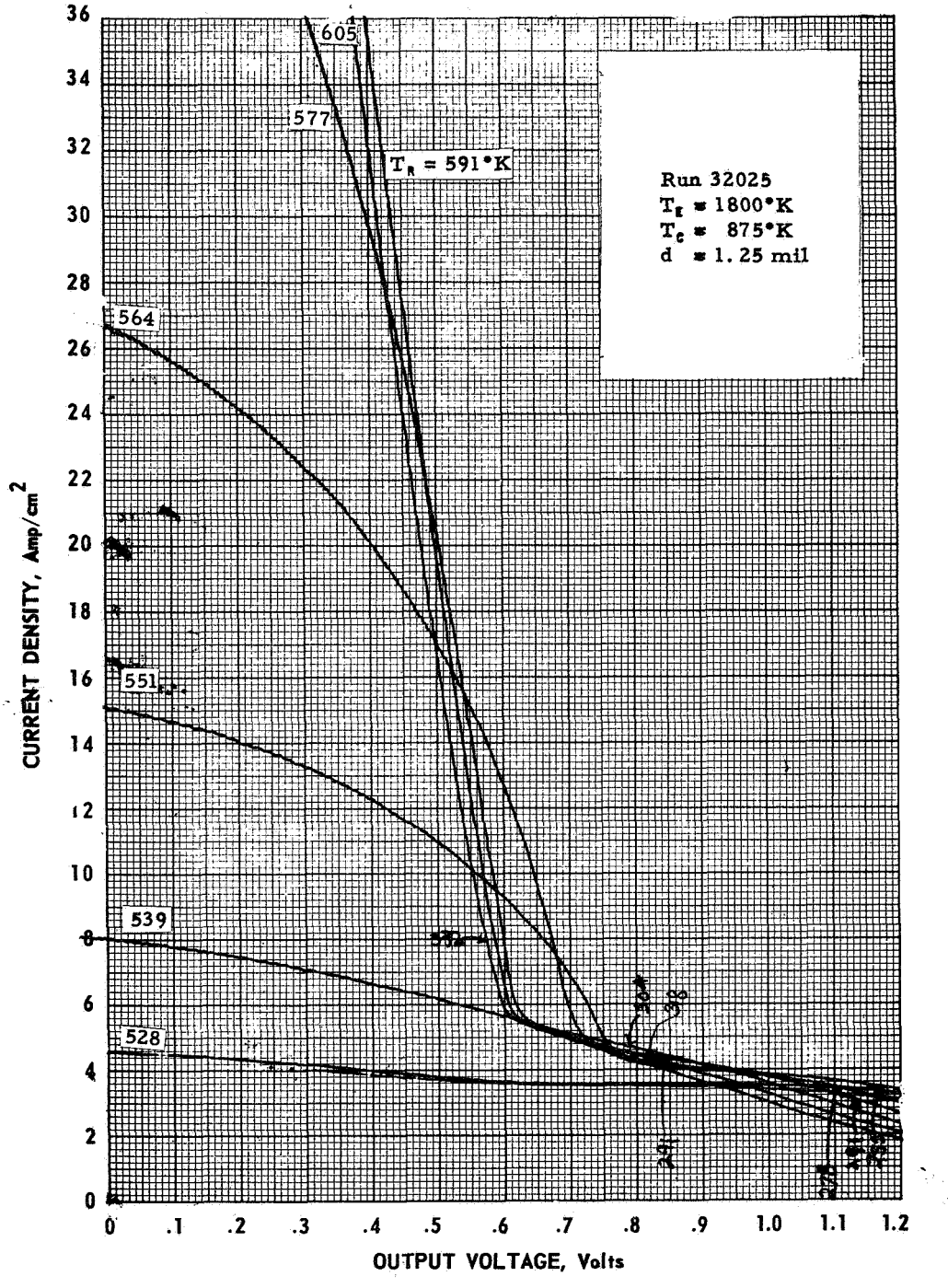

Figure IV-59. Variable Cesium Temperature Family at T_E = 1800° K and d = 1.25 mil.

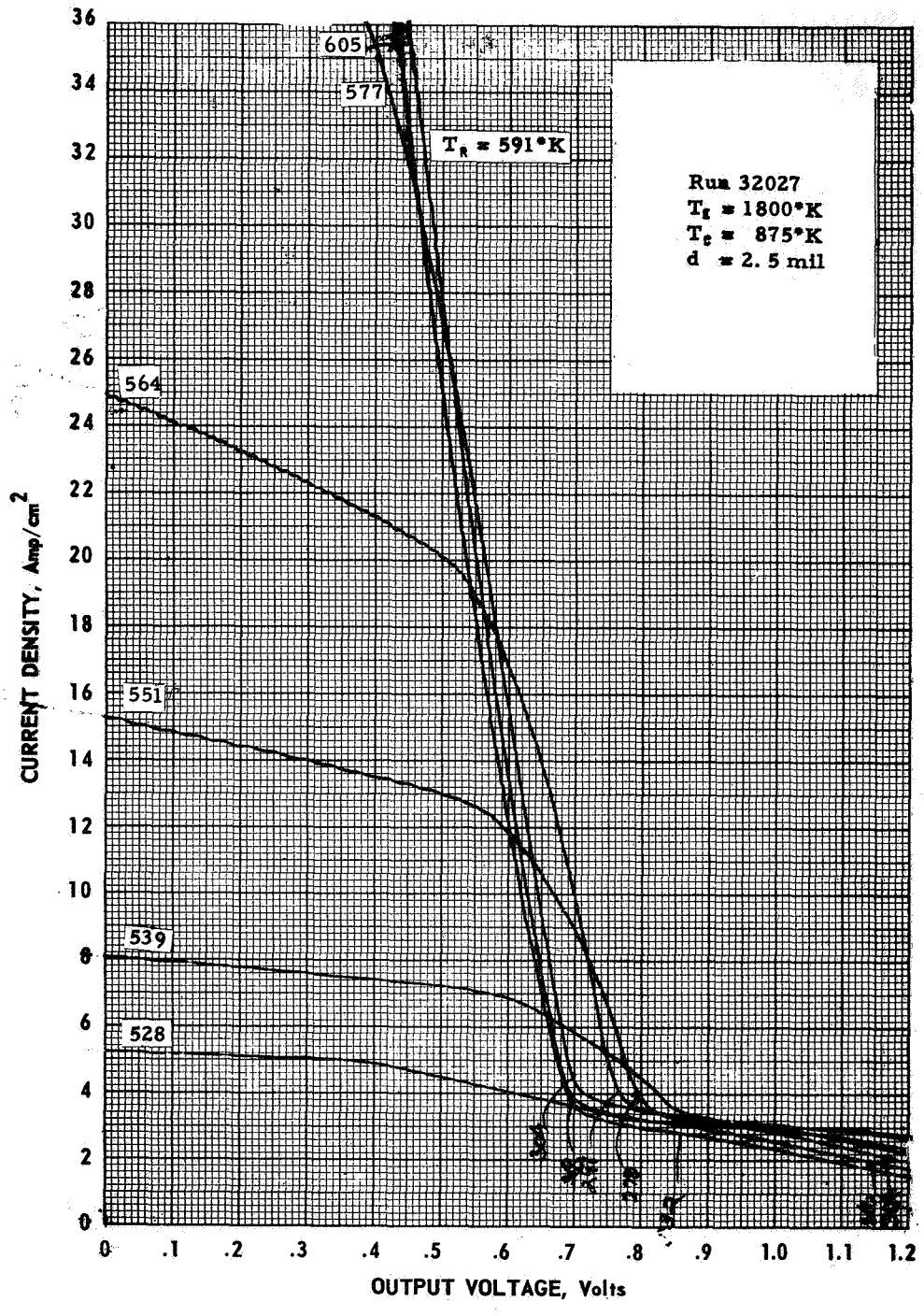

Figure IV-60. Variable Cesium Temperature Family at T_E = 1800° K and d = 2.5 mil.

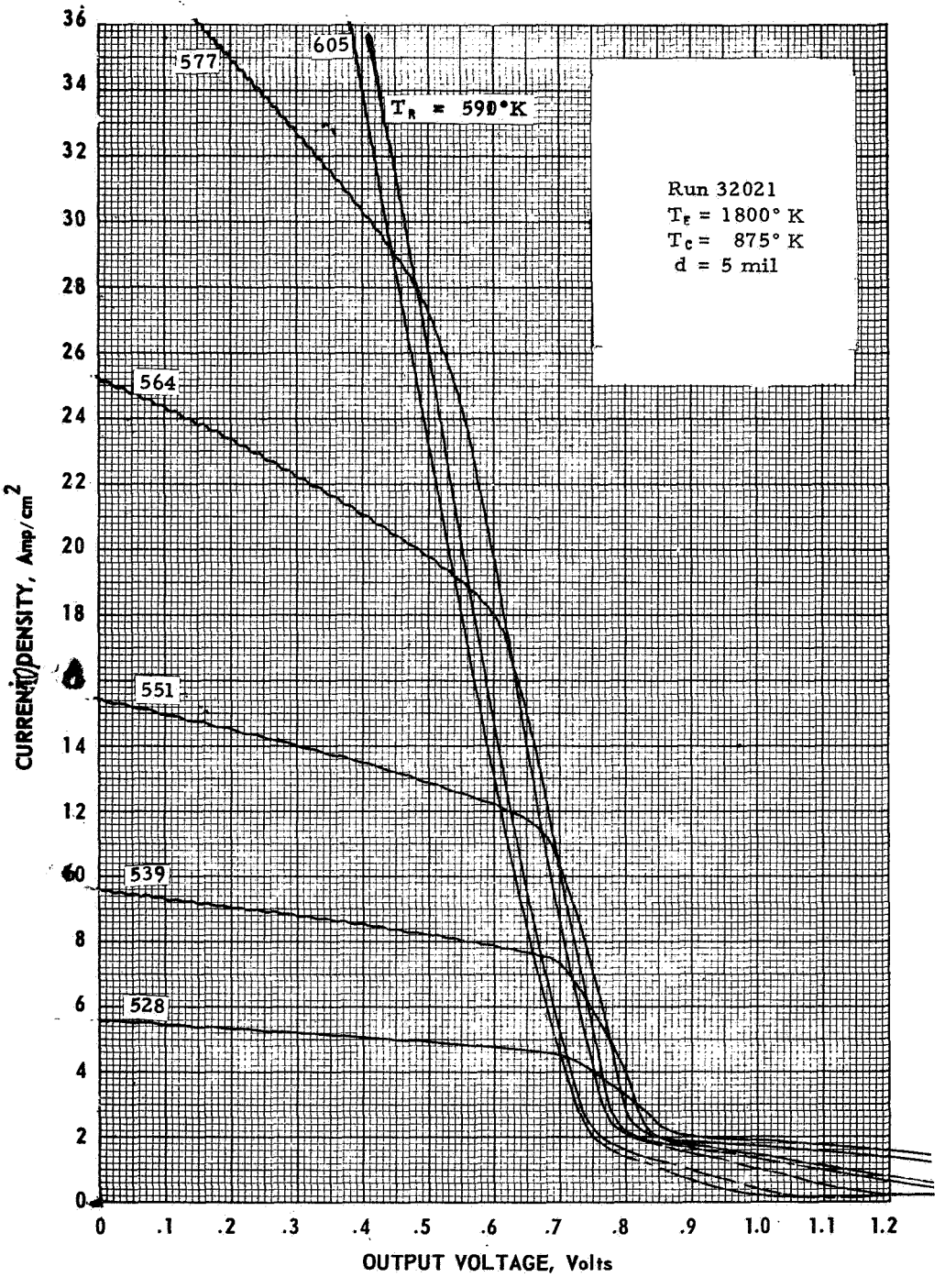

Figure IV-61. Variable Cesium Temperature Family at T_E = 1800° K and d = 5 mil.

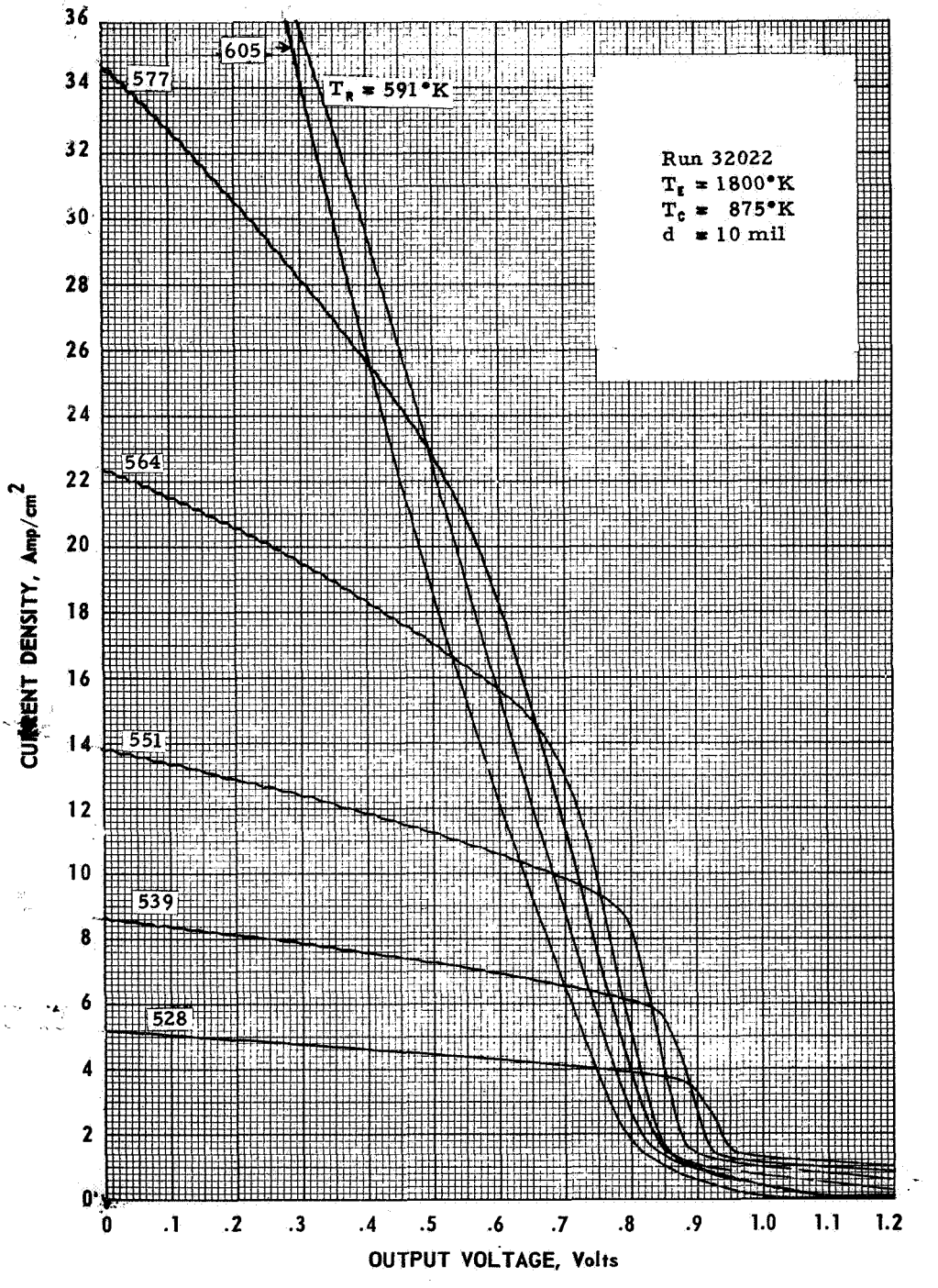

Figure IV-62. Variable Cesium Temperature Family at T_E = 1800° K and d = 10 mil.

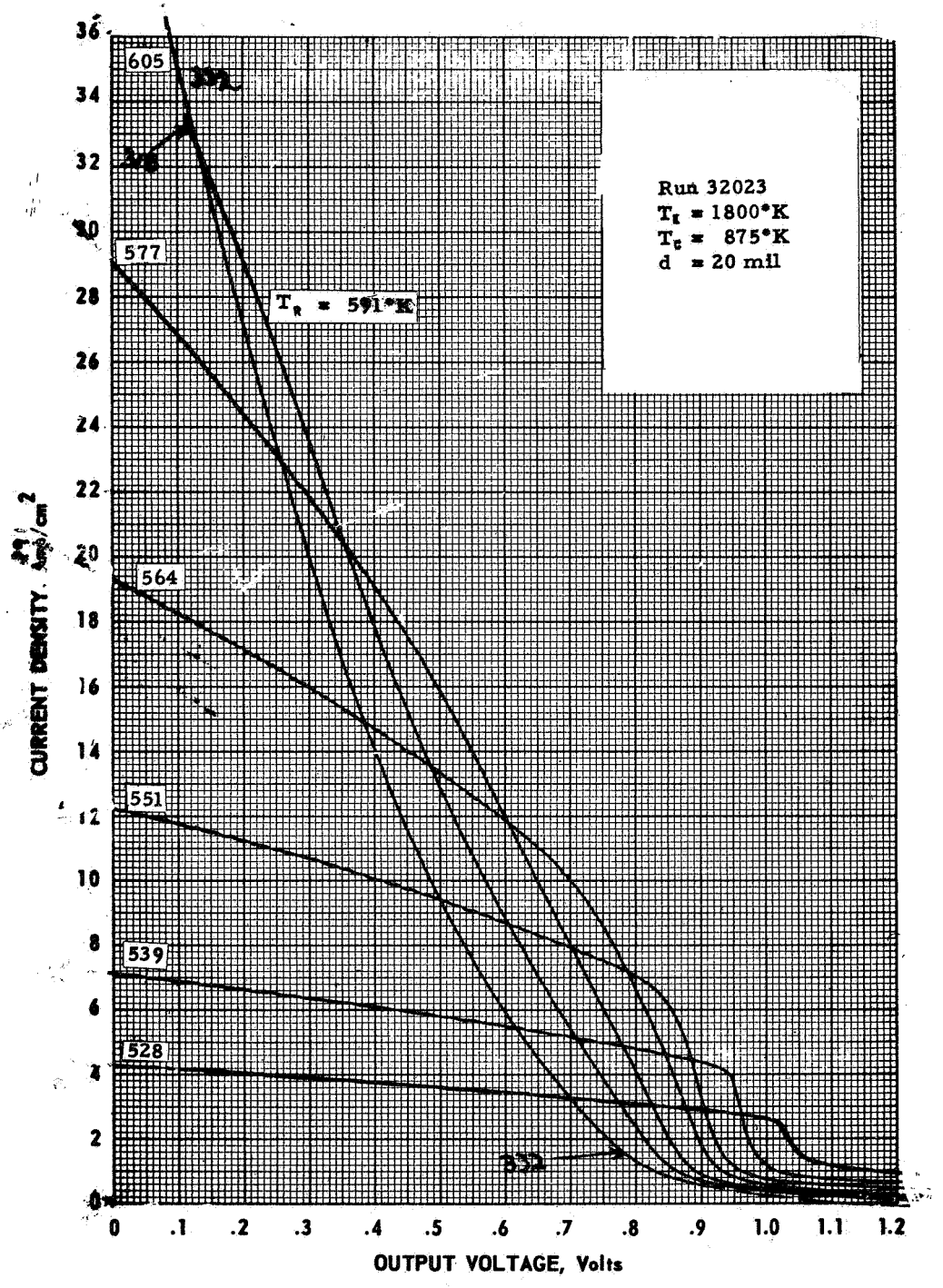

Figure IV-63. Variable Cesium Temperature Family at T_E = 1800° K and d = 20 mil.

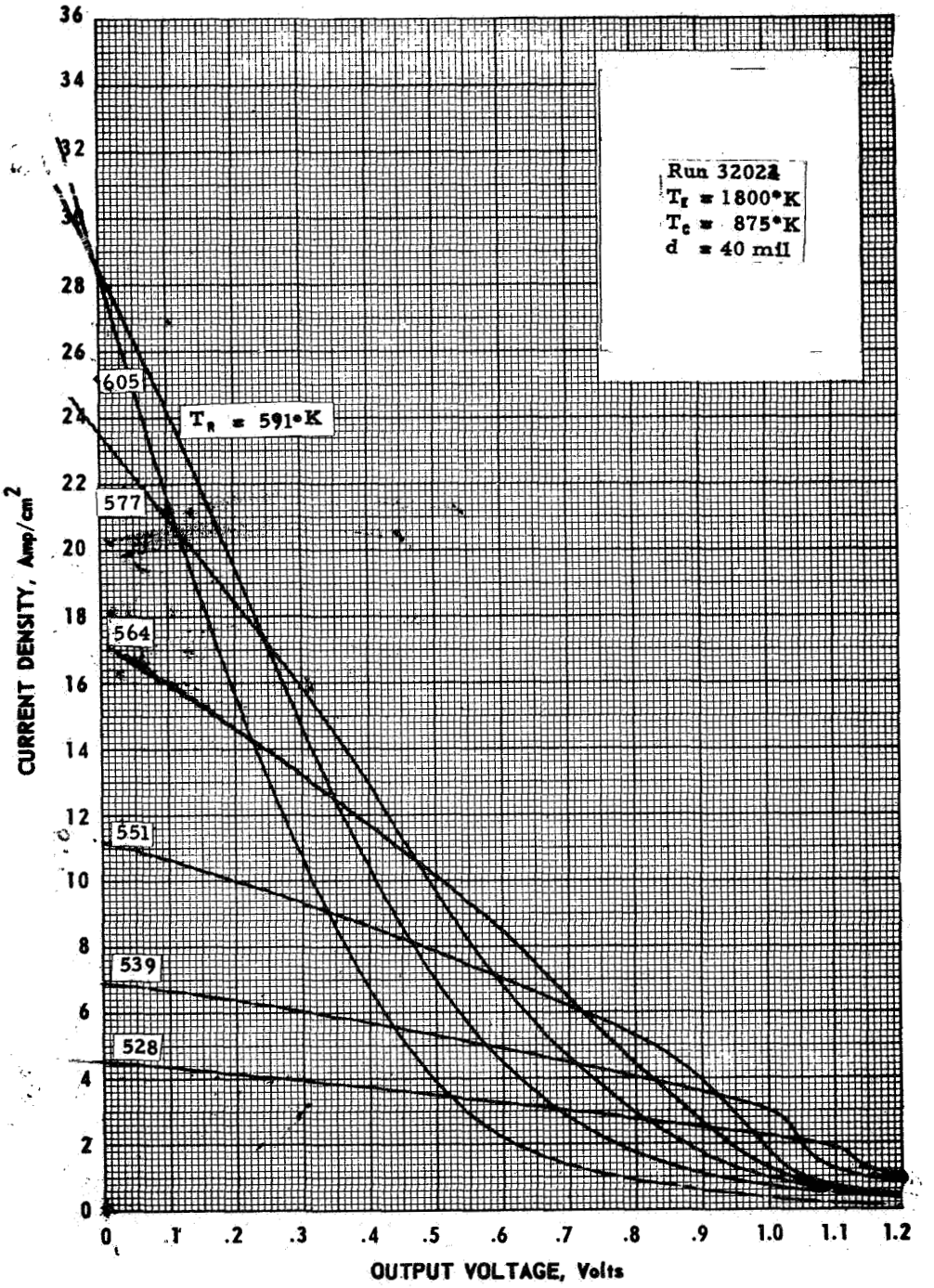

Figure IV-64. Variable Cesium Temperature Family at T_E = 1800° K and d = 40 mil.

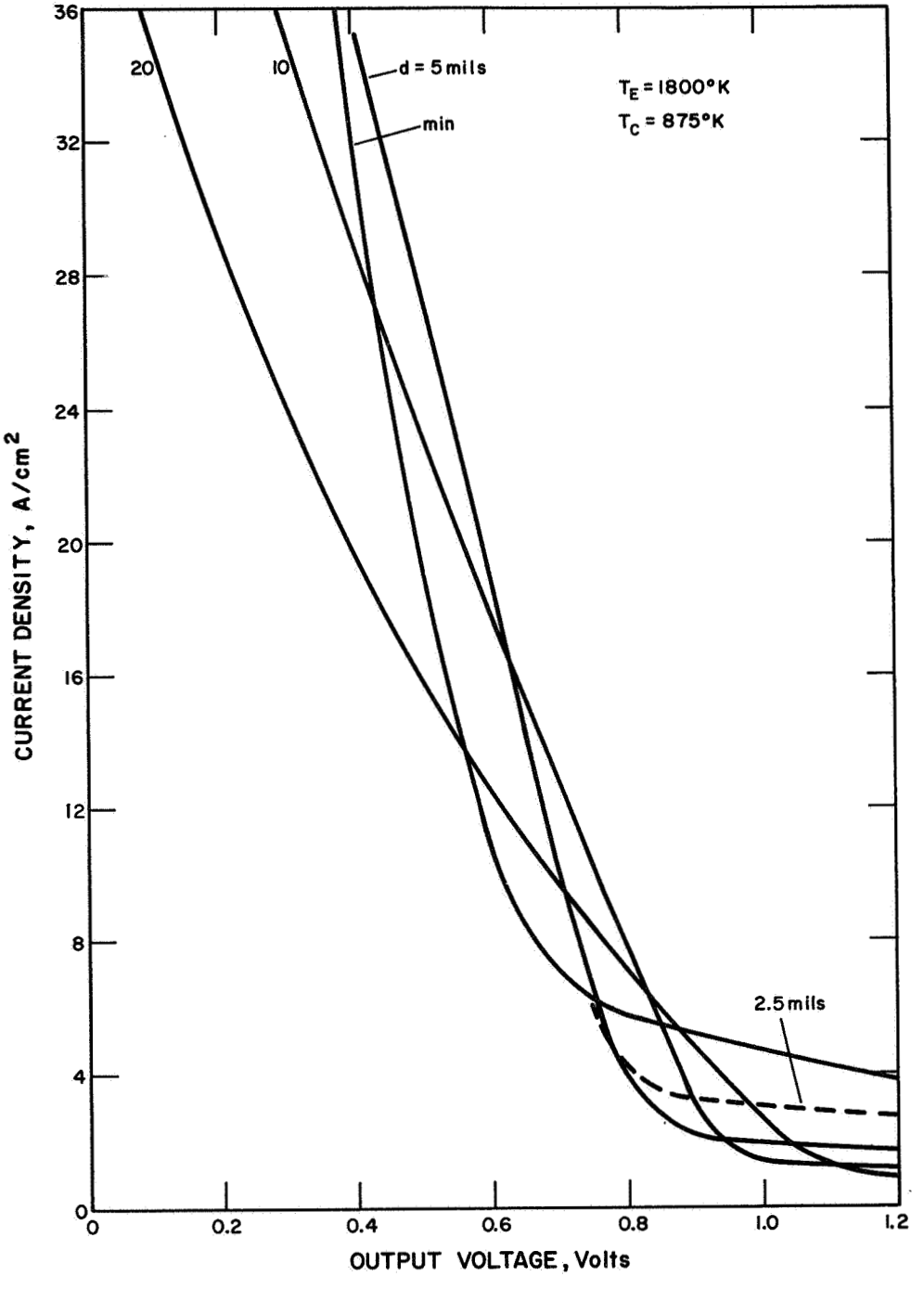

Figure IV-65. Summary of Cesium Envelopes at T_E = 1800° K.

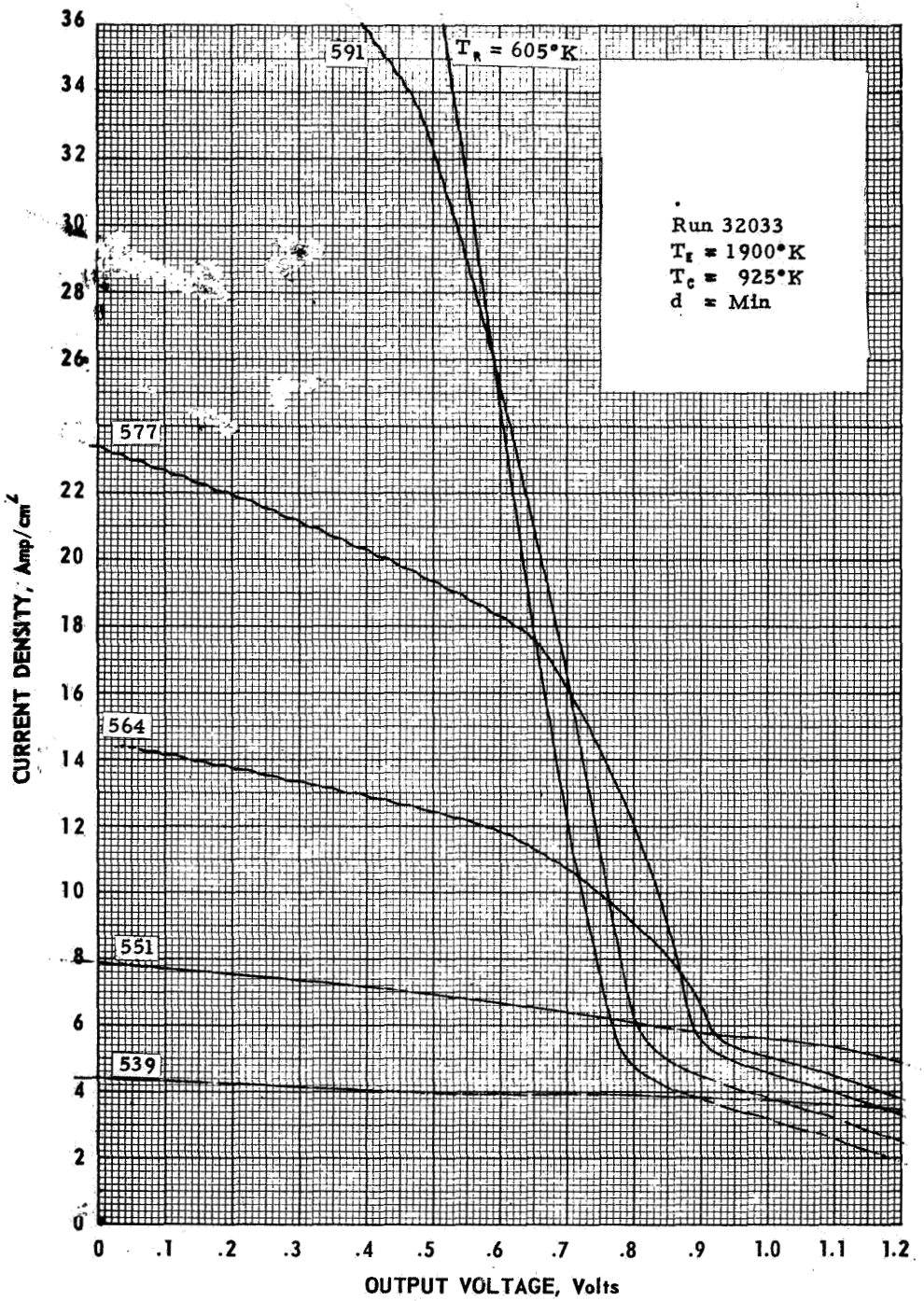

Figure IV-66. Variable Cesium Temperature Family at T_E = 1900° K and d = min.

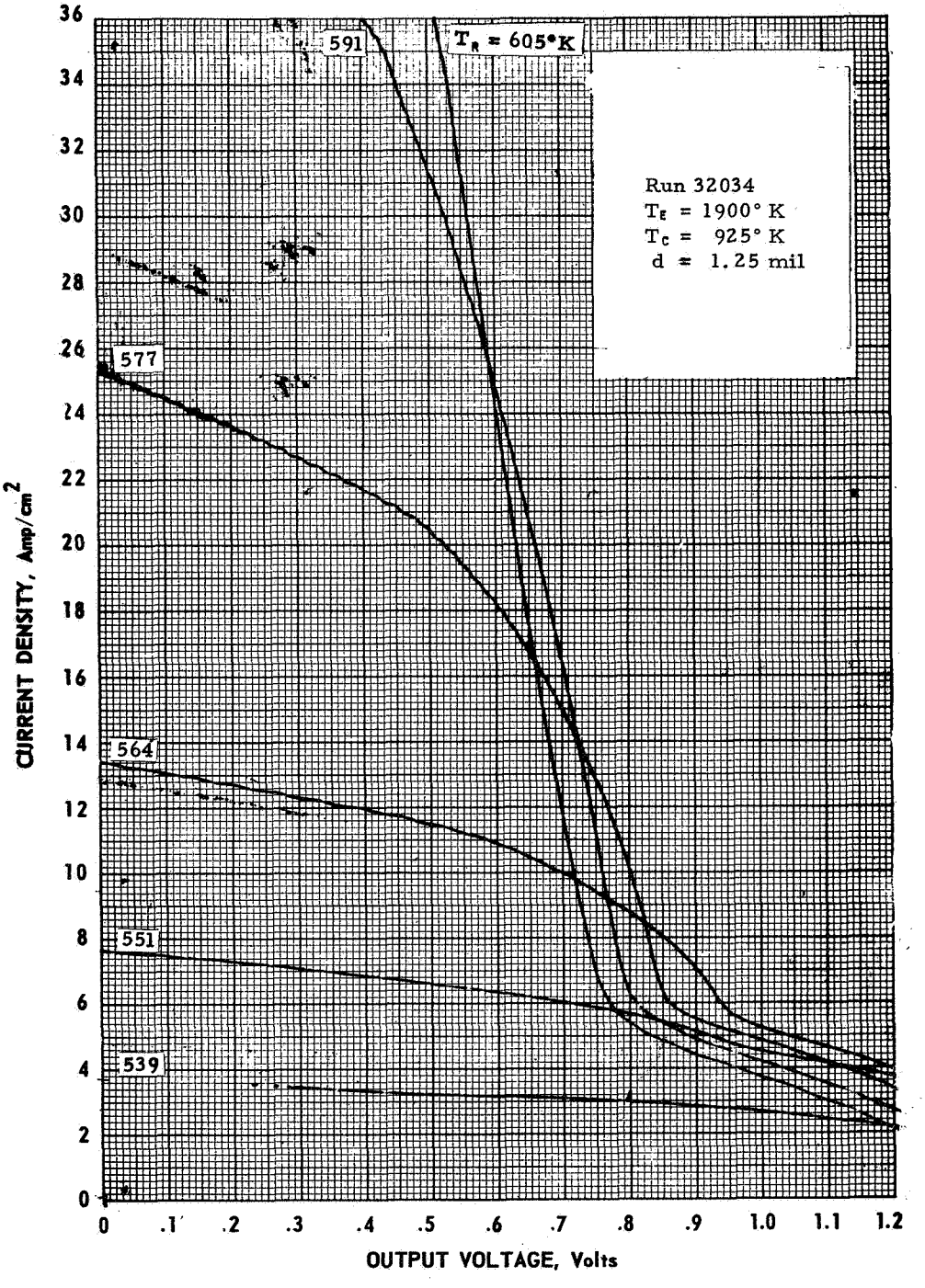

Figure IV-67. Variable Cesium Temperature Family at T_E = 1900° K and d = 1.25 mil.

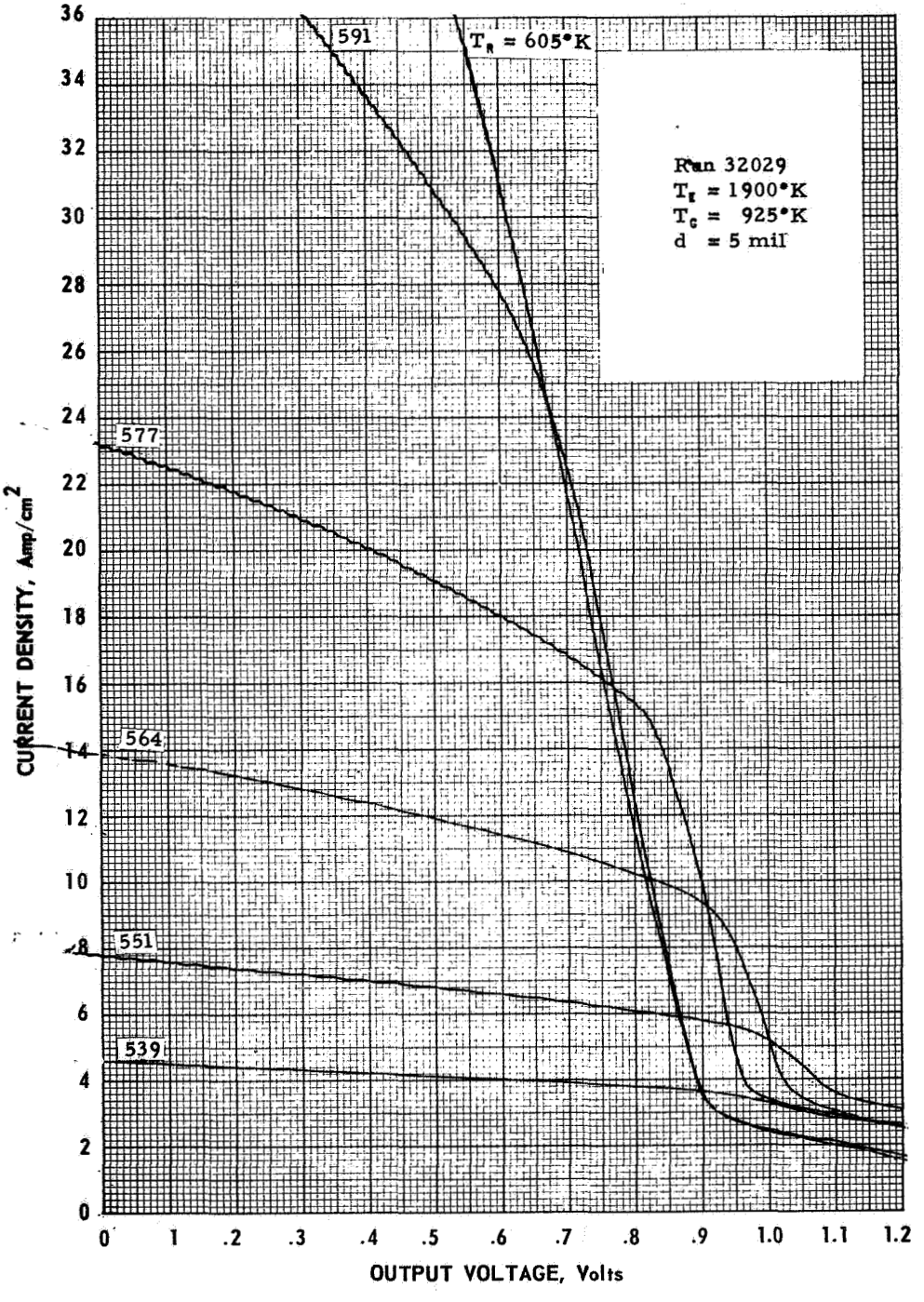

Figure IV-68. Variable Cesium Temperature Family at T_E = 1900° K and d = 5 mil.

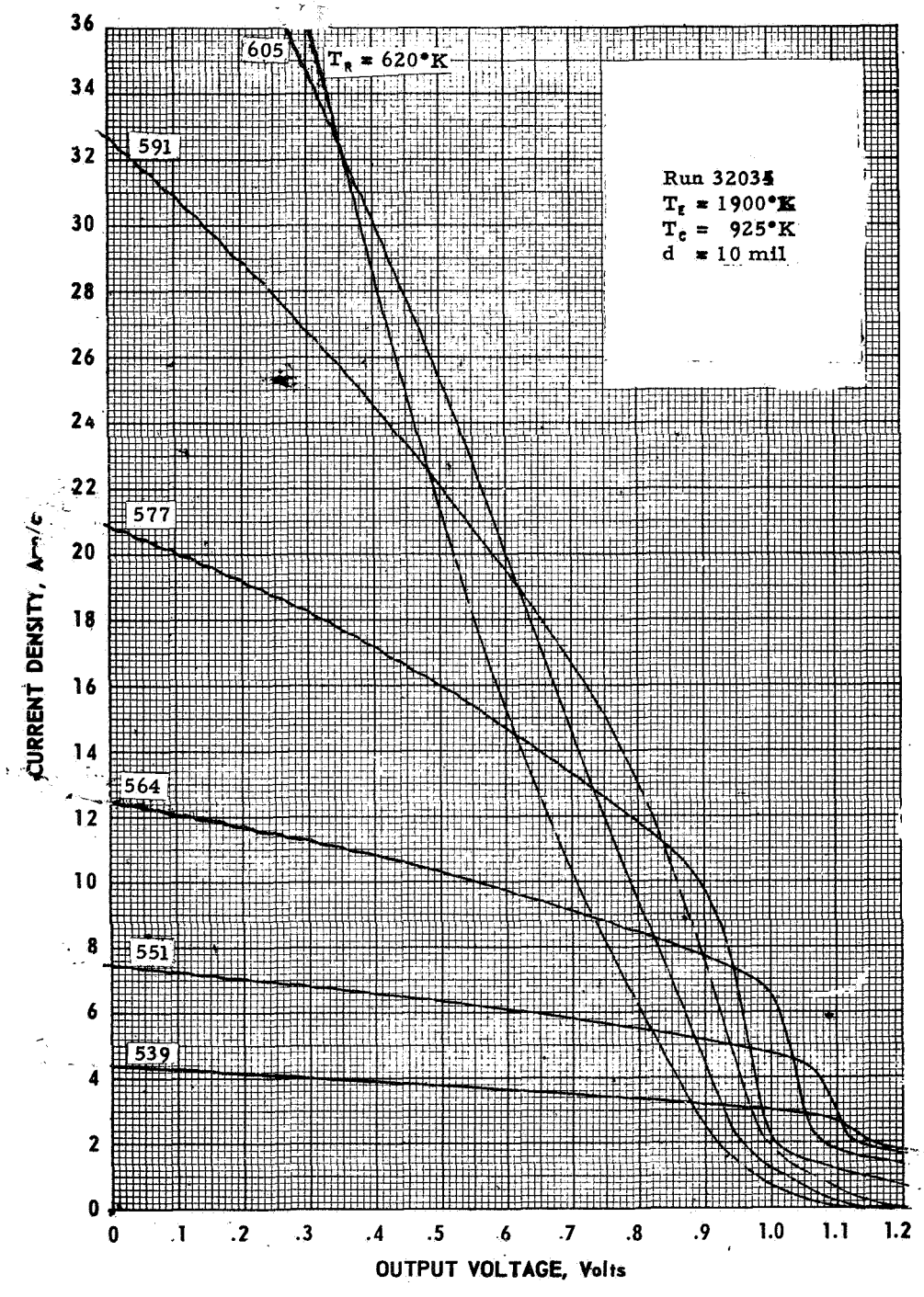

Figure IV-69. Variable Cesium Temperature Family at T_E = 1900° K and d = 10 mil.

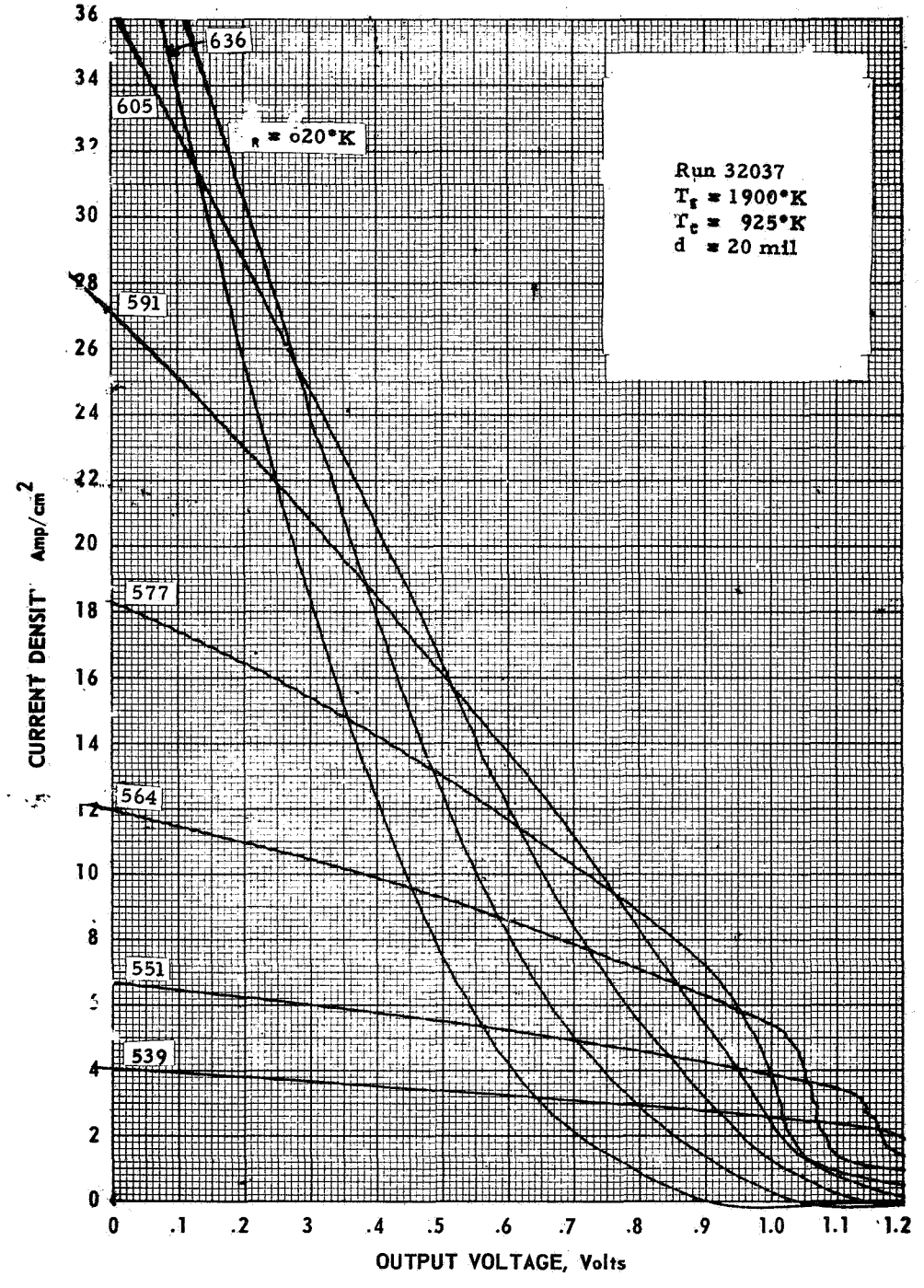

Figure IV-70. Variable Cesium Temperature Family at T_E = 1900° K and d = 20 mil.

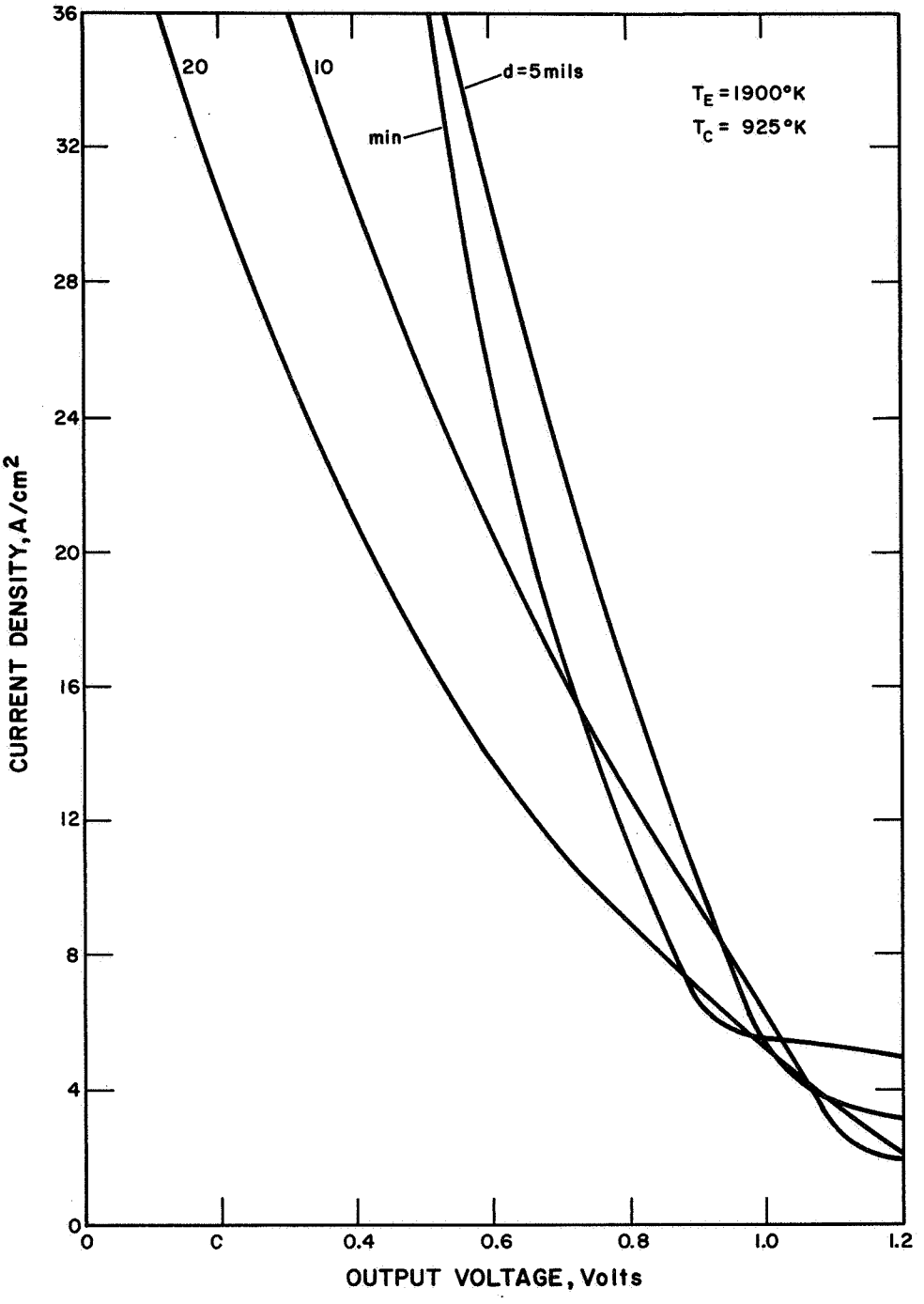

Figure IV-71. Summary of Cesium Envelopes at T_E = 1900° K.

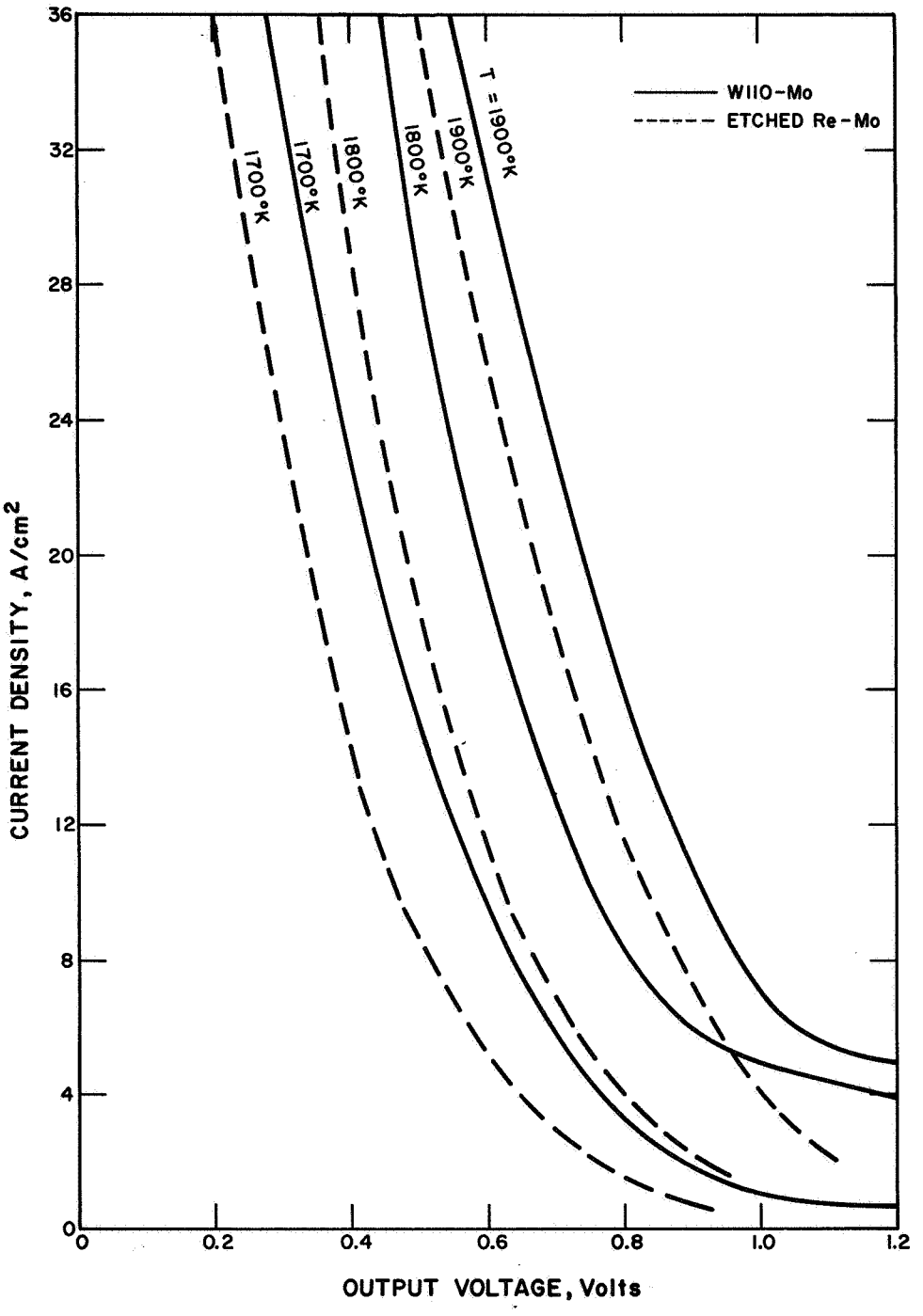

Figure IV-72. Comparison of Fully Optimized Performances of Tungsten and Etched Rhenium.

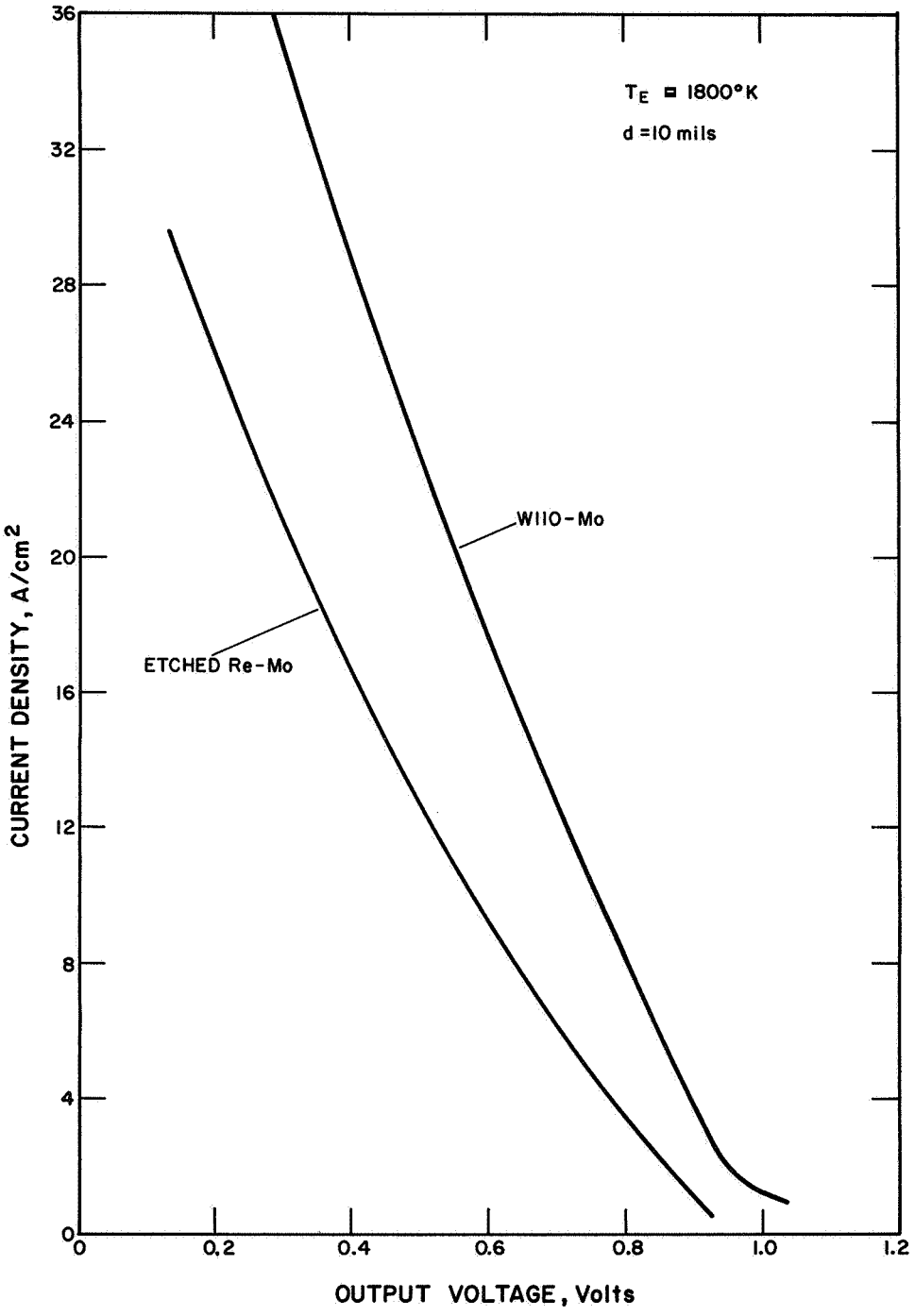

Figure IV-73. Comparison of Tungsten and Etched Rhenium at 10-mil Spacing.

C. VACUUM WORK FUNCTION MEASUREMENT APPARATUS

An apparatus has been designed and built in which accurate work function measurements can be made quickly and simply on clean emitters.

The work function is determined by solving the Richardson-Dushman equation:

$$J = AT^2 \exp - \frac{\phi}{kT} \text{ amp/cm}^2$$

The accuracy of the solution depends on an accurate knowledge of the following factors:

1. The emitter temperature T
2. The current flow from the emitter, and the area used to determine the current density.
3. The condition of the emitter, particularly with respect to the presence of or absence of adsorbed impurities.

The assumption is made that constant A in the equation has the value 120 amp/cm^2 °K^2. The other factors are dealt with by:

1. Measuring the temperature with an optical pyrometer sighted on a black-body hole in the emitter.
2. Having a collector significantly smaller than the emitter closely encircled by an electrically insulated guard ring. The collector area is 0.50 cm^2, and the current to this area defines the current density.
3. Having a large sputter ion vacuum pump attached to a fairly small vacuum system, which is water-cooled and uses all-metal seals so that low pressures can be obtained. Contamination of the emitter is known to

increase with decreasing emitter temperature and with increasing residual gas pressure. If significant changes in work function (>0.1 eV) are found to occur when the emitter temperature is varied, these can be attributed to residual gas contamination (usually by oxygen). Conversely, if data at high temperatures (>2000°K) show no systematic variation with temperature and the system pressure is found to be $\leq 10^{-7}$ torr, this is taken to mean that there is no contamination of the emitter.

The apparatus shown in Figure IV-74 was built to satisfy these conditions, and has proved satisfactory in service. A commercially available vacuum service cross is equipped with a pump and a shuttered view port. A collector/guard assembly and an emitter/electron gun assembly are inserted opposite each other. The emitter rests on its support structure without welds or brazes, and so can be changed easily. In service, a cycle time of 24 hours (between specimen changes) has been achieved routinely. The collector, guard, and cross are all water-cooled, using plastic hoses for electrical insulation. Interelectrode spacing can be varied by means of a screw in the emitter support structure, and is typically set to 0.04 inch cold, which changes to about 0.035 inch hot.

Useful data are obtained in the range of saturation currents from 10 μA to 100 mA. The lower limit is set by a combination of emitter contamination at the low temperature (~1700°K) and leakage current through the (~10 megohm) interelectrode insulation. The upper limit is set by electron cooling of the emitter, which causes a significant drop in measured current within a second of applying the test voltage.

Satisfactory measurements have been made at an emitter temperature of 2500°K. Collector and guard temperatures, monitored by thermocouples, are less than 100°C. However, some outgassing from the collector and guard is noted during measurements at higher saturation currents when these electrodes are effectively being electron-bombardment heated with the current from the emitter.

Emitter temperature can be controlled by a regulated electron-bombardment supply, which holds the filament potential below the emitter at ground potential. The temperature is measured to ± 5° with a micro-optical pyrometer. The power supply for measurements can go to 1250 volts to allow extensive Schottky data to be obtained, if desired. This raises the collector, guard, and x-y plotter above ground potential. No problems have occurred in the use of the two independent high voltage supplies.

Data are usually obtained for the current values corresponding to applied voltages up to 1225 volts. In low-current conditions, the polarity of the applied voltage is reversed to explore the leakage current due to the device resistance of about 10 megohms. The I-V curve in this direction is always linear, indicating a purely resistive leakage. It is not normal practice to take especially detailed data in the low voltage region around the origin, since this does not help to define the saturation current.

1. Ground and Annealed Tungsten Vapor-Deposited from the Fluoride

Specimen WF3 was ground on silicon carbide metallographic paper to #600, and annealed for 8 hours at 2000°C at a pressure in the range 5×10^{-6} to 5×10^{-7} torr before installation in the vacuum

emission apparatus. A summary of the data is shown in Figure IV-75. The diagonal lines represent constant values of work function. At emitter temperatures higher than 1850°K, the data points follow the work function line of 4.51 within ±0.01 eV, indicating that the partial pressure of oxygen at these temperatures is sufficiently low and does not interfere with the bare work function measurements. For emitter temperatures lower than 1850°K, the data points begin to drift towards higher work function lines, since the surface temperature is low and oxygen begins to adhere to the surface. Work function measurements on similar emitters, performed at Gulf General Atomics,[7] have shown a work function range of 4.53 to 4.50 eV.

2. Abraded and Annealed Single Crystal Tungsten

A slice of nominal single crystal of (110) orientation, purchased from the Linde Division of Union Carbide Corporation, was prepared for use in a parametric converter as follows: The surface was ground on a shop surface grinder, and then on #600 SeC abrasive paper; then it was abraded on a glass plate with an aqueous slurry of five micron Al_2O_3. After careful cleaning, it was fired in vacuum for 3 hours at 2450°C and then installed in the vacuum emission apparatus as specimen W31B. A representative current-voltage curve from this specimen is shown in Figure IV-76, and the corresponding Schottky plot in Figure IV-77. The data for this specimen are summarized in Figure IV-78, and they indicate a value of 5.15 eV ±0.02 eV.

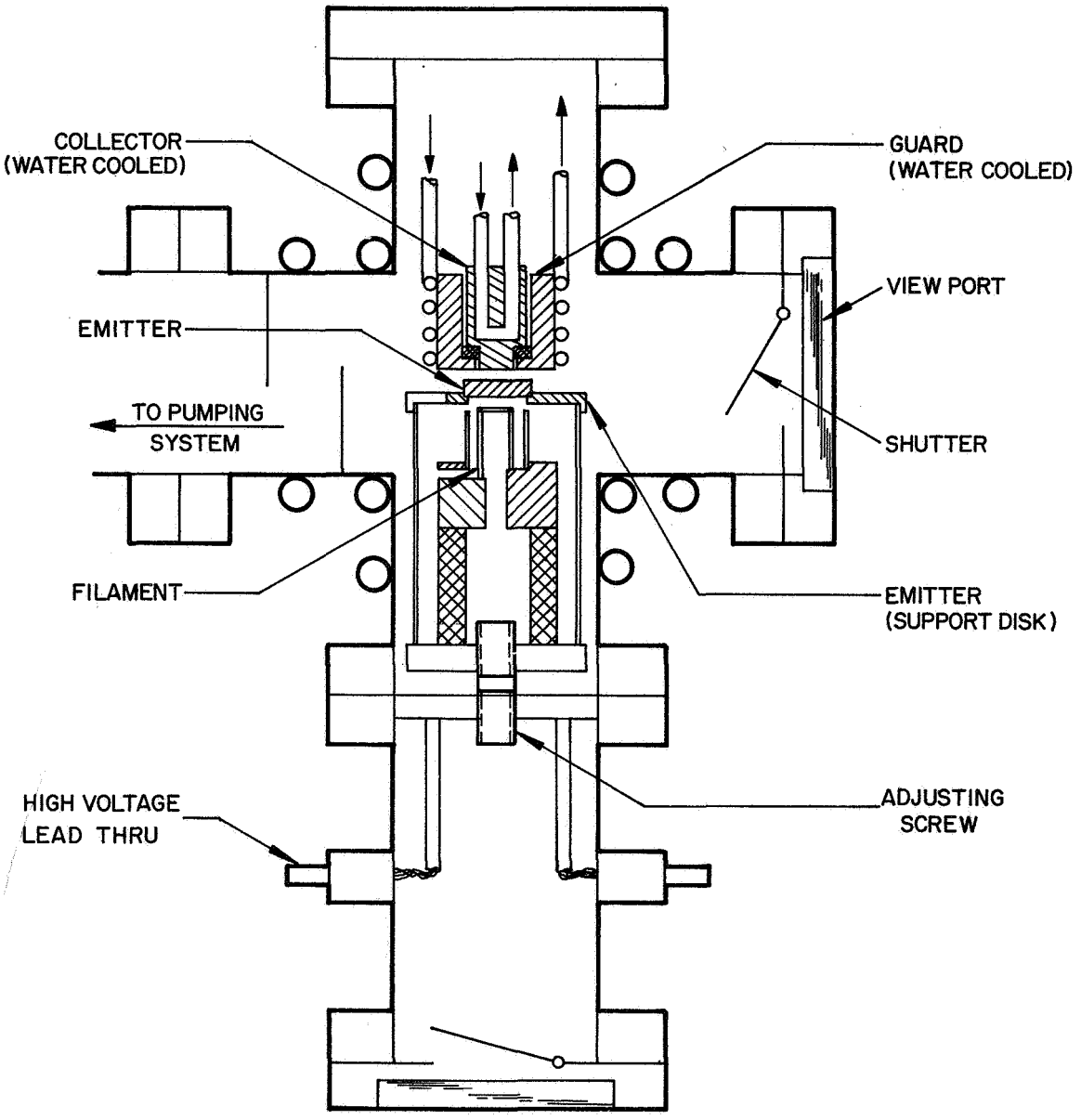

Figure IV-74. Apparatus for Vacuum Work Function Measurement.

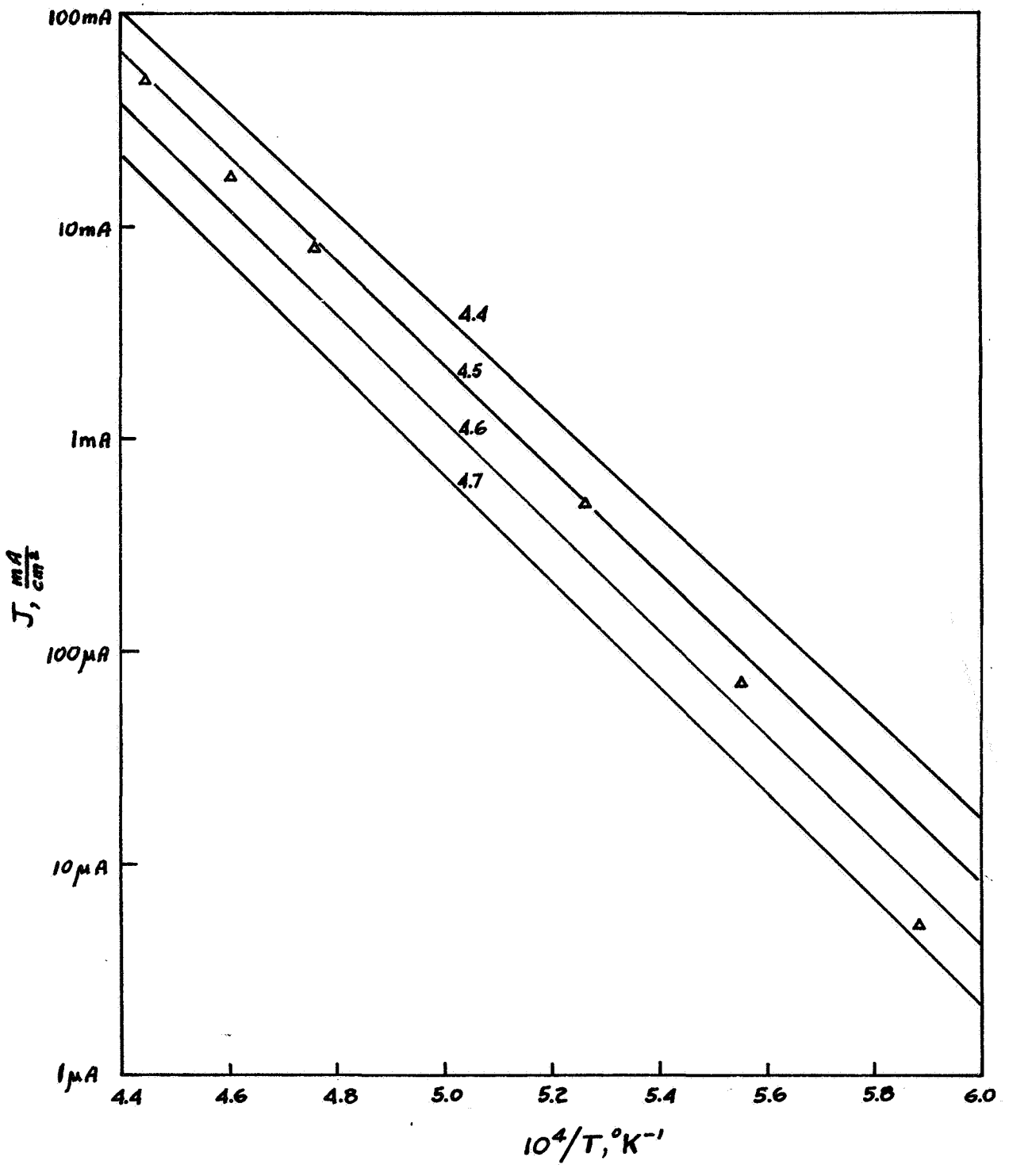

Figure IV-75. Vacuum Work Function Data for Fluoride Emitter WF3.

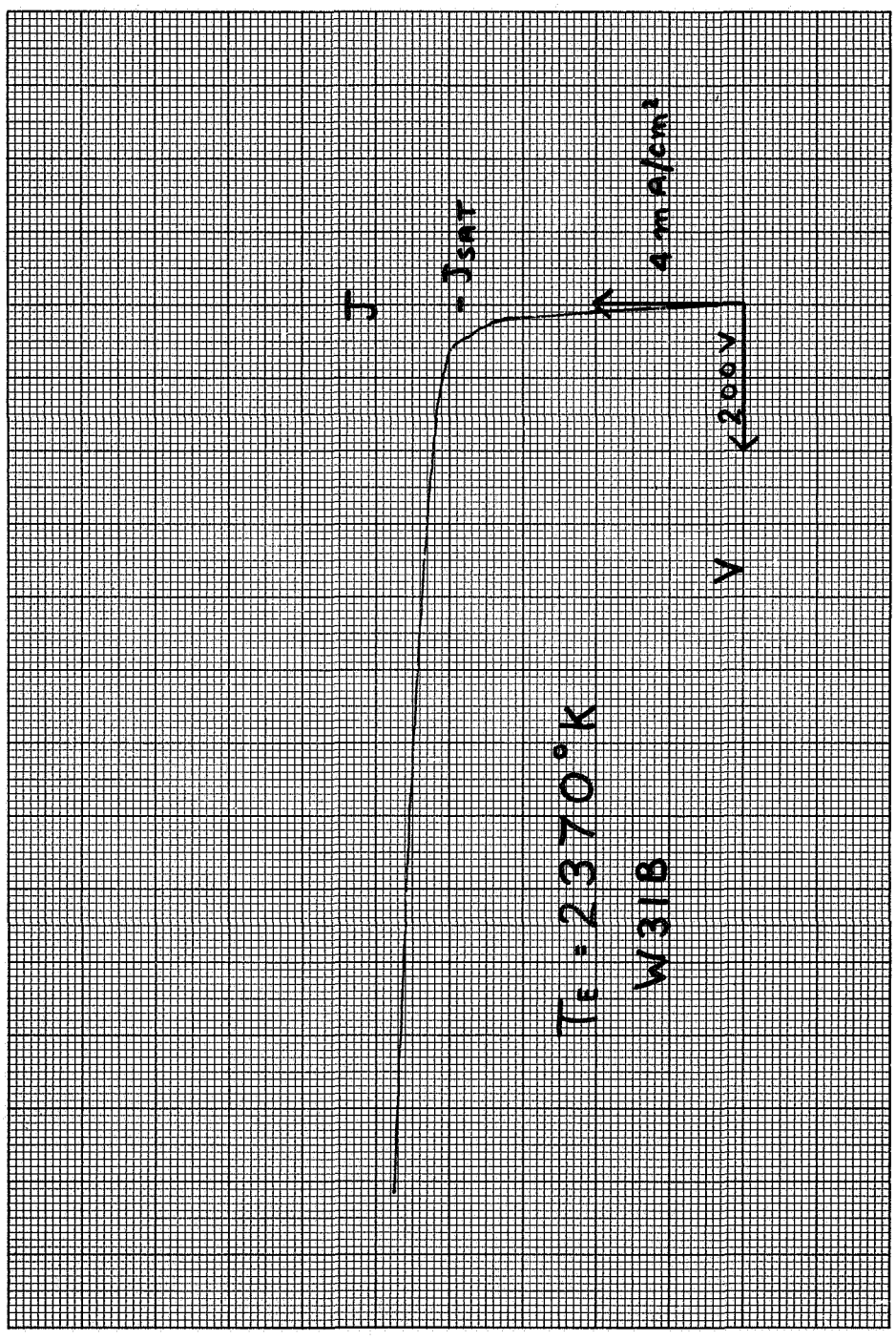

Figure IV-76. Typical J-V Characteristic From Vacuum Work Function Measurement Apparatus.

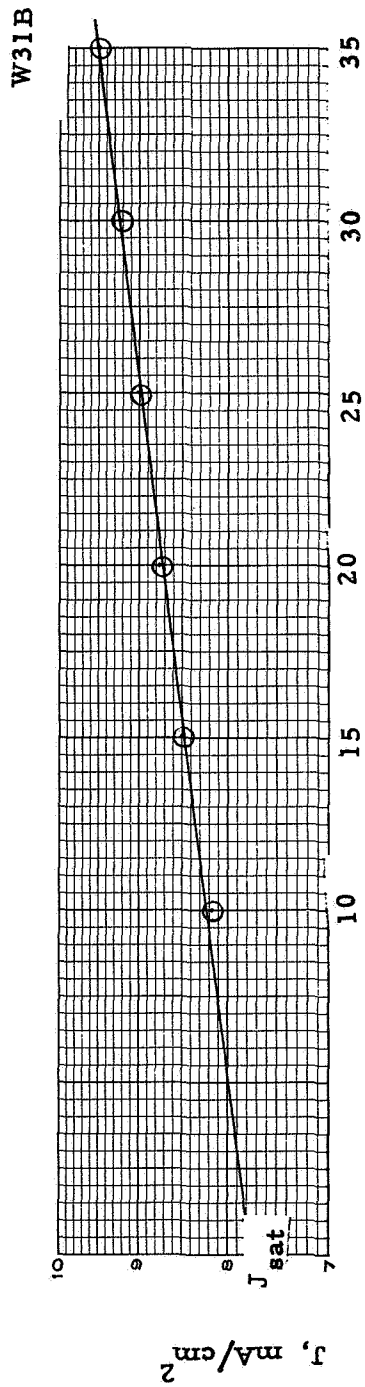

Figure IV-77. Typical Schottky Plot.

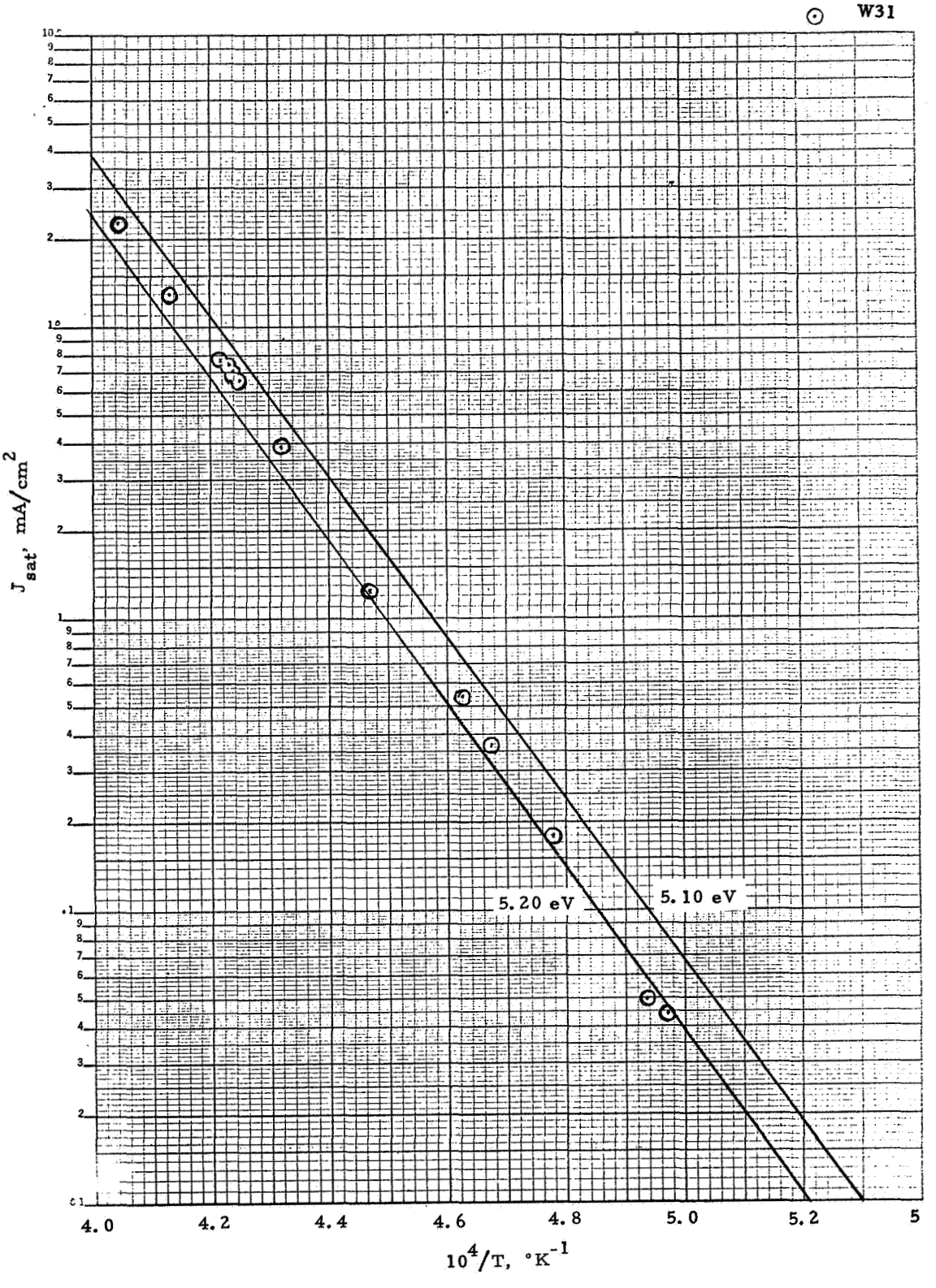

Figure IV-78. Work Function as a Function of Emitter Temperature.

D. ANALYSIS AND CORRELATIONS OF EXPERIMENTAL DATA

1. Voltage Loss Correlation

Several years ago, Kitrilakis[8] found a correlation between the deviation from ideal performance (V*) and the product of cesium pressure and interelectrode spacing (Pd). He stated, however, that the correlation was only true within a band of 0.1 volt. Using the present set of data, an attempt was made to determine if there are other dependencies contributing to the band. For this purpose, the voltage loss V* was defined as the difference in voltage between the Boltzmann curve and the J-V curve at the point of tangency to the cesium optimized envelope (Figure IV-79). According to this definition, V* is a measure of the deviation from ideal performance, and hence it is useful for indicating trends that may lead to an improvement in performance. The Boltzmann curve was established by the equation:

$$J = AT_E^2 \exp\left(\frac{\phi_C + V}{kT_E}\right)$$

where J is electron current, A is Richardson constant, T_E is emitter temperature, k is Boltzmann constant, V is electrode voltage, and ϕ_C is the collector work function for molybdenum.[9] Note that a correction of 1.5 mV per amp/cm^2 must be added to the output voltage of the J-V curves to obtain electrode voltage, or, alternatively, the Boltzmann curve must be modified to include this correction factor.

A summary of the results at the ion richness of 0.01 and the cesium pressures of 2, 4, and 8 is presented in Figure IV-80. The curves with lower cesium pressures exhibit a lower V*, but since each pressure corresponds to a particular emitter temperature

(Figure IV-80), the question arises whether this behavior is due to cesium pressure or emitter temperature. Similar plots made at constant emitter temperatures also showed a decrease in V^* with decreasing P; hence this effect appears to be mainly due to cesium pressure. The data for the ion richness conditions of 0.01, 0.05, 0.1 and 0.5 are shown in Figures IV-81 through IV-83. Note that at the ion richness of 0.5 the dependence of V^* on P begins to break down, probably because of approaching neutral conditions. A cross plot of the data from Figures 81, 82 and 83 is shown in Figure IV-84, indicating that at constant values of Pd, the voltage loss is an increasing function of cesium pressure. It also appears that β in the range of 10^{-2} to 10^{-1} has little influence on V^*.

2. Work Function Correlation

To examine the validity of theoretical expressions describing the plasma phenomena in thermionic converters, it is necessary to compare these expressions with experimental data for a wide range of converter operating conditions. Emitter work function is one of the most important parameters in the theoretical expressions, since it influences both electron emission and ion generation at the emitter surface. An accurate experimental measurement of emitter work function, however, can only be made under a narrow range of converter operating conditions, and the measured values must be extrapolated to cover the other regions of operation. In this section a new correlation technique is presented and compared with the T_E/T_R correlation.

The new correlation is based on the thermodynamic equation:

$$T \ln P = AT + B \tag{1}$$

where T is surface temperature, P is cesium pressure, and A and B are functions of the surface work function ϕ. The functions A and B are assumed to be of the form:

$$A = \alpha_1 \phi + \beta_1 \tag{2}$$

$$B = \alpha_2 \phi + \beta_2 \tag{3}$$

where α_1, α_2, β_1 and β_2 are constants. Equations 1 through 3 can be combined to give:

$$\ln P = (\alpha_2 \phi + \beta_2) \frac{1}{T} + \alpha_1 \phi + \beta_1 \tag{4}$$

This equation can be compared with experimental data in order to determine the constants α_1, α_2, β_1 and β_2.

The data[10] used for this correlation is plotted as a function of kT ln P in Figure IV-85. A cross plot of the data in terms of ln P versus $\frac{1}{T}$ is shown in Figure IV-86. Each constant work function line has an intercept I and a slope S. According to Equation 4, the intercept and the slope are given by:

$$\begin{aligned} I &= \alpha_1 \phi + \beta_1 \\ S &= \alpha_2 \phi + \beta_2 \end{aligned} \tag{5}$$

The intercept I is determined from the constant-work-function lines and is plotted as a function of ϕ in Figure IV-87. The constants α_1 and β_1 are determined from a least-squares fit to the data.

$$\alpha_1 = -3.29\ (eV)^{-1}$$
$$\beta_1 = 27.4 \qquad (6)$$

The slope S is determined from the constant-work-function lines in Figure IV-86 and is plotted as a function of ϕ in Figure IV-88. The constants α_2 and β_2 are determined from a least-squares fit to the data.

$$\alpha_2 = -9.29 \times 10^2 \ °K/eV$$
$$\beta_2 = -2.95 \times 10^4 \ °K \qquad (7)$$

In order to evaluate this correlation, the experimental data was compared with the calculated values, using Equations 4, 6, and 7. Figure IV-89 shows that the experimental and calculated values are in agreement within 30 millivolts. The same data correlated by the T_E/T_R plots show a scatter of about 100 millivolts (Figure IV-90).

The reduction in the scatter of the data makes it possible to extrapolate the work function values with a higher accuracy. This work however should be considered as a preliminary effort and further work is required to arrive at an optimum correlation.

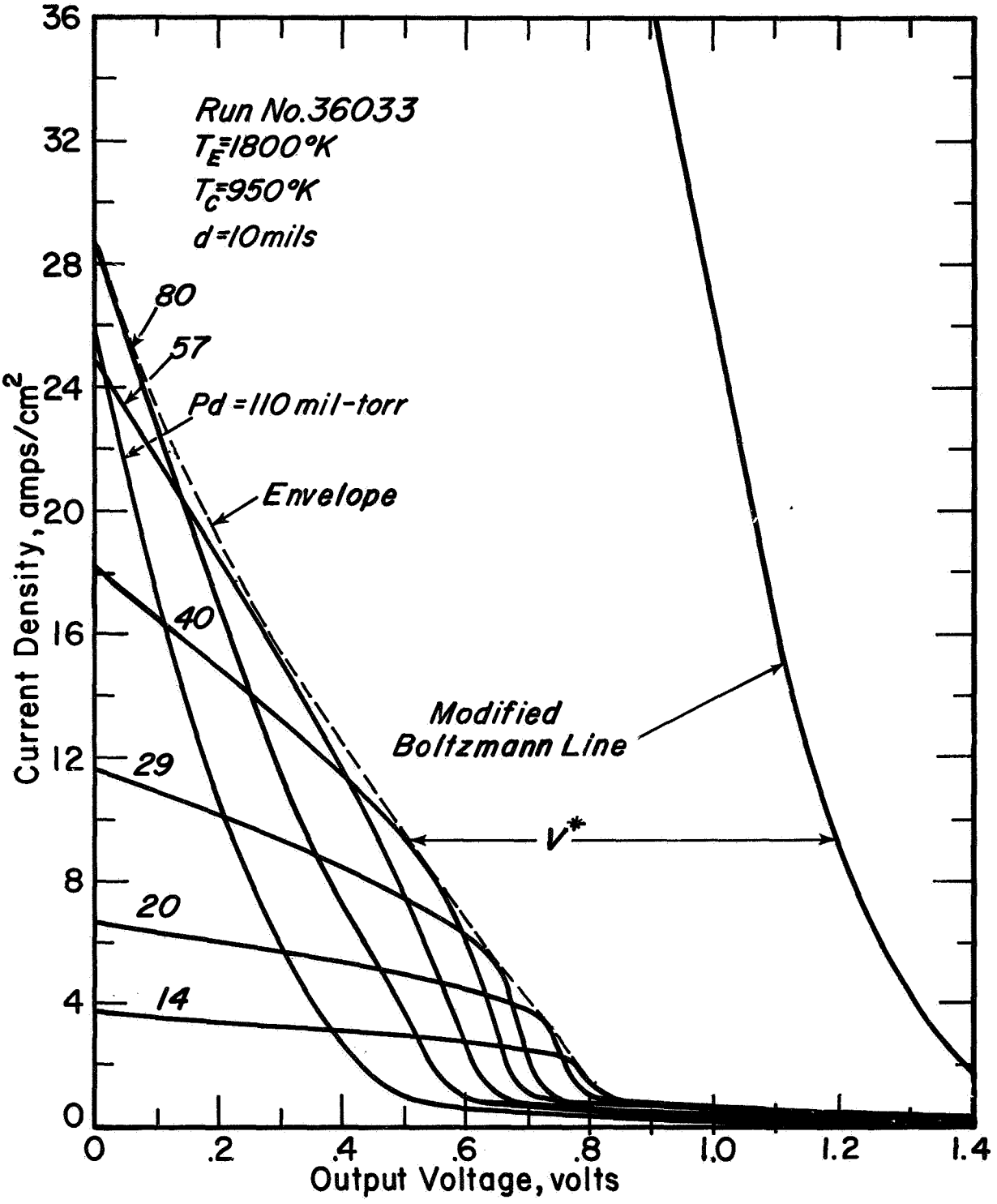

Figure IV-79. Cesium Family Illustrating Deviation from Ideal Performance.

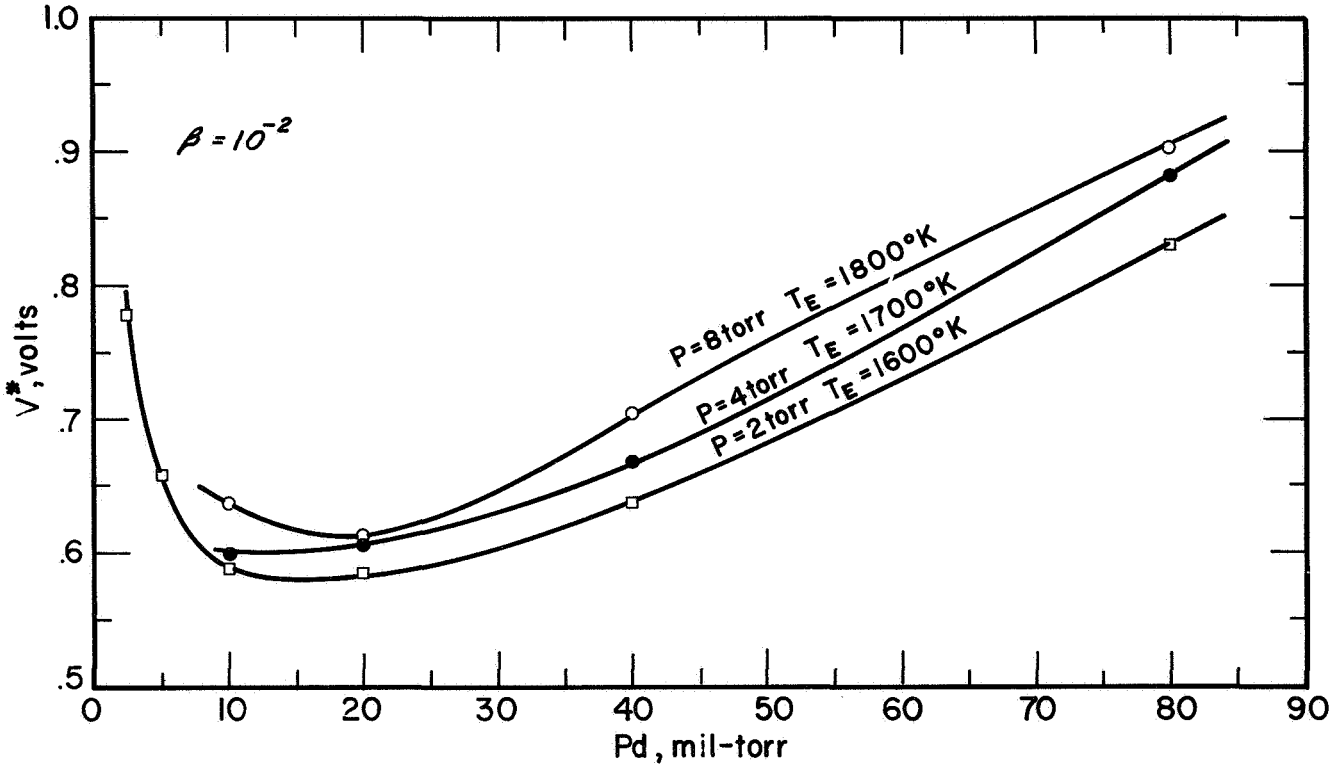

Figure IV-80 Voltage Loss Correlation for Several Cesium Pressures at $\beta = 10^{-2}$.

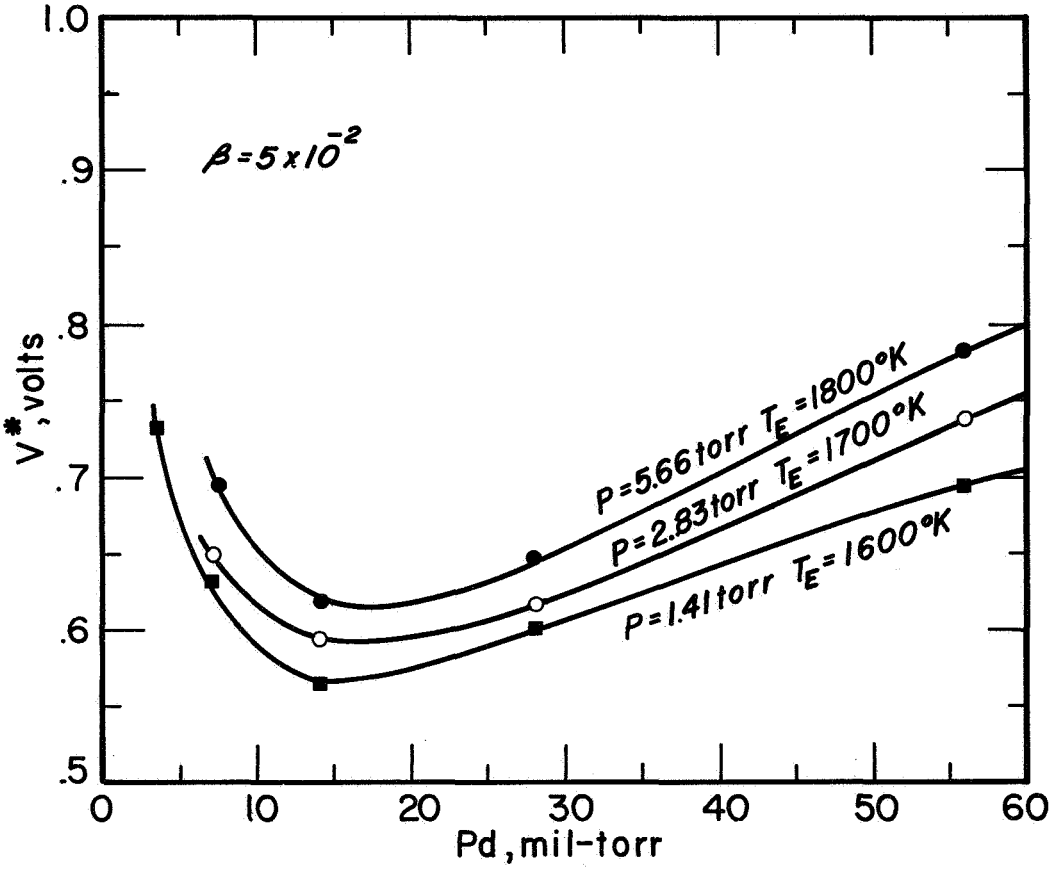

Figure IV-81. Voltage Loss Correlation for Several Cesium Pressures at $\beta = 5 \times 10^{-2}$.

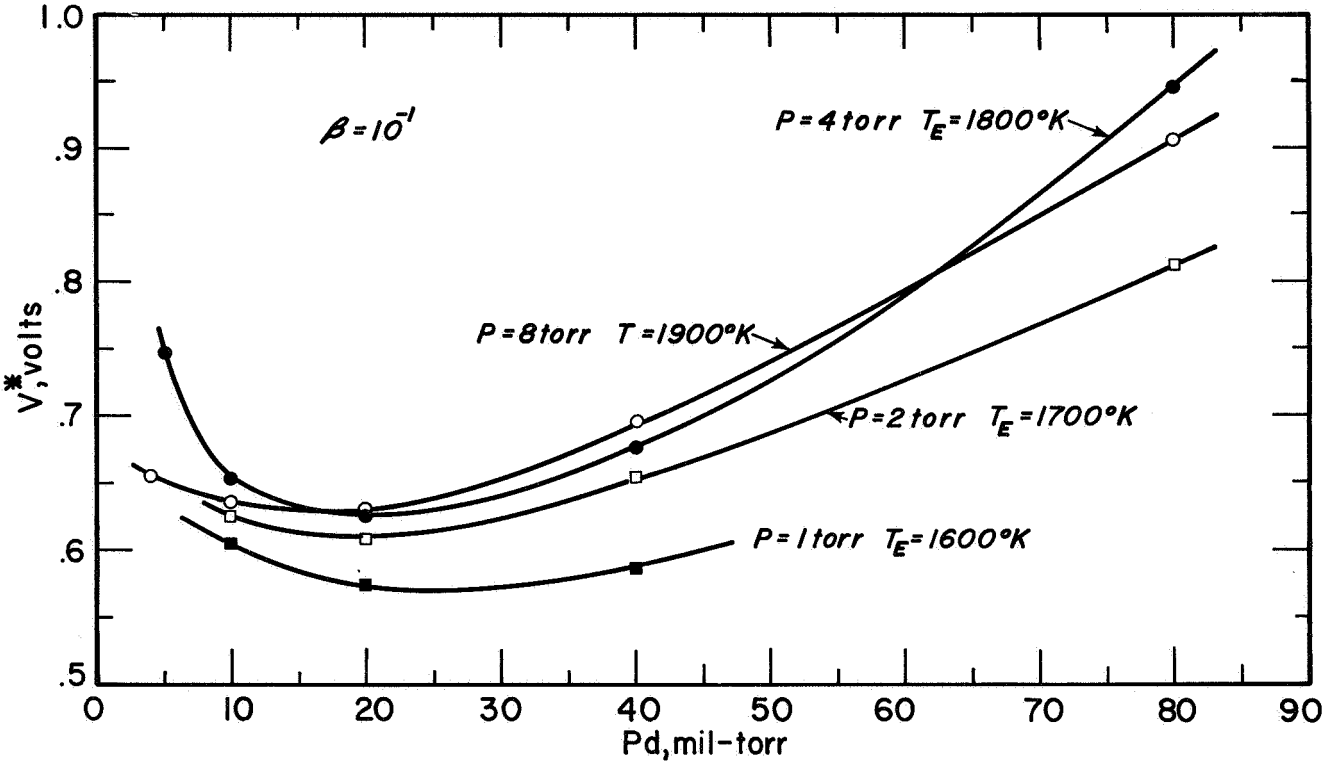

Figure IV-82. Voltage Loss Correlation for Several Cesium Pressures at $\beta = 10^{-1}$.

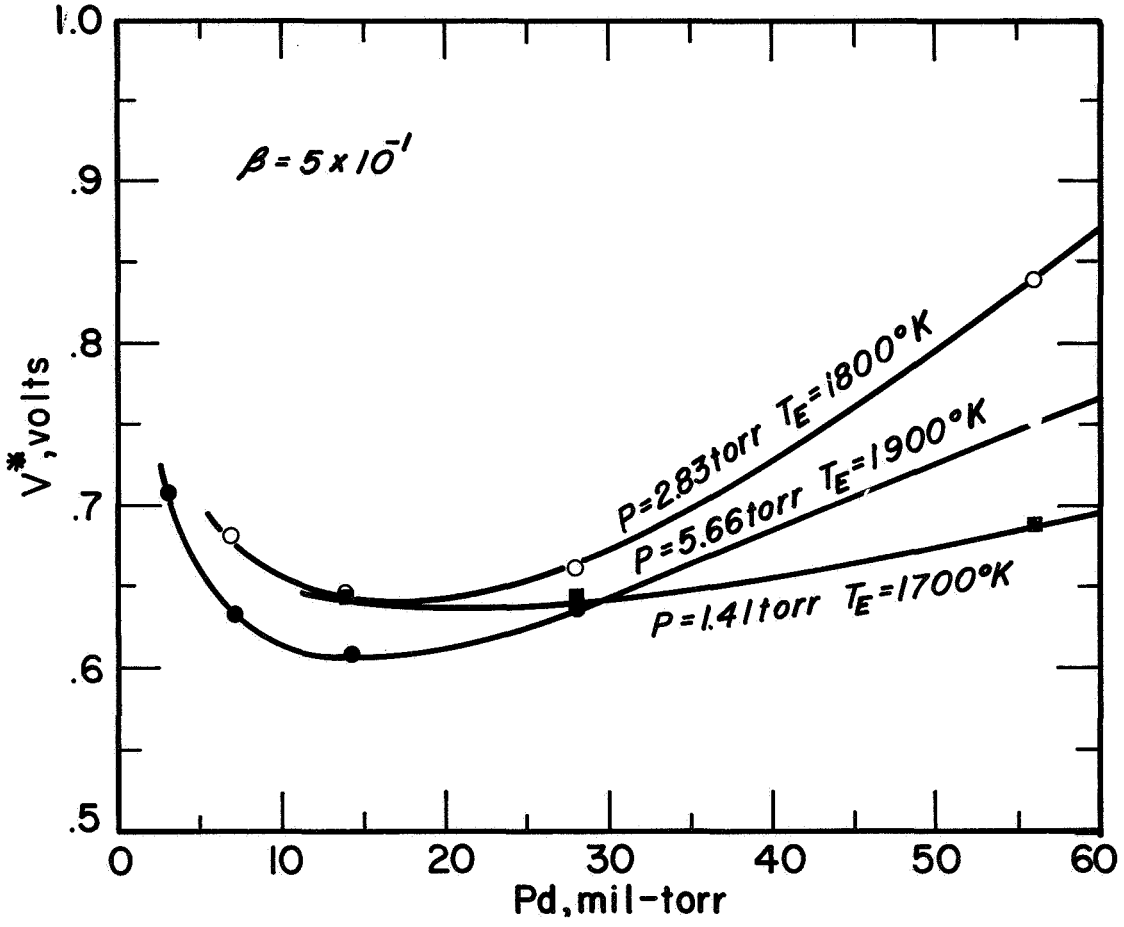

Figure IV-83. Voltage Loss Correlation for Several Cesium Pressures at $\beta = 5 \times 10^{-1}$.

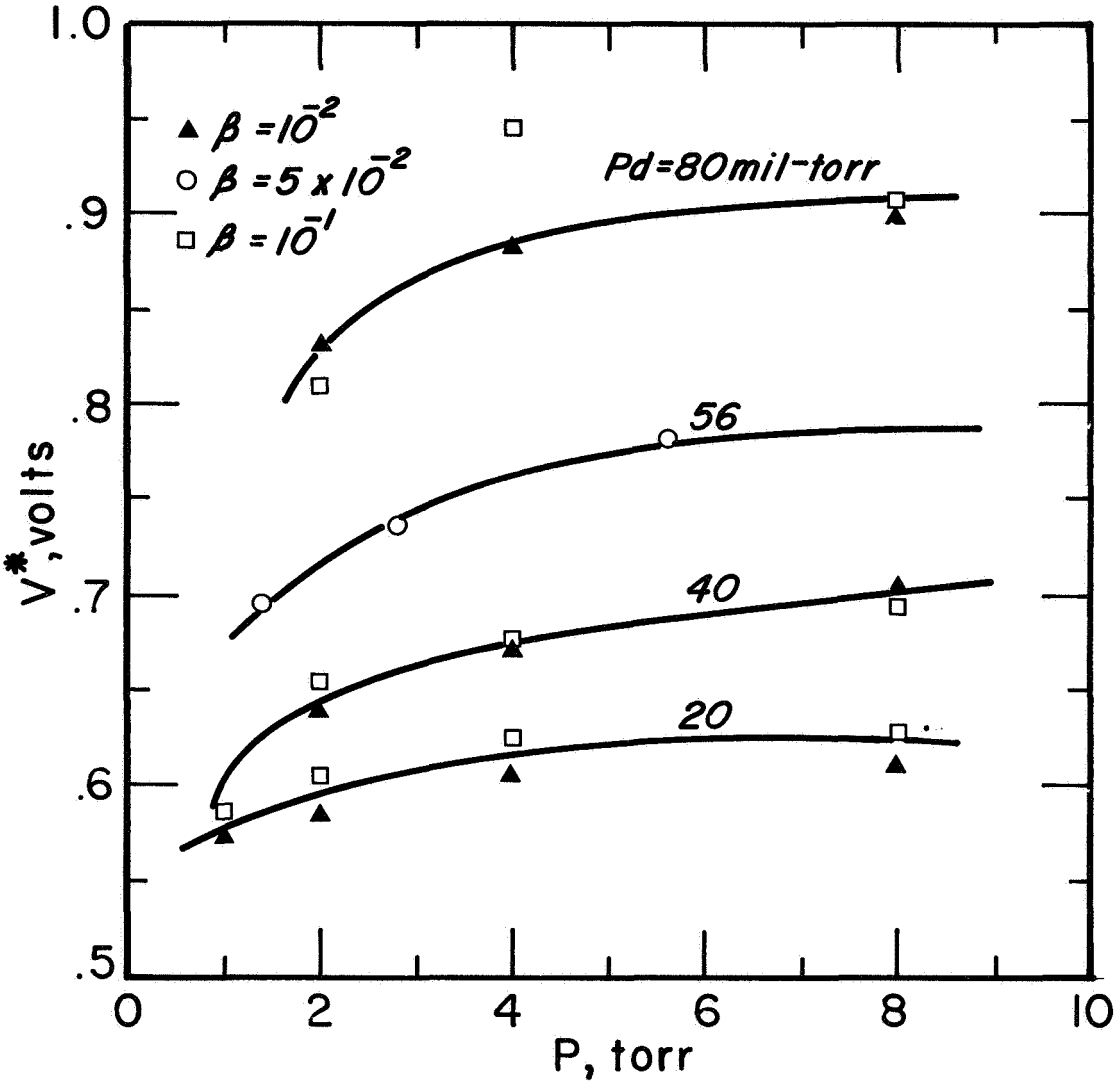

Figure IV-84. Dependence of V^* on Cesium Pressure and Ion Richness.

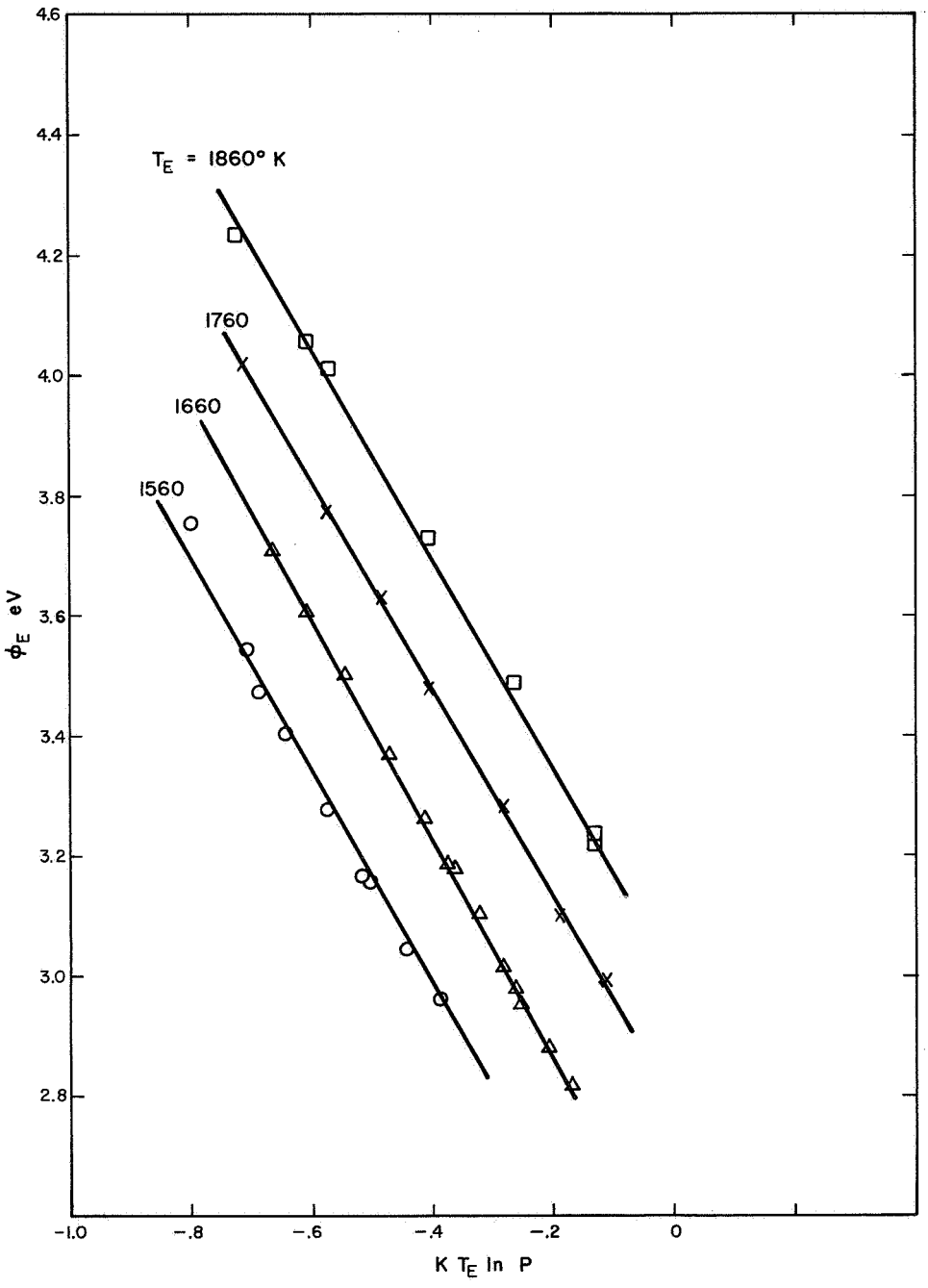

Figure IV-85. An Alternate Plot of Emitter Work Function Data for Various Emitter Temperatures.

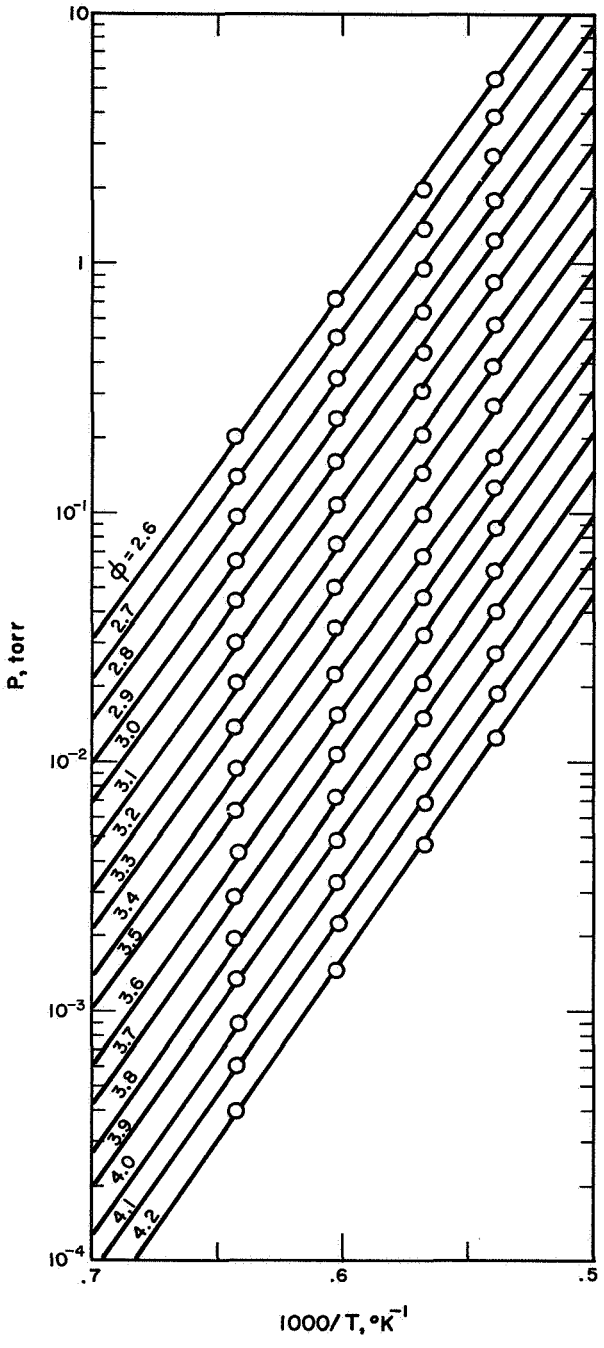

Figure IV-86. Cross-Plot of Figure IV-85.

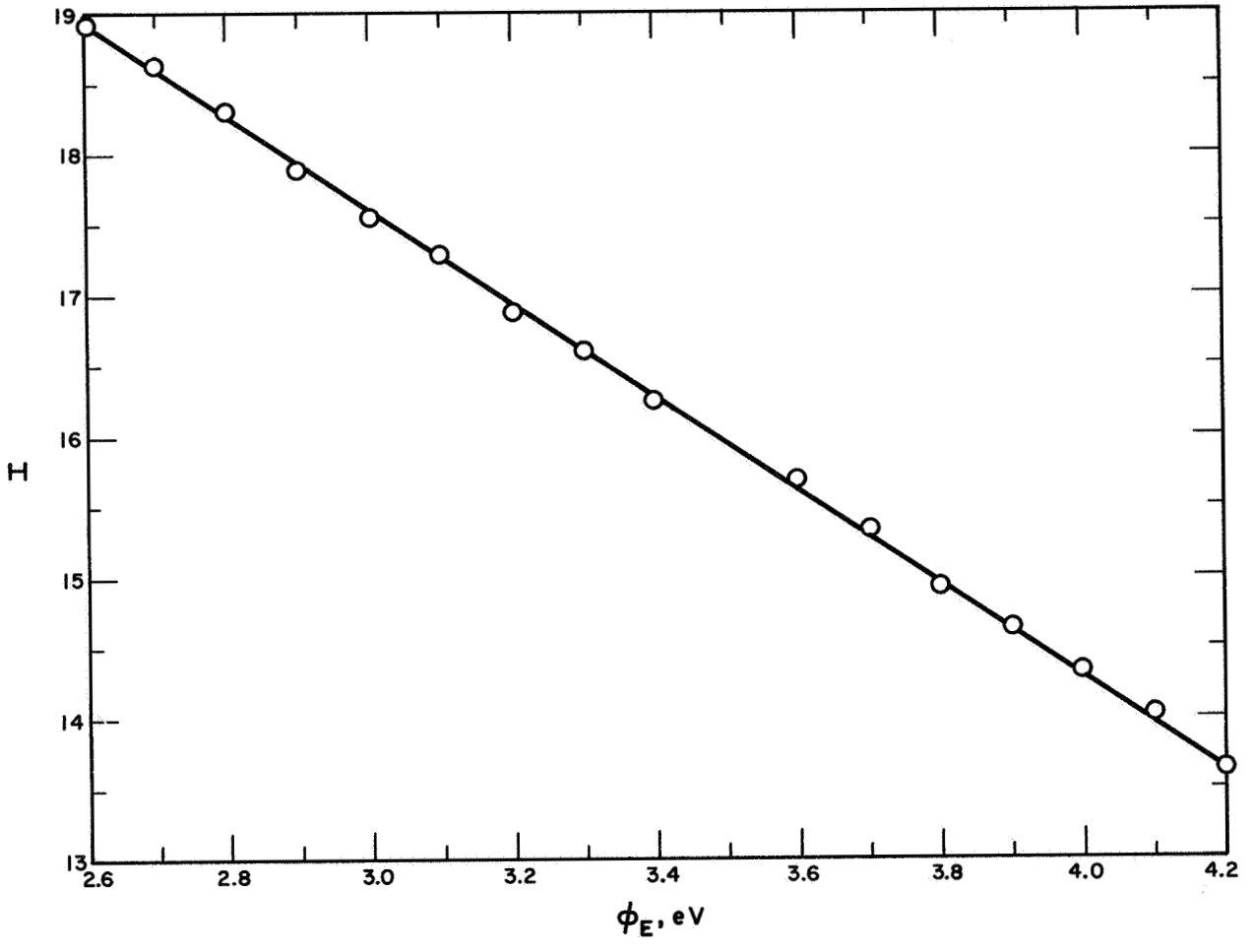

Figure IV-87. Parameter I Versus ϕ.

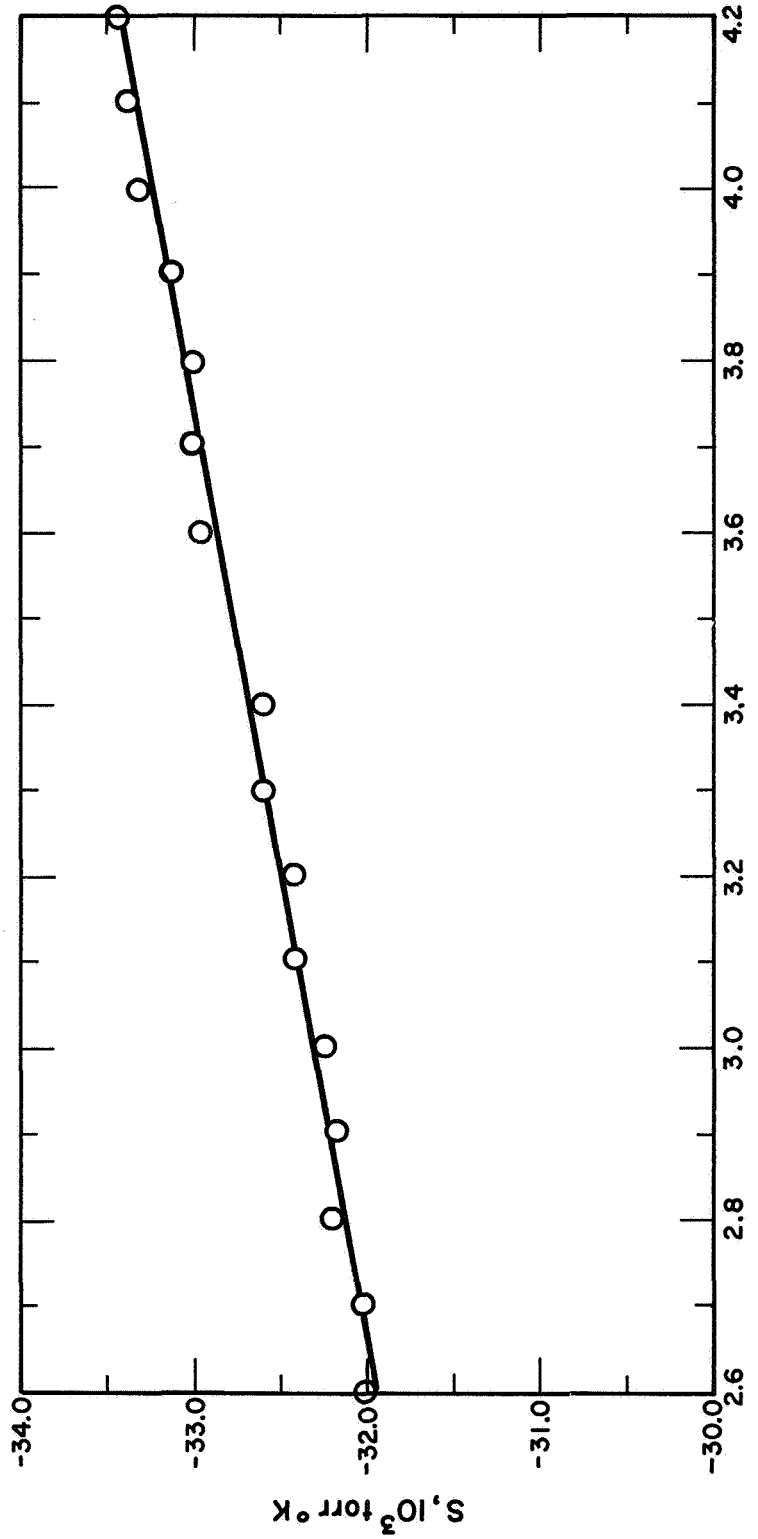

Figure IV-88. Parameter S Versus ϕ.

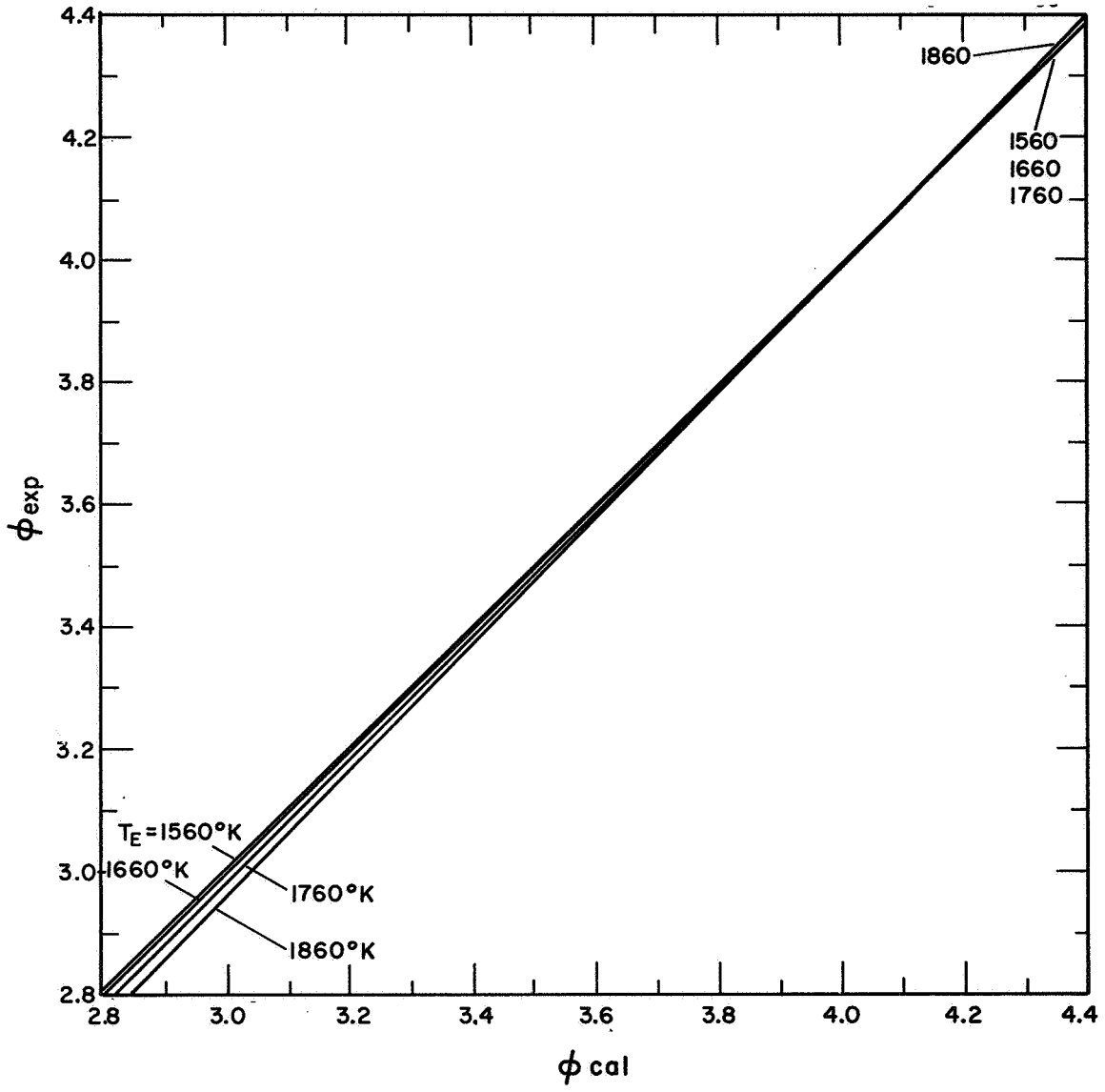

Figure IV-89. Comparison of Experimental and Calculated Values of Work Function.

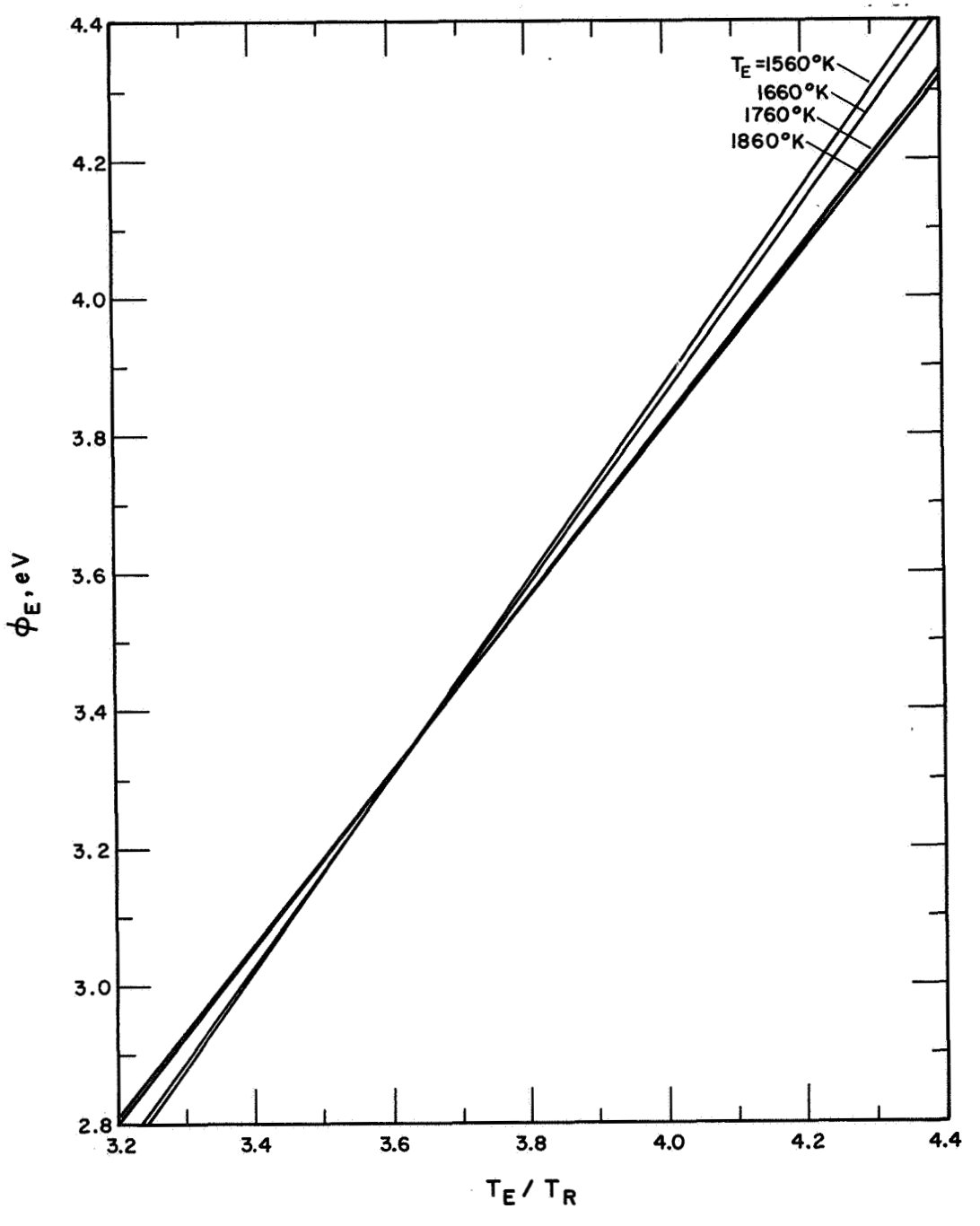

Figure IV-90. Experimental Values of Work Function Versus T_E/T_R Showing Spread.

REFERENCES FOR CHAPTER IV

1. C. C. Wang and J. J. Ward, "Performance of Chloride and Fluoride Vapor-Deposited Tungsten Emitters in Thermionic Converters," presented at the Thermionic Specialists Conference, Framingham, Massachusetts, October, 1968.

2. Hansen, L. K., "Anomalous Schottky Effect," Journal of Applied Physics, Volume 37, Number 12, November 1966, pp. 4498-4502.

3. Hansen, L. K., "Ion Current Effects in Cesium Diodes," Report on 25th Annual Conference on Physical Electronics, MIT, March 1965.

4. Wilkins, D. R., "An Improved Theoretical Description of Thermionic Converter Performance Characteristics, Report on 27th Annual Conference on Physical Electronics, MIT, March 1967.

5. Bullis, R. H., et al., "The Plasma Physics of Thermionic Converters," presented at the Thermionic Specialists Conference, San Diego, California, October, 1965.

6. S. Kitrilakis, D. Lieb, F. Rufeh and L. van Someren, "Final Report, Thermionic Research Program," Report No. TE12-67, for the Jet Propulsion Laboratory, August 1966.

7. L. Yang, "Studies of Thermionic Materials for Space Power Applications," Quarterly Report for the Period 1 March 1966 to 31 May 1966, General Atomics, Inc., GA 7244-NASA CR 72043, p. 25.

8. S. S. Kitrilakis and J. H. Weinstein, "Second Annual Technical Summary Report for the Thermionic Emitter Materials Research Program," Report No. TE27-64, for the Office of Naval Research, September 1963.

9. A. Shavit and S. S. Kitrilakis, "Report on the Effect of Electrode Configuration on Thermionic Converter Output Characteristics," Report No. TE7-65, for the Air Force Cambridge Research Laboratories, March 1964.

10. "Final Report, Research in Thermionic Conversion," Report No. TE 4072-49-68, for NASA, September 1967.

CHAPTER V

STUDIES ON VAPOR-DEPOSITED TUNGSTEN EMITTER MATERIALS

L. van Someren

Increasing interest in vapor-deposited tungsten for emitters has led us to study certain aspects of the physical metallurgy of commercially available forms of this material. The micro-structure and its response to heat treatment have been examined, and the preferred orientation has been examined quantitatively by X-ray diffraction methods.

Material was supplied by San Fernando Laboratories, Inc., California, in the form of square tubes made by deposition onto one-inch-square molybdenum mandrels. A deposit about 0.2 inch thick was made, and then the mandrel was dissolved in an acid etch solution. After receipt at Thermo Electron, each tube was slit longitudinally at the corners to produce four strips of flat material about an inch wide. Discs were then cut from these strips by spark-machining. In some cases a flat was ground at the edge of the disc, and the flat, together with areas of the plane surfaces of the disc, was prepared for metallography by electropolishing in dilute sodium hydroxide solution and etching with alkaline ferricyanide solution. The uppermost surface of the deposit was ground flat in some but not all cases.

Emission-spectroscopic examinations were carried out on the as-received fluoride and chloride material, and they gave the following results for metallic impurities in parts per million:

	10 to 100	1 to 10	0.3 to 3	0.1 to 1 ppm
Chloride	Si	Cu	Fe Ni Mo	Mg
Fluoride	–	Si Mo	Cu	Mg

Thus the chloride material was probably better than 99.995% pure W, and the fluoride better than 99.998% pure, excluding gases and interstitials.

A. FLUORIDE MATERIAL

1. As-Received

The surface of the material next to the mandrel is a close replica of the mandrel surface. It bears visible traces of the grinding marks on the mandrel, but is quite smooth. The grain size is about 5 μ (40,000/mm^2). A longitudinal cross section of the deposit (Figure V-1) reveals well-defined columnar grains several millimeters long growing from a thin layer of small equi-axed (randomly oriented) grains at the mandrel surface. The grain diameter increases with deposit thickness, as some grains grow in diameter at the expense of their neighbors. However, small new grains sometimes occur. The upper surface of the deposits (0.2 inch thick) is confused and rough on a scale large compared with the depth of focus of an optical microscope, so that it is not possible to photograph it. However, the grain size can be determined if the material is lightly ground and then electropolished and etched. Figure V-2 shows a transverse section of the top surface prepared in this way, and reveals the wide range of grain sizes present. Excluding the smallest grains, the average size is about 70 μ (200/mm^2), implying a change in linear grain dimensions by a factor of 15 or so

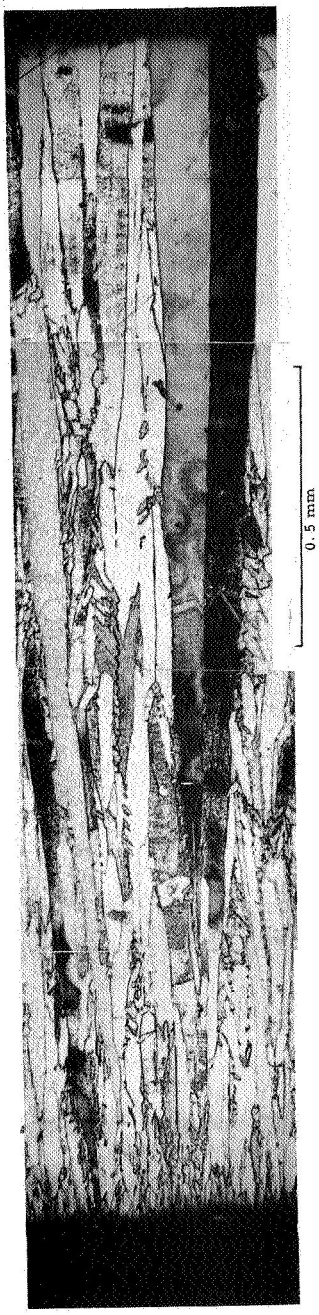

Figure V-1. Cross Section of Deposit from Tungsten Hexafluoride, as Received. WF.
(The scale for this figure applies to all other cross sections of this type.)

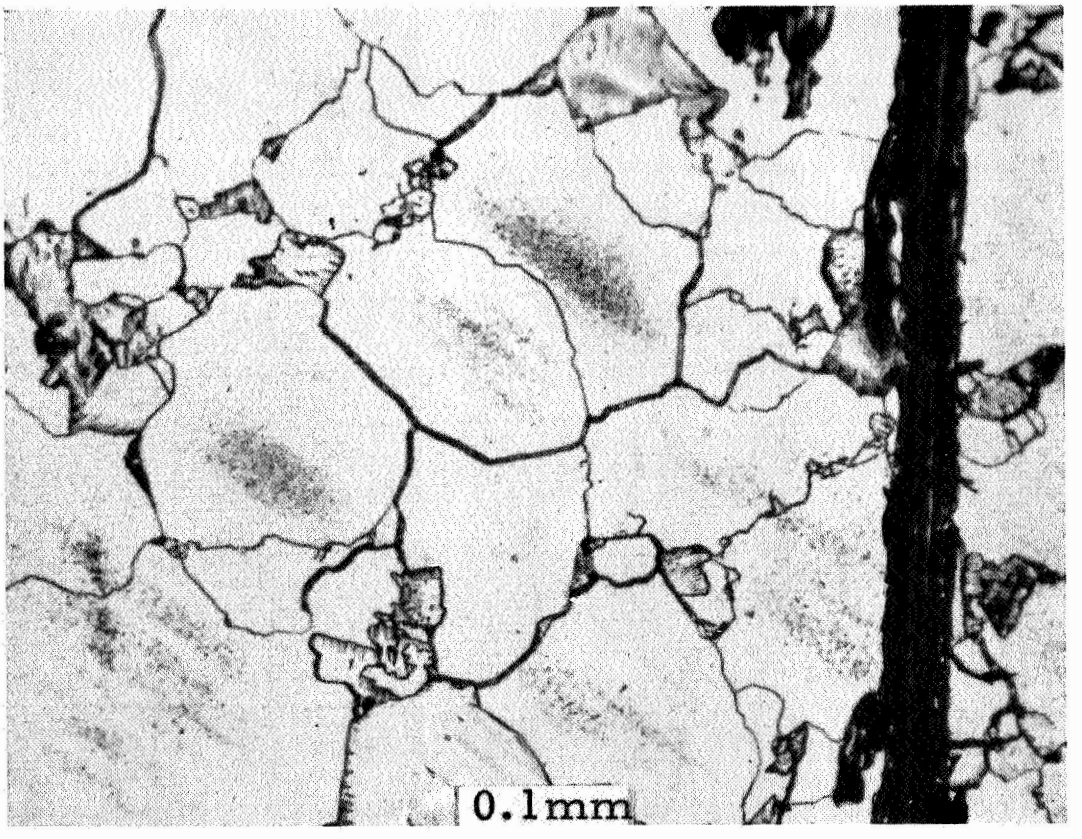

Figure V-2. Top Surface of Deposit Prepared to Show Grain Size. WF2A.

between the two surfaces of the deposit. It seems that the change occurs most rapidly at the start of the deposit. At the mid-plane the grain size is closer to that at the top than to that at the bottom.

The grains are unusually irregular in comparison with material formed by more conventional methods. Grain boundaries are highly angular when examined in both longitudinal and transverse sections. They do not show the tendency to form smooth curves meeting at triple points found in annealed material.

Figure V-3 shows a discontinuity in the grain structure near the mid-plane (just visible in Figure V-1). Total interruption of deposition usually results in the nucleation of a complete new set of grains when deposition is restarted: in the present case the grains continue across the interruption, so this discontinuity may have been caused by a minor perturbation in the environment during growth.

The material was quite brittle in tension (for example, under a hammer blow), but no samples have been broken by a drop from the bench to the floor. Preferred-orientation studies are described below.

2. Heat Treatment

Various specimens were heated by electron bombardment in a cold-walled furnace evacuated by a Vac-Ion pump to a pressure in the range of 10^{-5} to 10^{-7} torr. This technique is well established, and it has been shown that no contamination of the specimen occurs. Specimen temperatures were measured with an optical pyrometer sighted on the surface; a correction was applied to the observed reading, assuming the specimen emissivity was 0.4.

Composite photographs of the cross section of specimen WF2 before and after heat treatment are shown in Figures V-4 to V-7. These photographs show (4) the initial appearance, and the appearance of the same surface after exposure to (5) 6 hours at 2000°C and (6) 1 hour at 2400°C, and (7) the appearance after repolishing and etching the latter surface. Figure V-4 is very similar to Figure V-1, and together they indicate the variation in initial microstructure between samples. Figure V-5 shows the coalescence of some groups of small irregular grains, and the lessening of contrast between grains as the etched surfaces became smoothed by heat treatment. Signs of new grain boundaries are visible to the bottom of the deposit (near the reference scratch). The more intensive heat treatment, 1 hour at 2400°C, prior to Figure V-6 produces further coalescence of grains, rounding of individual grains, and development of new boundaries near the bottom of the deposit. These are more clearly revealed in Figure V-7, which shows that the large number of columnar grains present within 0.2 mm of the bottom of the deposit has been replaced by a smaller number of non-columnar grains there. However, in the rest of the thickness of the material the grossly columnar structure is retained; while the irregular groups of grains have been lost, some angularities at boundaries have become smoothed, and some columnar grains have coalesced without loss of orientation. Figures V-8 and V-9 are of specimen WF2, and show the top of the deposit in the as-received condition and after the two heat treatments. The former, Figure V-8, shows the irregularity of grain outlines and the wide range of grain sizes, and the latter, Figure V-9, confirms the conclusions from sections of the material such as Figure V-7. The small grains have been absorbed by the larger ones, with only slight changes in the mean

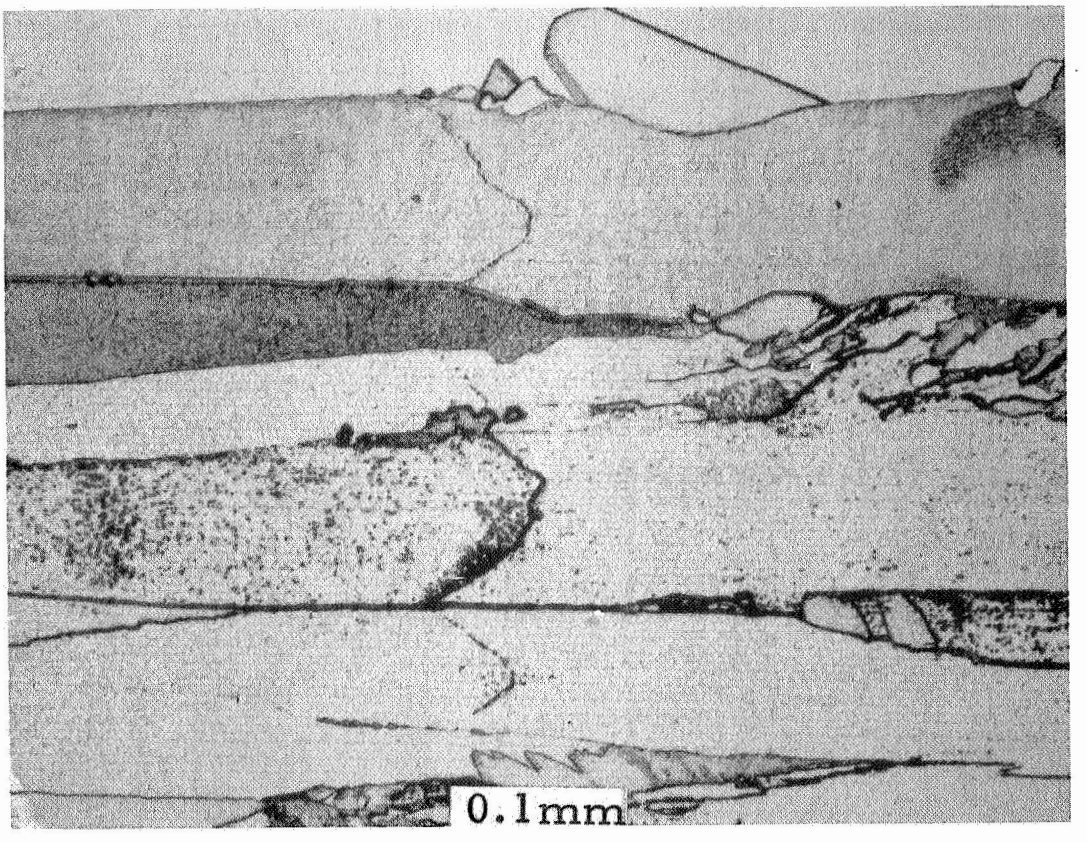

Figure V-3. Detail of Discontinuity in Middle of Deposit Thickness. WF.

68-R-4-10

Figure V-4. Cross Section, as Received. WF2A.

68-R-4-11

Figure V-5. Cross Section After 6 Hours at 2000°C. WF2B.

68-R-4-12

Figure V-6. Cross Section After 6 Hours at 2000°C and 1 Hour at 2400°C. WF2C.

68-R-4-13

Figure V-7. Cross Section After 6 Hours at 2000°C and 1 Hour at 2400°C, Repolished and Etched. WF2C.

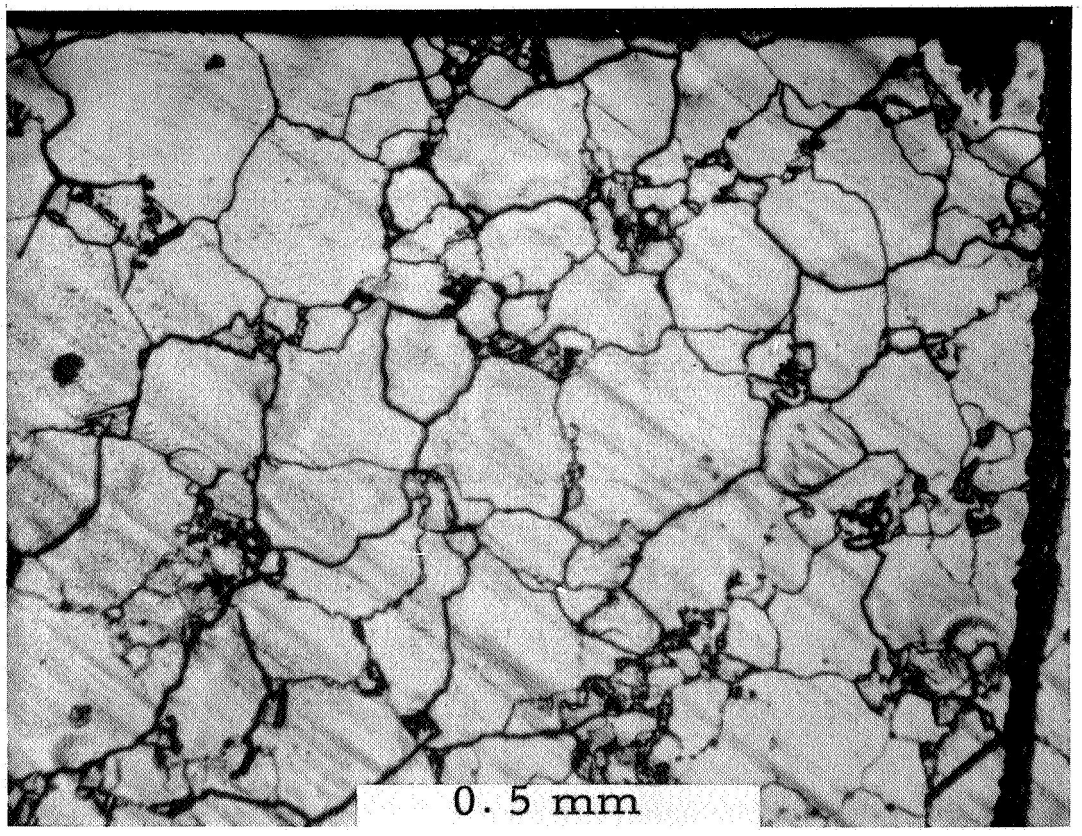

Figure V-8. Top of Deposit as Received, Ground, Polished, and Etched. WF2.

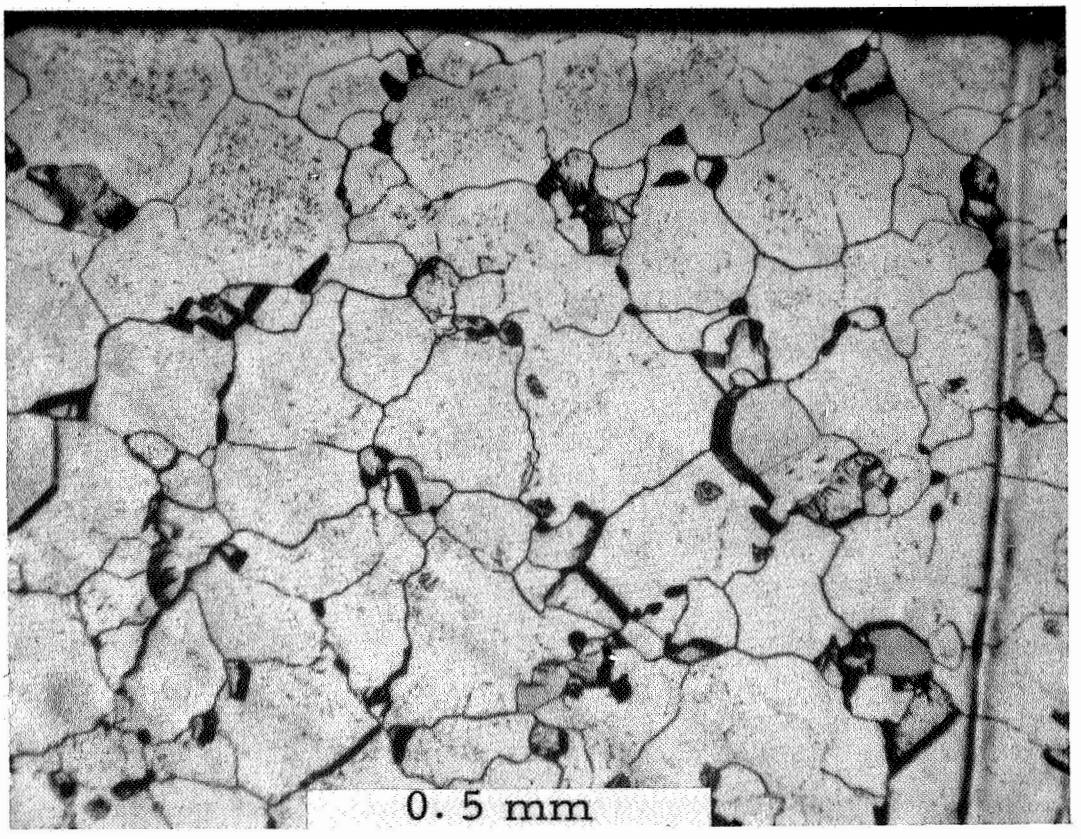

Figure V-9. Top of Deposit, After 6 Hours at 2000°C and 1 Hour at 2400°C, Repolished and Etched. WF2C.

grain size, and some smoothing of the irregular boundaries of the large grains has occurred. The effect of a more intensive heat treatment, 6.5 hours at 2600°C, is shown in Figure V-10, a cross section after repolishing. Here one grain runs through almost the whole thickness of the specimen, except for a narrow (less than 0.5 mm) layer of grains at the top surface of the deposit. This sample had the top surface ground before this heat treatment.

The effect of milder heat treatments, such as might be used in preparing an emitter for operation, is shown in Figures V-11 and V-12 for specimens heated 20 minutes at 1900°C and 6 hours at 1800°C. The structure is changed relatively little from that found in the as-received material.

Sample WF3 was subjected to heat treatment for 6 hours at 2400°C, and the resulting grain structure showed a change at the discontinuity near the center of the deposit (Figure V-13). The grains at the bottom of the deposit showed grain growth and smoothing of grain boundaries, as expected, but in certain regions of the specimen, including that shown in Figure V-13 the upper part of the deposit showed massive grain growth to give grains with dimensions of a few millimeters. These grains terminated at the discontinuity near the middle of the deposit.

Sample WF4 was subjected to successive heat treatments, each at 1800°C, for 6 hours, 6 + 24 = 30 hours, and 6 + 24 + 70 = 100 hours. Cross sections at each stage are shown in Figures V-14, -15 and -16. While the first two figures cover the same area, it was not possible to identify this area after 100 hours, owing to changes in the grain structure. The difference in contrast between grains in the latter figures is due to differences in etching techniques.

68-R-4-16

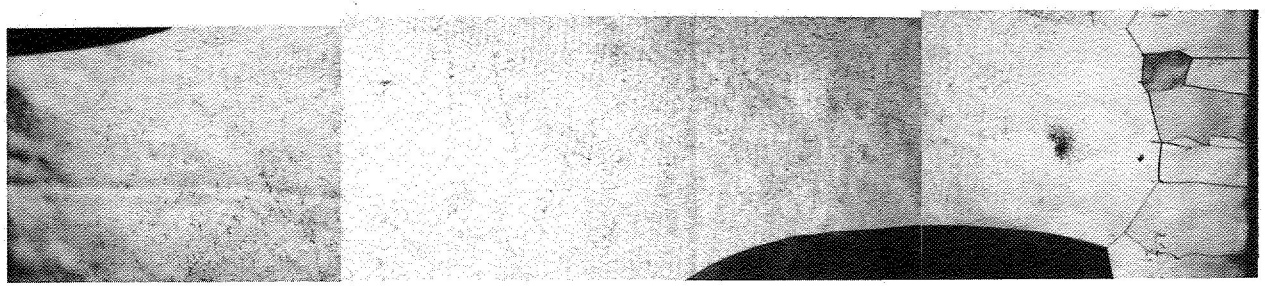

Figure V-10. Cross Section After 6.5 Hours at 2600°C, Repolished and Etched. WF7C′.

68-R-4-17

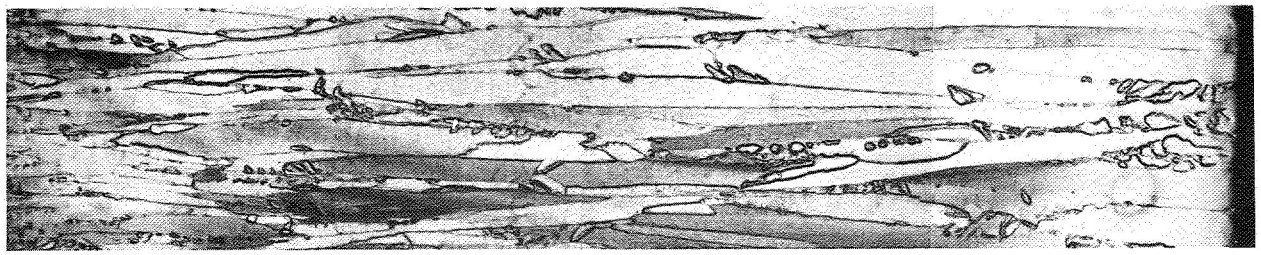

Figure V-11. Cross Section After 20 Minutes at 1900°C, Repolished and Etched. WF5.

68-R-4-18

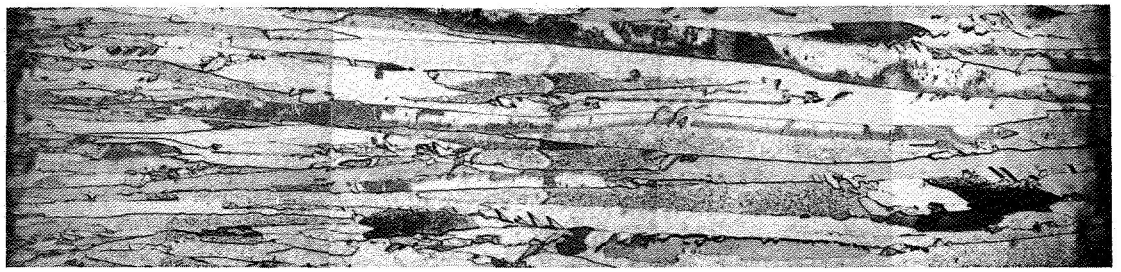

Figure V-12. Cross Section After 6 Hours at 1800°C, Polished and Etched. WF4.

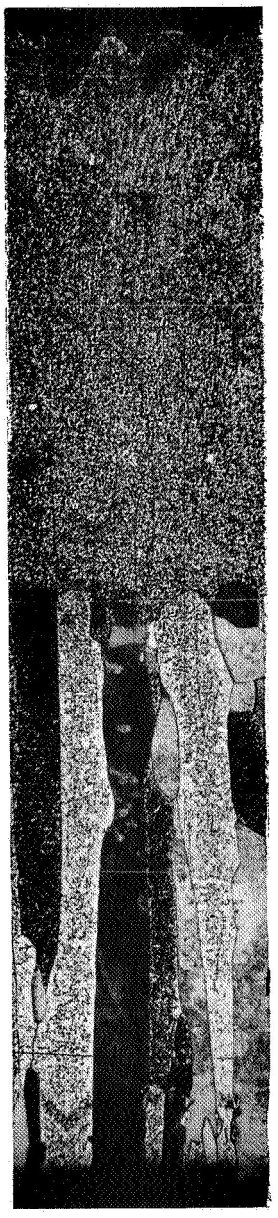

Figure V-13. Cross-section of sample WF3B' after 6 hours at 2400°C.

68-R-6-59

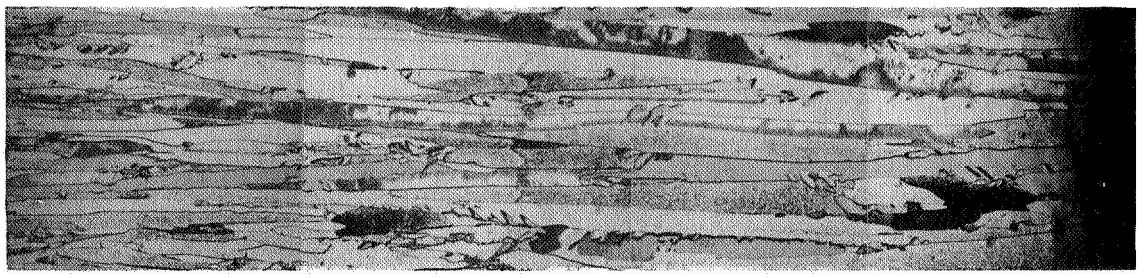

Figure V-14. Cross section of sample WF4B' after 6 hours at 1800°C.

68-R-6-60

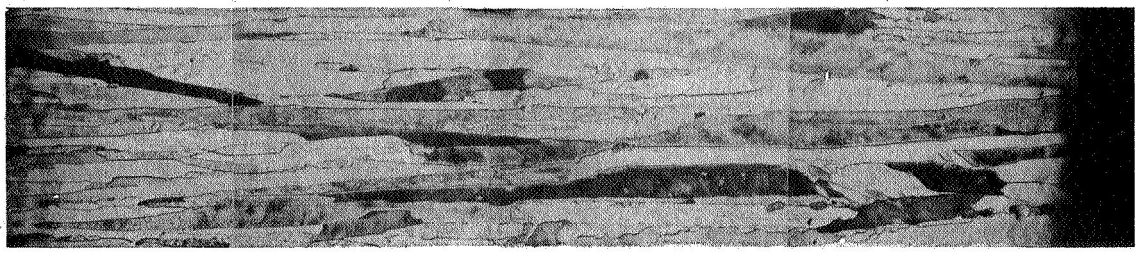

Figure V-15. Cross section of sample WF4C' after 30 hours at 1800°C.

68-R-6-61

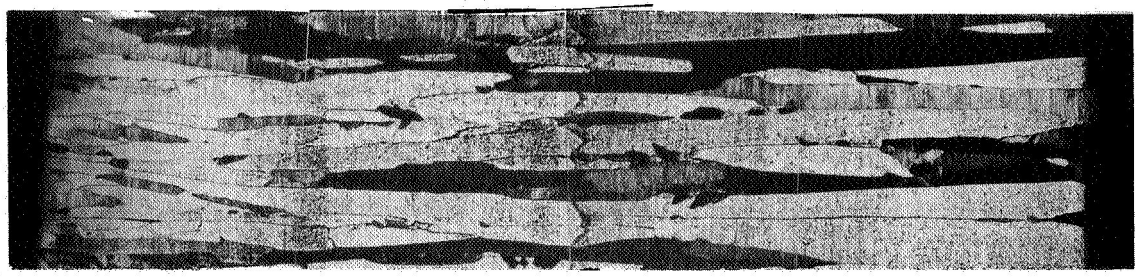

Figure V-16. Cross section of sample WF4D' after 100 hours at 1800°C.

Grain growth has continued to occur during the heat treatment, accompanied by the elimination of some of the angularities along the grain boundaries. Comparison of Figure V-4 with Figure V-1 indicates that further grain growth does occur in specimens exposed to higher temperatures. It is not clear whether the configuration in Figure V-4 would change further at 1800°C or would require a higher temperature to initiate further changes.

B. CHLORIDE MATERIAL

1. As Received

This material is deposited at a higher temperature than the fluoride material, and because of technical problems associated with this temperature, two shorter square tubes were supplied in place of the single long tube of fluoride material. The deposit surface appears slightly smoother to the eye and to the touch than does that of fluoride material.

Cross sections revealed gross differences between the two techniques. While the fluoride deposits contained some grains running through the whole thickness of the deposit, the chloride material was composed of layers varying in thickness and grain size. In each deposit, nominally 0.2 inch thick, there were 11 distinguishable discontinuities, varying from gross porosity (#9) or layers of foreign material (#2) to simple renucleations of the deposit (#10 and #11) or mere lines (#7). Cross sections of each of the two ingots are shown in Figures V-17 and V-18 with the discontinuities numbered. Though the ingots were made and shipped at different times, there are similar types of discontinuities at similar positions in the deposits.

68-R-4-18

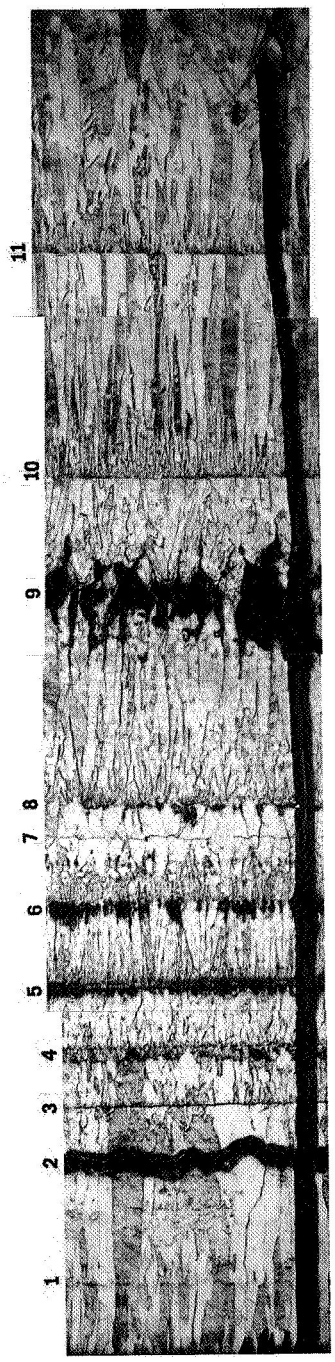

Figure V-17. Cross Section of Deposit from Tungsten Chloride, as Received. 1WC.

68-R-4-19

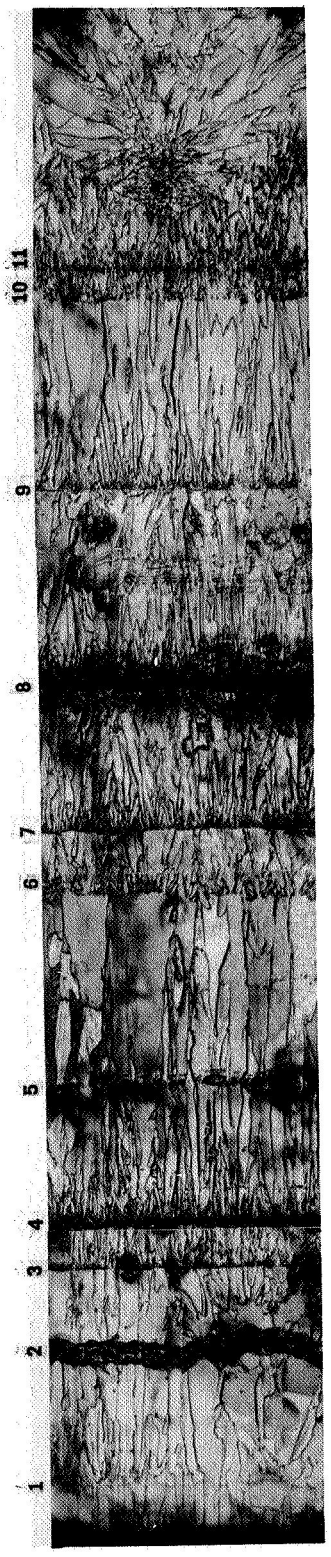

Figure V-18. Cross Section of Deposit from Tungsten Chloride, as Received. 2WC.

In the course of preparing samples for metallography the following curious observation was made: a specimen was electropolished (5% NaOH, 10 volts), and when the cross section was rinsed and pressed on a paper towel to dry it, a liquid with a distinct blue color oozed from #9 in the middle of the deposit and left marks on the towel. Under the microscope more liquid could be seen oozing from the pores near the middle of the deposit, and in fact it proved difficult to eliminate this effect.

About two-thirds of the way up through the deposit No. 2 (Figure V-18) is a region between #8 and #9 showing a continuous grain structure with layers of varying etch response. Detailed examination revealed several of these striated regions, in some cases associated with porosity (Figure V-19) and in some cases not (Figure V-20). This appearance resembles that reported for Federite, a non-equilibrium structure found in W-Re alloys made by vapor deposition.

The first layer of conspicuous material in the deposit, #2, is found about 0.7 mm from the bottom of the deposit, and is clear in Figures V-17 and V-18. A detail of this zone in ingot 2 after electropolishing (without etching) is shown in Figure V-21. Reference to Figure V-18 shows that the grain structure is continuous across this layer. The sharp contrast in electropolishing behavior strongly suggests that it is not pure tungsten. However, continued polishing removes the material (Figure V-22).

2. Heat Treatment

Specimens from ingot 1 WC of chlorine material were heat-treated in exactly the same way as the fluoride specimens discussed above. Two differences were noticed. During the first stages of heating

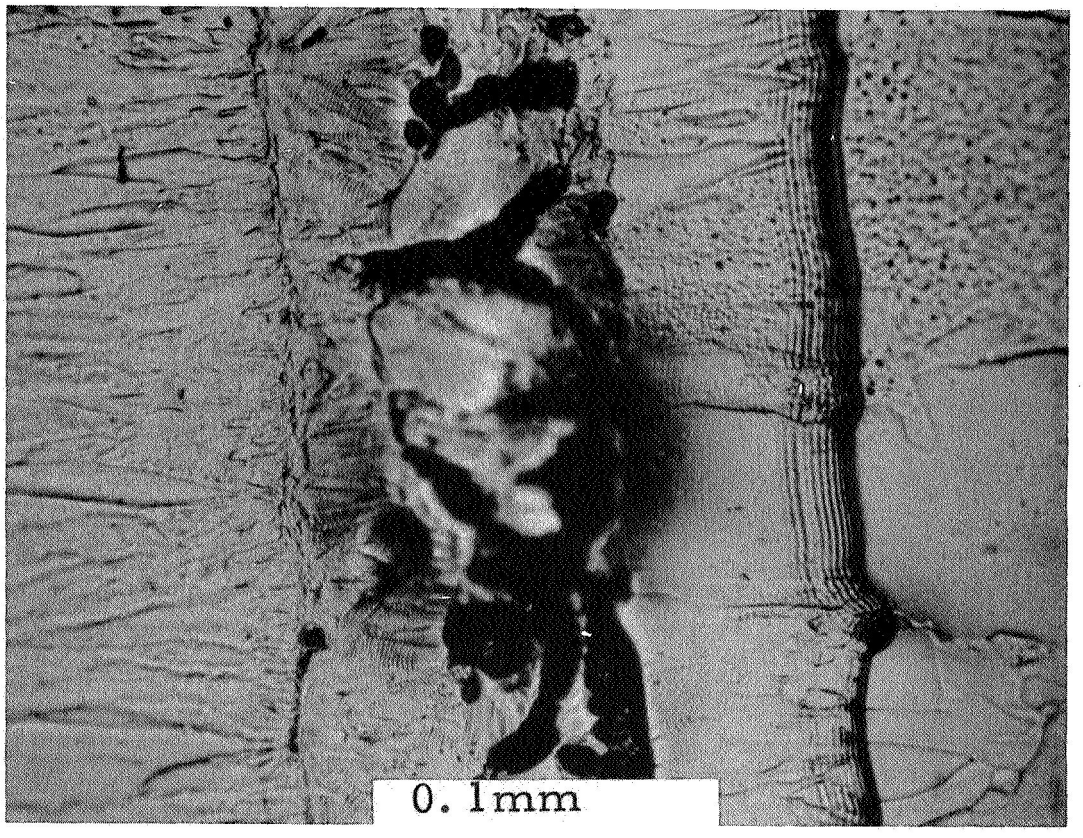

Figure V-19. Detail of Striated Zones Near Porosity in Ingot. 2WC.

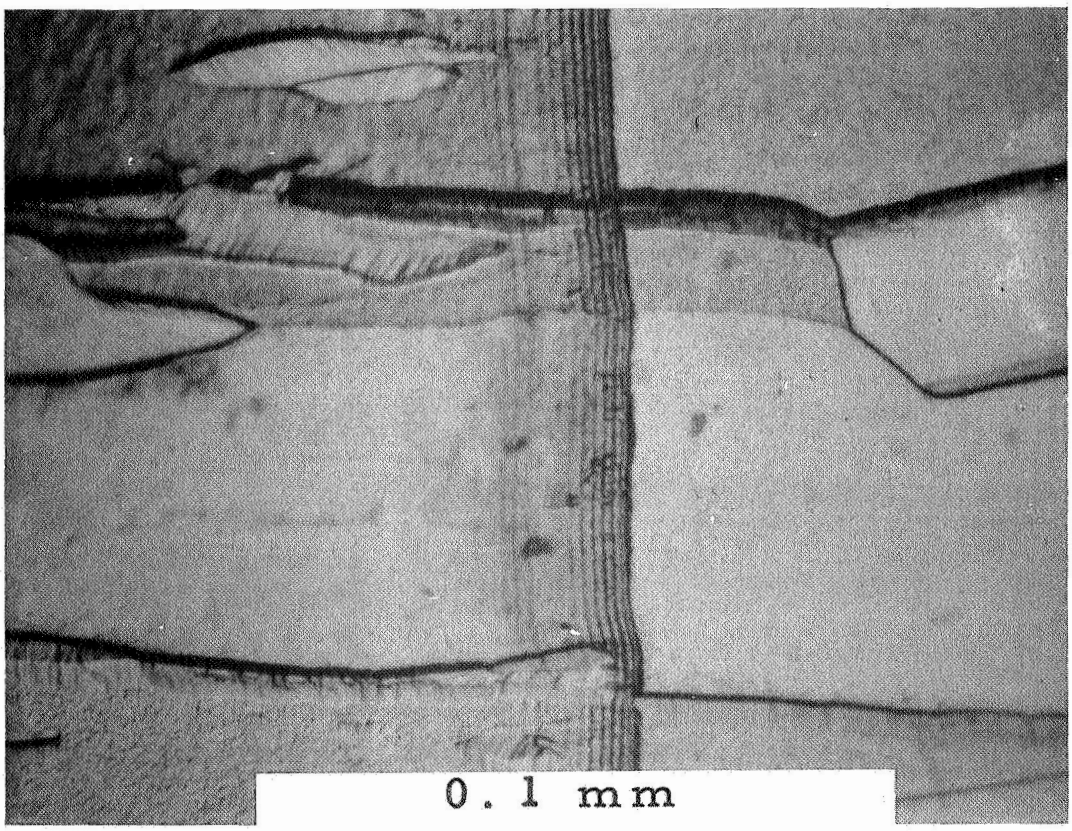

Figure V-20. Detail of Striated Zones without Porosity in Ingot 2WC.

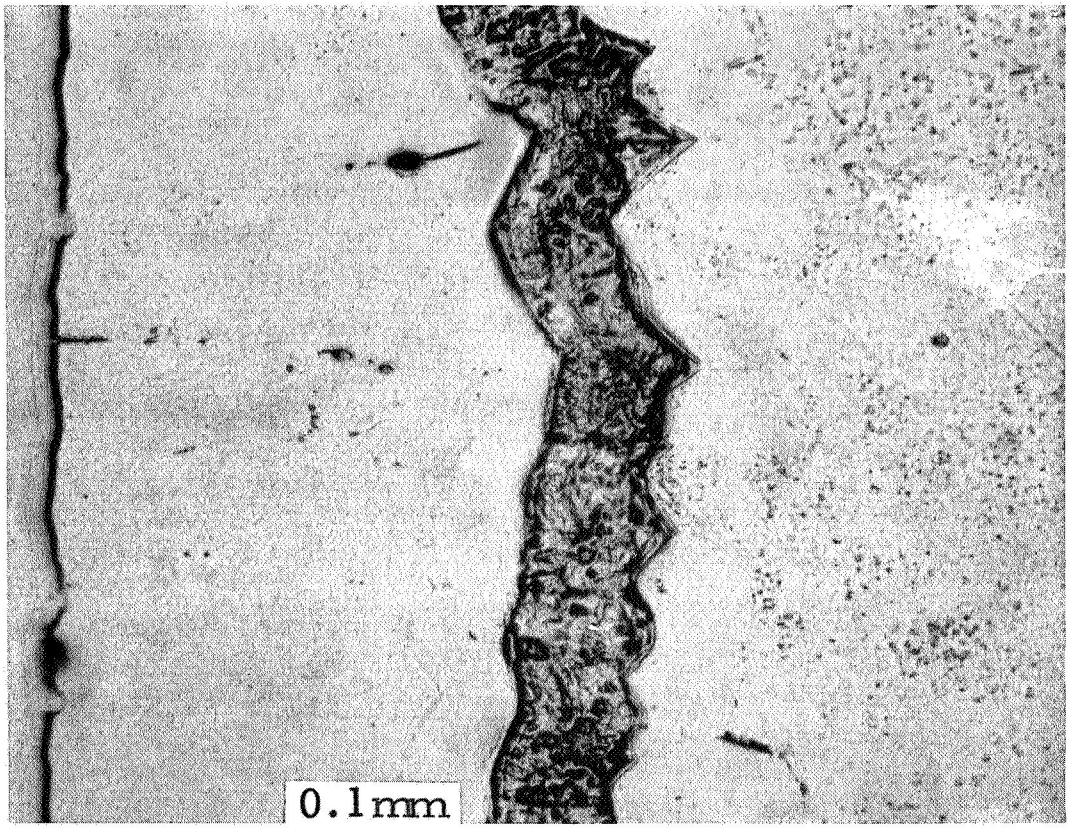

Figure V-21. First Foreign Layer, #2, Electropolished Only. 2WC.

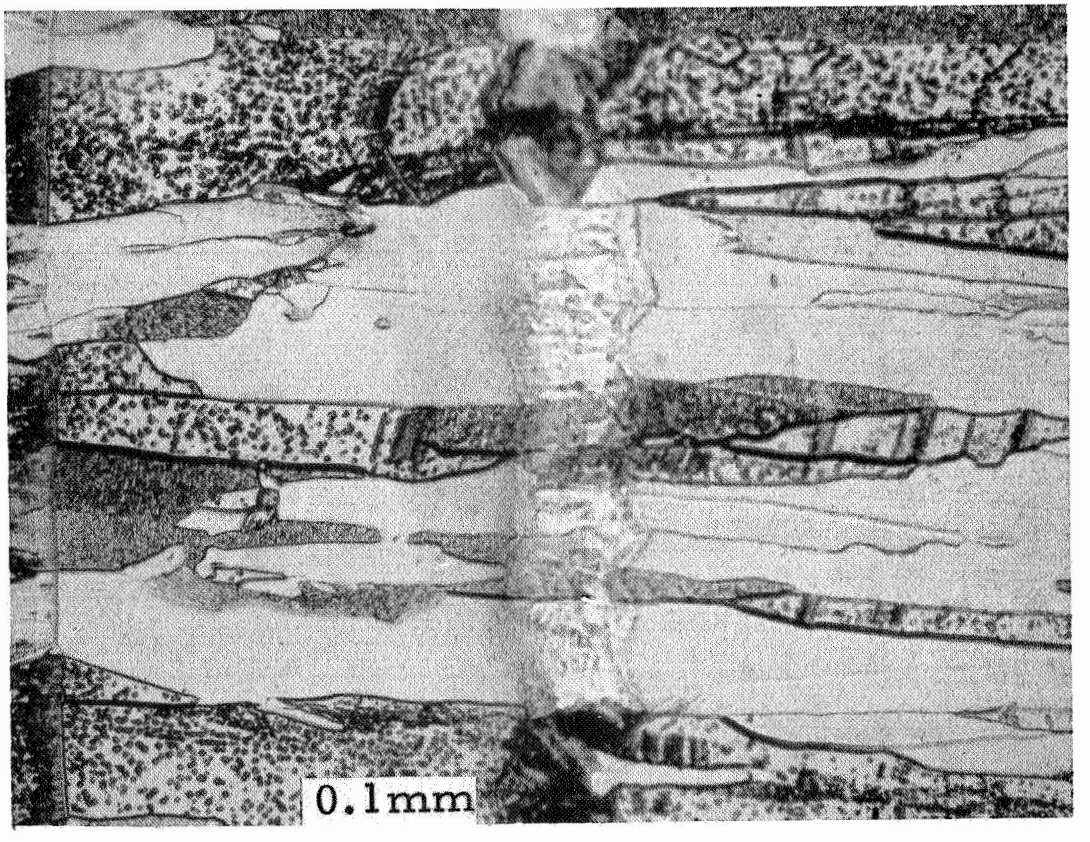

Figure V-22. Same Region After Prolonged Electropolishing.

the specimen from room temperature to red heat considerable outgassing occurred, and this limited the rate at which the temperature could be raised. Furthermore, during one run in which the specimen attained 2230°C, considerable evaporation occurred from the specimen while at temperature, and condensation on the bell jar seriously interfered with temperature measurement. Such evaporation did not occur when the specimen was at 2100°C, and does not occur from pure tungsten at 2230°C.

Specimens which were heat-treated showed progressive changes in the microstructure as follows:

After 6 hours at 1800°C considerable recrystallization has occurred; in some regions, Figure V-23, such as 0 to #2 and #10 to #11, the columnar structure is retained, while in others, such as #11 to the top surface and around #9, the grains adopt a more nearly equiaxed arrangement. While greater changes occur in the wider zones, the converse is not always true. Zones #4 to #5 and #5 to #6 are of nearly equal width, but show unequal changes in structure after this heat treatment.

Treatment for an hour at 2100°C developed the structure shown in Figure V-24, in which considerable further coarsening has occurred in some layers, #9 and #10, while others, such as #5 to #6, have changed little. The striations around #7 are seen in Figure V-25 to be bands of etch pits, rather than the layered appearance of Figures V-19 and V-20.

The corresponding views of the prepared surface of the top of the deposit are given in Figures V-26 to V-28, and show the striking loss of angularity of the grains during the mildest heat treatment, together with an increase in grain size.

Figure 30 shows the effect of exposure to 1 hour at 2230°C on the sample whose prior appearance is shown in Figure V-29. The layers seen here correspond to those in Figure V-17, though they differ in thickness.

Coarsening of the grain size has occurred to an extent which varies erratically between layers. The largest grain size is now found between #9 and #11, but, in contrast to Figure V-24, this coarse structure does not extend to the surface of the deposit. However, in Figure V-31 we see that more intensive treatment (1 hour at 2370°C) produces a large grain size from #9 to the surface. This also eliminates the layer of the material at #2 and produces porosity there and at other interfaces.

Specimen WC1 was subjected to heat treatment for 6 hours at 1900°C. Photomicrographs of cross sections before and after are shown in Figures V-32 and V-33. Massive grain growth has occurred, particularly in the outer layers which originally contained the longest columnar grains.

Specimen WC6 was subjected to heat treatment for 1 hour at 2000°C, and the resulting cross section is shown in Figure V-34. Grain growth has occurred to an extent similar to that in WC1B, Figure V-33. These observations confirm those reported previously that the grain structure of chloride material is far less stable to heat treatment than is that of fluoride material.

68-R-4-23

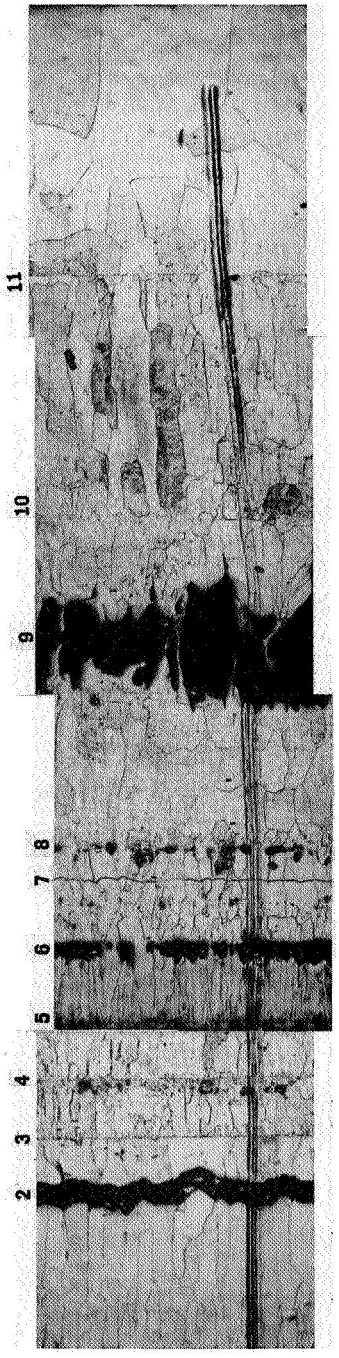

Figure V-23. Cross Section After 6 Hours at 1800°C, Repolished and Etched. WC2B'.

68-R 4-24

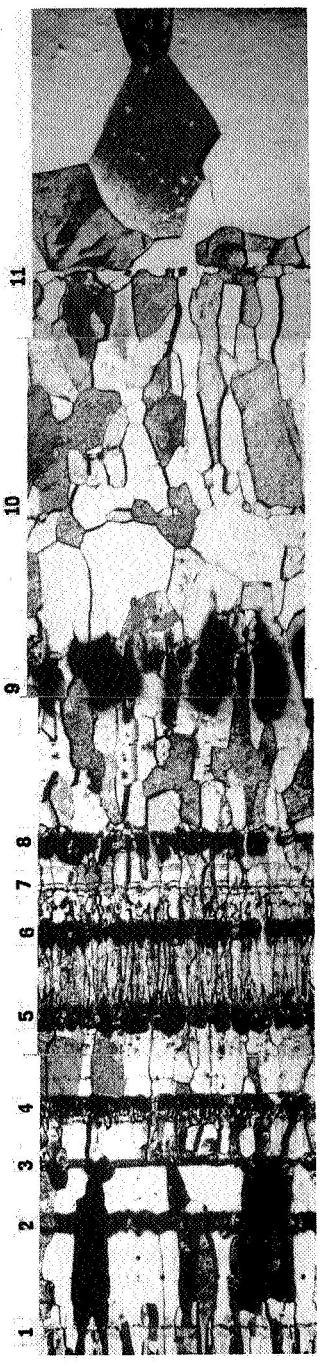

Figure V-24. Cross Section After 1 Hour at 2100°C, Repolished and Etched. WC3B'.

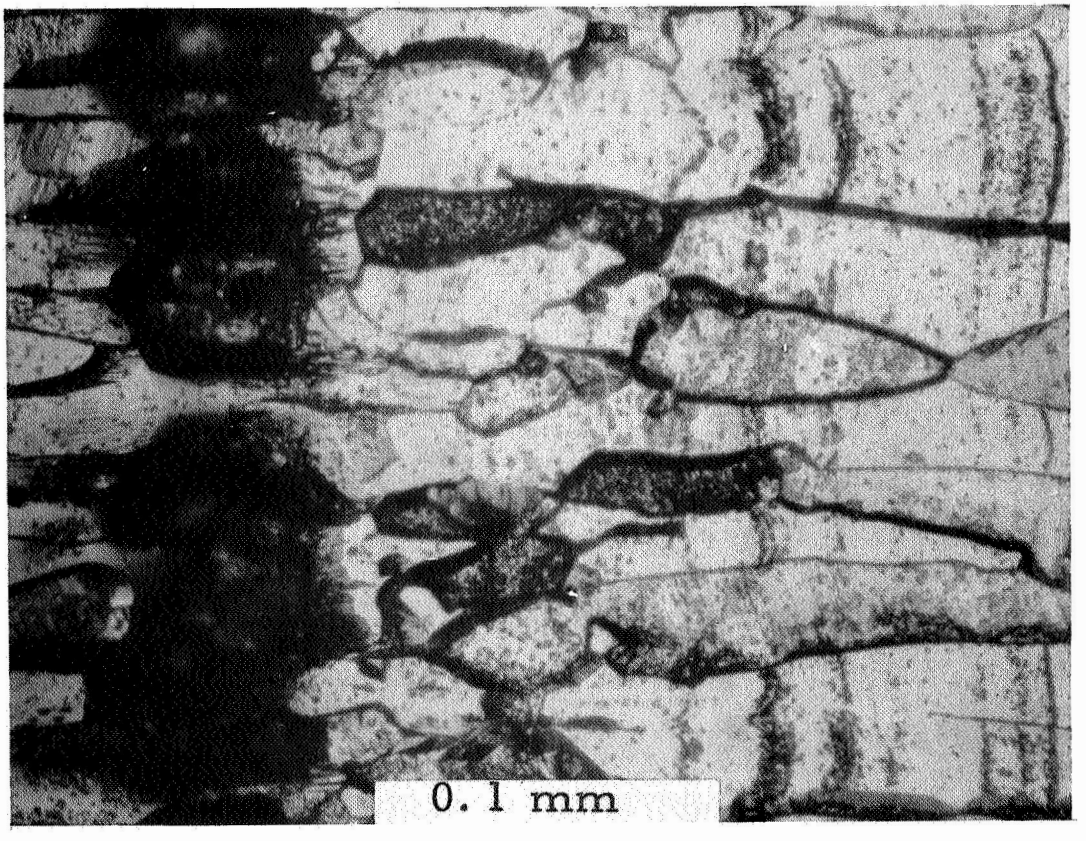

Figure V-25. Detail Near #7 from Figure V-19.

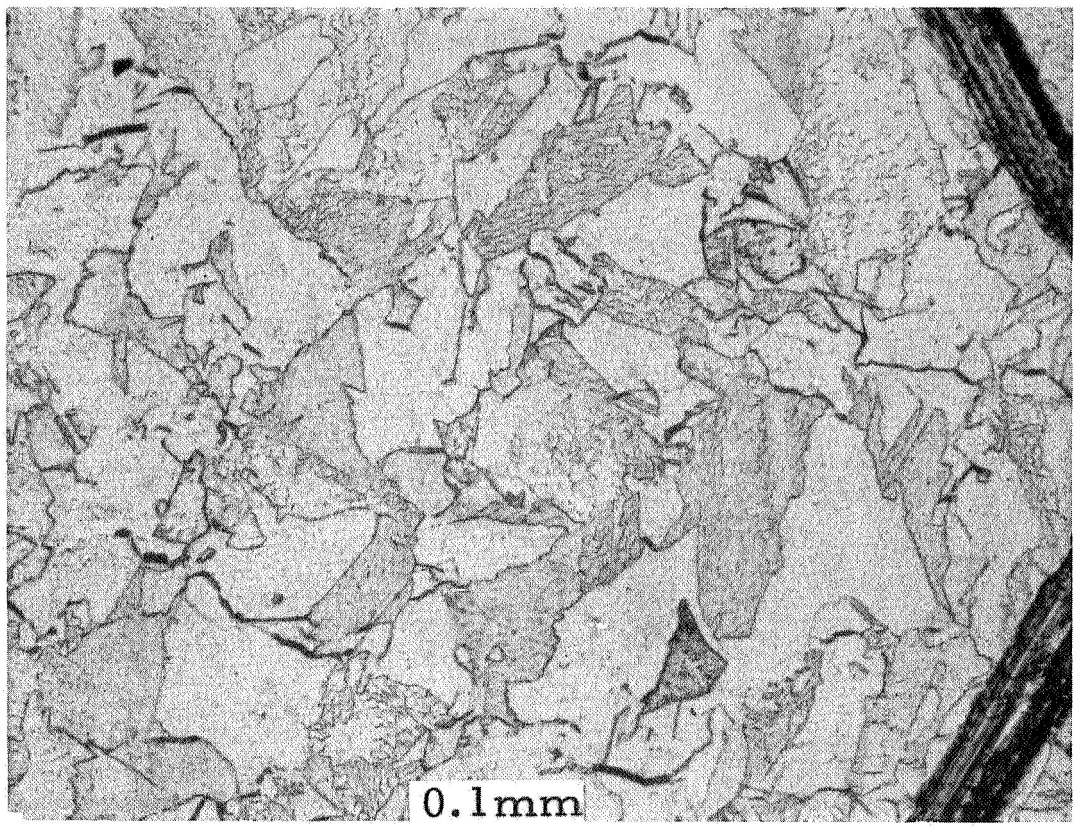

Figure V-26. Ground and Polished Top Surface of As-Received Sample WC2A.

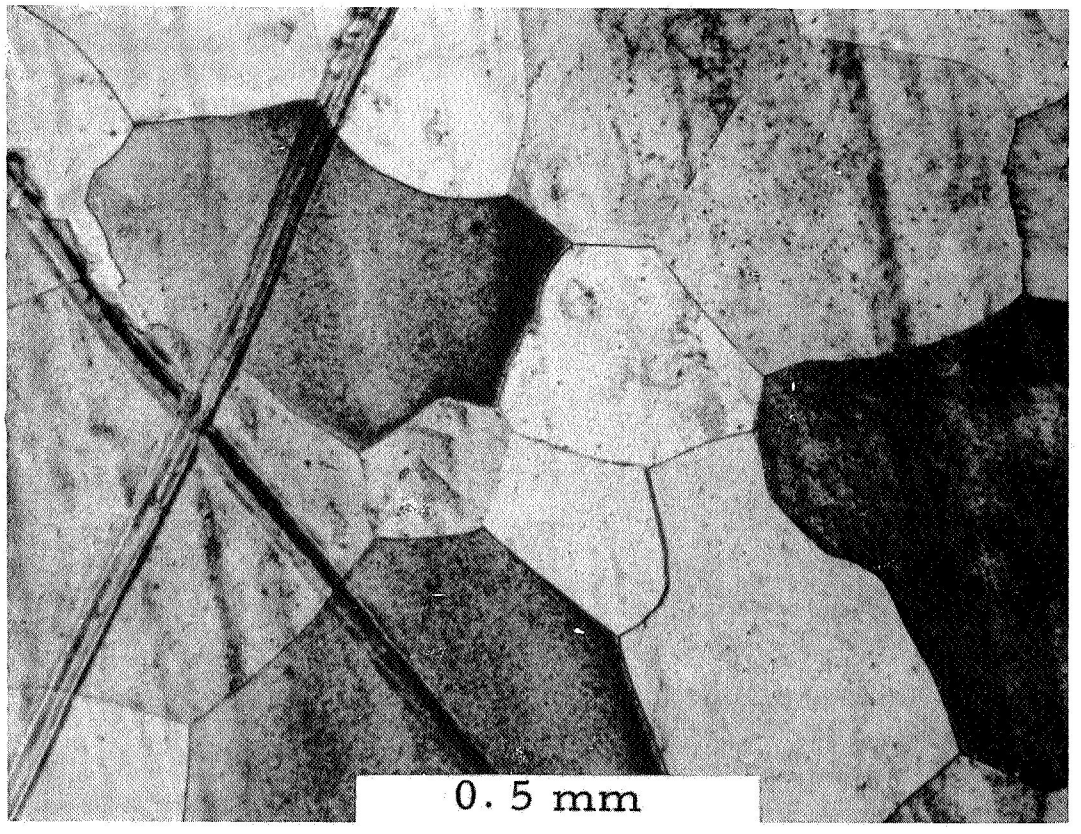

Figure V-27. Ground and Polished Top Surface of Sample after 6 hours at 1800° C. WC2B'.

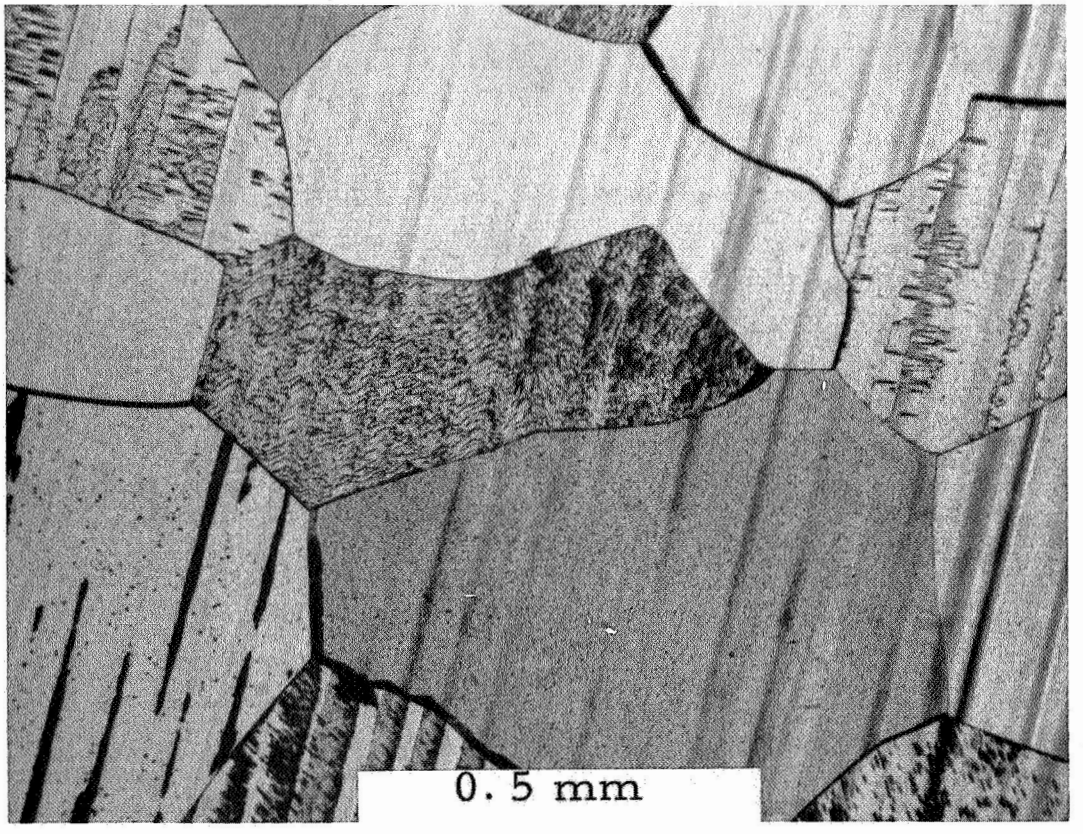

Figure V-28. Ground and Polished Top Surface of Sample after 1 hour at 2100° C. WC3B'.

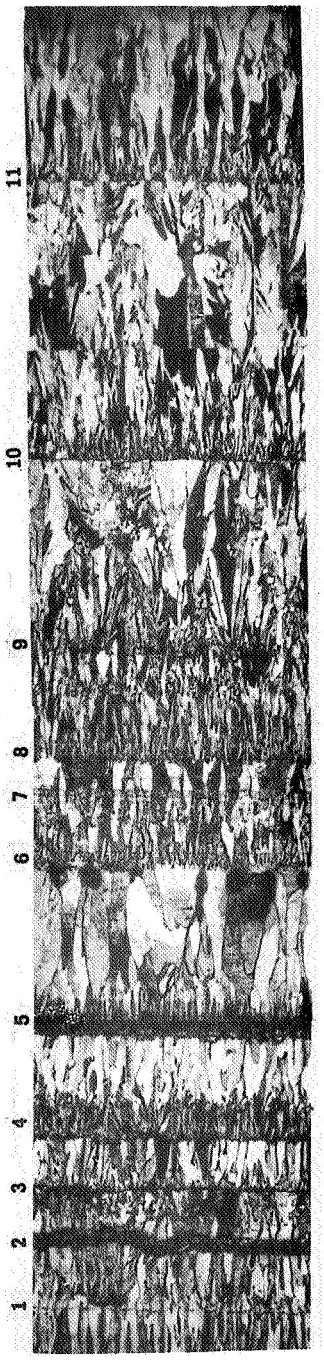

Figure V-29. Polished and Etched Cross-Section of As-Received Sample. WC4A.

68-R-4-27

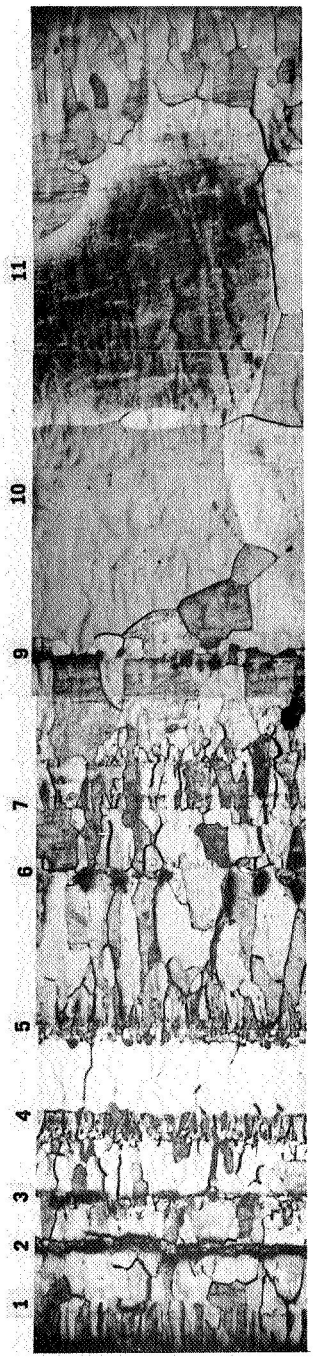

Figure V-30. Ground and Polished Cross-Section of Sample after 1 hour at 2230° C. WC4B.

68-R-4-28

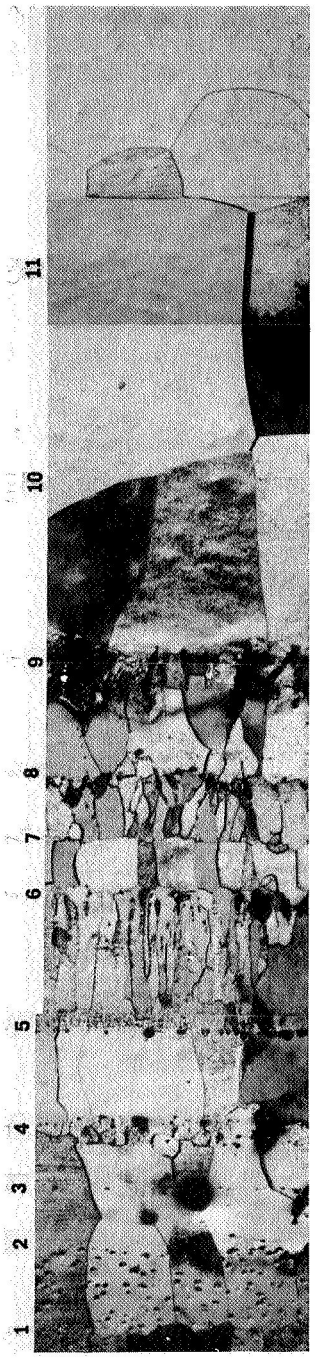

Figure V-31. Ground and Polished Cross-Section of Sample after

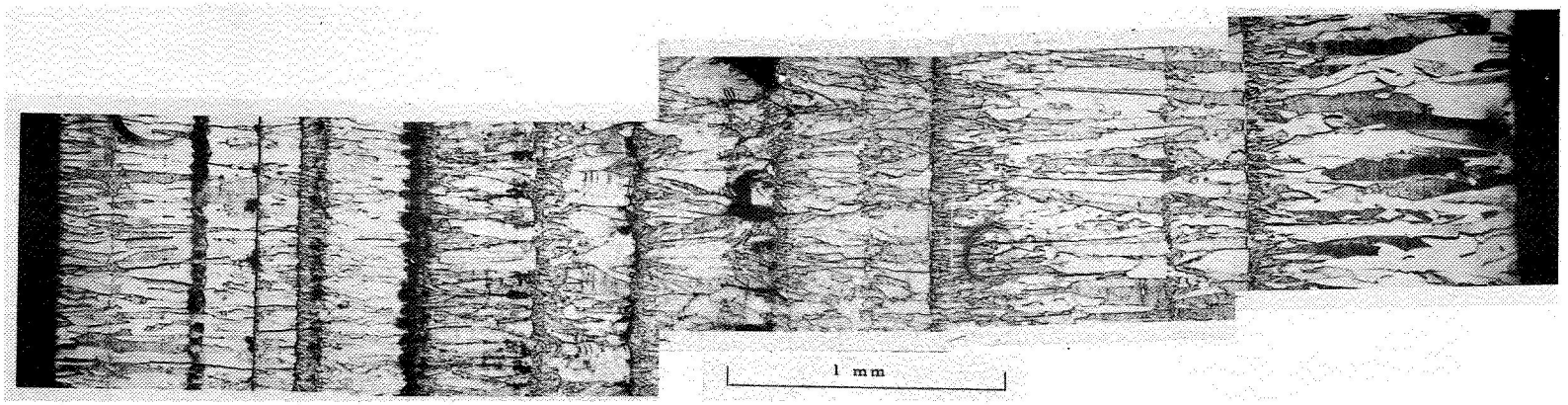

Figure V-32. Cross section of sample WC1A as received. The scale for this figure applies to all other cross sections of this type.

68-R-6-63

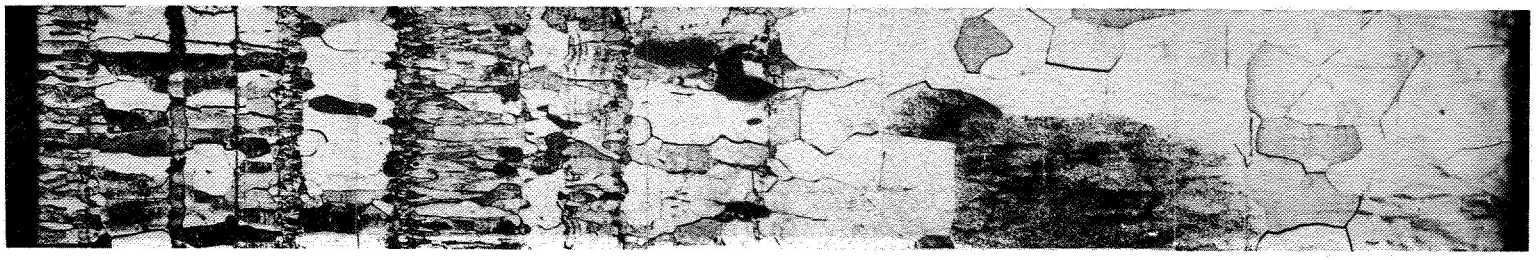

Figure V-33. Cross section of sample WC1B' after 6 hours at 1900°C.

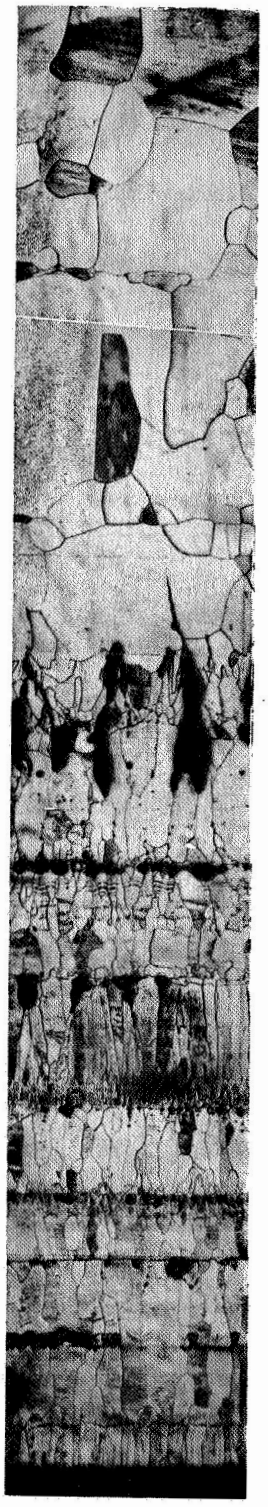

Figure V-34. Cross section of sample WC6B' after 1 hour at 2000°C.

It was mentioned in section B-2 of this chapter that in certain cases material evaporated from chloride specimens during their heat treatment. In an effort to determine the origin and nature of the material, a sample was collected and examined by emission spectroscopy. It was found to be tungsten, containing small traces ($<0.01\%$) of Cr, Fe, Ni, Si, and Mo. Since metallic tungsten would not have evaporated at the temperatures in question, the manufacturer was consulted, who suggested that unreduced tungsten chlorides might have been present in the material, which could also account for the striated appearance of certain regions of the material, such as that in Figure V-20. The chlorides are much more volatile than tungsten metal. They are also soluble in water, and so a preliminary attempt was made to dissolve some, by boiling crushed fragments of chloride tungsten in distilled water. This did not extract enough chloride to give a visible precipitate when silver nitrate solution was added, but the manufacturer's hypothesis cannot be ruled out.

C. MORPHOLOGY OF DEPOSITS

In the course of examination of fluoride material, it became possible to show that the bounding surface of the deposit was composed largely of pyramids bounded by {111} planes. This is consistent with the unsupported observation of Holman and Huegel.[1] Slightly below the surface of the deposit in some areas, there lay a zone of material with a high etch-pit density. This is visible in Figure V-34 and is shown in more detail in Figure V-35. This zone presumably represents

---

[1] W. R. Holman and F. J. Huegel, CVD Tungsten Process Development in "CVD of Refractory Metals...," Report on ANS-AIME Conference at Gatlinburg, Tenn., Sept. 1967, Ed. A. C. Schaffhauser, page 144.

a small perturbation in the growth conditions, similar to that found near the mid-plane of the deposit and discussed above. We shall make the assumption that the zone was everywhere parallel to the surface of the deposit at the time when the zone was growing. The view in Figure V-35 is perpendicular to the plane of the deposit and shows a slice through the four-sided pyramids which terminate each columnar grain. These pyramids might be composed of four {110} planes or four {111} planes.

A section in the plane of the deposit (on another specimen from the same ingot) is shown in Figure V-36. Here the photograph plane passes through the high-etch-pit-density (or "dark-etching") zone at about the position indicated by dark marks on Figure V-35, and reveals that the dark-etching zone is square and surrounds a clear zone in each grain. This is consistent with the ideas that each grain terminates in a four-sided pyramid and that the dark-etching zone was parallel to the pyramidal growth surface.

It can be shown that a pyramid of {110} planes will have a square trace on a (100) plane with edges lying in ⟨100⟩ directions, while a pyramid of {111} planes will have a square trace on a (100) plane with edges lying in ⟨110⟩ directions. Therefore, the choice between these two types of pyramidal plane resolves to determining the crystallographic direction which the edges of the dark-etching zone make in each grain. Examination of many grains, of which that in Figure V-37 is typical, shows that the dark-etching zone edges always lie at a 45° angle to the edges of individual etch pits. An independent experiment using a (100)-oriented single crystal revealed that the etch pits have edges along ⟨100⟩ directions;[2] therefore, the dark-etching zone has edges in ⟨110⟩ directions, and the pyramid surfaces are {111} planes.

[2] This confirms the conclusion of I. Berlee, J. Applied Phys. 33:198(1962)

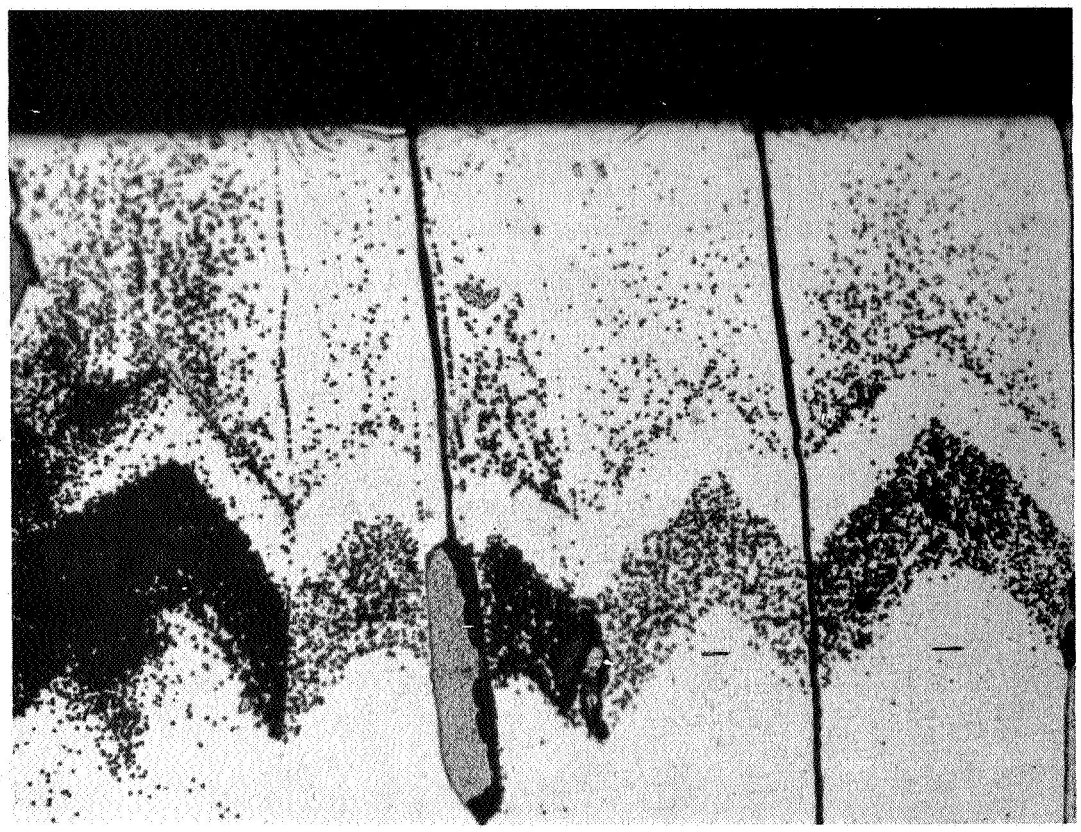

Figure V-35. Cross section of sample WF2C' showing high-etch-pit-density zone near ground surface. (225X)

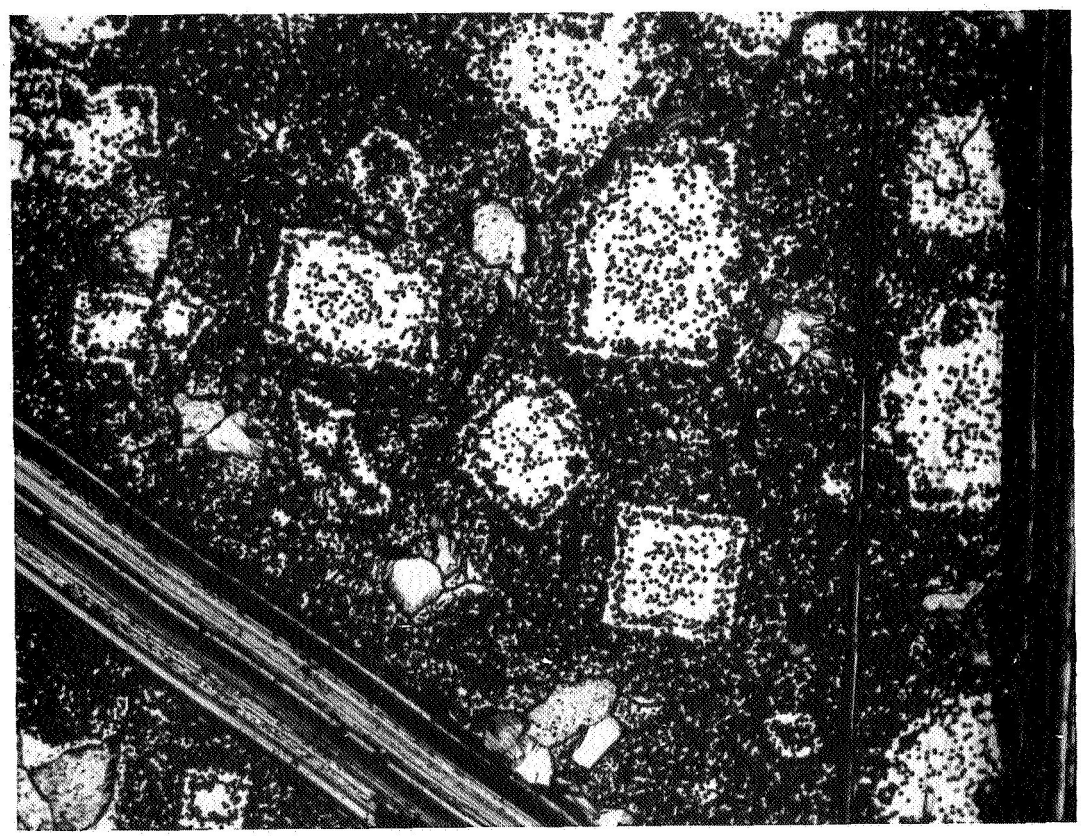

Figure V-36. Section parallel to plane of deposit through WF4C' showing dark-etching zones in each grain. (225X)

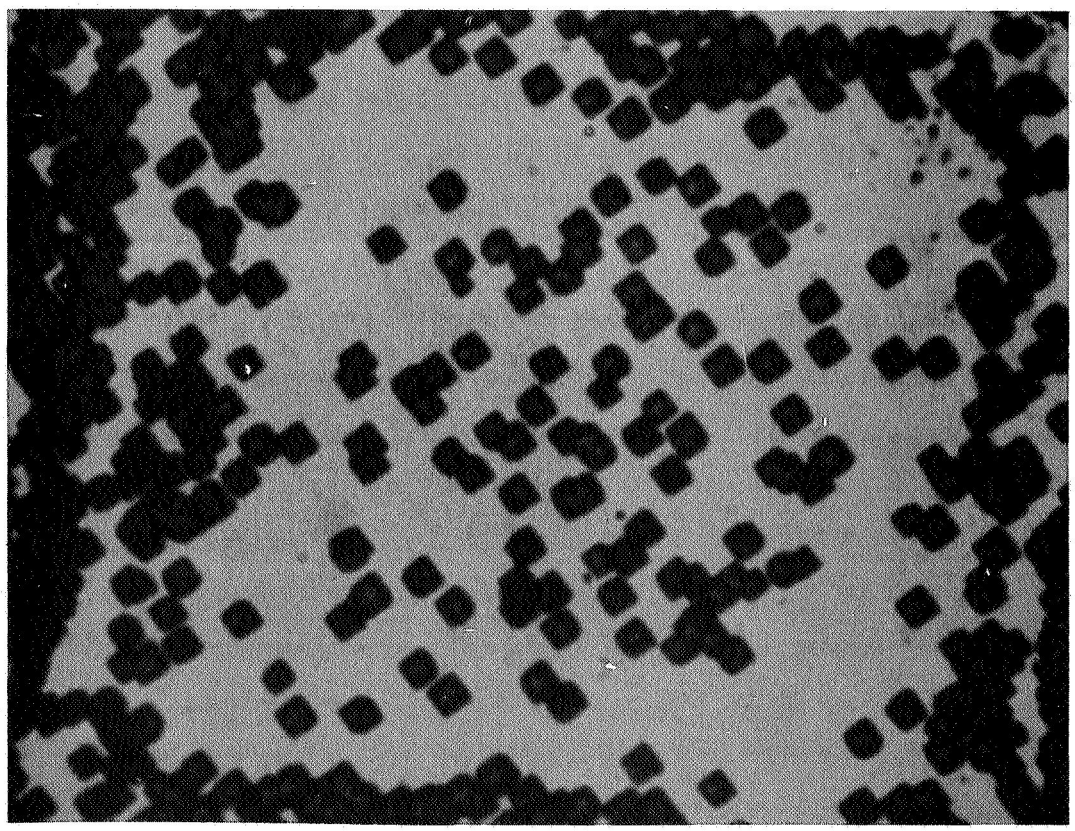

Figure V-37. Detail from Figure V-9, showing that dark etching zone has sides making 45° angle with etch pits. (1620X)

Following the work of Dr. Ling Yang at Gulf General Atomic, studies of the preferred orientation of fluoride and chloride samples have been made. A standard Norelco Pole Figure accessory is used in a simplified mode. The specimen is set with its surface on the diffractometer axis, and its surface normal bisecting the incident and diffracted beams, while the angle between the later is chosen to fulfill the Bragg condition only for the type of crystal plane which is expected to occur parallel to the surface (e. g., $2\theta \sim 40°$ for deposits from the chloride having (110) planes parallel to the surface for the radiation used here). Then the surface normal is rotated out of the plane defined by the x-ray beams through an angle α, and the intensity of the desired reflection is recorded as a function of α. A normalized cumulative integral of the I-versus-α curve is derived algebraically and identified with the distribution curve showing the fraction of the specimen having the chosen planes with angle α of the surface normal. This curve runs from 0 at $\alpha = 0$ to 1 at some α between 10° and 30°. Its convexity upwards is a measure of the preferred orientation in the sample. The raw data from a well oriented sample takes the form of a symmetrical smooth curve rising from $\alpha = -20$ to a peak at $\alpha = 0$ and dropping to $\alpha = +20$.

The beam width is about 2 mm. Sampling of a number of grains is obtained by oscillating the specimen along a line in its own plane perpendicular to the incident beam, through an amplitude of 1. 5 cm. The period of the sampling oscillation is kept small compared to the time constant of the recording circuit, in order to reduce oscillations in the recorded signal due to any single strongly-reflecting grain.

Laue back reflection photographs of the material consist of uniform rings, indicating that the material is isotropic in that there is no preferred orientation along certain directions in the deposit. That is to say, there is no analog of the rolling direction or transverse direction found in rolled sheet. Consequently, the rotation of the sample about its own surface normal will not alter the x-ray data obtained from it.

Most measurements have been made without any slits between the specimen and the detector (scintillation counter) opening. This leads to a loss in angular resolution accompanied by a smoothing of the output data curve. Most measurements have been made over a range of α from -20° to +20°, and the average of two readings for α was processed to give the final data. Unfiltered Cu K α radiation is used, from a tube operating at 35 kV and 15 mA.

1. Results

The results are best presented in the form of graphs showing the fraction of the x-ray intensity originating within an angle α of the symmetrical ($\alpha = 0$) position, as a function of α. Such graphs will be called pole figures. These can be interpreted as indicating the fraction of the grains present having the investigated crystal planes within an angle α of the surface. (The investigated plane is (110) for chloride samples and (100) for fluoride samples). Such curves are necessary to present the data, since a curve cannot in general be represented by a few simple parameters without making assumptions about its shape. However, it may sometimes be convenient to summarize the data from a curve by using numerical indices, such as angles necessary to include 50% and 90% intensity. These figures may be interpreted to

mean that 50% of the grains have, say, (100) planes within the specified number of degrees of the surface. Any inference about the thermionic behavior of the surface must await empirical correlations between curve shape and material performance.

2. As-Received Material

The curve derived from data taken from the top surface of fluoride material in the as-received (unground) condition is shown in Figure V-38. This pole figure shows a strong preferred orientation, in that half the area is oriented with 1.7 degrees of the (100) planes. A random sample would give a straight line from 0° to 20°, with a 50% angle of 10°. Another piece of material was ground flat (on a conventional surface grinder) and then electropolished to remove material damaged by grinding. A pole figure was obtained after about 0.002 inch (50 microns) had been removed by polishing, and this is shown in Figure V-39. It indicates a preferred orientation almost equal to that of the as-received material. The reverse surface of the deposit, next to the mandrel, was examined briefly and found to give an intensity of (100) reflection invariant with α, implying that it had a random orientation. The penetration depth of x-rays into the sample is a few microns, comparable with the diameter of the grains found at the bottom of the deposit, and presumably only this thin non-columnar layer of material is contributing to the signal, and is shielding the better-oriented structure from the x-rays.

If the material is ground, sandblasted or abraded to produce mechanical damage, the damaged layer has a random or disordered structure, at least to a depth of a few microns, and it gives a straight-line pole figure characteristic of random material. Annealing the

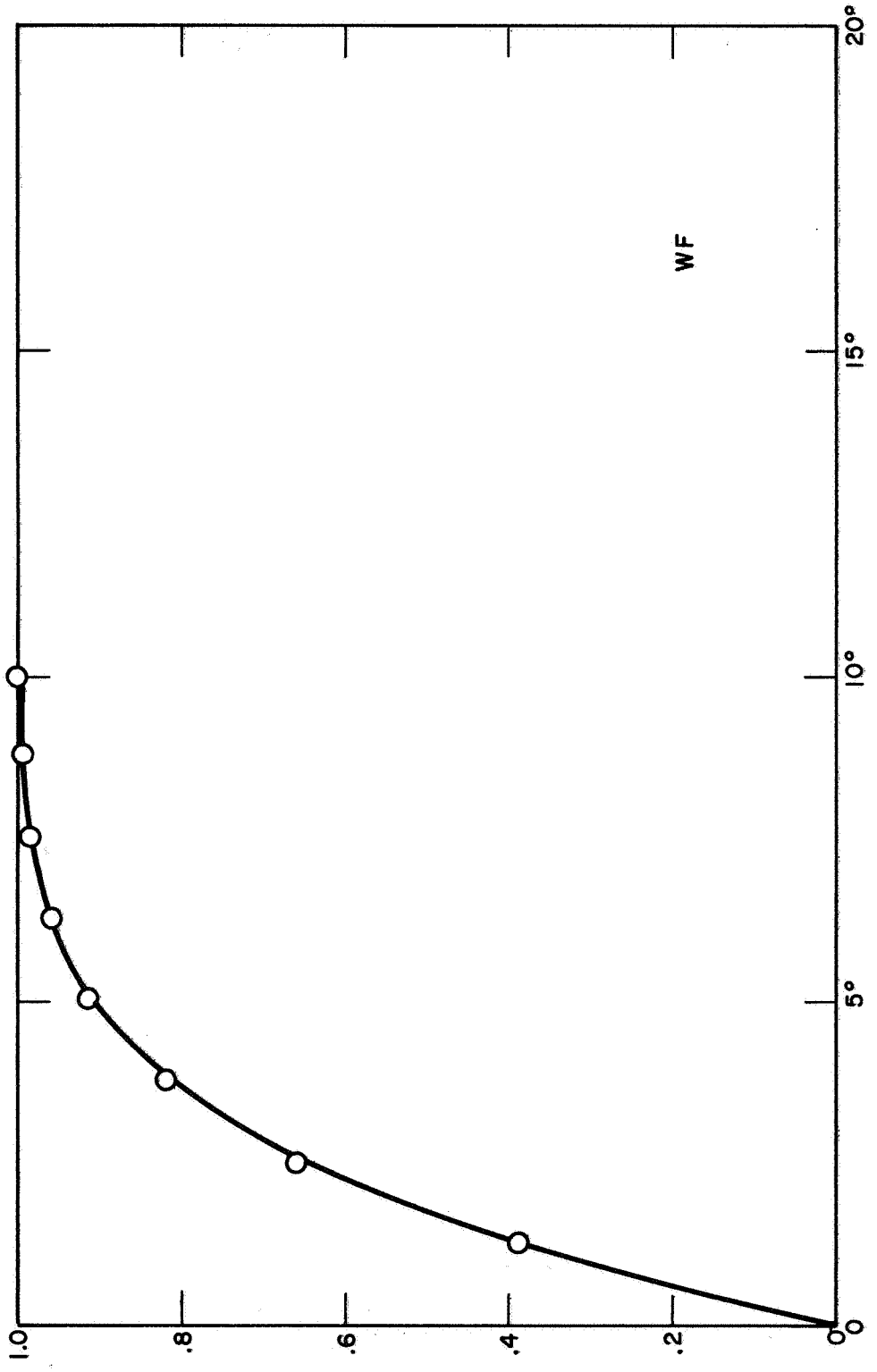

Figure V-38. Pole Figure Curve for Top Surface of As-Received Material. WF.

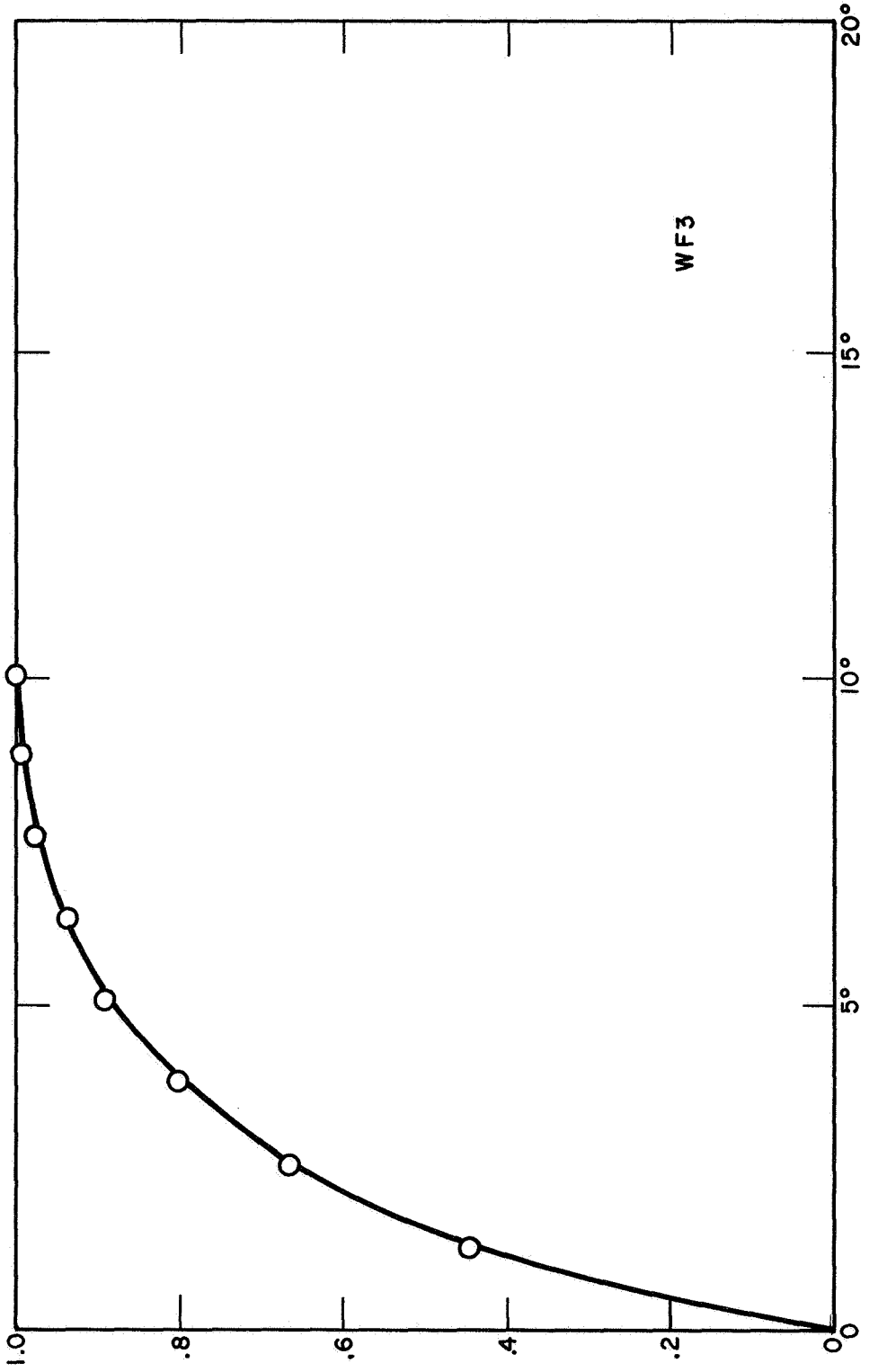

Figure V-39. Pole Figure for Material Ground and Electropolished. WF3'.

ground surface allows the random material to recrystallize and recover the structure and orientation of the underlying undisturbed material. The effect of certain treatments which might be used to prepare emitters for thermionic converters was studied.

Sample WF5 was ground and annealed 20 minutes at ~1900°C and then gave the pole figure in Figure V-40. This clearly shows a much milder preferred orientation than the as-deposited material, and approaches the straight line that a random sample would give (from 0 at 0° to 1 at 20°). If such a surface were used as an emitter (at temperatures below 1900°C) it would have a performance characteristic not of fluoride vapor-deposited material but of that heat treatment which had been applied to the material.

If a more drastic heat treatment is applied the ground surface layer can regain the orientation of the underlying deposit. If, however, further treatment causes recrystallization, and grain growth, the coarse new grains will not necessarily share the preferred orientation of their predecessors, and in any case the x-ray technique makes it difficult to sample coarse grains. For if at any time one grain illuminated by x-rays is oriented correctly, it can produce a very strong contribution to the measured diffracted intensity, which produces a large perturbation of the I-versus-α curve and a corresponding perturbation of the derived $\int$ I-versus-α curve. This effect occurs in Figure V-41 and more conspicuously in Figure V-42 around 0.85 on the ordinate.

Figure V-41 indicates that when a ground surface is treated for 1 hour at 2400°C, the resulting surface has some of the preferred orientation of the deposit, at least at large α, but the chance of finding (100) planes within two degrees of the surface is near that for a random

sample. More intensive treatment, such as 6.5 hrs at 2600°C (Figure V-42), restores a large part of the preferred orientation, while also producing recrystallization and a large grain size (Figure V-10).

Considerable difficulty was experienced in examining samples of chloride material, because even mild heat treatment produced grain growth to the point that the region of the sample illuminated by the x-rays contained only a few large grains. The effect of this was to produce a highly irregular curve of intensity versus tilt angle α lacking symmetry about $\alpha = 0$ and composed of a few large, randomly distributed peaks. Such raw-data curves were not reduced to pole figures because it was clear that the pole figure would consist of a few steps instead of the smooth convex curve which can characterize the material. This problem was found with specimens WC2, WC3 and WC5, for which heat treatments varied from 6 hours at 1800°C to 1 hour at 2230°C.

Chloride material in the as-received condition gave the pole figure in Figure V-43, showing a fairly strong preferred orientation, but one much less strong than that of fluoride material in the same condition (Figure V-38).

After 1.2 hours at 2230°C, specimen WC4B gave the curve in Figure V-44 for the unground top surface. Comparison of this with Figure V-43 indicates relatively slight changes, presumably associated with the changes found in the grain structure.

The sample of fluoride material examined in the as-received condition, WF, whose pole figure is Figure V-38, was re-examined

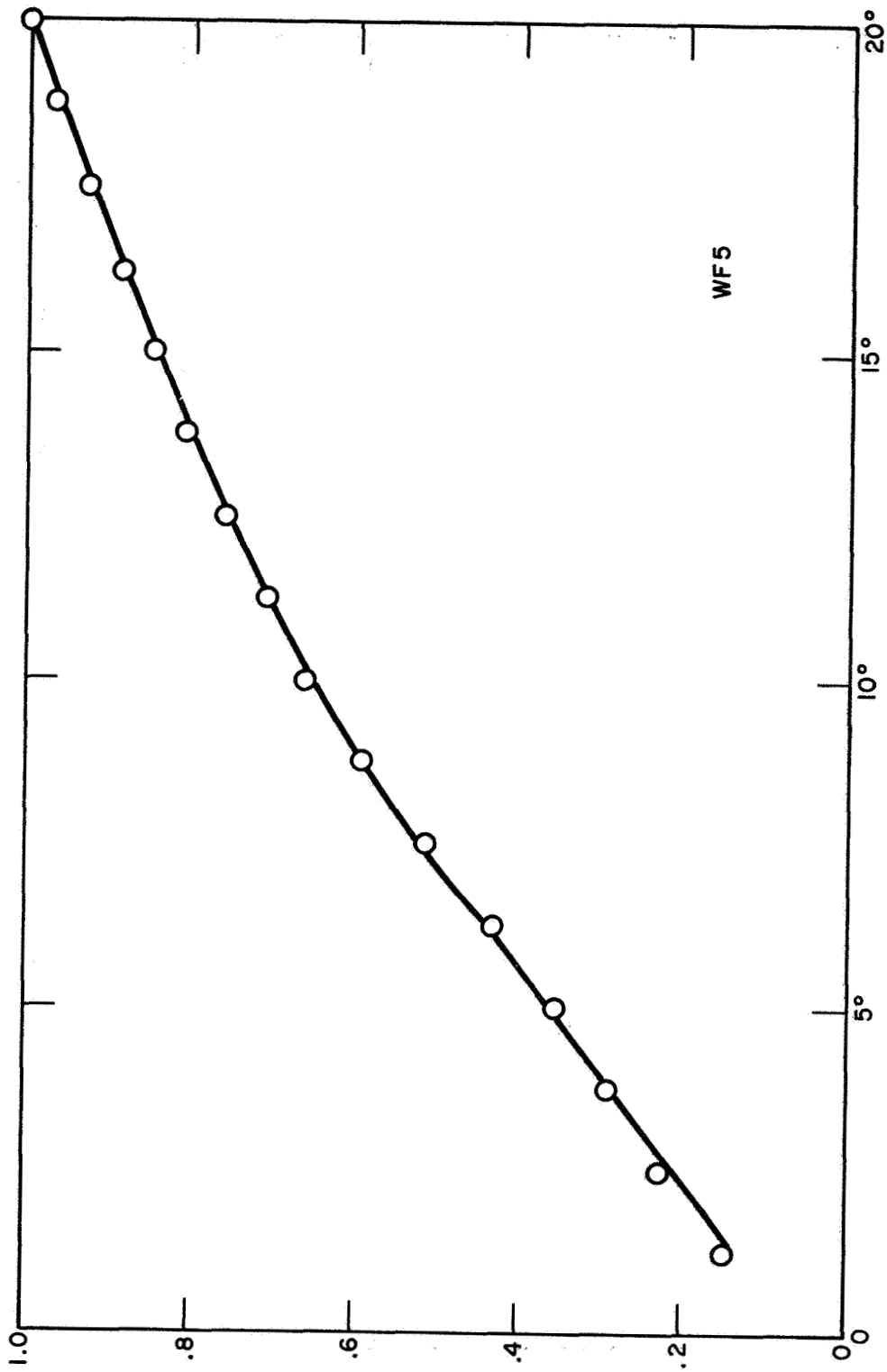

Figure V-40. Pole Figure for Material Ground and Annealed 20 Minutes at 1900°C. WF5.

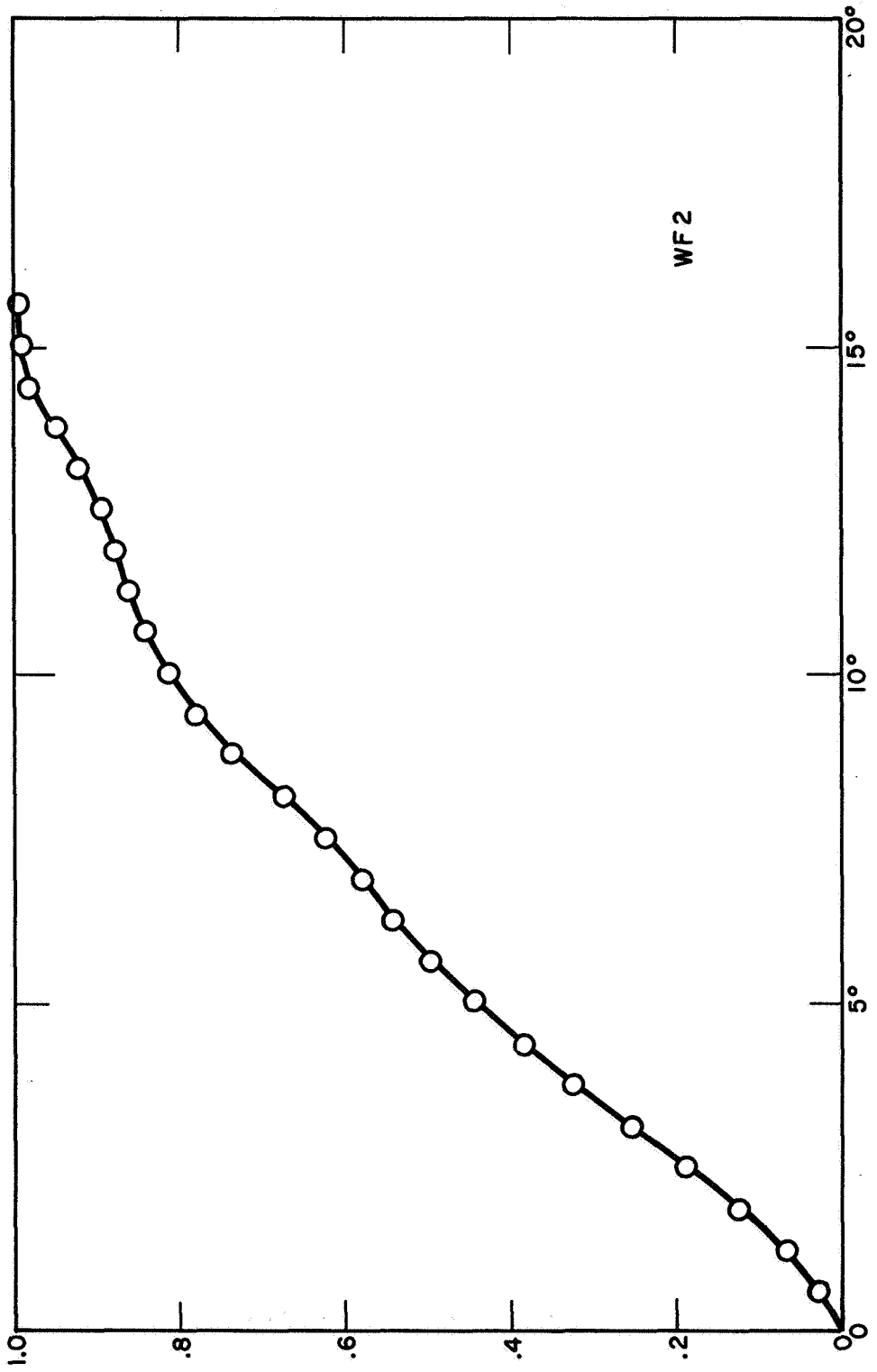

Figure V-41. Pole Figure for Material Heat-Treated for 1 Hour at 2400°C (Compare Figure V-6). WF2.

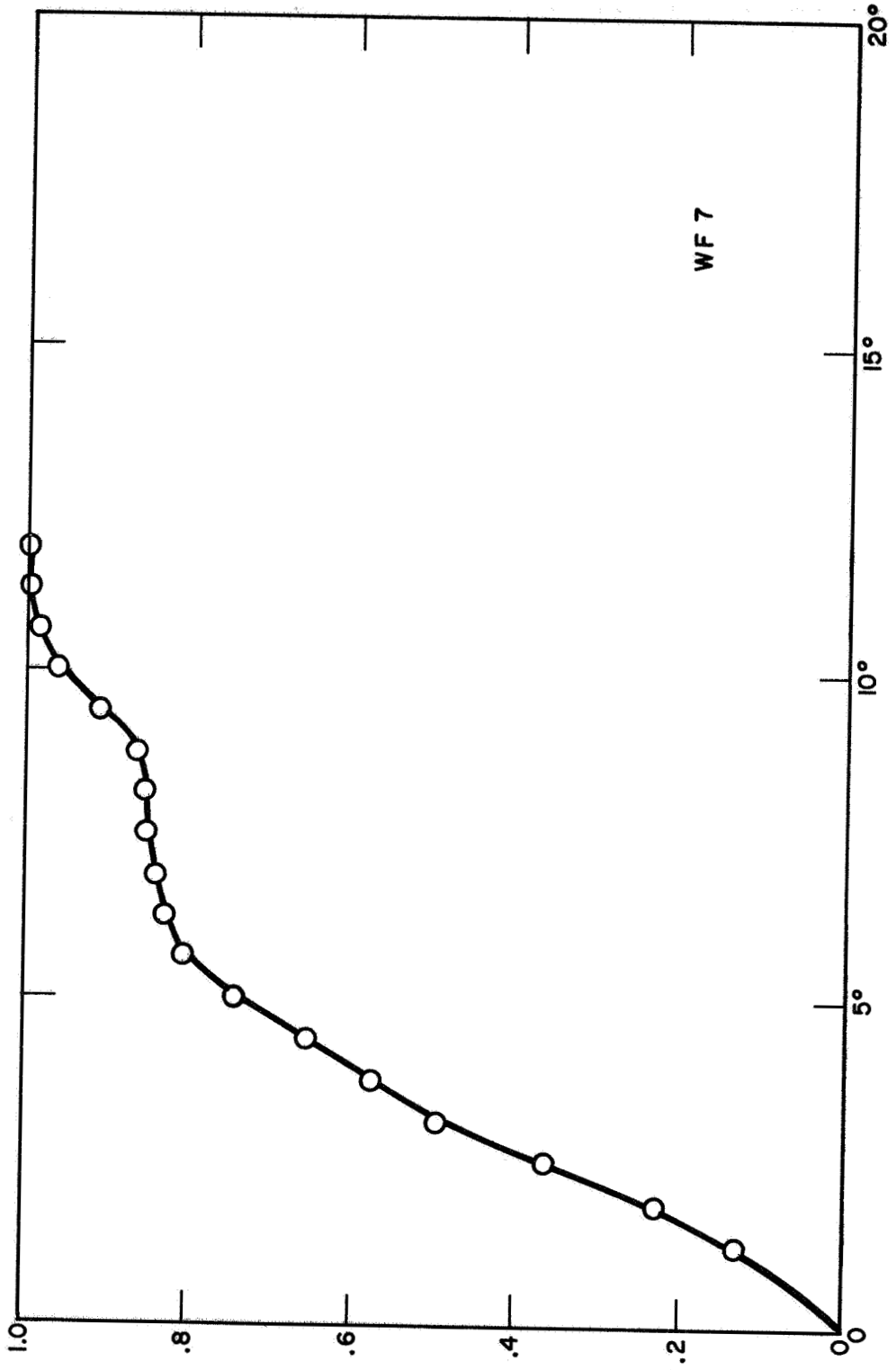

Figure V-42. Pole Figure for Material Heat-Treated for 6.5 Hours at 2600°C (Compare Figure V-10). WF7C.

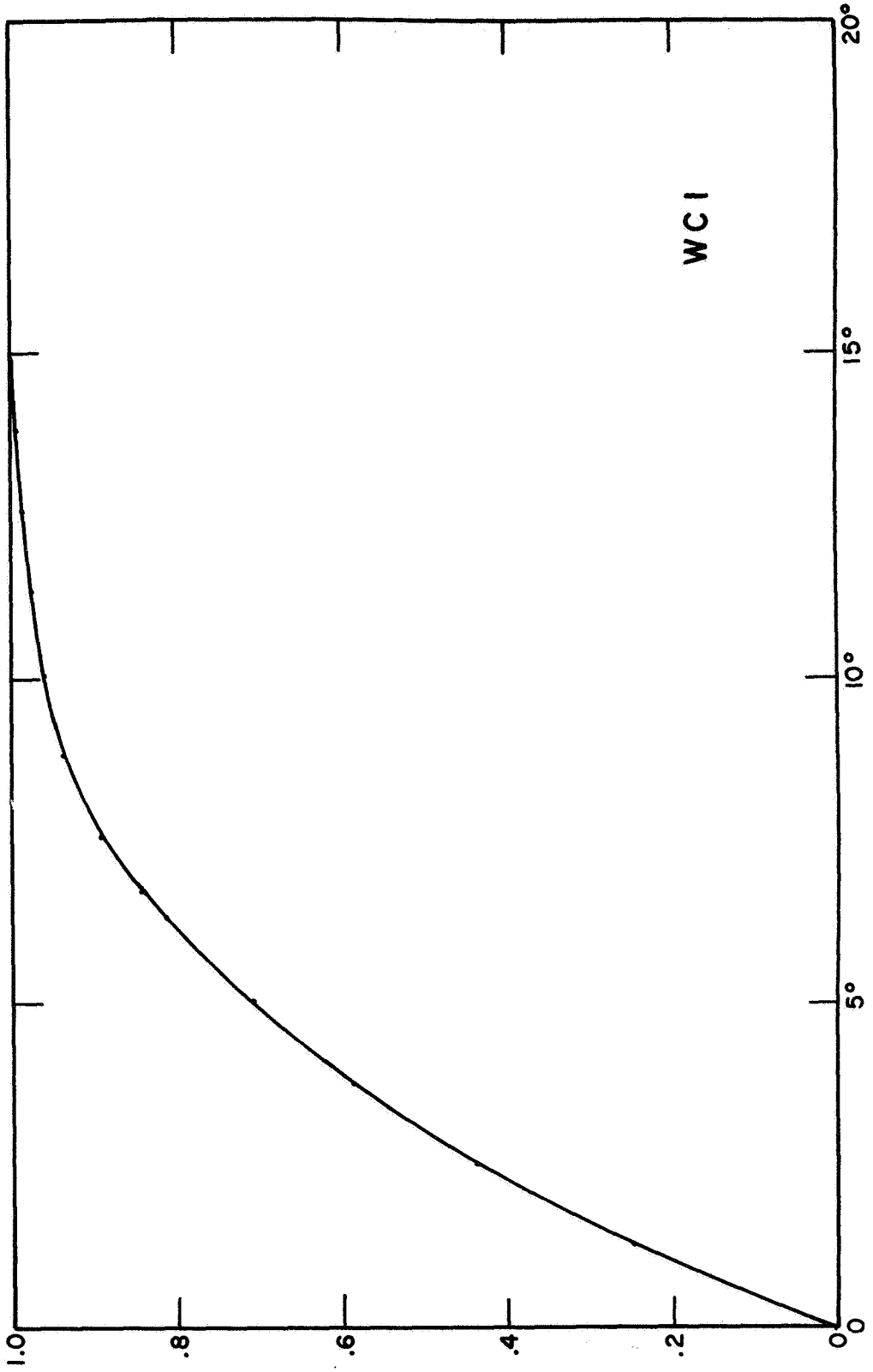

Figure V-43. Pole figure for WC1, as received.

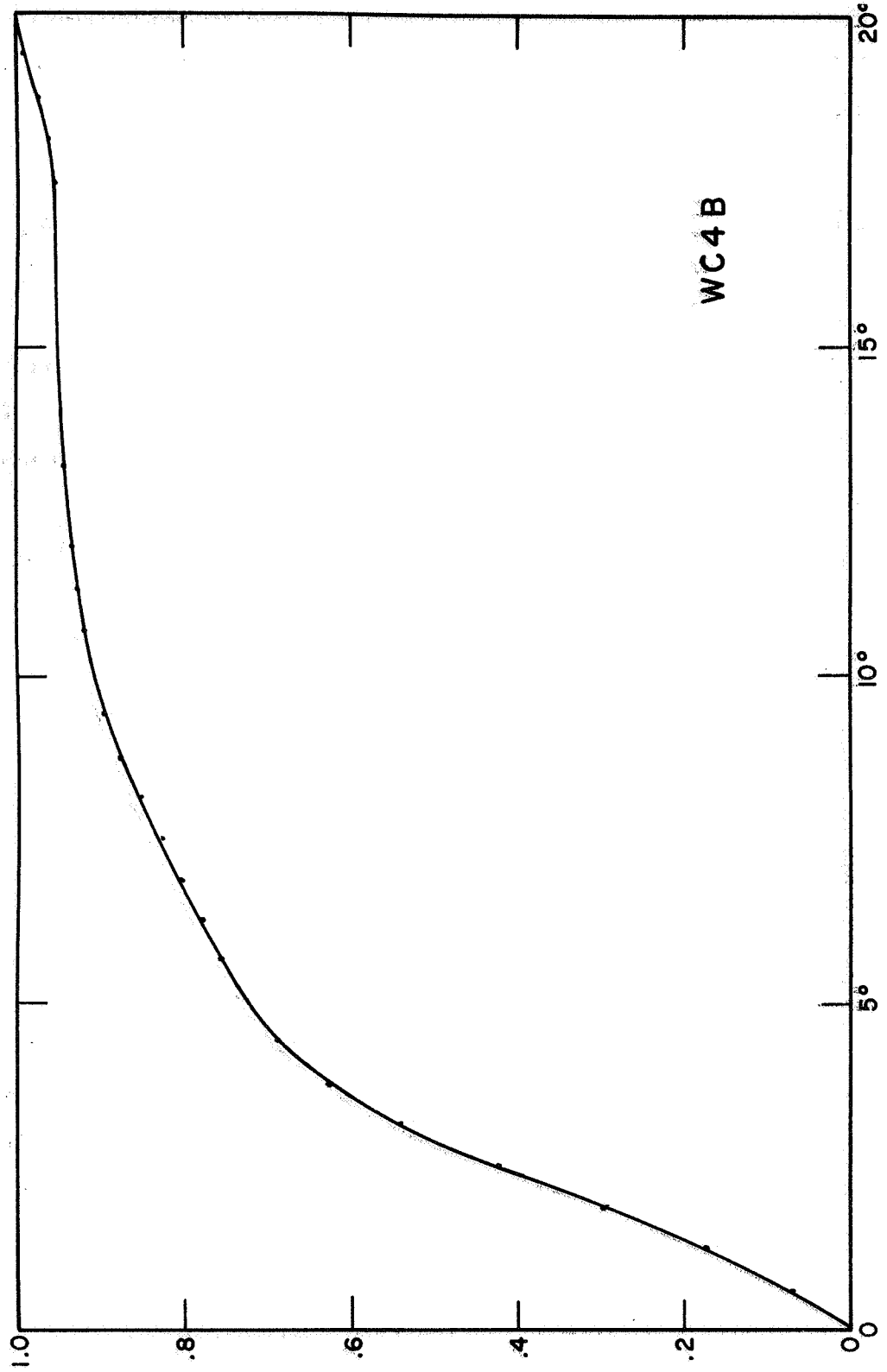

Figure V-44. Pole figure for WC4B, after 1.2 hours at 2230°C.

to determine the instrumental error on a sample believed to be homogeneous. The resulting curve superimposed on the original curve with a maximum error of 0.25° (at small α) and an error of less than 0.1° over most of the curve.

Sample WF4 was examined in various conditions, and the resulting pole figures for heat treatments, all at 1800°C, of 6, 30, and 100 hours on the ground surface are shown in Figure V-45. Corresponding curves for the region of WF4 electropolished for metallographic purposes are shown in Figure V-46. Each of these figures indicates that very little change in spatial distribution of ⟨100⟩ axes occurs, despite considerable changes in the microstructure, shown in Figures V-14 through V-16. Together they indicate the large degree of disordering which accompanies grinding a surface, and which is not eliminated by 1800° heat treatment, but is eliminated by electropolishing.

This observation is supported by the pole figures in Figure V-47, for an as-deposited surface subject to several heat treatments of increasing severity. The grain structure of fluoride material changes with heat treatment, but the spatial distribution of ⟨100⟩ axes does not change correspondingly.

D. DISCUSSION AND CONCLUSIONS

The material deposited from the fluoride has a grain structure which is stable under relatively severe heat treatments. Changes occur first in the grains near the bottom of the deposit, where the columnar structure is not well-developed. On heating, these grains form larger equi-axed grains. During one hour at 2400°C the columnar structure is retained, but small irregularities in the grain boundaries become

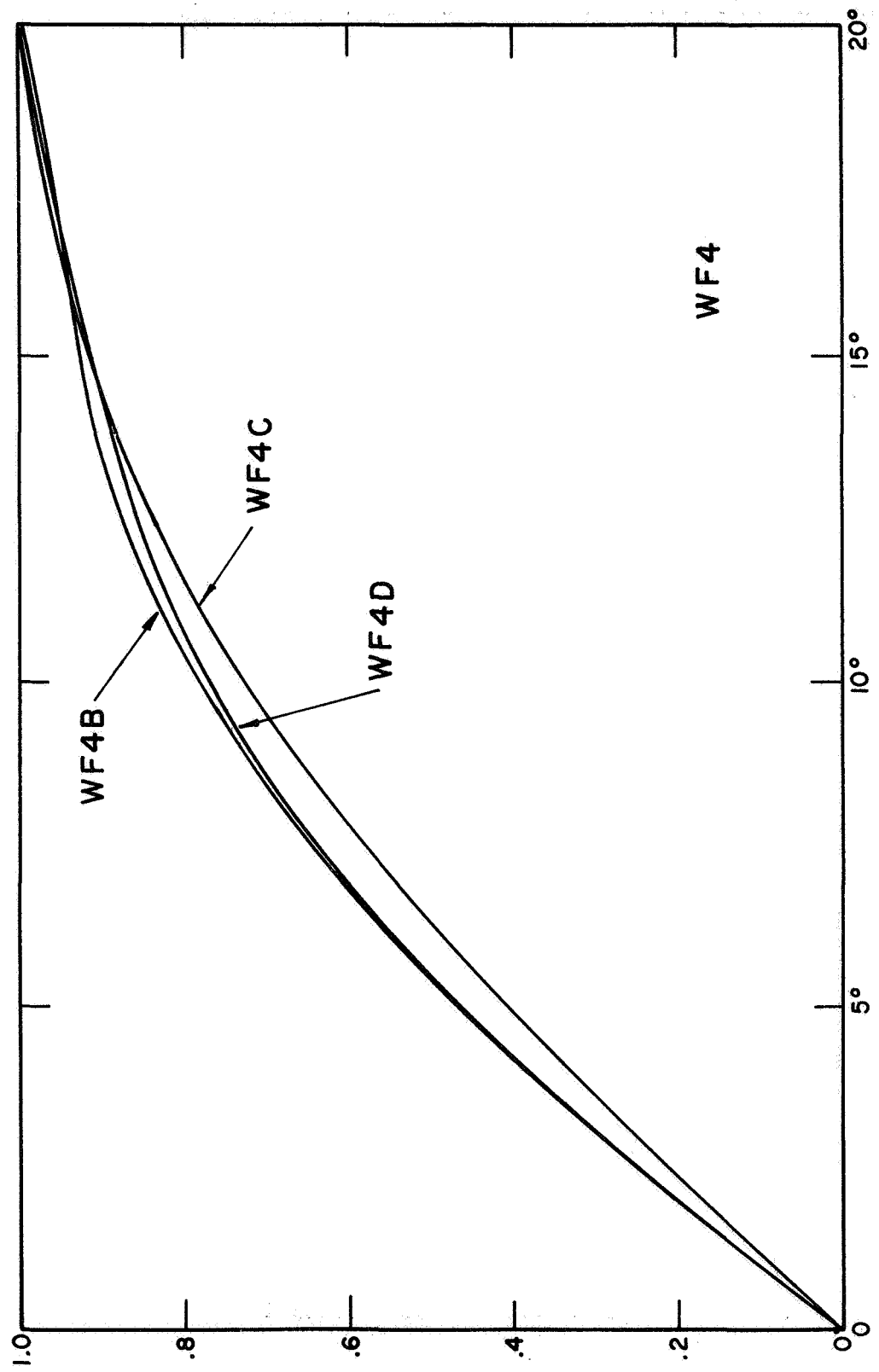

Figure V-45. Pole figures for WF4B, C, D after 6 hours, 30 hours, and 100 hours at 1800°C.

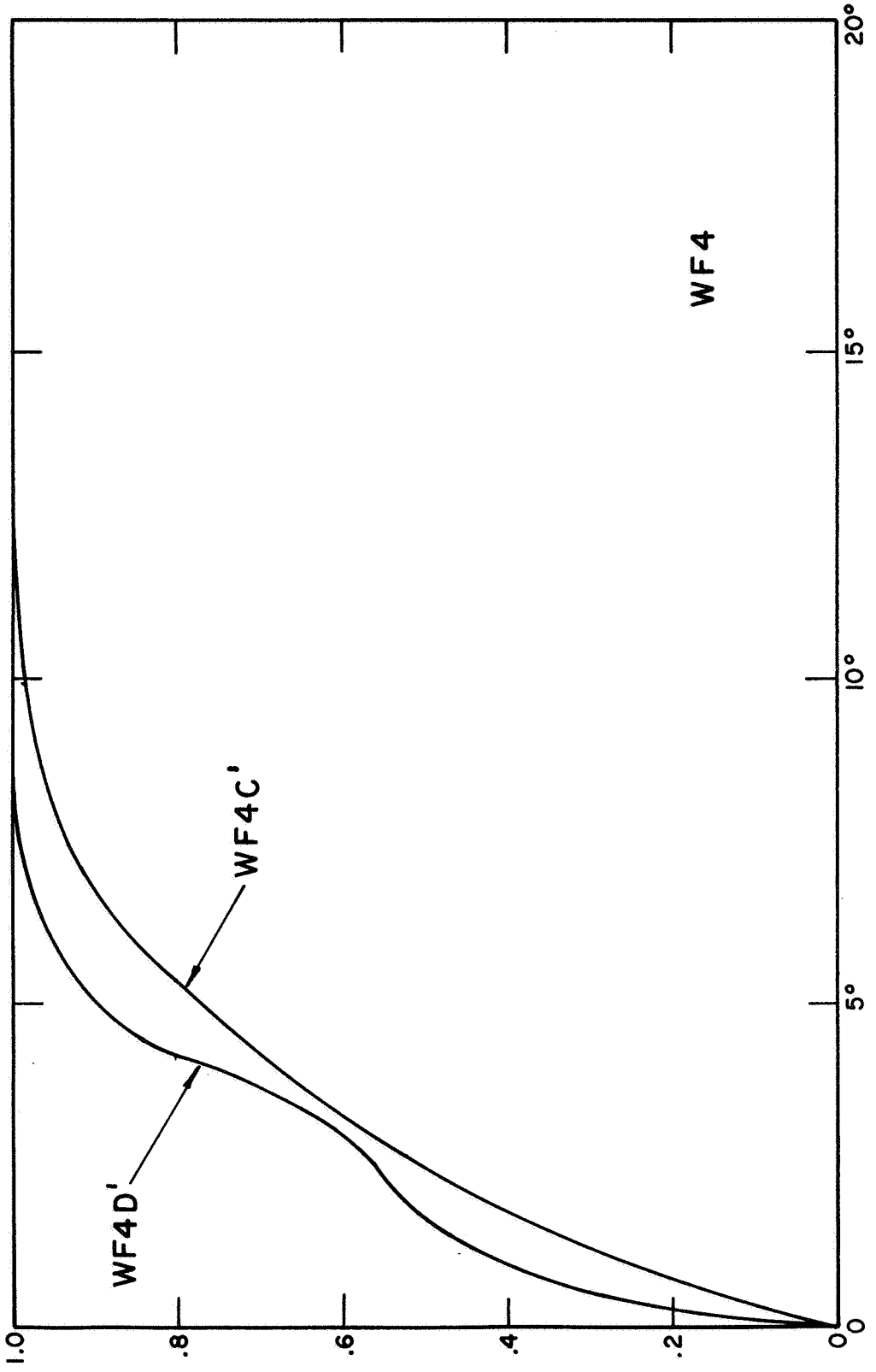

Figure V-46. Pole figures for WF4C' and D' after 30 hours and 100 hours at 1800°.

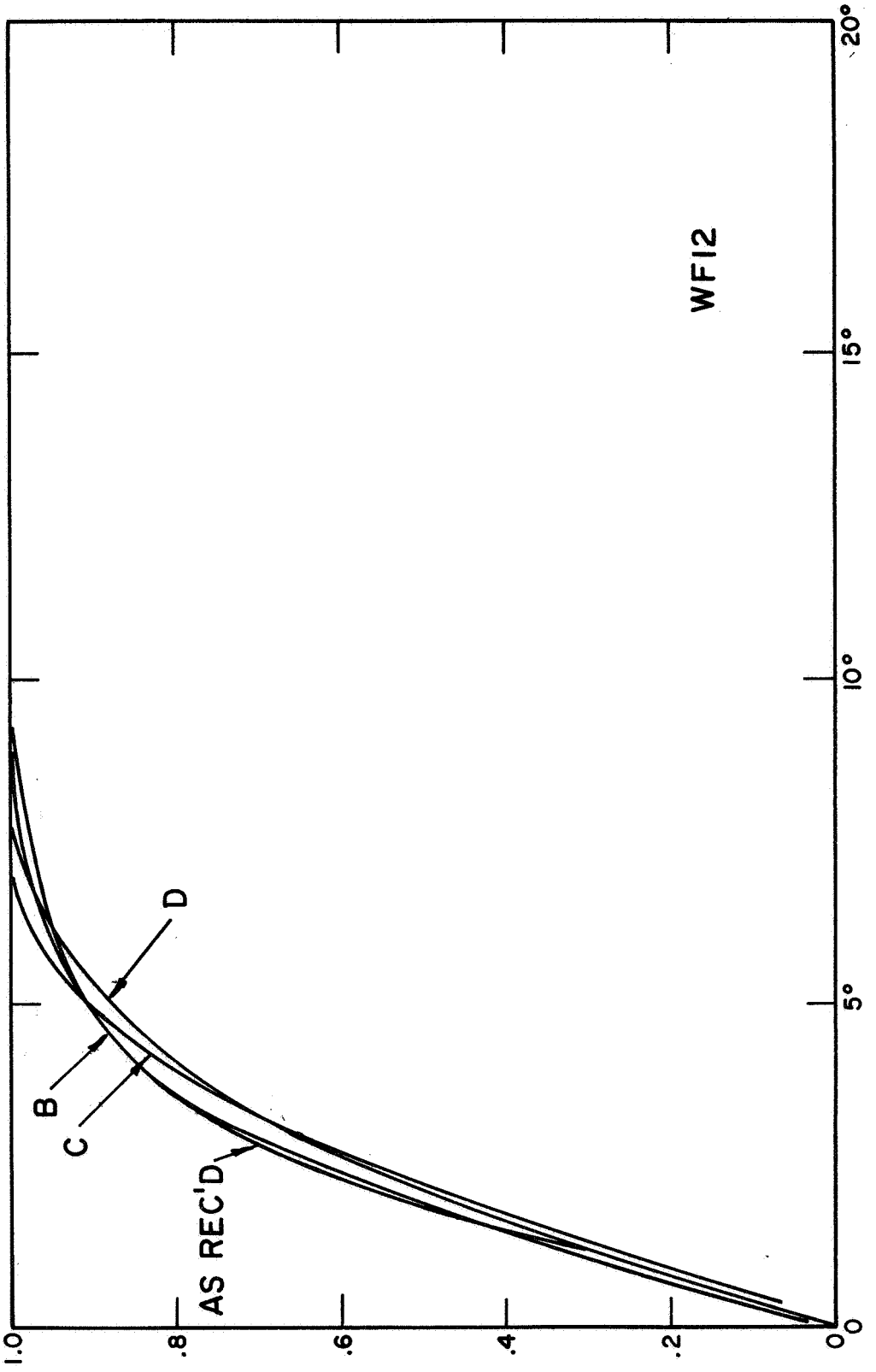

Figure V-47. Pole figures for WF12 - as received and after 1 and 6 hours at 2000° and 1 hour at 2230°C.

smoothed out and transverse sections of the deposit clearly show grain growth. Treatment for 6.5 hrs at 2600°C completely eliminates the columnar structure and gives a coarser equi-axed structure.

The changes which occur are not accompanied by corresponding changes in the partial pole figures, at least on the specimens which retain a columnar structure and whose grain size remains small enough to yield satisfactory pole figures.

The chloride material has a structure which is much less stable to heat treatment than that of the fluoride material. This may be related to differences in the grain boundary pinning effect of residual halides in the two materials, either because residual fluorine is intrinsically better than residual chlorine at obstructing grain boundary movement, or because there is more residual fluorine than chlorine. However, there may be an effect of deposit layer thickness on grain stability. The observation that the near-mandrel part of the fluoride deposit is less stable than the better-developed columnar part cannot be explained in terms of residual halide pinning unless the residual halide content varies through the thickness of the deposit. If it does not, then an explanation may be sought in terms of the stability of columnar structures as against equi-axed structures. Since the columnar structure becomes better developed as the deposit thickness increases, it may be that part of the relative instability of the chloride material is due to the absence of a well-developed columnar structure. The complete explanation must be more complicated, however, as there was no clear correlation between microstructural changes and layer thickness in the multi-layered chloride sample.

Grain growth in chloride samples precluded obtaining satisfactory pole figure data from most of the heat-treated material, but there are no indications to contradict the suggestion that structural changes are again not accompanied by changes in the pole figure.

CHAPTER VI

PLASMA ANALYSIS

D. Lieb

A. INTRODUCTION

This chapter describes a theoretical study of the plasma phenomena in a cesium thermionic converter. Using a set of plasma equations and an associated computer program, both of which were developed under an earlier contract,* numerical solutions were obtained for different boundary conditions and for various values of the plasma parameters. The emphasis in this task has been to study the effects of introducing different assumptions rather than to obtain J-V curves which may be compared to experimental data. The validity of comparisons with experimental data is doubtful at this stage, since an accurate knowledge of electron and ion mobilities, surface work function and other parameters is not available. It is possible, however, to compare trends due to changes in a variable such as spacing; a few such curves are shown.

B. DISCUSSION

Since the equations and the computer technique used to find the solutions have already been described[1] they will only be summarized here. Table VI-1 contains a list of all the symbols used.

1. Equations and Assumptions

Assuming charge neutrality through the plasma and neglecting the ion energy component, three transport relations can be written:

*Contract NAS7-508

TABLE VI-1

θ	-	temperature multiplied by Boltzmann's constant, i.e., kT
J	-	current
J_r, Js	-	electron random and saturation currents
I_r, I_s	-	ion random and saturation currents
P	-	pressure
n	-	particle density
μ	-	particle mobility
d	-	spacing
K	-	coefficient of thermal conductivity
V_i	-	ionization energy of cesium
V	-	potential difference
e	-	electronic charge
n_s	-	Saha equilibrium particle density
$\dot{\xi}$	-	net ionization rate
Q	-	energy
x	-	distance from emitter edge of plasma
$\bar{x}$	-	normalized distance = $\frac{x}{d}$
α	-	parameter describing generation and recombination rates
N_o	-	neutral particle density

Primes refer to differentiation with respect to $\bar{x}$.

Subscripts:

e, i, n	-	electron, ion and neutral components
o, 1	-	values at emitter and collector edges of plasma, respectively
ε, c	-	values for emitter and collector side of sheath

$$J_e = \mu_e(\theta_e)\left[\theta_e \frac{dn}{dx} + en\frac{d\psi}{dx}\right] \tag{1.1}$$

$$J_i = \mu_i(\theta_i)\left[\theta_i \frac{dn}{dx} - en\frac{d\psi}{dx}\right] \tag{1.2}$$

$$Q_e = J_c\left(\frac{5}{2} + \psi\right) - K_e \frac{d\theta_e}{dx} \tag{1.2}$$

The continuity relations give three more equations:

$$\frac{dQ_e}{dx} = -V_i\dot{\xi} \tag{1.4}$$

$$\dot{\xi} = \frac{dJ_e}{dx} \tag{1.5}$$

$$\frac{dJ_e}{dx} = \frac{dJ_i}{dx} \tag{1.6}$$

Finally, there is the ionization equation assumed as:

$$\dot{\xi} = \alpha(n_s^2\, n - n^3) \tag{1.7}$$

and the ion temperature variation, which was assumed to be constant:

$$\theta_i = \frac{\theta_\varepsilon + \theta_c}{2} \tag{1.8}$$

These eight equations and the eight unknowns (θ_e, θ_i, J_e, J_i, ψ_i, n, $\dot{\xi}$, Q_e) form a complete set which may be solved numerically, given the required number of boundary conditions.

At the emitter with an accelerating sheath, the equations are

$$J_{eo} = J_{sE} - J_{ro} \exp(-V_E/\theta_{eo}) \tag{2.1}$$

$$J_{io} = I_{sE} \exp(-V_E/\theta_E) - I_{ro} \tag{2.2}$$

$$Q_{eo} = J_{sE}(2\theta_E + V_E) - (J_{sE} - J_{eo})(2\theta_{eo} + V_E) \tag{2.3}$$

Similarly, for the collector with an accelerating sheath,

$$J_{el} = J_{rl} - J_{sc} \exp(-V_c/\theta_c) \tag{3.1}$$

$$J_{il} = I_{rl} \exp(-V_c/\theta_{ei}) - I_{sc} \tag{3.2}$$

$$Q_{el} = 2 J_{rl} \theta_{el} - 2 J_{sc} \theta_c \exp(-V_c/\theta_c) \tag{3.3}$$

and for the retarding sheath collector,

$$J_{el} = J_{rl} \exp(-V_c/\theta_{el}) - J_{sc} \tag{4.1}$$

$$J_{il} = I_{rl} - I_{sc} \exp(V_c/\theta_c) \tag{4.2}$$

$$Q_{cl} = -J_{sc}(2\theta_c + V_c) + (J_{sc} + J_{el})(2\theta_{el} + V_c) \tag{4.3}$$

With the additional initial conditions of J_{eo} (the operating point on the J-V characteristic) and $\psi_o = 0$ (the voltage reference value), the system of equations forms a complete set which may be solved numerically using a digital computer. Values must be given for relating parameters μ, α, and σ to the plasma variables. The relations used were described in Reference 1.

2. Computer Technique

In solving these equations, a set of initial conditions was chosen and the solution advanced step by step across the plasma until one of the sets of collector boundary relations could be satisfied or until the values for a particular step became unreasonable. The distance reached was then examined, and the initial conditions were modified in a manner allowing the integration to proceed further. A new integration from the emitter was carried out next. The process was continued until a set of collector boundary conditions was matched at the desired spacing. Values of the variables as a function of position for the final step were printed out. Particle density and electron temperature were the initial conditions varied to obtain the solution.

During the early part of the study, the computer program used the Euler[2] integration technique, which is simple and requires only that derivatives at a point and the distance to the next point be known. However, because of a buildup of errors with this method, extremely small steps were required, and the resulting calculations proceeded too slowly.

After some experiments, the program was modified to use a Runge-Kutta technique[3] which requires four calculations of a variable for each step but retains sufficient accuracy that relatively large steps may be used. Since only values at a single point need be retained, this system has the advantage over some of the other methods.

A factor of two to three improvement in running time was observed with this method. Further improvement was required in the

searching techniques for initial values. It was found that, in many cases, convergence was very slow, and extremely good initial guesses were required to produce valid solutions. Because of these limitations it was possible to examine only a few cases with different parameters.

3. Directed Current Boundaries

In the boundary equations shown above, particle currents entering and leaving the plasma boundaries were expressed in terms of random current.

At the emitter,

$$\overleftarrow{J}_{eo} = J_{ro} \exp\ (-V_E/\theta_{eo}) \tag{5}$$

At the collector with accelerating sheath,

$$\overrightarrow{J}_{el} = J_{rl} \tag{6}$$

At the collector with retarding sheath,

$$\overleftarrow{J}_{el} = J_{rl} \exp\ (V_c/\theta_{el}) \tag{7}$$

where J_{ro} and J_{rl} are the electron random currents at the emitter and collector sheaths, respectively, $\overleftarrow{J}_{eo}$ and $\overrightarrow{J}_{el}$ are the electron currents from the plasma into the emitter and collector sheaths, V_E and V_c are the emitter and collector sheath heights, and θ_{eo} and θ_{el} are the electron temperatures in the plasma at the sheaths. Similar equations apply for the ion current components.

In nuclear reactor theory and some plasma analyses,[4, 5] the boundary conditions for the particle current are expressed in terms of directed current. The plasms boundary conditions are then:

$$\overleftarrow{J}_{eo} = J_{ro} \exp(-V_E/\theta_{eo}) - J_{eo}/2 \tag{8}$$

$$\vec{J}_{el} = J_{rl} + J_{el}/2 \tag{9}$$

$$\vec{J}_{el} = J_{rl} \exp(V_c/\theta_{eo}) + J_{el}/2 \tag{10}$$

where J_{eo} and J_{el} are the net electron currents at the sheaths. At the emitter sheath, for the cases examined so far, the random current is typically an order of magnitude higher than the net electron current. The effect of using the directed current will be small. At the collector sheath, however, where random current is almost equal to the net electron current, significant changes can be expected.

Substituting the directed current for random current in the collector boundary equations gives:

$$\frac{J_{ei}}{2} = J_{rl} - J_{sc} \exp(-V_c/\theta_c) \tag{11}$$

and

$$\frac{J_{il}}{2} = I_{rl} - I_{sc} \exp(V_c/\theta_c) \tag{12}$$

Since J_e and J_i are practically constant near the collector and the random currents fall with particle density, solutions with a directed-current boundary condition must occur closer to the emitter. To maintain the same spacing, a larger initial particle density is

is required. The particle density distributions for the two boundary conditions are compared in Figures VI-1 and VI-2. Other than the slight increase in initial concentration, the results are similar. For most of the cases studied the directed-current boundary condition can be expected to produce only small deviations from random-current boundary solutions.

4. Influence of Pressure and Spacing on Plasma Characteristics

Changes in the plasma characteristics associated with cesium pressure or interelectrode spacing variations form an extremely useful group of parameters for the evaluation and understanding of the analytical results. This is particularly true in the case of spacing, since electrode work functions will remain constant. Thus valid comparisons can be made between experimental and calculated J-V curves and their variations with spacing.

Cesium pressure enters into the normalized plasma equations[1] through its effect on the ion and electron mobilities, which can then be expressed as:

$$\mu_e = \frac{F_e(\theta_e, \sigma_{en})}{N_o} \tag{13.1}$$

$$\mu_i = \frac{F_i(\theta_i, \sigma_{in})}{N_o} \tag{13.2}$$

where N_o may be determined from the pressure p by the ideal gas law:

$$p = N_o \theta_n \tag{14}$$

Note that the mobility relations neglect electron-ion collisions which have been shown to be significant.[6] However, since this factor has

been neglected throughout the analysis, these results will serve as a basis for evaluating the effects of these collisions when they are included in the future work. Rewriting the normalized plasma relations to include equations 13.1 and 13.2 gives:

$$n' = -\left(\frac{J_e'}{e F_i(\theta_i, \sigma_{in})} + \frac{J_e}{e F_e(\theta_e, \sigma_{en})}\right)\frac{Pd}{(\theta_e + \theta_i)\theta_n} \qquad (15.1)$$

$$\psi' = \frac{1}{n}\left(\frac{J_i}{\theta_i e F_i(\theta_i, \sigma_{in})} - \frac{J_e}{\theta_e e F_e(\theta_e, \sigma_{en})}\right)\frac{Pd}{\left(\frac{1}{\theta_e} + \frac{1}{\theta_i}\right)\theta_n} \qquad (15.2)$$

$$\theta_e' = \frac{J_e'}{J_e}\left(\theta_e + \frac{2}{5}\psi + \frac{2}{5}V_i\right) - \frac{2}{5}\psi + \frac{2}{5}\frac{K_e}{J_e}\theta_e'' + \frac{2}{5}\frac{K_e'}{J_e}\theta_e' \qquad (15.3)$$

$$J_e' = J_i' = e d \alpha n (n_s^2 - n^2) \qquad \begin{matrix}(15.4)\\(15.5)\end{matrix}$$

$$Q_e = \left(\frac{5}{2}\theta_e + \psi\right) J_e - K_e \theta_e' \qquad (15.6)$$

From the equations it is seen that d appears in the diffusion and field equation (15.1 and 15.2) only in combination with the pressure, and in the ionization equation (15.5) together with the Saha equilibrium density, n_s. Since this density is also a function of neutral density, namely,

$$n_s^2 = \left(\frac{2\pi n_e \theta_e}{h^2}\right)^{3/2} N_o \exp(-v_i/\theta_e) \qquad (16.1)$$

or

$$n_s^2 = PS(\theta_e, \theta_n) \qquad (16.2)$$

equation 15.5 becomes:

$$J_e' = e P d \alpha n \left(S(\theta_e, \theta_n) - \frac{n^2}{P}\right) \qquad (17)$$

It is only in the last term of the equation that spacing appears alone rather than in a spacing-pressure product. Thus, in those cases where the net ionization rates are small over a large fraction of the plasma width, the plasma characteristics should be independent of spacing, provided the Pd product is held constant.

Calculated current-voltage points for two pressures are shown in Figure VI-3. Except for the two large Pd points, where convergence difficulties were encountered, changing pressure with constant Pd has little effect. Figure VI-4 shows a comparison of the plasma variable distribution at small Pd and Figure VI-5 shows the comparison at moderate Pd. For the low Pd case, there is relatively little ionization, so that the distribution curves for 1 torr and 2 torr are coincident on the plot. However, with larger values of Pd (greater spacing), the carrier concentration becomes greater, and significant generation and recombination take place across the plasma. The distributions now have a pressure dependence. From equation 17, the effect of increased pressure is to reduce the value of the recombination term (n^2/p), thereby establishing a slightly higher concentration level. The particle density and ionization curves, Figure VI-5, illustrate these changes.

The effect of spacing was evaluated by calculating points on J-V curves having different interelectrode spacings. Figure VI-6 shows a set of these J-V curves. Since all curves have the same cesium pressure and emitter temperature, the voltage differences are dependent on plasma changes only, and may be compared to similar experimental variable-spacing families. Only the changes from curve to curve may be compared, not the absolute voltage levels. An actual

spacing family from the single crystal tungsten converter described elsewhere in this report is shown in Figure VI-7. A comparison of these two sets of curves shows that they indicate the same trends with spacing for both the lower mode region and the saturation region. However, at the knee and at the "de-ignition" point, there is a significant discrepancy in voltage relationships. Part of the difficulty may be due to the limited number of calculated values defining this region. The experimental data indicate a set of parallel curves, each having the same "de-ignition" point, while the calculated curves show a distinct trend towards lower "de-ignition" point voltages with smaller spacing. Spacing families often show the opposite trend, increasing "de-ignition" point voltages with decreasing spacing. Since the small spacing curve corresponds to a Pd of only 5 mil-torr, it is likely that the generation region at the emitter edge of the plasma is being squeezed so that ionization is less efficient. At these narrow widths, there may not be sufficient collisions for the electrons to thermalize; thus the assumption of a Maxwellian distribution breaks down at this spacing. Figure VI-8 compares the distributions for 2.5 mil and 10 mil spacings at $J_{eo}/J_{sE} = .5$. Notice that the generation region extends over a large fraction of the spacing. Because these plots have been normalized, it is difficult to visualize the actual extent of the generation region. Figure VI-9 shows the plots in real distance; the ionization region is seen to extend over a similar distance for the two spacings. The crowding of the ionization region is evident in the 2.5 mil spacing case.

5. Ion Mobility

A theoretical analysis of this type provides the facility to study parameter changes and their influence on the J-V characteristics. These studies can be used to help separate and define the influence of various plasma parameters. The ability to examine the changes produced by varying one parameter while holding the others constant can be used to accentuate the effects of a particular variable. The importance of ion mobility was examined in this manner.

Distributions were calculated, first for the reference value of an ion-neutral cross-section, and then for a value an order of magnitude smaller. All other parameters were held constant. Computed J-V points for the two cases are shown in Figure VI-10. Only a slight change in the characteristics can be seen. The higher mobility points (with lower cross-section) show slightly lower output values. While the complete J-V curve was not obtained, the trend is evident. Distributions for the two nearly equal current values are compared in Figures VI-11 and VI-12. Even though the distributions have been significantly changed by the new value for ion mobility, there is only a slight shift of the J-V characteristic. This effect again shows that the J-V characteristic is relatively insensitive to the details of the plasma.

Increased ion mobility has allowed a greater diffusion current for a given carrier density gradient resulting in a lower peak particle density. At the plasma ends, the higher mobility causes greater ion currents to flow into the electrodes. The J_i curves of Figure VI-12 indicate these currents, with J_i positive near the collector and negative near the emitter. Because of the increased ion losses

at the ends, there must be a significant generation rate throughout the plasma. The ξ curves of Figure VI-11 show the increased ion generation. It is quite likely that the energy required for this generation nearly makes up for the current increase expected due to the ion mobility increase. The ψ curves of Figure VI-12 show the greater voltage loss through the plasma for the high mobility case. Thus, it is seen that an increase in ion mobility is associated with many compensating effects which leave the performance characteristics of a converter relatively unchanged. Experimental evidence of this phenomenon was shown in the inert gas experiments.[7,8] The addition of the gas obviously greatly modified the atom and ion mobility, yet it only slightly reduced the performance.

6. Conclusions

These studies have shown that, in the cases examined, the substitution of directed current for random current boundary conditions caused only slight changes in the plasma distributions. However, because of the lower particle densities at the collector, it was more difficult to obtain solutions with the directed current boundary.

The plasma equations indicate that the solutions should be relatively independent of pressure and spacing as long as their product is held constant. Calculated points verified this relation, but showed density variation at moderate Pd's which would lead to further deviations if ion-electron collisions were included in the calculations. Points calculated at various spacings indicated the proper spacing dependence, but also indicated the need for corrections to the ionization term, particularly at small spacings.

The results obtained when ion mobility was varied show considerable changes in the distributions but only slight changes in the J-V characteristics. These results are in agreement with experimental data in which the introduction of inert gases modified the performance much less than would be expected.

REFERENCES FOR CHAPTER VI

1. "Final Report on Research in Thermionic Conversion," Thermo Electron Report No. TE4072-49-68, prepared for National Aeronautics and Space Administration, Pasadena, under Contract NAS7-508, 1968.

2. F. B. Hildebrand, Introduction to Numerical Analysis, McGraw-Hill Book Company, New York: 1956, p. 198.

3. Ibid., p. 233.

4. C. Warner, and L. K. Hansen, "Transport Effects in the Electron-Rich Unignited Mode of Cesium Diodes." J. Appl. Phys. 38 (1967), p. 491.

5. Davidson, B., Neutron Transport Theory. Oxford University Press, New York, 1957.

6. William L. Nighan, "Electron Transport Phenomena in Thermionic Converter Plasmas," Report on Thermionic Conversion Specialist Conference, Houston, Texas, November 1966, pp. 276-286.

7. F. Rufeh and D. Lieb, "Electron Scattering in Thermionic Converters by Xenon, Krypton, and Argon," presented at the Second International Conference on Thermionic Electrical Power Generation, Stresa, Italy, May 1968.

8. F. Rufeh and D. Lieb, "The Influence of Inert Gases on the Characteristics of Thermionic Converters," Final Report for the Air Force Cambridge Research Laboratories, Contract No. F19628-67-C-0091, September 1968.

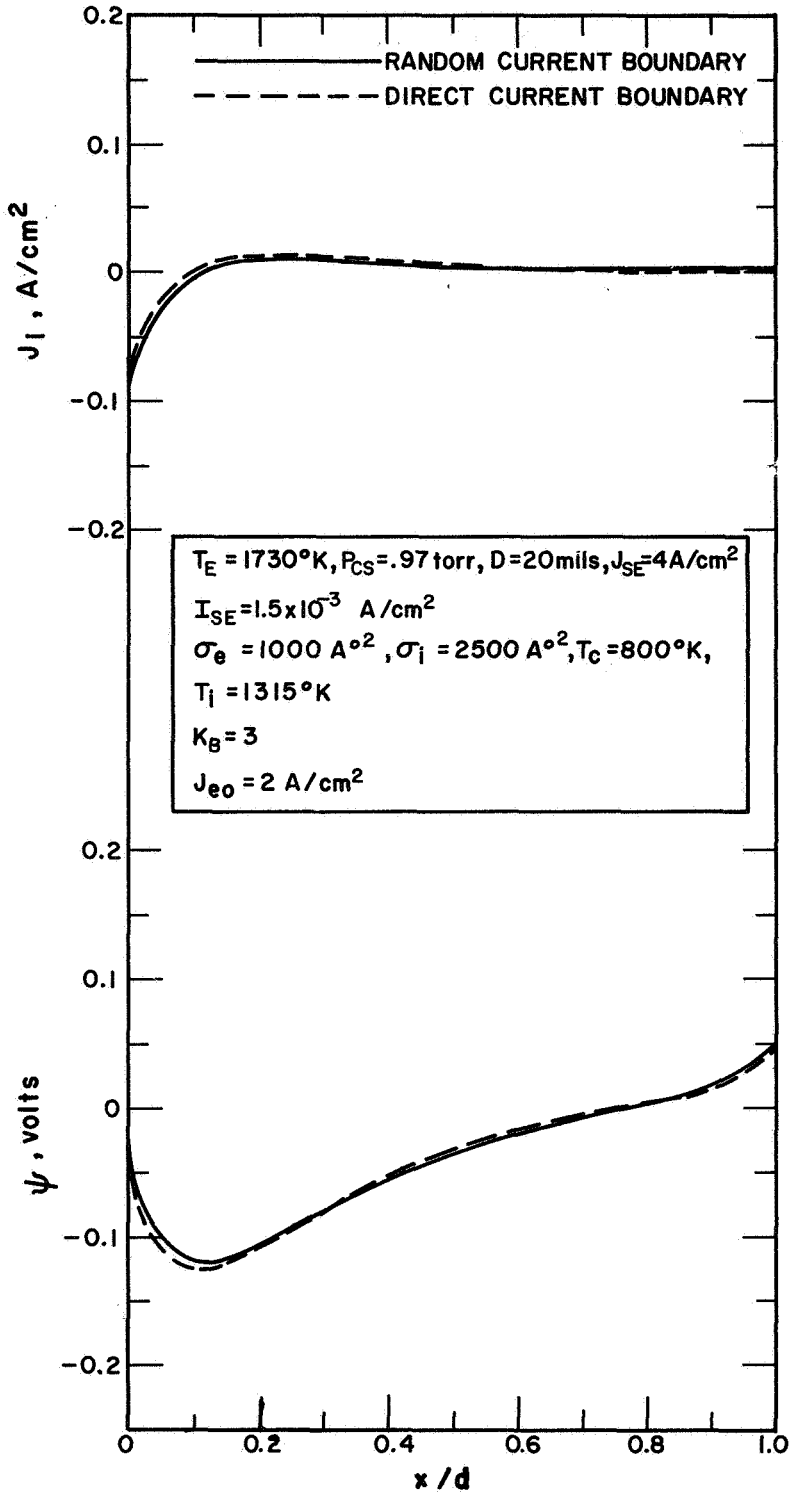

Figure VI-1. Comparison of Plasma Distributions for Different Boundary Conditions.

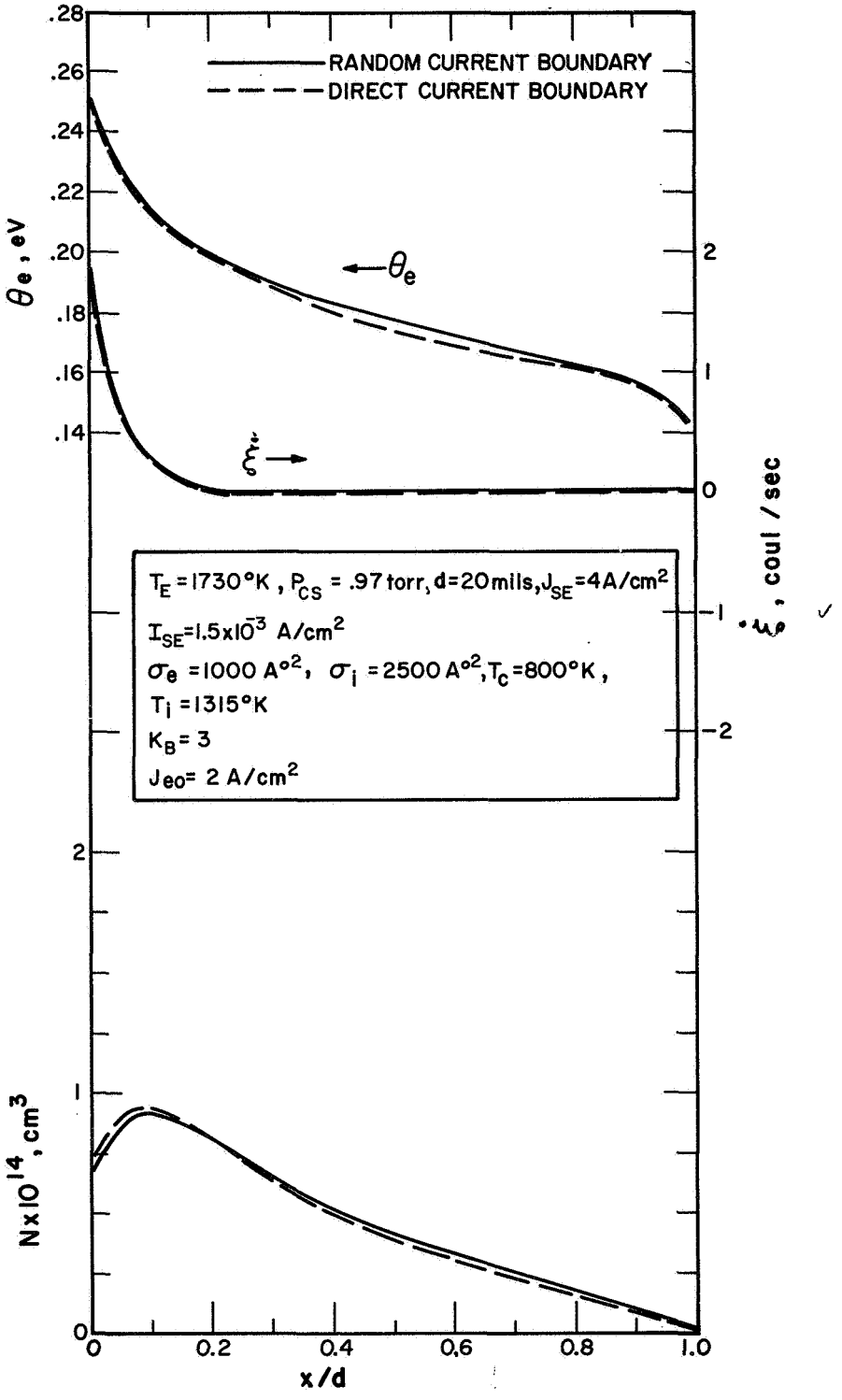

Figure VI-2. Comparison of Plasma Distributions for Different Boundary Conditions.

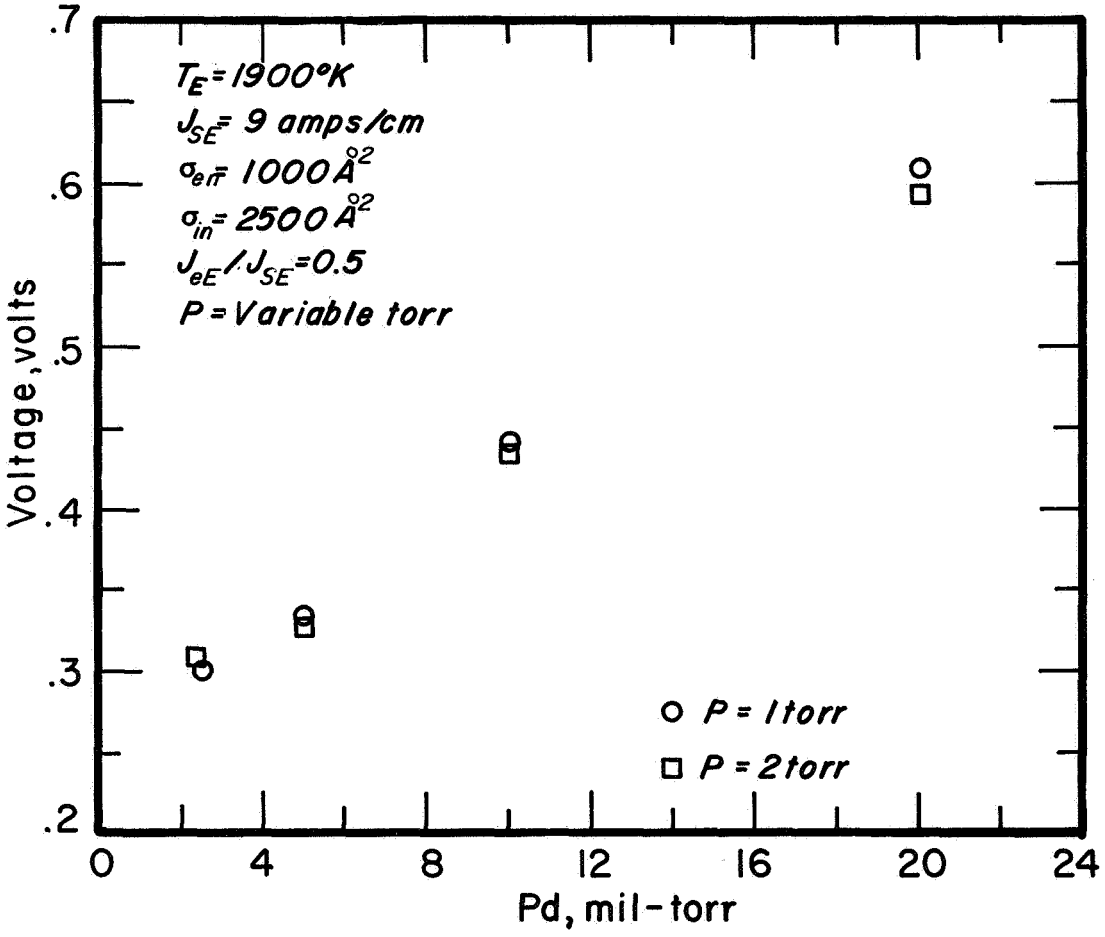

Figure VI-3. Plasma Voltage Drop as a Function of Pd for P = 1 torr and P = 2 torr.

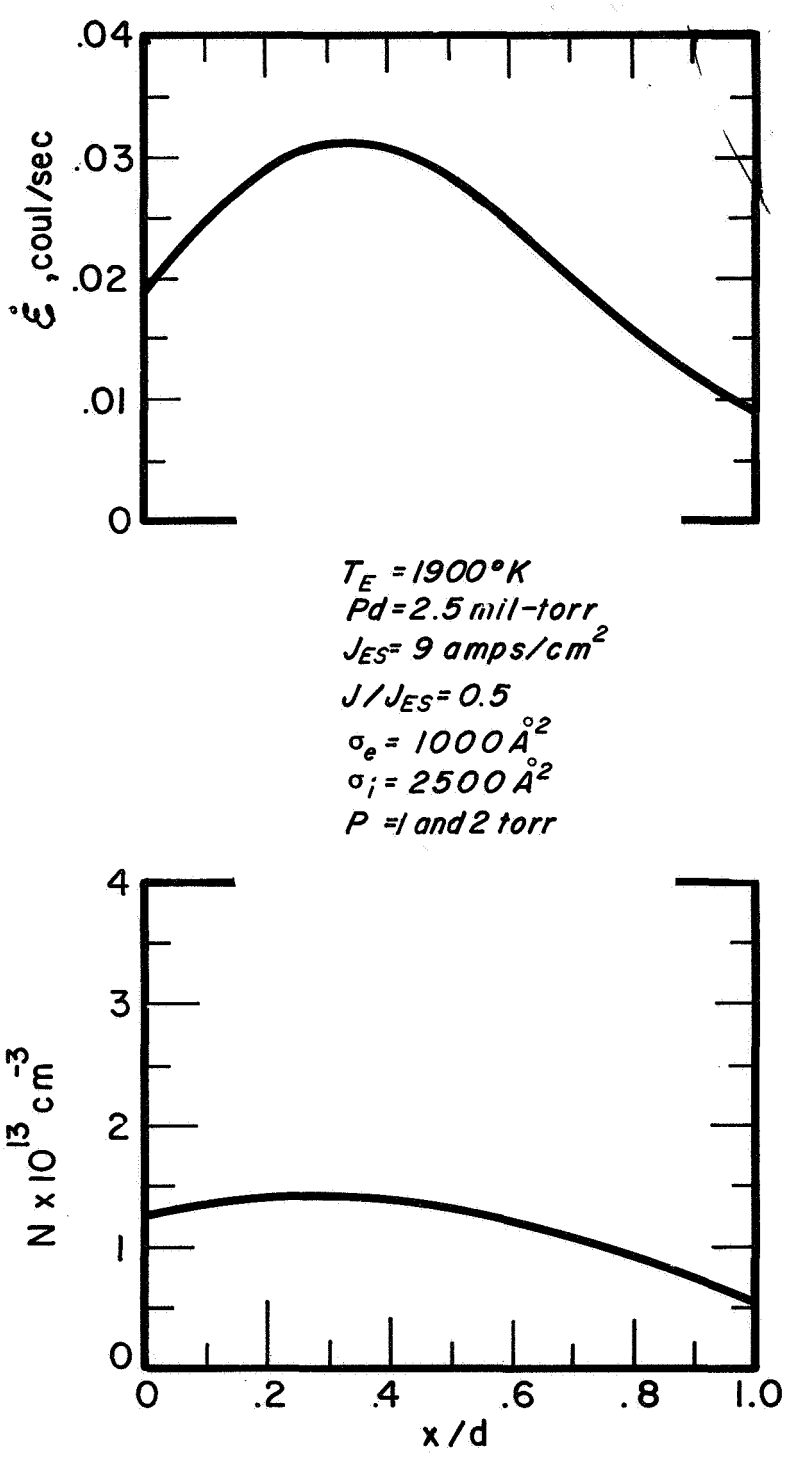

Figure VI-4. Plasma Distributions for Small Pd.

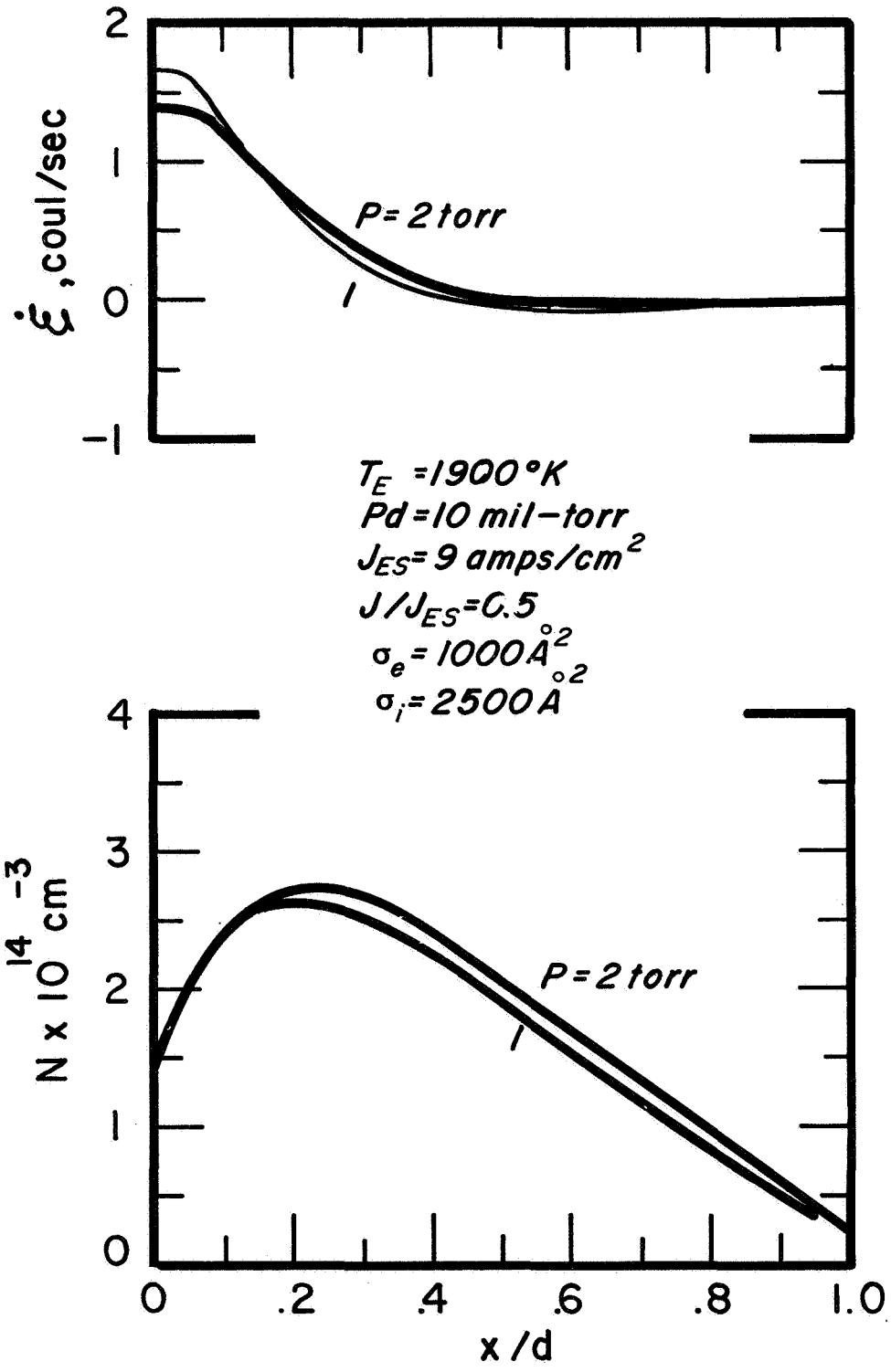

Figure VI-5. Plasma Distributions for Moderate Pd.

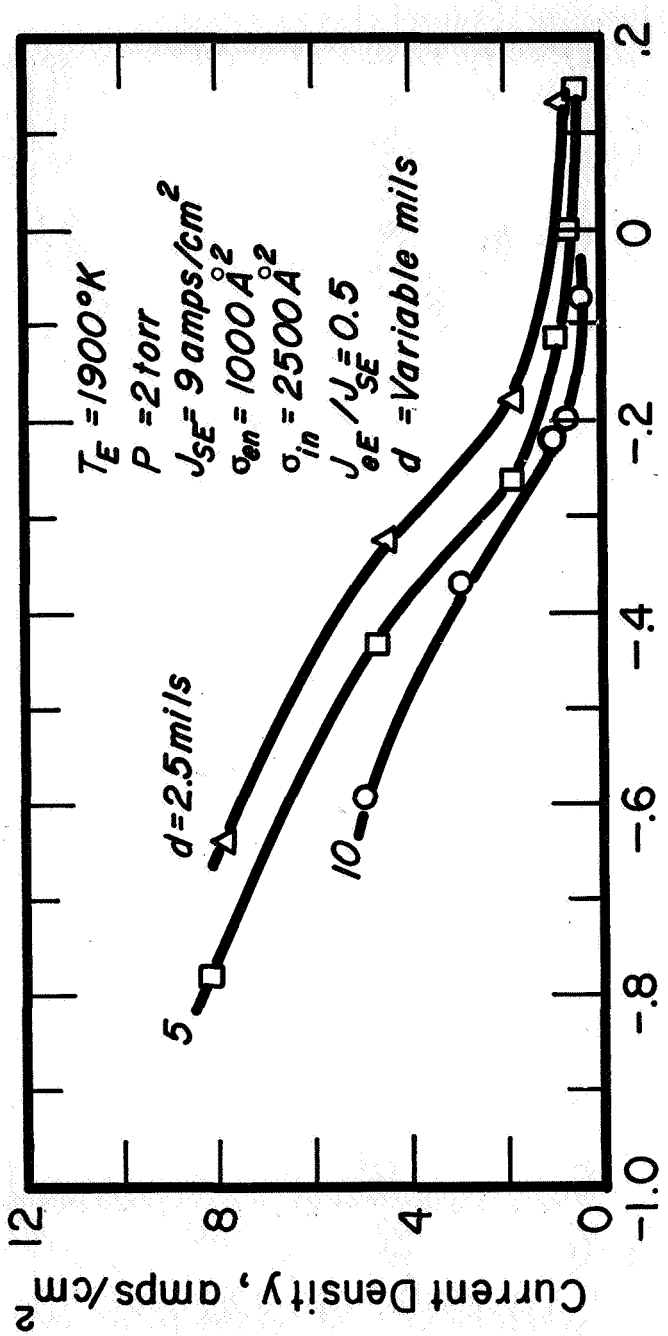

Figure VI-6. Calculated J-V Curves for Various Spacings.

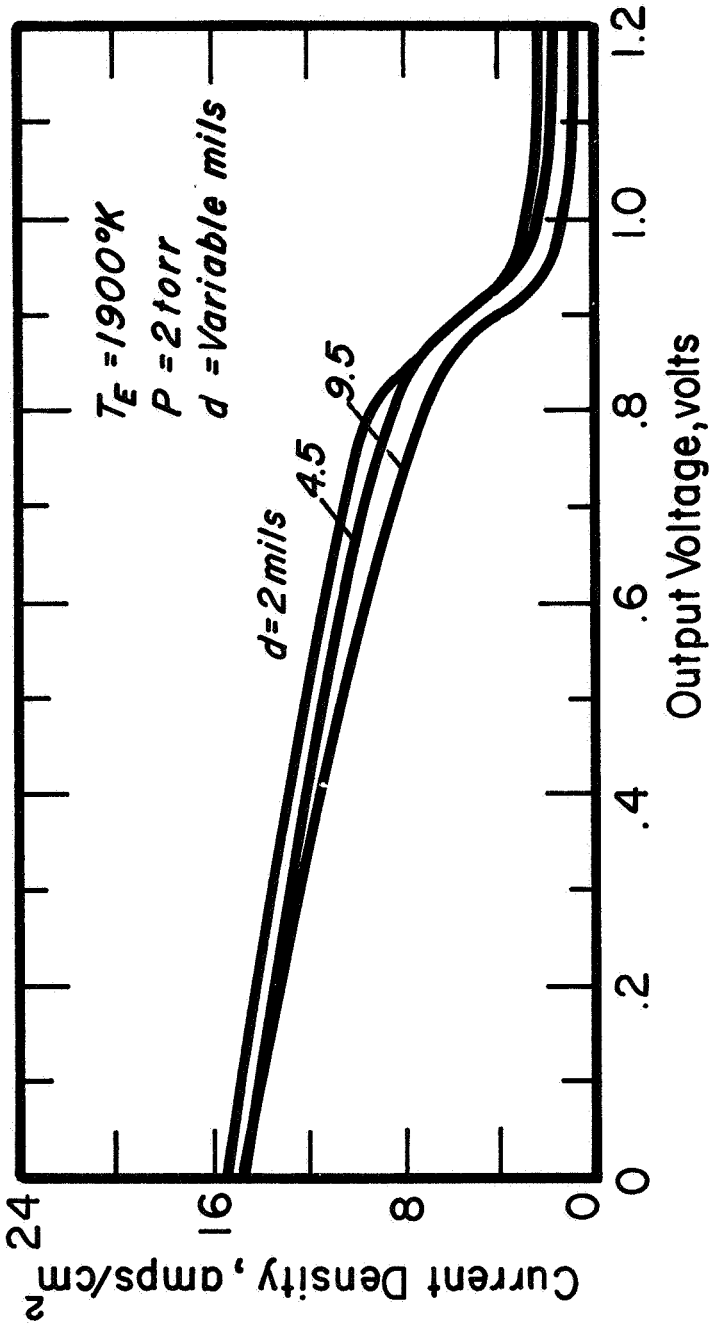

Figure VI-7. Experimental J-V Curves for Various Spacings.

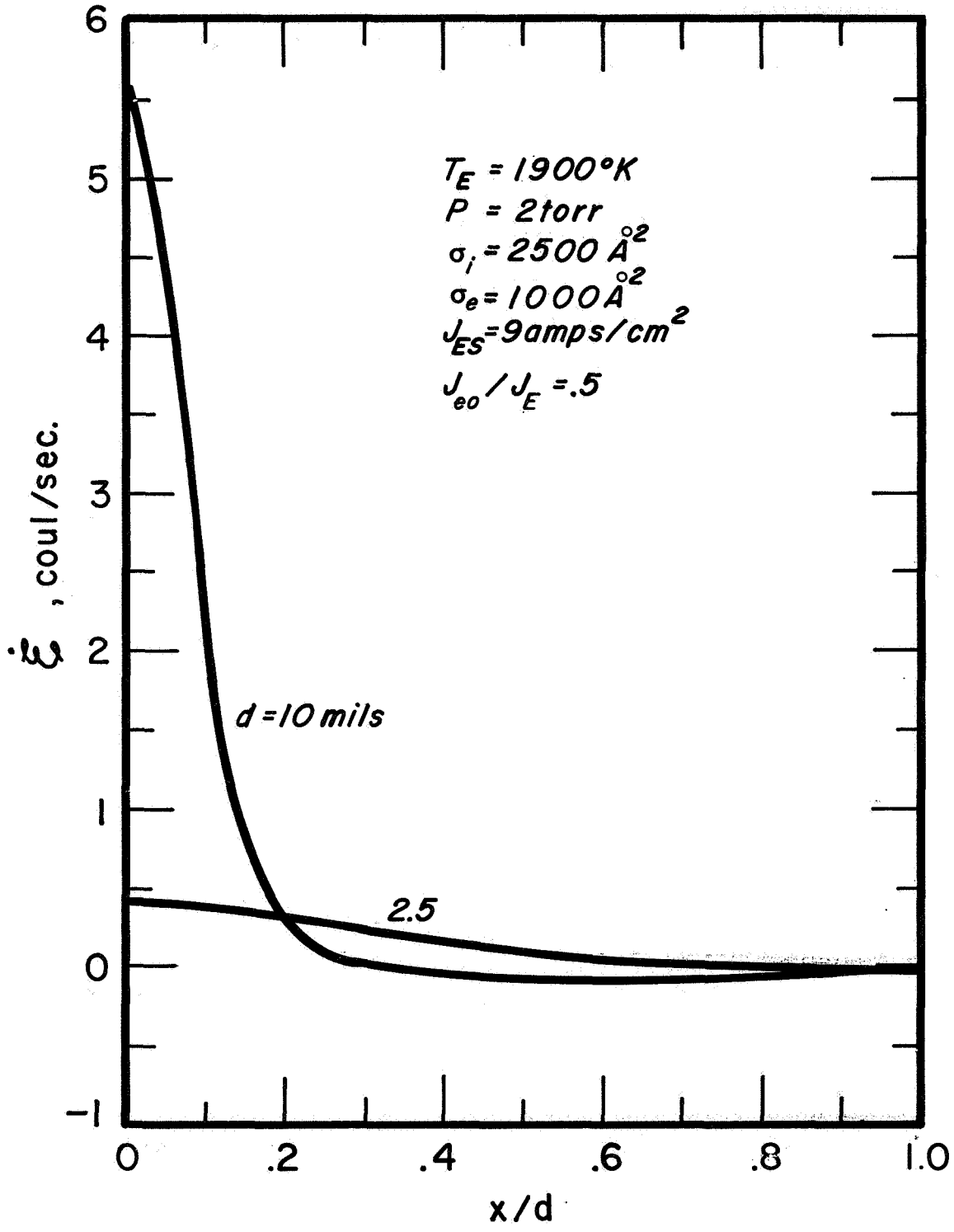

Figure VI-8. Comparison of Generation Rates for Small and Large Spacing (Normalized Distance).

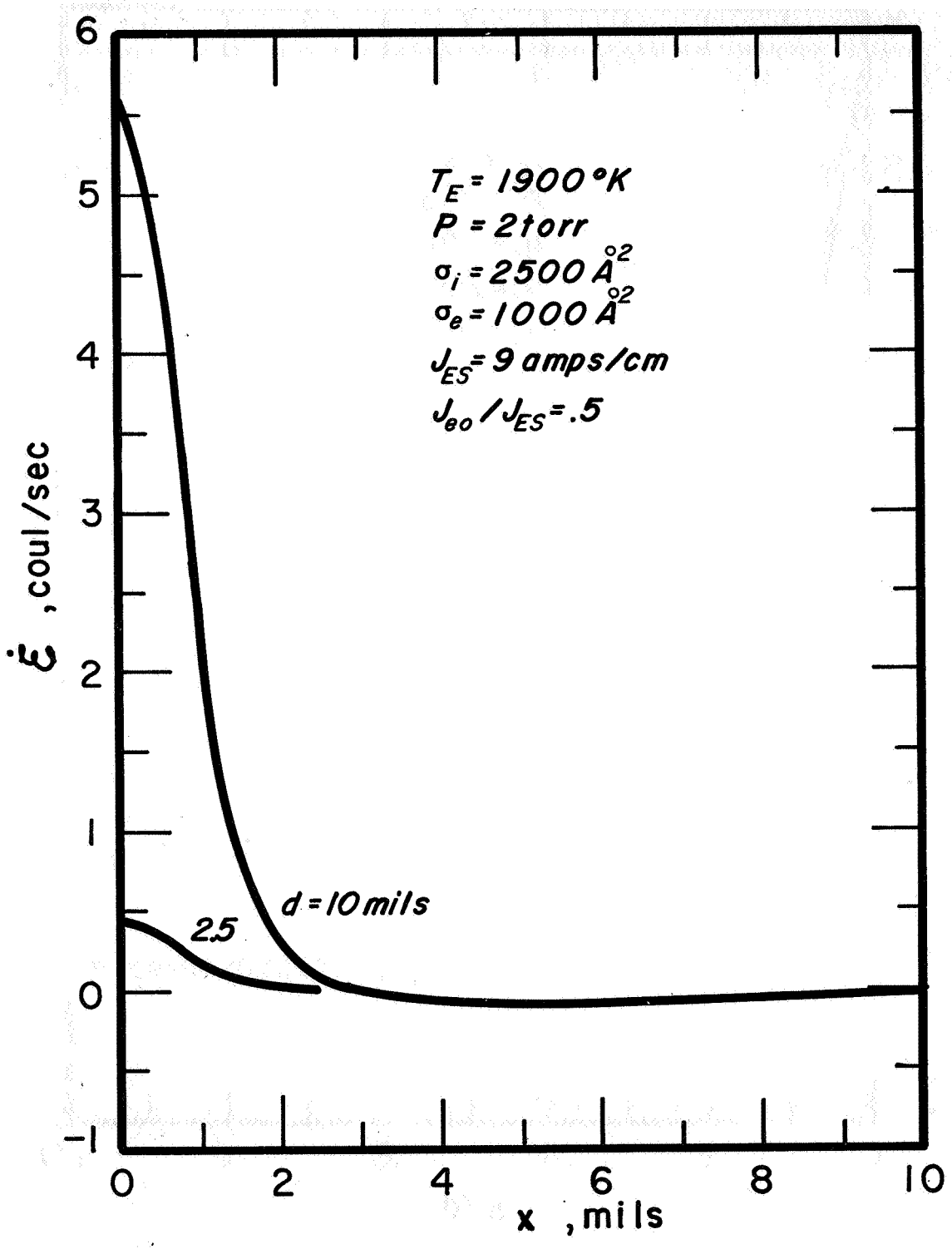

Figure VI-9. Comparison of Generation Rates for Small and Large Spacing (Actual Distance).

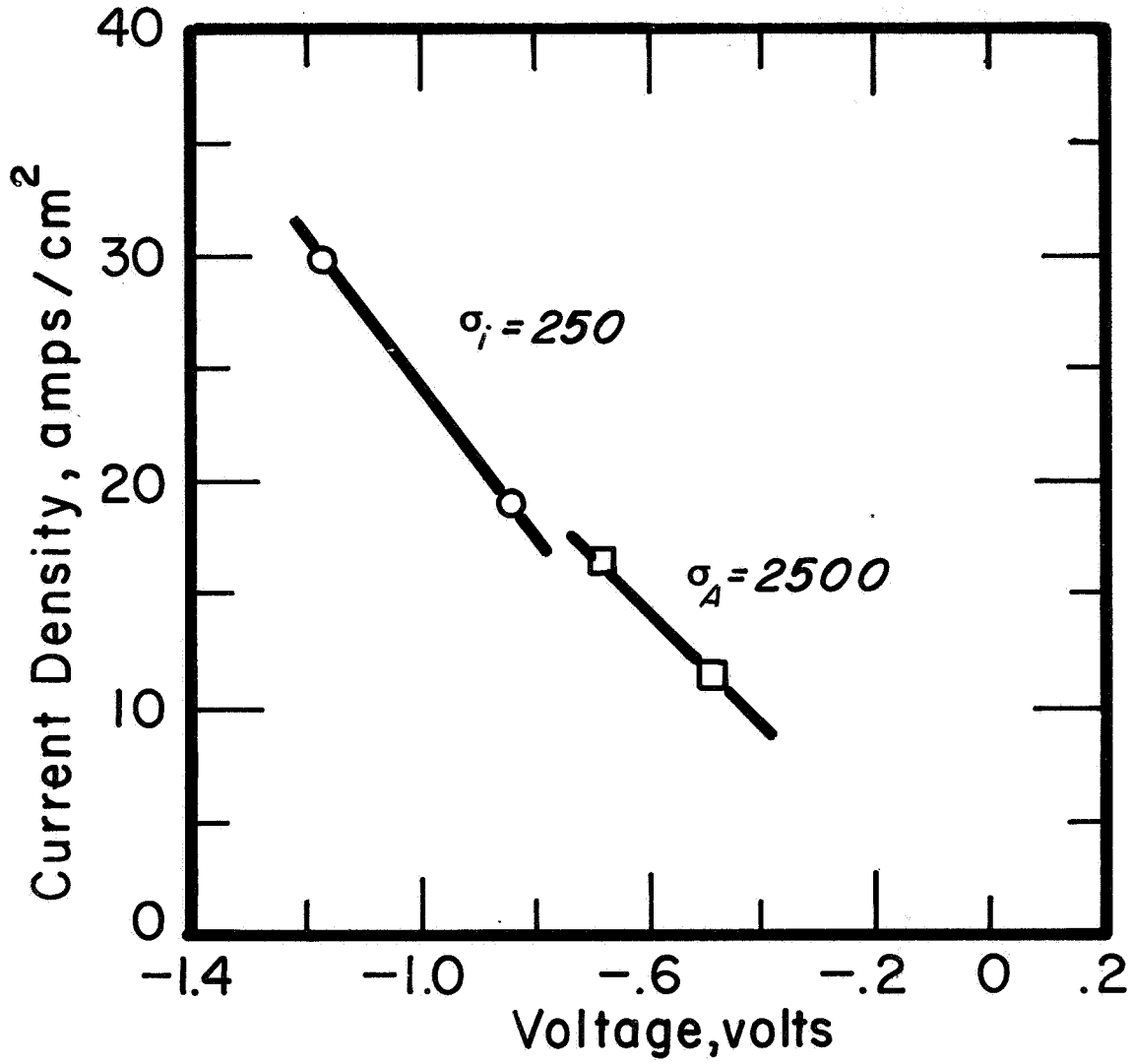

Figure VI-10. Comparison of Calculated Current-Voltage Points For Different Ion Mobilities.

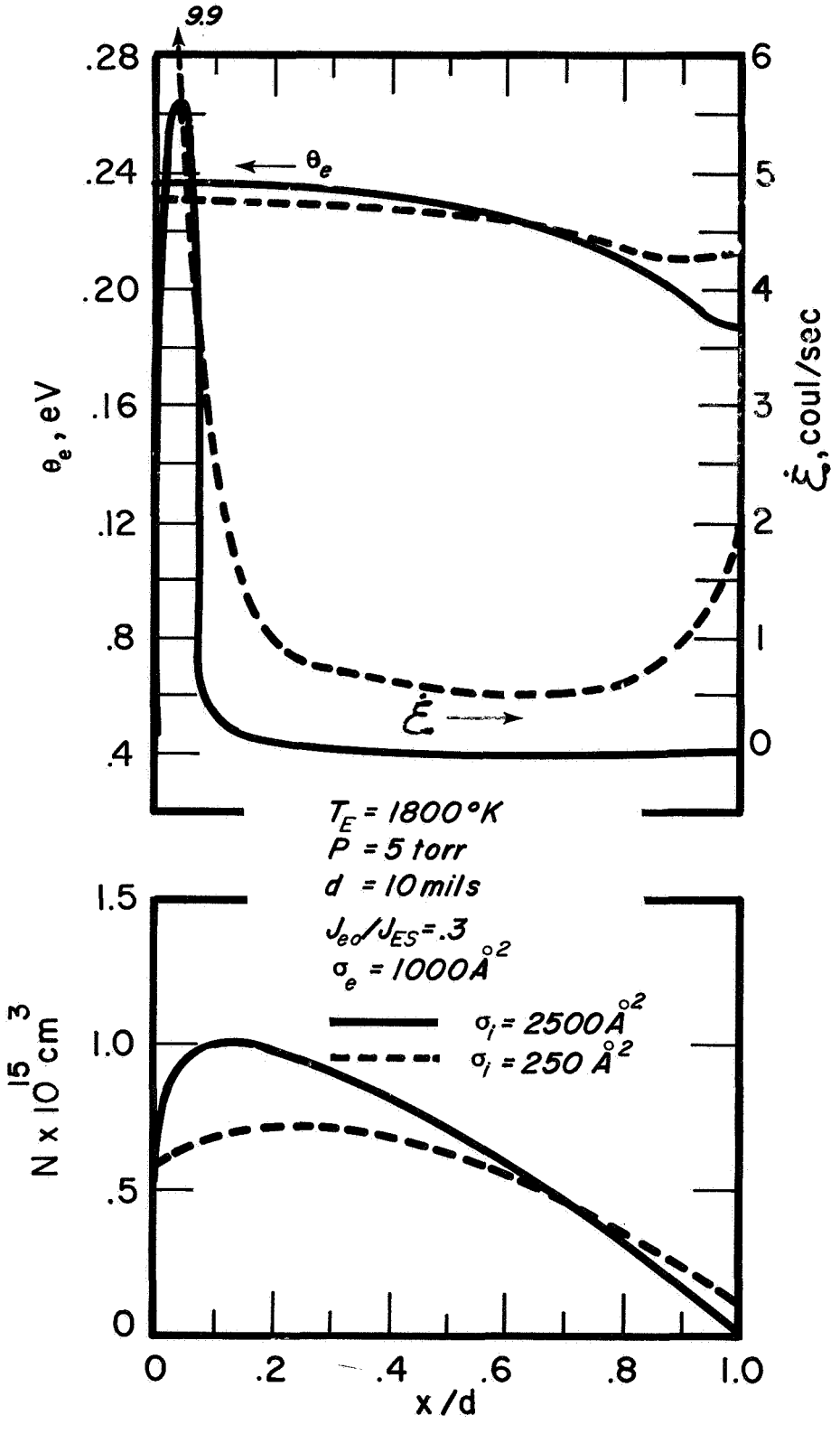

Figure VI-11. Comparison of Plasma Distributions for Different Ion Mobilities.

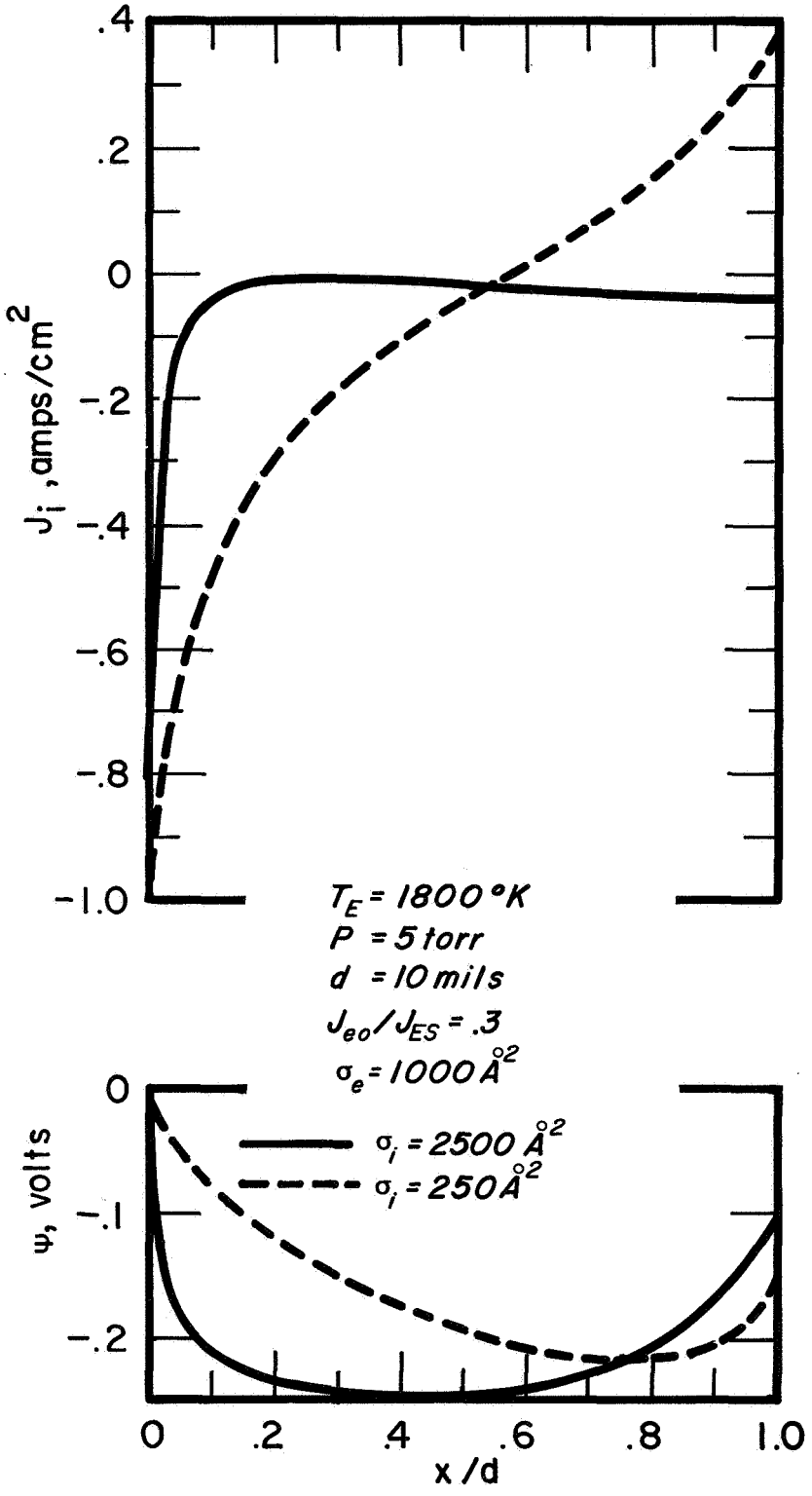

Figure VI-12. Comparison of Plasma Distributions for Different Ion Mobilities.